

POLITECNICO DI MILANO

Dipartimento di Chimica, Materiali e Ingegneria Chimica “G. Natta”



**Spectroscopic investigation
of structure-property relationships
in organic molecular and polymeric crystals
from first-principle methods**

PhD in Materials Engineering, XXV cycle

Supervisor:
Dr. Mirella Del Zoppo
Tutor:
Prof. Chiara Castiglioni

Candidate:
Claudio Quarti

Coordinator of the doctoral program: Prof. Chiara Castiglioni

Aknowledgements/Ringraziamenti

Quando si scrivono i ringraziamenti di un lavoro lungo e che ha richiesto un così grande sforzo sia da parte mia, sia da parte di molti collaboratori, colleghi e insegnanti, si ha sempre il timore di dimenticare qualcuno o di non dare il giusto rilievo a tutti. Premesso questo, credo onestamente che il mio primo e più vivo ringraziamento debba andare ai miei colleghi Alberto Milani e Daniele Fazzi (l'ordine è puramente alfabetico), che sono stati un aiuto prezioso e un esempio e con i quali nel tempo si è sviluppato un profondo rapporto di stima e amicizia. A loro, sento di dover dire solo una cosa: *“Il mio obiettivo in tre anni è stato diventare bravo almeno la metà di voi”*.

Oltre a loro, meritano un vivo ringraziamento le nostre care colleghe Daria e Ester. Un grazie alle ragazze e ai ragazzi della controparte sperimentale del gruppo, che hanno sempre cercato di mantenere un ambiente vivo e piacevole. Un grazie a Gigi e Andrea, per avermi fornito gli spettri e, in definitiva, per avermi dato il materiale su cui lavorare. Un grazie a Matteo per il supporto tecnico/informatico/matematico/umano.

Un grazie a Mirella del Zoppo e a Chiara Castiglioni, che mi hanno dato la splendida opportunità di svolgere questo dottorato di ricerca e che sono state sempre infinitamente disponibili nei miei confronti.

Un grazie ai miei amorevoli genitori e a mia sorella Lisa, per l'affetto e il supporto costante. Un grazie a Nicola e a tutti gli amici di sempre, per avermi sempre ricordato che il mondo reale sta al di fuori del laboratorio.

Un grazie al Dottor Paolo Colla per i suggerimenti e le massime di saggezza.

a nonna Liliana e nonno Francesco

Contents

Aknowledgements/Ringraziamenti	i
Abstract	vii
1 Introduction	1
2 Excitons in molecular crystals	5
2.1 Introduction	5
2.2 Describing excitons in molecular crystals	8
2.2.1 Exciton Hamiltonian: the Frenkel Hamiltonian	8
2.2.2 Methods for the evaluation of the exciton coupling	11
2.2.3 Transition Density Matrices (TDM) projection method	14
2.3 Publications	15
2.3.1 attachment a	21
2.3.2 attachment b	29
3 Vibrational spectroscopy of polymeric crystals	41
3.1 Introduction	41
3.2 Methods	44
3.2.1 Description of the van der Waals interactions	44
3.2.2 Eigenvector projection method	47
3.3 Publications	49
3.3.1 attachment c	55
3.3.2 attachment d	78
3.3.3 attachment e	92
Appendices	
A Organic and hybrid nanostructures for SOLar energy CON- version (SOLCO)	107
A.1 Introduction	107
A.2 Experimental results	109
A.3 Theoretical calculations	110
A.3.1 Optical properties of the isolated molecule	110

A.3.2	Calculations with PCM	111
A.3.3	Explicit interaction models	114

Abstract

Organic materials present a unique combination of features that make them suitable for a large variety of applications. However, the development and the optimization of these materials requires an in-deep knowledge of the *structure-property* relationships. In the last two decades, *quantum chemical* methods for electronic structure calculations have proven to be useful tools in the study of structure-property relationships but their application to extended, complex systems such as organic molecular crystals and polymeric materials, whose properties are dictated by both intra- and inter-molecular interactions, has been quite limited. In this thesis we apply state-of-the-art quantum chemical methods to study the structure, the electronic properties and the spectroscopic response of some molecular and polymeric crystals.

In the first part of the thesis, we have investigated the exciton properties of molecular crystals. The Frenkel exciton Hamiltonian has been used to model excitons in crystals and the main parameters of this Hamiltonian, the *exciton couplings*, have been calculated by using quantum chemical simulations. We have tested our methodology to a test case, the crystal of *para-nitro-aniline*, and then we have studied the exciton properties of some molecular crystals of technological interest, acenes and their derivatives. In this case in particular, we were interested in finding useful guidelines for the design of materials which show efficient *Triplet-Triplet Annihilation* (TTA). Through this study we highlighted the effect of the chemical substitution on the exciton mobility in these crystals and we have addressed some of the molecular requirements necessary to obtain materials with efficient TTA.

In the second part of the thesis, we have studied the structure and the InfraRed (IR) spectroscopic response of polymeric crystals. The structure and the IR spectrum of the α form of *nylon 6,6* and of the α and γ forms of *nylon 6* have been calculated. For the first time these calculations have been carried out on 3-D periodic models, instead of on infinite chains or on oligomeric models. The good agreement between theoretical and experimental spectra demonstrates that quantum chemical methods are nowadays suitable to study complex systems such as polymeric crystals. On the basis of the theoretical calculations, we have revised the interpretation of the IR spectra of these polymers, solving the ambiguities and the controversial assignments found in the literature. A thorough study has been

carried out to revise the interpretation of the IR spectrum of crystalline *poly(tetrafluoroethylene)*, PTFE, in particular on the assignment of the doublet at 626-638 cm^{-1} . On the basis of quantum chemical calculations we were able to address the contributions to the IR spectrum from the ordered phase, from conformational defects and from the amorphous phase. In addition, we have assigned the low frequency component of the 626-638 cm^{-1} doublet to the formation of helical-reversal defects.

Finally, we present the results of some DFT and TD-DFT calculations aimed to explain the optical properties of an organic dye, the 4-*hexylamino*-7-*nitro*-2,1,3-*benzoxadiazoles* in solution. UV-Vis and photoluminescence spectroscopies have showed that this chromophore presents a non monotonic shift of both the absorption and emission energy with the solvent's polarity.

Chapter 1

Introduction

In the last decades organic materials have been subject to an extraordinary success and they currently find application in a huge variety of fields. Organic materials are successfully used for structural applications, in textile as well as in transport industry, in optics [1] and electronic applications [2] and finally their use has been extended to innovative fields as biology and nanomedicine [3]. The success of this class of materials resides in a unique combination of properties like mechanical flexibility, low density, possibility to produce devices and manufactures with complex forms (for instance in thin film) and with low cost production techniques (printing and solution techniques). However, the main peculiarity of this class of materials is probably represented by the large possibilities of property tailoring, that allows to optimize the material properties for the specific requirements needed for a given application. This happens by properly modifying the material structure at the molecular scale, in a so called “*molecular engineering*” approach. The practical application of this approach requires a very deep knowledge of the *structure-properties* relationship. Traditionally, these *structure-properties* relationships were investigated through the use of materials characterization techniques, spectroscopic, diffraction, electrochemical and microscopic techniques. In particular, vibrational spectroscopy techniques, both Raman and Infrared, has been widely used in the past to study the structure and the properties of organic polymeric materials. For instance, Zerbi and its group in the late 80ies applied succesfully the Raman technique to study the electronic properties of π -conugated semiconducting polymers [4, 5]. In spite of the wide use of these characterization techniques, the interpretation and the assignment of the experimental spectroscopic features of organic molecular and polymeric materials is not simple. These materials in fact present a quite heterogeneous structure and their spectroscopic response is generally the sum of many contributions coming from fully ordered regions, disordered regions, local defects, surfaces, different regular structures (polymorphism) and so on. As a result, it is not unusual to find ambiguities and

contradictions in the literature on the interpretation of the spectroscopic features of organic systems, with subsequent debates on their structure and properties.

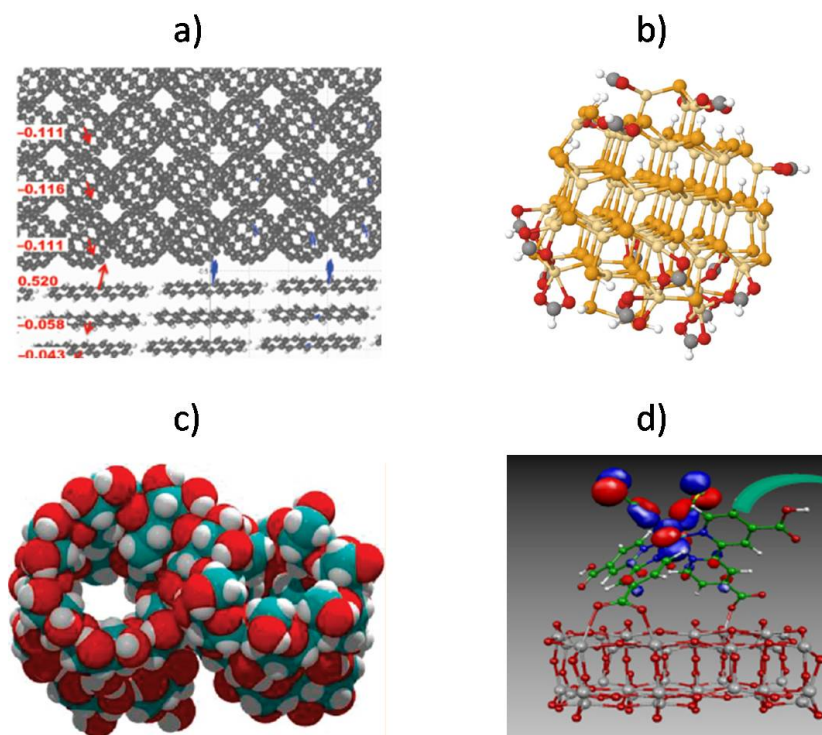


Figure 1.1: Examples of recent applications of quantum chemical calculation to extended systems. a) Electronic properties of the pentacene-C₆₀ interface [6] b) Inorganic CdSe nanocrystal [7] c) Equilibrium structure of cyclomaltohexaicosasaose [8]. d) Electron structure of Ruthenium based sensitizer on the surface of TiO₂ cluster [9].

Another tool for the investigation of the *structure-properties* relationships that has emerged in the last decades is represented by computer simulation techniques and in particular by *quantum-chemical* calculations. In the last two decades, these techniques have been fruitfully applied to highlight the connections between the structure-properties relationships of organic systems [10, 11, 12]. In addition, quantum chemical calculations are able to predict the spectroscopic response of the systems under investigation, thus providing a unique connection between *structure-spectroscopic response-properties*. With the development and the implementation of the *Density Functional Theory* (DFT) [13] and of its dynamic version, the *Time Dependent-Density Functional Theory* (TD-DFT) [14, 15], quantum chemi-

cal calculations have gained a huge success and nowadays they are considered as standard research tools in many fields as chemistry, physics, physical chemistry, biology and material science.

With the continuous increase of the computational resources and the development of efficient codes, quantum chemical calculations have been applied to more and more complex and large systems and the current frontier is the simulation of extended structure such as molecular aggregates, interfaces [6], polymers [12], of biological systems such as small polypeptides [16] or carbohydrates [8], and of nanostructures such as nanoparticle [7] and nanotubes [17]. However, the application of the available quantum chemical methods to describe complex systems is far from being a standard in computational chemistry. A number of complications arises for the description of these systems. The description of intermolecular interactions and in particular of van der Waals interactions, the description of the IR and Raman intensity with complex formalisms like the Berry phase approach, the proper description of the optical properties of molecular aggregates [18] are just a few examples of the complications that are encountered when dealing with large and complex systems. This work of thesis sets in this trend. Here, we use quantum-chemical calculations to study the structure, the electronic properties and the spectroscopic response of molecular and polymeric crystals, abandoning the “*single molecule*” approach in favor of a “*supramolecular*” approach, that takes into account the effects due to intermolecular interactions explicitly. The aim of the present work is to solve real problems encountered in the study of the properties of organic materials (and in their spectroscopic characterization) by taking advantage of the “supramolecular” approach.

The remaining part of this thesis is organized as follows. Chapter 2 deals with the exciton properties of organic molecular crystals. Excitons in molecular crystals are described within the Frenkel Hamiltonian and quantum chemical calculations carried out on molecular aggregates (dimers) are used to estimate the molecular parameters of interest, i. e. the *exciton couplings*. Our methodology is tested on the *para-nitro-aniline* crystal, taken as a case of study. Then it is used to study the exciton properties of the crystals of some acenes and their derivatives, which find many applications in molecular electronics and in photovoltaics. Chapter 3 deals with the simulation of the IR spectroscopic response of some polymeric crystals. We have simulated the IR spectrum of the α crystalline form of nylon 6,6 and both the α and γ polymorphs of nylon 6, considering both isolated infinite polymeric chains as models as well as 3-D crystal models, thus taking into consideration also the crystal packing. In addition, we have studied the IR spectrum of the *polytetrafluoroethylene*, considering both finite oligomeric models and isolated infinite chain models. In Chapter 4 we present some introductory results on a side project aimed to develop organic and hybrid nanostructures for the solar energy conversion. Also in this case, the “supramolecular” approach

has proven to be very useful. The nanostructures proposed for the frequency (down)-conversion of the solar light are formed by an absorber/donor moiety, which in this case is the 4-*hexylamino*-7-*nitro*-2,1,3-*benzoxadiazoles*, a *benzofurazan* derivative, and an emitter/acceptor moiety, which is an inorganic QD. Starting from some UV-Vis absorption and emission measurements, we have carried out quantum chemical calculations on the structure and optical properties of the benzofurazan derivative, considering both the isolated molecule and some supramolecular configurations, in order to enlight the possible role of specific *host-guest* interactions.

Chapter 2

Excitons in molecular crystals

2.1 Introduction

In the last two decades, organic materials have raised great interest for their possible application in molecular electronics and opto-electronics [19, 1, 2, 20], in particular in the field of energy conversion and photovoltaics [21, 22, 23, 24, 25]. The low cost of production and the possibility of property tailoring make organic materials suitable for a low cost/large volume industrial production of organic optical and electronic devices. Devices based on highly pure single molecular crystals show interesting charge and energy transport properties, with large exciton mobilities and long exciton diffusion (respectively $10^1 \text{ cm}^2 \text{ V}^{-1} \text{ s}^{-1}$ and 70 nm in pentacene [26, 27]).

Differently from their inorganic counterpart, the optical properties of organic materials are excitonic in nature, that is, the absorption of light in these materials does not give rise to free charges but to an interacting electron-hole pair, named *exciton*. Excitons play a fundamental role in the opto-electronic properties of these materials and they are ubiquitous in nature in both technology and biology.

Exciton properties in molecular solid depend on both single molecule properties and intermolecular interactions, the latter being described mathematically by the *exciton coupling* parameter J_{ab} . With respect to the optical properties, strong intermolecular interactions, i. e. large exciton couplings, result in a large shift of the absorption spectrum in going from the gas to the condensed phase, in a general broadening and also in the formation of new bands [28]. Intermolecular interactions are the main responsible also of the energy transport properties and strong interactions result in fast exciton diffusion. Within the widely used Marcus-Jortner-Levich theory, the transfer rate of an exciton from a molecular site to another is proportional to the square of the exciton coupling J_{ab} [29, 10]. Excitons can be either

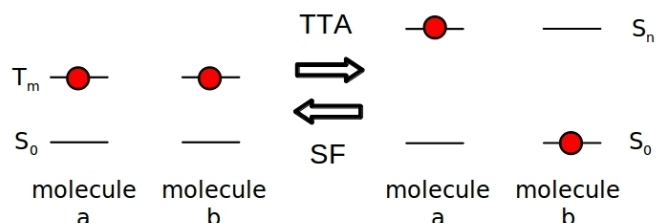


Figure 2.1: Schematic representation of the *triplet-triplet annihilation* (TTA) process and of the *singlet fission* (SF) process

singlet or triplet with respect to the spin of their wavefunction and this fact turns out to have a great influence on the exciton transport properties. Singlet excitons diffuse fast within the materials (diffusion coefficient $D \sim 10^{-2} \text{ cm}^2 \text{ s}^{-1}$) but have a very short lifetime (of the order of 10^{-9} s), thus their diffusion length is limited to about 10 nm. Triplets diffusion is slower ($D = 10^{-4} \text{ cm}^2 \text{ s}^{-1}$) but their lifetime is much longer, going from 10^{-4} s to 10^1 s , thus their diffusion length can be of the order of μm . Large exciton diffusion is of great importance in bulk heterojunction solar cells for overcoming the so called “exciton bottleneck”, that consists in the fact that excitons must diffuse to an interface before they can separate and generate free charges (exciton separation) [11]. Materials with strong exciton interactions should have excitons with longer diffusion length, that are likely to reach the donor-acceptor interface and then they are expected to improve the overall efficiency of the photovoltaic process.

Organic systems are gaining the attention of scientists also for their capability of showing multi-exciton processes, *singlet fission* (SF) and *triplet-triplet annihilation* (TTA). Singlet fission (SF) is a process in which an organic chromophore in an excited singlet state, S_n shares its excitation energy with a neighboring ground state, S_0 , chromophore and both are converted into triplet excited states, T_m . Triplet-triplet annihilation (TTA) is the opposite process, where the energy of two chromophores in their triplet state, T_m , is completely transferred to one of such chromophores, which populates its singlet state, S_n , while the other decays in its ground state [30]. SF and TTA are schematically represented in Figure 2.1.

Multi-exciton processes are known since a long time in acenes crystals, where they were originally proposed to explain the photophysics of anthracene single crystals in 1965 [31]. More recently they have been studied in a large number of organic systems, like other molecular crystals

[32, 33, 27, 34], carotenoids [35, 36], conjugated polymers [37, 38], disordered molecular films [39, 40], and in solutions with sensitizer [41, 42, 43, 44, 45]. Multi-exciton mechanisms are currently at the center of intense studies since it is believed that they can improve the efficiency of the photovoltaic process. SF is a quite intriguing mechanism since it gives rise to two produced electron-hole pairs for each absorbed photon, thus it can potentially increase the short circuit current of photovoltaic devices. TTA instead has been proposed to up-convert the lower frequency region of the solar spectrum above the energy gap, thus increasing the portion of light available for the photovoltaic process. Detailed balance models estimate that, taking advantage of SF and TTA mechanisms, the maximum theoretical efficiency of a solar conversion device increases from 31% of the Shockley-Queisser limit to 49% [46, 47].

In order to have efficient SF, it is required that the global process is exothermic, that is, the energy of the singlet state, S_n must be larger than the sum of the energies of the two triplet states, T_m , that is $S_n > 2T_m$. For having an efficient TTA the opposite condition is required, $2T_m > S_n$. Intermolecular interactions in aggregate phase affect substantially the efficiency of multi-exciton processes. In particular, strong interactions can give rise to a large shift of the energy levels, thus influencing the global energetic of the multi-exciton processes. Moreover, for TTA it is required that two triplet excitons, formed in two separate crystalline regions, diffuse in the material until they come close enough to interact and give rise to the transition from two triplets to one singlet. Such diffusive step was proposed as that limiting the efficiency of the TTA process [48]. Experimental confirmation of this suggestion was obtained by Tubino et Al. for systems with a sensitizer and an emitter in solution [42]¹. No experimental evidences about the importance of the diffusive step in the TTA process in solid state were obtained so far, at least at the best of the author's knowledge.

The study of exciton in condensed phase is therefore very important for the comprehension of the opto-electronic properties of organic based technological devices and is fundamental for the development and optimization of new and more performing materials. The comprehension of the exciton properties in the solid phase requires, on one hand, intense experimental investigations and, on the other hand, a solid work of modeling and the use of simulation techniques, able to predict the electronic structure and the response of the system under investigation. In this chapter we present our work on the modeling of the exciton properties in organic crystalline materials. Excitons are described with the Frenkel Hamiltonian and the parameters

¹The sensitizer molecules absorb photons in the long wavelength region of the solar spectrum and they populate their first triplet excited state through intersystem crossing. Then, the triplet excitons are transferred to the emitters, which diffuse in the solution till they decay to the ground state or till two emitters come close enough to give rise to TTA, with the resulting emission of a short wavelength photon.

of interest, the exciton couplings, J_{ab} , are calculated with state-of-the-art quantum chemical tools. For the evaluation of the exciton couplings, we use the so called “energy gap based” approach, in connection with the *transition densities matrices projection* method developed by us, that allows to analyze critically the results of quantum chemical calculations and to obtain reliable estimation of the exciton couplings J_{ab} .

The Frenkel exciton Hamiltonian for the study of the excited states of molecular aggregates, the approaches reported in the literature for the calculation of the exciton couplings and the TDM projection method are presented extensively in section 2.2. In attachment **a** (C. Quarti, D. Fazzi and M. Tommasini; “A density matrix based approach for studying excitons in organic crystals” *Chem. Phys. Lett.*, 496:284-290, 2010) our methodology is tested to the case of the *para-nitro-aniline* (PNA) crystal. In attachment **b** (C. Quarti, D. Fazzi and M. Del Zoppo; “A computational investigation on singlet and triplet exciton couplings in acene molecular crystals” *Phys. Chem. Chem. Phys.*, 13:18615-18625) we applied our methodology to a case of technological interest, crystals of acenes and derivatives.

2.2 Describing excitons in molecular crystals

2.2.1 Exciton Hamiltonian: the Frenkel Hamiltonian

The Frenkel Hamiltonian of a molecular aggregate, composed of N molecule, is the following [28, 49, 50, 51, 52]:

$$\mathbf{H} = \sum_a^N \mathbf{H}_a + \sum_a^N \sum_{b < a} \mathbf{V}_{ab} \quad (2.1)$$

where \mathbf{H}_a is the many-body electronic Hamiltonian of the isolated a -th molecule and \mathbf{V}_{ab} is the Coulomb interaction between an electron located on the a -th molecule and another one located on the b -th molecule. The Frenkel Hamiltonian considers the nuclei fixed and it neglects any coupling between electronic and nuclear degrees of freedom (*exciton-phonon* coupling). In order to consider such interactions, more involved descriptions are required (Holstein or SSH Hamiltonian).

The hypothesis at the basis of the Frenkel Hamiltonian is that the intermolecular interactions are weak enough not to heavily modify the properties of the single molecule, thus the set of the *adiabatic states*, that are the solutions of the electronic problem for the isolated molecule ²:

$$\mathbf{H}_a \varphi_a^f = \epsilon_a^f \varphi_a^f \quad (2.2)$$

²In our notation, the subscript refers to the a -th molecule and the superscript refers to the f -th excited state

is convenient for the description of the excited states of the aggregate. The Frenkel hamiltonain is represented in the basis set χ_a^f where a molecule is in its f -th excited state, while all the other are in their ground state, with appropriate antisymmetrization:

$$\begin{cases} \Psi_a^f &= \varphi_a^f \prod_{b \neq a} \varphi_b^0 \\ \chi_a^f &= N^{-1/2} \sum_{\nu} (-1)^{\nu} p_{\nu} \Psi_a^f \end{cases} \quad (2.3)$$

From the hypothesis of weak intermolecular interactions it is reasonable to assume that the single molecule states, said also diabatic states, preserve the orthogonality also in the aggregate. In other words, different excited states χ_a^f and χ_a^g remain orthogonal, i. e. the Frenkel Hamiltonian is diagonal with respect to the single molecule's excited states.

The *ansatz* used for representing the *adiabatic states* of the aggregate is the linear combination of the basis of Eq. 2.3

$$\Phi = \sum_{a=1}^N c_a \chi_a^f \quad (2.4)$$

By inserting the *ansatz* of Eq. 2.4 in the Frenkel Hamiltonian of 2.1, subtracting the energy of the ground state ϵ_a^0 from the resulting equation, multiplying for $(\varphi_a^f \prod_{b \neq a} \varphi_b^0)^*$ and integrating over the spatial coordinates, we get:

$$\sum_a \left(\Omega_a^f \delta_{ab} + J_{ab}^f \right) c_a = E_b c_b \quad (2.5)$$

where:

$$\Omega_a^f = \epsilon_a^f - \epsilon_a^0 + W_a \quad (2.6)$$

$$J_{ab}^f = \langle \varphi_a^f \varphi_b^0 | V | \varphi_a^0 \varphi_b^f \rangle + \left\langle \sum_{\nu} (-1)^{\nu} P - 1 \right\rangle \varphi_a^f \varphi_b^0 | V | \varphi_a^0 \varphi_b^f \rangle \quad (2.7)$$

The matrix elements in Eq. 2.5 have the following meanings:

- The diagonal term (Eq. 2.6) is just the excitation energy for the isolated a -th molecule plus a stabilization term W_a due to the crystalline field.
- The off-diagonal term (Eq. 2.7) is the so called *exciton coupling* or *resonance energy coupling* and it represents the interaction energy between the a and b molecules. This term consists of two contributions. The first one is the Coulomb interaction between the variation of electron densities on the a -th and b -th molecule, due to the excitation. This term is electrostatic in nature and it has a long-range character.

The other terms are the interactions due to the exchange of any couple of electrons between the two molecule. This is a quantum contribution and it is proportional to the overlap between the wavefunctions of the a and b molecule [53], thus it is effective only at very small intermolecular distances ($< 5 \text{ \AA}$).

The Coulomb and the exchange contributions play a different role for singlet and triplet excitons. In molecular solids and aggregates the intermolecular distances are rarely shorter than 5 \AA and the exchange contribution assumes values of about $5\text{-}10 \text{ cm}^{-1}$ [51, 54, 55]. In the case of singlet excitons, typical values of the Coulomb contribution are of the order of 10^2 cm^{-1} , thus the exchange contribution can be safely neglected. In the case of triplet excitons instead, Coulomb interaction assumes smaller values ($\sim 10^0, 10^1 \text{ cm}^{-1}$), because of the spin orthogonality, and exchange contributions cannot be neglected anymore.

In the following we apply the Frenkel Hamiltonian to two cases of interest, in order to highlight concepts and equations that will be important from here on.

Molecular pair) Consider the case of a couple of identical molecules a and b . By expressing the Frenkel Hamiltonian on the basis of the diabatic states of Eq. 2.3, we get the following matrix representation:

$$\mathbf{H}_{ab} = \begin{pmatrix} \epsilon_a & J_{ab} \\ J_{ab} & \epsilon_b \end{pmatrix} \quad (2.8)$$

where $\epsilon_a = \epsilon_b = \epsilon_0$.

The eigenstates of this Hamiltonian, named also *Davydov components*, are:

$$\Phi^\pm = 1/2(c_a\chi_a + c_b\chi_b) \quad (2.9)$$

which have energy

$$\epsilon_\pm = \epsilon_0 \pm 2J_{ab} \quad (2.10)$$

the exciton coupling term can be obtained, in both absolute value and sign, knowing the energy of the adiabatic states, ϵ_+ and ϵ_- :

$$J_{ab} = \frac{\epsilon_+ - \epsilon_-}{2} \quad (2.11)$$

For the case of two inequivalent molecules ($\epsilon_a \neq \epsilon_b$), the absolute value of the exciton coupling can be obtained from the knowledge of the energy of both the diabatic (ϵ_a and ϵ_b) and adiabatic states (ϵ_+ and ϵ_-):

$$|J_{ab}| = \sqrt{(\epsilon_+ - \epsilon_-)^2 - (\epsilon_a - \epsilon_b)^2} \quad (2.12)$$

General 3D crystal) The Frenkel Hamiltonian of a 3D crystal, composed by σ molecules per unit cell, can be conveniently expressed in this form:

$$\mathbf{H} = \sum_{\mathbf{n}\alpha} \mathbf{H}_{\mathbf{n}\alpha} + \sum_{\mathbf{n}\alpha < \mathbf{m}\beta} \mathbf{V}_{\mathbf{n}\alpha, \mathbf{m}\beta} \quad (2.13)$$

In this notation, the latin index identifies the unit cell and the greek index identifies the molecule within the cell.

The *ansatz* of the exciton wavefunction of the aggregate is the usual:

$$\Phi = (\sigma N)^{1/2} \sum_{\mathbf{n}\alpha} a_{\mathbf{n}\alpha} \chi_{\mathbf{n}\alpha}^f \quad (2.14)$$

where the basis set $\chi_{\mathbf{n}\alpha}^f$ is the same as that of Eq. 2.3.

The coefficients of the exciton wavefunction must satisfy the Bloch theorem:

$$a_{\mathbf{n}\alpha} = B_{\alpha} e^{i\mathbf{k}\mathbf{n}} \quad (2.15)$$

By introducing the ansatz in Eq. 2.13, multiplying by $\chi_{\mathbf{m}\beta}^f$ and integrating, we get

$$\sum_{\alpha} L_{\alpha\beta} B_{\alpha} = \epsilon^f B_{\beta} \quad (2.16)$$

where:

$$L_{\alpha\beta} = (\sum_n \langle \varphi_{\mathbf{n}\alpha}^f \varphi_{\mathbf{m}\beta}^0 | V | \varphi_{\mathbf{n}\alpha}^0 \varphi_{\mathbf{m}\beta}^f \rangle + \langle [\sum_{\nu} (-1)^{\nu} P - 1] \varphi_{\mathbf{n}\alpha}^f \varphi_{\mathbf{m}\beta}^0 | V | \varphi_{\mathbf{n}\alpha}^0 \varphi_{\mathbf{m}\beta}^f \rangle) e^{i\mathbf{k}(\mathbf{n}-\mathbf{m})} \quad (2.17)$$

2.2.2 Methods for the evaluation of the exciton coupling

In Eq. 2.5 the two set of parameters of interest are the *on-site energies* Ω_a^f and the *exciton couplings* J_{ab}^f . The on-site energies determine the energetic center of the exciton structure, thus they are often fit from experiments. The exciton couplings, J_{ab} , determine the form of the exciton structure and their evaluation from experiments, when possible, is very complex. The evaluation of such quantities is the typical field where quantum chemical calculations can provide an invaluable contribution. In the literature there is plenty of examples where exciton couplings J_{ab} are evaluated with quantum chemical tools and several methods for this task have been proposed. [55, 56, 57, 58, 18, 54, 59, 53, 60, 61, 62, 51, 52] All these methods can be classified in four main approaches [63].

- **A)** Energy gap based or *adiabatic states* based scheme

This approach is based on the knowledge of the properties of the adiabatic states of the molecular aggregate, in particular of molecular dimers. It consists in calculating the excited states of the dimer, recognizing the two Davydov components, Φ^{\pm} (see Eq. 2.9) associated to

the excited state of interest, φ^f , and estimating the exciton coupling as half of the energy splitting (Eq. 2.11 or 2.12).

The present method is conceptually the simplest one and it generally provides accurate results but nevertheless it shows some limitations. It cannot distinguish between Coulomb and exchange contributions but it provides the global interaction. Since it requires the knowledge of the adiabatic states of the dimer, it is computationally more demanding than the *diabatic states* based methods (see later). Some of the widely used quantum chemical formalisms for the excited states calculation, for instance *Time Dependent- Density Functional Theory* (TD-DFT) with the widely used B3LYP and PBE0 exchange-correlation functionals, overestimate the exciton coupling. Usually, this fact is due to an unbalanced description of the excited states involved in the molecular aggregate. In some instances, the lowest Davydov component is too low and, in general, fictitious low lying excited states with charge transfer character are predicted, which make the evaluation of the exciton coupling difficult or incorrect [18].

In general, the recognition of the two Davydov components associated to the excited state of interest is a relevant practical problem. The presence of fictitious low lying states, due to these limitations of the computational method [18], or of nearly degenerate excited states makes the calculation of the exciton coupling through this approach somehow difficult and arbitrary. We developed a method, named *Transition Density Matrix projection* method that allow to overcome this problem (see section 2.2.3).

- **B)** Direct coupling or *diabatic state based scheme*

This approach is based on the knowledge of the diabatic states $|\varphi_{a/b}^{0/f}\rangle$ and on the direct evaluation of the exciton coupling through Eq. 2.7. It requires a relatively small computational cost and it provides separate estimations of the Coulomb and the exchange contributions. However this approach requires the evaluation of complicated one- and two-electron matrix elements and it does not provide very accurate results.

A recent improvement is given by the *constrained density functional theory* (CDFT), proposed by Van Voorhis and co-workers [54]. This formalism allows to define rigorously localized diabatic states and to obtain reliable estimations of the exciton coupling.

- **B1)** Direct calculation of the Coulomb interaction

Conceptually similar to the previous one, this approach is based on the knowledge of the properties of the diabatic states, i. e. the transition multipole moments of the molecule. It consists in neglecting the exchange contribution J_{exch} to the exciton coupling (see Eq. 2.7)

and approximating the Coulomb contribution through a multipole expansion. In this way the Coulomb interaction is written as the sum of a dipole-dipole interaction term (J^{d-d}), plus a dipole-quadrupole (J^{d-q}), quadrupole-quadrupole (J^{q-q}) and so on.

$$J = J^{d-d} + J^{d-q} + J^{q-q} \dots \quad (2.18)$$

By considering only the first order term in the multipole expansion, one get the so called *point dipole approximation* (PDA) [64], that historically has been the first approach used for calculating the exciton coupling of singlet states:

$$J = \frac{\boldsymbol{\mu}_a \cdot \boldsymbol{\mu}_b}{R^3} - 3 \frac{(\boldsymbol{\mu}_a \cdot \mathbf{R})(\boldsymbol{\mu}_b \cdot \mathbf{R})}{R^5} \quad (2.19)$$

where $\boldsymbol{\mu}_{a/b}$ is the transition dipole moment of the a/b -molecule and \mathbf{R} is the vector between the center of mass the a -th and b -th molecule. PDA approximation provides accurate results when intermolecular distance is large (~ 20 Å). In the case of molecular crystals, where intermolecular distances are of the order of 5 Å, PDA is no more accurate but it is useful for a qualitative rationalization of the intermolecular interactions.

Obviously, in the case of triplet excited states the PDA and in general the present approach are not accurate at all, since exchange contribution to the exciton coupling (Eq. 2.7) is dominant.

- **C)** Use of additional operators

A recent and completely different approach for the evaluation of the exciton coupling relies on the use of an additional operator. Such operator, ΔA represents the difference in excitation number (for singlet excitons) or the difference in spin (for triplet excitons) of the diabatic states of the molecular dimer. The exciton coupling is then obtained by properly rotating the two state Hamiltonian:

$$J_{ab} = \frac{(E_1 - E_2) |\Delta A_{12}|}{\sqrt{(\Delta A_1 - \Delta A_2)^2 + 4\Delta A_{12}^2}} \quad (2.20)$$

The present approach is generally accurate but computationally it is the most demanding and, for the moment, it is still considered an expert approach.

In Table 2.2.2 we classify some papers where the exciton coupling is computed on the basis of the approach used.

Table 2.1: Classification of some papers found in the literature with respect to the approach used for calculating the exciton coupling. For each paper we report also the publication year and the journal (jctc=J. of Chem. Theory and Comput.; jcp=J. Chem. Phys; jacs=J. Am. Chem. Soc.; jpc=J. Phys. Chem.)

paper	approach A	approach B	approach B1	approach C
Mennicci jctc 2010 [57]	X			
Mennucci jcp 2007 [58]	X			
Mennucci jacs 2005 [18]	X	X		
Hsu jpca 2011 [55]				X
Hsu jpcb 2001 [56]			X	
Van Voorhis jpcc 2010 [54]	X	X		X
Beljonne jcp 2000 [60]	X		X	
Cornil jacs 1998 [61]	X			
Scholes jpcb 1998 [59]			X	
Scholes jpc 1994 [53]		X	X	
Philpott jcp 1982 [62]		X	X	
Jortner jcp 1965a [51]		X		
Jortner jcp 1965b [52]		X		

2.2.3 Transition Density Matrices (TDM) projection method

As outlined above, all the approaches for the estimation of the exciton coupling J_{ab} their some advantages and limitations. Within the energy gap based approach (approach A) we have developed a procedure, named *transition density matrix projection method*, that allows to overcome the main limitation of this approach, that is to find the two Davydov components of a dimer, Φ^\pm , associated to the generic excited state of the molecule $\varphi_{a/b}^f$ in a unarbitrary and unambiguous way. The transition density matrix (TDM) projection method is based on the knowledge of the TDMs associated to the excited states of the dimer and of the isolated molecules. The TDM, ρ^j , of the j -th excited state of a system is defined as [65]:

$$\rho^j = \langle g | c_n^\dagger c_m | j \rangle \quad (2.21)$$

where $|g\rangle$ and $|j\rangle$ are the wavefunctions respectively of the ground and of the j -th excited state and c_n^\dagger and c_m are respectively the creation and the annihilation operators for the n -th and m -th atomic orbital. In the TDM projection method, the generic excited state of the dimer Φ^g and that of the isolated molecule φ_a^f are compared mathematically, by projecting their

respective TDMs, ρ_{ab}^g and ρ_a^f , with the following inner product:

$$(\rho_a^f, \rho_{ab}^g) = Tr \left[(\rho_a^f)^* \cdot \hat{P}_a (\rho_{ab}^g) \right] \quad (2.22)$$

where the operator \hat{P}_a projects the matrix of the dimer onto the subspace of the basis functions belonging to the a -th molecule. The inner product in Eq. 2.22 corresponds to a Frobenius product and we have verified in that it is the correct inner product for the space of TDMs \hat{i}) expressed in an orthonormal basis set (overlap matrix $\mathbf{S} = \mathbf{I}$) and $i\hat{i}$) where the excited states are orthonormal by the usual definition of the inner product between wave functions.

Since the generic excited state φ_a^f of the isolated molecule and its Davydov components, Φ^\pm , have the same character, the products of their respective TDMs (ρ_a^f, ρ^\pm) are expected to be much larger than the products with the TDMs associated to all the other single molecule excited states.

The TDM projection method is robust and general and it works with singlet excitons as well as with triplet ones. The use of such method in connection with the energy gap based method gives accurate results for the exciton coupling, since it allows to rule out unphysical charge transfer states due to the limitation of the computational method used. In addition, TDM projection method potentially provides information of the sign of the exciton coupling.

2.3 Publications

Attachment a)

“A density matrix based approach for studying excitons in organic crystals” Claudio Quarti, Daniele Fazzi and, Matteo Tommasini; *Chem. Phys. Lett.* 496:284-290, 2010.

In the first publication on this topic, the present method for studying excitons in organic crystals is presented and tested on the *para-nitro-aniline* (PNA) crystal, taken as a case study. The exciton associated to the first, dipole allowed excited state of the PNA crystal was described with the Frenkel Hamiltonian (see section 2.2.1), thus neglecting vibrational and vibronic effects. The molecular parameters of interest, i. e. the *exciton couplings* J_{ab} , were evaluated with quantum chemical calculations, both at semiempirical ZINDO and *ab-initio* TD-B3LYP/6-31G(d,p) theory level.

As a first step, we carried out a structural analysis of the experimental X-ray crystal structure of the PNA, in order to classify all the non equivalent interactions between nearest neighbor molecular pairs, in the following referred as dimers. Nine non equivalent interactions, or dimers, have been found. For each dimer we calculated the exciton coupling, J_{ab} with the TDM projection method, presented above. Thus we have calculated the excitation

energies and the TDM associated to the six low lying excited states of both the dimer and the constituting molecules and we have projected the TDMs of the dimer on the TDMs of the single molecules with the metric in Eq. 2.22. In this way, we can recognize the two Davydov components associated to the first dipole allowed singlet excited state and we can estimate the exciton coupling J_{ab} with the “energy gap approach” (see Eq. 2.11 and 2.12). The results of the projection procedure for one of the dimers of PNA, dimer A, and the list of the exciton couplings obtained from ZINDO and TD-B3LYP/6-31G(d,p) calculations are reported respectively in Table 1 and 3 of attachment **a**.

Once all the exciton couplings were determined, we reconstructed the Frenkel Hamiltonian of the crystal, Eq. 2.16 and we calculated the exciton Density of States (eDOS) and the exciton dispersion bands.

The exciton Density Of States (eDOS) was compared with the experimental UV-Vis absorption spectrum, recorded by Dr. A. Lucotti in our laboratory ³. UV-Vis spectrum finds nice correspondences with some features of the eDOS between 2.5 and 4 eV (see Figure 3 of the attachment **a**), including *i*) no absorption below 2.7 eV; *ii*) a change in the slope of the spectrum at 2.9 eV; *iii*) a maximum of the absorption band at 3 eV *iv*) a change of UV-Vis spectrum slope at 3.5 eV and *v*) a small absorption band at 4 eV.

In addition, we calculated the exciton dispersion bands from Γ to the high symmetry points of the first Brillouin zone of monoclinic lattice. These bands provide useful information about the exciton mobility. As expected, the exciton bands associated to the first singlet dipole allowed state are four, since the PNA crystal is composed by four translationally non equivalent molecules. The low lying band has large bandwidth along the $\Gamma \rightarrow B$ and $\Gamma \rightarrow Z$ directions.

In conclusion, we used the Frenkel Hamiltonian for describing the first dipole allowed exciton of the PNA crystal. The parameters of the Hamiltonian, i. e. the exciton couplings J_{ab} , were calculated with quantum chemical tools in conjunction with an innovative approach, named the TDM projection method. Exciton Density of State (eDOS) obtained from theory well explain the experimental spectroscopic data, thus the methodology adopted is valid and the TDM projection method proposed for the determination of the exciton couplings provides reliable estimations for these parameters, both in absolute value and in sign.

³Rashba demonstrated that under the assumption of *a*) negligible vibrational bandwidth of the populated phonons and *b*) for k -independent transition probability, the electronic transition is no more restricted to $k = 0$ and the UV-Vis spectrum (I_{abs}) is proportional to the exciton density of states (eDOS) [66].

$$I_{abs} \propto eDOS(E)$$

Attachment **b)**

“A computational investigation on singlet and triplet exciton couplings in acene molecular crystals” C. Quarti, D. Fazzi and M. Del Zoppo; *Phys. Chem. Chem. Phys.* 13:18615-18625, 2010.

In this work, the *transition density matrix* approach for the study of excitons in molecular aggregates is applied to a case of technological interest: acene crystals and their derivatives. Crystalline acenes are among the most promising and studied materials for applications in molecular electronic and a thorough study of their exciton properties in solid state can be useful for the comprehension and the optimization of their performances in technological devices. Here we considered *anthracene* (An) and *tetracene* (Te) and two anthracene derivatives, *9,10-di(phenyl)anthracene* (DPA) and *9,10-bis(phenylethynyl)anthracene* (BPEA). In addition to their high exciton and charge transport mobility, An and Te were considered because of their capability of showing multi-exciton processes, SF and TTA. Multi-exciton mechanisms of SF and TTA were first invoked in 1965 to explain the photophysics of crystalline An [31] and they were found in 1968 in crystalline Te [67]. For DPA and BPEA instead, TTA was observed up to now only in solution with a sensitizer [41, 42, 43, 44, 45] and no study in condensed phase was presented before, at least at the best of the author’s knowledge.

The aim of this work is twofold. On one hand, we carry out a thorough characterization of the exciton properties of acenes and their derivatives the in solid state, in order to gain a deeper insight into the properties of these largely used systems. On the other hand, we aim at correlating the effect of chemical substitution to the acene backbone on the exciton properties of molecular crystals, in order to find useful guidelines for the development of new materials with improved exciton interactions, that are expected to prove enhanced performances in the field of solar energy conversion.

A thorough characterization of the properties of both the first singlet and triplet exciton of the isolated molecules was carried out at the semi-empirical (ZINDO) and the *ab-initio* (TD-DFT) level of theory, with B3LYP and CAM-B3LYP exchange-correlation functionals. Our calculations show that An, DPA and BPEA match the energetic requirements for having efficient TTA, while Te matches those for having efficient SF. Unfortunately, our calculations provide an unbalanced description for the singlet and the triplet excitons, slightly underestimating the excitation energies of the latter. Actually, experimental evidences show that An in solid state [31] and DPA and BPEA [41, 42, 43] in solution with a sensitizer give efficient TTA, as found in our calculations. Te instead is a very peculiar case since the energy of the first singlet matches very well with twice the energy of the first triplet, thus both SF and TTA are found [30]. Moreover, our calculations show that the transition dipole moment associated to the transition from the ground to the first singlet excited state, $\mu^{S_0 \rightarrow S_1}$, that for these molecules is directed along the short acene axis, is strongly affected by the introduction

of π -conjugated chemical substituents along this direction. In fact, going from An to BPEA $\mu^{S_0 \rightarrow S_1}$ increases from 1.65 atomic units (au) to 4.05 au at ZINDO level, from 0.86 au to 3.76 au at TD-B3LYP level and from 0.98 au to 3.58 au at TD-CAM-B3LYP level (see Table 1 of attachment *b*). Note that in going from An to DPA, the transition dipole moment shows only a small increase since in DPA the benzene rings are nearly orthogonal with respect to the acenic part of the molecule, thus limiting the π -conjugation in the short acene axis. These considerations on the transition dipole moment $\mu^{S_0 \rightarrow S_1}$ will be important when we discuss the singlet exciton couplings (see later).

Once the exciton properties of the isolated molecules were addressed, we focused on the exciton properties in the crystalline phase; in particular, we estimated the exciton couplings for these crystals. As in the previous work, we carried out a thorough structural characterization of the An, Te, DPA and BPEA experimental crystal structures in order to recognize all the different types of interactions between nearest neighbor molecular pairs, or dimers. We found four dimers for An, eight for Te and five for both DPA and BPEA. For all these dimers we calculated the exciton couplings associated to the first singlet and triplet excited state, at three theory levels: ZINDO, TD-B3LYP and TD-CAM-B3LYP. For the calculation of the exciton coupling we have used the “energy gap” approach (see Section 2.2.2) in connection with our TDM projection method. Thus, we calculated the energy and the TDM of the low lying excited states for both the dimer and the constituting molecules and we projected the latter on the former with Eq. 2.22 in order to recognize the two Davydov components associated to the excited state of interest. Then, we used Eq. 2.11 and 2.12 for the evaluation of the exciton couplings. The exciton couplings estimated for the four crystalline structures for both the first singlet and triplet state are reported in Table 3 of attachment **b**, together with the center of mass distance of each dimer.

The results of our calculations for the singlet exciton couplings are the following. ZINDO and TDCAMB3LYP results are qualitatively similar with each other and they are consistent with the estimation reported in the literature⁴. At the opposite, TD-B3LYP predicts very strong interactions for all the systems. This fact has been recently explained by Mennucci and coworkers as a limit of the widely used B3LYP functional[18]. For these reasons, we refer only to the ZINDO and TD-CAM-B3LYP results for the discussion of the singlet exciton couplings. For An and Te, the stronger interactions are found respectively for the A, B and A, A1, B and B1 dimers, which lie in the high density packing {0,0,1} crystalline plane. In DPA the interactions are weaker, being at maximum 100 cm⁻¹. In BPEA instead all the interactions are very strong (larger than 100 cm⁻¹) also for those dimers with large center

⁴For the exciton coupling associated to the first singlet excited state of the dimer B of anthracene, Beljonne et Al. provide an estimation of 242cm⁻¹ [68]

of mass distance. These results can be rationalized on a qualitative ground on the basis of the point dipole approximation (PDA) (see Eq. 2.19). As outlined before, the presence of π -conjugated *phenylethynyl* group in 9 and 10 position in BPEA provides a very large transition dipole moment $\mu^{S_0 \rightarrow S_1}$. Thus within PDA, which describes the exciton interactions as an interaction between transition dipole moments, the exciton couplings in BPEA crystal become very large. In addition, in all the dimers of BPEA molecular transition dipole moments are nearly parallel, thus the scalar product of Eq. 2.19 is maximized. Summarizing, the introduction of chemical substituents in acene core that increases π -conjugation along the short acene axis, together with an efficient crystal packing, is a possible route for having materials with improved exciton interactions.

The results of our calculations for the triplet excitation couplings are the following. In this case, the estimations obtained by us at the three different levels of theory are consistent with each other and with the estimations reported in the literature⁵. Triplet exciton couplings are in general smaller than their singlet counterpart, as expected by the fact that Coulomb contribution to the exciton coupling is much smaller for the former than for the latter. Nevertheless, we find that for some interactions, like dimer A of BPEA, triplet exciton coupling assumes values comparable to those of the singlets, e. g. 102 cm^{-1} . This new and quite interesting suggests that exchange contribution to exciton coupling can be much stronger than what believed previously and that triplet excitons can diffuse as fast as singlets. Moreover, this result may explain a recent finding of very long triplet diffusion length in crystalline rubrene [69]. We found that the triplet exciton couplings are much more selective than singlet ones. Indeed, while the singlet exciton couplings of all the BPEA dimers are sizable, there is only one dimer with a large triplet exciton coupling, namely dimer A. Note that such dimer is characterized by a very short intermolecular distance. In the same way, also for An and Te, the largest triplet exciton couplings are found in correspondence of the dimers with short intermolecular distances and in DPA, where all the intermolecular interactions are large, the triplet exciton couplings are all negligible. This result can be explained by recalling that the dominant interaction for the triplet exciton coupling is of the exchange type, that is, they are proportional to the overlap of the molecular wavefunctions and are thus very sensitive to the intermolecular distance.

From the screening of the exciton properties of both the first singlet and triplet excited state, carried out on two acenes (An and Te) and two derivatives in the solid phase, we can derive some important considerations. In acenes crystals, stronger exciton interactions are found in the herringbone packing plane $\{0,0,1\}$, consistently with the general belief that exciton

⁵For anthracene, Jortner estimated triplet exciton couplings of the order of 5 cm^{-1} with PPP wavefunctions [51]

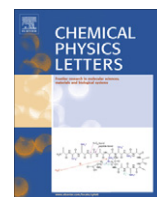
diffusion in this class of molecular crystals is mainly constrained to this plane (two dimensional diffusion). Nevertheless, chemical substitutions can modify heavily this behavior. For instance, in BPEA the introduction of π -conjugated chemical substituents along the short acenic axis results in an increase of the molecular transition dipole moment and a correspondent increase of all the exciton couplings. Thus, within a molecular engineering approach, this route can be used to develop new materials with improved exciton interactions, that might be used, for example, to improve the performance of photovoltaic devices. On the contrary, large singlet exciton couplings can be detrimental for singlet fission process since they can result in a red shift of the singlet exciton energy, in going from the gas to the crystalline phase, that makes the singlet fission endothermic. For triplet exciton we find that exciton couplings are in general smaller with respect to their singlet counterpart but in some cases they are comparable. This new can explain some recent evidence of triplet exciton with very long diffusion length [69]. Nevertheless, triplet diffusion is always much more anisotropic than singlet diffusion, being effective only along particular crystalline planes or directions.

2.3.1 attachment a



Contents lists available at ScienceDirect

Chemical Physics Letters

journal homepage: www.elsevier.com/locate/cplett

A density matrix based approach for studying excitons in organic crystals

Claudio Quarti^{a,b}, Daniele Fazzi^c, Matteo Tommasini^{a,b,*}^a Politecnico di Milano, Dipartimento di Chimica, Materiali e Ingegneria Chimica 'G. Natta', piazza Leonardo da Vinci 32, 20133 Milano, Italy^b INSTM, UdR Politecnico di Milano, Italy^c Center for Nano Science and Technology, CNST, IIT@PoliMi, via Pascoli 70/3, 20133 Milano, Italy

ARTICLE INFO

Article history:

Received 8 June 2010

In final form 16 July 2010

Available online 21 July 2010

ABSTRACT

A theoretical analysis of molecular excitons in crystalline *p*-Nitro-Aniline (PNA) is presented. The approach is general and can be straightforwardly extended to the calculation of the exciton structure of other molecular crystals or aggregates. Based on the evaluation of transition density matrices (TDM), the method allows to easily classify the excited states of interacting molecules on the basis of those of the constituent molecules. Exciton couplings of selected dimers within the PNA crystal have been evaluated and the exciton dispersion has been determined. The experimental absorption spectrum of PNA powders can be analysed in details based on the exciton density of states.

© 2010 Elsevier B.V. All rights reserved.

1. Introduction

In the last decades organic conjugated materials have been assuming a growing interest for their use as active materials in opto-electronic applications [1]. In order to achieve a satisfactory description of their optical and electronic properties a detailed understanding of their photophysics both in solution and in solid state is required. Up to now, most of the theoretical investigations on conjugated materials have been carried out on isolated molecules (mimicking the molecular behaviour in inert matrices or dilute solutions), however there is a growing interest for the simulation of optical properties in condensed phases, to predict the behaviour of films, polymers and organic crystals. A very popular theoretical framework commonly adopted for this task is the *molecular exciton theory* [2,3]. This theory assumes that the excited states wave functions in aggregates are weakly influenced by intermolecular forces, so that they are well approximated through the excited state wave functions of isolated molecules. Two are the most commonly adopted approaches in the framework of molecular exciton theory: the Frenkel exciton hamiltonian [4], that neglects the effects due to the nuclear dynamics (i.e. *free exciton*), and the Holstein hamiltonian [5,6], which explicitly includes the exciton–phonon interaction (i.e. *dressed exciton*). Both Frenkel and Holstein hamiltonians have been successfully employed for the description of excitons in molecular aggregates [7].

The main parameter of the molecular exciton model is the *exciton coupling*, which describes the interactions between two molecules and the easiness of exciton transfer from site to site [8].

* Corresponding author at: Politecnico di Milano, Dipartimento di Chimica, Materiali e Ingegneria Chimica 'G. Natta', piazza Leonardo da Vinci 32, 20133 Milano, Italy.

E-mail address: matteo.tommasini@polimi.it (M. Tommasini).

The exciton coupling (also named *resonance coupling integral* [9]) strongly depends both on the electronic structure and the supra-molecular organization (packing) of the molecules, as thoroughly reported [10,11].

In this Letter, we present a theoretical modeling of excitons in *p*-Nitro-Aniline (PNA) crystal. This theoretical approach is general and it can be easily extended to the calculation of the exciton structure of any other molecular crystal or aggregate. We have considered in this work PNA thanks to the experimental data available on both crystal structure [12] and absorption spectroscopy [13–15].

To describe the excitonic structure of PNA in its crystal phase we have developed a systematic method (named *density matrix projection method*), based on the calculation of transition density matrices (TDMs), which allows to greatly ease the calculation of the exciton coupling and the classification of the excited states of molecular aggregates and crystals. Based on this method and on crystallographic data we have evaluated all the possible exciton couplings between pairs of nearest neighbour PNA molecules. Once the Frenkel hamiltonian of PNA crystal is known, exciton density of states (eDOS) and exciton dispersion curves for the crystal can be easily obtained. Finally, based on these results and on Rashba theory [2,16], it has been possible to analyse the experimental UV–Vis spectrum of solid PNA powders on the basis of the calculated eDOS.

2. Theoretical method

We briefly recall here the molecular exciton theory within the framework of Frenkel approximation [2]. Considering a dimer (*ab*) formed by two identical molecules *a* and *b*, its hamiltonian operator *H* is given by the sum of the hamiltonians *H_a* and *H_b* of the single molecules, and by the interaction term *V_{ab}*:

$$H = H_a + H_b + V_{ab} \quad (1)$$

Assuming that V_{ab} is a weak perturbation we can express an approximate eigenfunction of H as [2]:

$$|\phi\rangle = c_a |\psi'_a \psi_b\rangle + c_b |\psi_a \psi'_b\rangle \quad (2)$$

where $|\psi_a\rangle$ ($|\psi_b\rangle$) and $|\psi'_a\rangle$ ($|\psi'_b\rangle$) are respectively the ground and the excited state wave functions of a (b) molecule and are eigenstates of the single molecule operator H_a (H_b); $|\phi\rangle$ is the excitonic wave function of the dimer.

In absence of intermolecular interactions ($V_{ab} = 0$) the excited states of the dimer are given by the degenerate states $|\psi'_a \psi_b\rangle$, $|\psi_a \psi'_b\rangle$. The effect of the intermolecular interactions is to remove the degeneration: the eigenfunctions of the hamiltonian in Eq. (1) are described by an *in-phase* combination of the previously degenerate states, ϕ_+ (c_a and c_b with same sign), and by an *out-of-phase* combination, ϕ_- (c_a and c_b with different sign). The states ϕ_+ and ϕ_- are splitted in energy by the quantity $2J_{ab}$ [2]:

$$J_{ab} = \langle \psi'_a \psi_b | V_{ab} | \psi_a \psi'_b \rangle \quad (3)$$

J_{ab} is called *exciton coupling* or resonance coupling integral and it is a measure of how easily the excitation energy can be transferred between the molecular site a and b (resonance coupling integral). The sign of the exciton coupling determines if the lower energy excitonic state is associated to the ϕ_+ ($J_{ab} < 0$) or ϕ_- ($J_{ab} > 0$) wave function [2]. In particular, by recognising the *in-phase* and *out-of-phase* nature of the excited states in a dimer, it becomes straightforward the evaluation of the exciton coupling (in sign and modulus) from the Davydov splitting $2J = E_{\phi_+} - E_{\phi_-}$.

These results can be extended to the case of a generic molecular aggregate or a crystal composed by N identical molecules. Upon crystal formation, from a single molecular excited state one obtains N excited states which form an exciton band. The width of the exciton band is proportional to the exciton coupling integral J [2]. The Frenkel hamiltonian of a crystal can be expressed on the basis set of the excitonic wave functions $|p\rangle$ in which only one molecule at site p is excited while all the others ($p \neq q$) are in their ground state:

$$H = \sum_{p=1}^N |p\rangle \Omega_p \langle p| + \sum_{p,q=1}^N |p\rangle J_{pq} \langle q|; \quad |p\rangle = |\psi'_p\rangle \prod_{q \neq p} |\psi_q\rangle \quad (4)$$

where Ω_p is the *on-site excitation energy* (required to excite a molecule at site p) and J_{pq} represent exciton couplings.

The eigenfunctions of the crystal hamiltonian given by Eq. (4) are named crystal exciton wave functions $|\Phi_k\rangle$, here expressed as a linear combination of localised wave functions:

$$|\Phi_k\rangle = \sum_{p=1}^N c_{kp} |p\rangle \quad (5)$$

In the case of an organic crystal with M molecules per cell, the Bloch theorem can be applied to the wave function $|\Phi_k\rangle$ in Eq. (5) and the crystal hamiltonian can be cast into a block-diagonal form, where each block has dimension $M \times M$ and depends on the choice of the wave vector \mathbf{k} , which can be expressed in terms of the associated phase factors θ_i :

$$\theta_i = \mathbf{k} \cdot \mathbf{a}_i; \quad i = 1, 2, 3 \quad (6)$$

where \mathbf{a}_i are the fundamental translations of the crystal lattice. When written on the basis of Bloch wave functions, each \mathbf{k} -dependent block of the hamiltonian of Eq. (4) assumes the following form:

$$H(\theta_1, \theta_2, \theta_3) = \mathbf{A} + \sum_{n_1, n_2, n_3=1}^{N_1 N_2 N_3} [\mathbf{B}^{n_1 n_2 n_3} \cdot e^{i(n_1 \theta_1 + n_2 \theta_2 + n_3 \theta_3)} + (\mathbf{B}^{n_1 n_2 n_3})^\dagger \cdot e^{-i(n_1 \theta_1 + n_2 \theta_2 + n_3 \theta_3)}] \quad (7)$$

Matrix \mathbf{A} collects interactions among molecules located within the same cell (intra-cell interactions), while matrix $\mathbf{B}^{(n_1 n_2 n_3)}$ contains the interactions between molecules in the reference cell (taken as origin) and the cell identified by the lattice translation $\mathbf{R} = n_1 \mathbf{a}_1 + n_2 \mathbf{a}_2 + n_3 \mathbf{a}_3$.

In order to obtain the matrix elements of the exciton hamiltonian (Eq. (7)) from quantum chemical methods, one can compare the full calculation of a dimer (or aggregate) with that of the components. To foster this task it is highly desirable a method that allows to make a reliable correspondence between the excited states of the constituent molecules and those of the aggregate. Here we propose a direct method for classifying excited states of organic crystals or aggregates based on the transition density matrix (TDM) approach. TDMs can describe in details excited states and have been successfully used in the literature [17,18]. The TDM between the ground $|g\rangle$ and a generic excited state $|j\rangle$ of a system, is defined as [17]:

$$\rho^j = \langle g | c_n^\dagger c_m | j \rangle \quad (8)$$

where c_n^\dagger , c_m are respectively the creation and the annihilation operators for the n th and m th atomic orbitals, usually assumed to be orthonormal. ρ^j describes the excitation process $|g\rangle \rightarrow |j\rangle$ in terms of changes in the electronic density and it can be thought as a vector in Liouville space [17].

When assuming the Frenkel exciton picture for the j th excited state of the dimer (see Eq. (2)), the associated TDM takes the form:

$$\rho_{ab}^j = c_a \langle \psi_a \psi_b | c_n^\dagger c_m | \psi'_a \psi_b \rangle + c_b \langle \psi_a \psi_b | c_n^\dagger c_m | \psi_a \psi'_b \rangle \quad (9)$$

where $\psi'_{a/b}$ refers to some fixed excited state of the monomer (a or b) with associated TDM ρ_a^i (or ρ_b^i). By recalling the definition given by Eq. (8) and considering the subspaces associated to the molecules a and b , it can be shown that the dimer TDM has the following structure:

$$\rho_{ab}^j = \begin{bmatrix} c_a \rho_a^i & 0 \\ 0 & c_b \rho_b^i \end{bmatrix} + \rho_{ab}^{j-CT} \quad (10)$$

The use of atomic orbitals easily allows partitioning in Eq. (10) the contributions over blocks associated to molecule a and b . The diagonal blocks of ρ_{ab}^j are the TDMs of the single molecules weighted with their own exciton coefficients (c_a and c_b , see Eq. (2)), while the off-diagonal contribution ρ_{ab}^{j-CT} , associated to intermolecular charge transfer contribution, is defined as:

$$\rho_{ab}^{j-CT} = c_a \begin{bmatrix} 0 & \langle \psi_a \psi_b | c_n^\dagger c_m | \psi'_a \psi_b \rangle \\ \langle \psi_a \psi_b | c_n^\dagger c_m | \psi'_a \psi_b \rangle & 0 \end{bmatrix} + c_b \begin{bmatrix} 0 & \langle \psi_a \psi_b | c_n^\dagger c_m | \psi_a \psi'_b \rangle \\ \langle \psi_a \psi_b | c_n^\dagger c_m | \psi_a \psi'_b \rangle & 0 \end{bmatrix} \quad (11)$$

We have verified that for the lower energy exciton states of PNA dimers here considered the elements belonging to the off-diagonal blocks of the TDMs are much smaller than those of the diagonal blocks (by about two orders of magnitude).

Our aim is the analysis of the TDMs of the dimer based on the TDMs of the isolated molecules. The following procedure allows to determine the exciton wave function coefficients c_a and c_b . The comparison between TDMs of different excited states (i.e. state $|i\rangle$ and $|j\rangle$) requires the introduction of an inner product in Liouville space where TDMs are considered as vectors [17]:

$$(\rho^i, \rho^j) \equiv \text{Tr}(\rho^{i\dagger} \cdot \rho^j) = \sum_{n,m} (\rho_{nm}^i)^* \rho_{nm}^j \quad (12)$$

The inner product in Eq. (12) corresponds to the Frobenius product between matrices [19]. If $|i\rangle$ and $|j\rangle$ are different excited states, the product between the corresponding orthogonal TDMs is zero,

otherwise its value gives the square of the normalisation constant of the TDM, which can be assumed to be 1.

Calculations of excited states and TDMs have been carried out by using the semiempirical ZINDO method, that meets the hypothesis of orthogonal AOs and provides accurate results for the excited states of conjugated molecules [17,20]. The GAUSSIAN03 suite of programs [21] has been used to carry out all quantum chemical calculations here reported. For the sake of completeness also time-dependent DFT calculations (TD-B3LYP/6-31G^{**}) have been considered using the same projection method and roughly approximating the atomic orbitals basis set to be orthogonal. Such an approximation does not introduce any error in the determination of the exciton couplings, which are obtained as half of the energy difference between properly classified excited states of the dimers. The classification procedure does not require the accurate determination of the numerical value of the wavefunction coefficients c_a and c_b . For a given excited state of interest, one only needs to know whether c_a and c_b are substantially different from zero and their relative signs.

The Frobenius product is here applied for projecting the dimer TDMs ρ_{ab}^i over those of the constituent molecules ρ_a^i, ρ_b^i . In this way, we can classify the aggregate (dimer) excited states on the basis of those of the single molecules (a, b) and thus we represent the excitonic wave functions $|\phi_{\pm}\rangle$ by determining directly the coefficients c_a and c_b :

$$\left(\begin{bmatrix} \rho_a^i & 0 \\ 0 & 0 \end{bmatrix}, \rho_{ab}^j \right) = \left(\begin{bmatrix} \rho_a^i & 0 \\ 0 & 0 \end{bmatrix}, \begin{bmatrix} c_a \rho_a^i & 0 \\ 0 & c_b \rho_b^i \end{bmatrix} \right) = c_a (\rho_a^i, \rho_a^j) = c_a \delta_{ij} \quad (13)$$

Similarly, in the case of molecule b , the Frobenius product of Eq. (13) involving ρ_b^i on the left hand side gives $c_b \delta_{ij}$.

3. Application to the PNA crystal

The TDM approach presented above is applied here to the PNA crystal. PNA is a well-known compound thanks to its non-linear optical properties, known since long time [22,23]. In solid state it establishes stable dipole–dipole interactions and hydrogen bonds. PNA single crystal has a monoclinic unit cell with four symmetry-equivalent molecules per cell [12].

Despite the fact that PNA is a well-known organic compound, widely studied from a spectroscopic point of view both in gas phase [13] and in solution [14,15], to date no experimental and theoretical UV–Vis spectra have been reported for solid state PNA. We aim at the interpretation of the UV–Vis absorption spectrum of crystalline powders of PNA in order to describe the aggregation effects in terms of changes in the optical properties (from gas phase [13] and solution [14,15], to solid state). Moreover, PNA provides a benchmark for testing the applicability of the molecular exciton theory to a system with interactions somewhat stronger than systems for which the Frenkel exciton approximation is usually considered.

As a first step, starting from the X-ray crystal structure of PNA [12] we classified, through a systematic structural analysis, all possible nearest neighbour pairs of molecules, finding nine non equivalent molecular dimers that are reported in Fig. 2. For each of them we have evaluated the exciton coupling J_{pq} in order to write the crystal hamiltonian given by Eq. (7). By symmetry of the PNA crystal, the on-site excitation energy Ω_p is equal for all molecules. It has been set equal to the excitation energy evaluated with ZINDO for the first dipole-allowed excited state (see below). Preliminary calculations carried out on molecular aggregates obtained from the experimental crystal structure suggest that non nearest neighbour interactions have a negligible contribution. Therefore, interactions

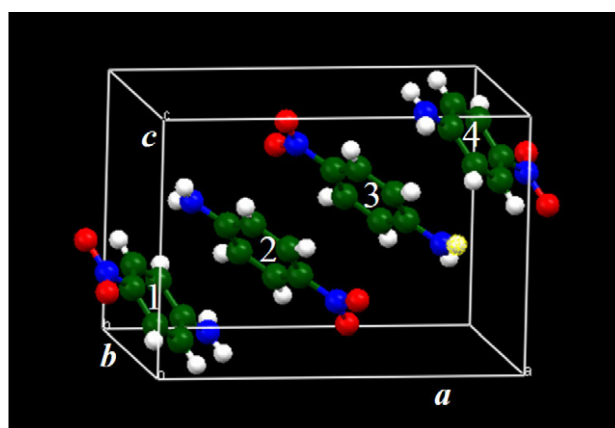


Fig. 1. The four symmetry-equivalent PNA molecules in the crystalline monoclinic unit cell according to X-ray diffraction analysis [12]. Atom colour scheme is the following: green carbon, red oxygen, blue nitrogen, white hydrogen. PNA molecules are labeled according to the same scheme followed to write the exciton hamiltonian. (For interpretation of the references to colour in this figure legend, the reader is referred to the web version of this article.)

farther than nearest neighbour have not been considered in this work.

The procedure for the evaluation of the exciton couplings belongs to the so-called supramolecular approach [11]. Here below we report in details the application of the TDM projection method for the evaluation of the exciton coupling relative to the A dimer (see Fig. 2). The same procedure has been employed for all other cases.

Dimer A consists of two PNA molecules positioned face-to-face with anti-parallel dipoles at a distance of 3.83 Å between the centre of mass. The lowest six excited states have been calculated, by using ZINDO and TD-DFT (B3LYP/6-31G^{**}), for the dimer (ab) and the single molecules (a) and (b). The molecular geometries have been obtained directly from crystal structure data [12] and no geometry optimization has been applied.

According to ZINDO calculations for the single molecule, the first two excited states $S_{a/b}^1$ (2.42 eV) and $S_{a/b}^2$ (2.81 eV) are dipole forbidden while state $S_{a/b}^3$ is dipole-allowed (oscillator strength $f = 0.47$) with an excitation energy of 3.47 eV and mainly a HOMO–LUMO character. Three higher excited states of the monomer have been also taken into consideration in order to better validate the projection method here proposed.

In dimer A the first five excited states ($S_{ab}^1 = 2.46$ eV, $S_{ab}^2 = 2.46$ eV, $S_{ab}^3 = 2.85$ eV, $S_{ab}^4 = 2.85$ eV, $S_{ab}^5 = 3.13$ eV) are dipole forbidden while S_{ab}^6 , with an excitation energy of 3.39 eV, is dipole-allowed ($f = 0.85$). For each excited state of dimer A we have applied the TDM projection method (see Eqs. (12) and (13)) in order to classify the excited states of the dimer on the basis of those of the monomer units (both a and b). To this aim, we have projected according to Eq. (13) the TDMs of the first six excited states of the dimer (ρ_{ab}^j , $2N \times 2N$ matrix, with $j = 1, 6$ and N the number of atomic orbitals of the PNA single molecule) onto those of the single molecules ($\rho_{a/b}^j$, $N \times N$ matrix, with $j = 1, 6$). The results of this procedure, corresponding to the exciton wave function coefficients c_a and c_b , are reported in Table 1. We observe that the first four excited states of the dimer are originated from single excitons of the isolated molecules (e.g. S_{ab}^1 derives from S_a^1 , S_{ab}^2 derives from S_b^1 , etc.), consistently with the fact that these states are degenerate and do not couple. The relevant result reported in Table 1, is that the dipole-allowed single molecule excited state of a (S_a^3) and b (S_b^3) combine originating the two Davydov split levels: S_{ab}^5 (*in-phase* exciton ϕ_+) is the lower energy one and S_{ab}^6 (*out-of-phase* exciton

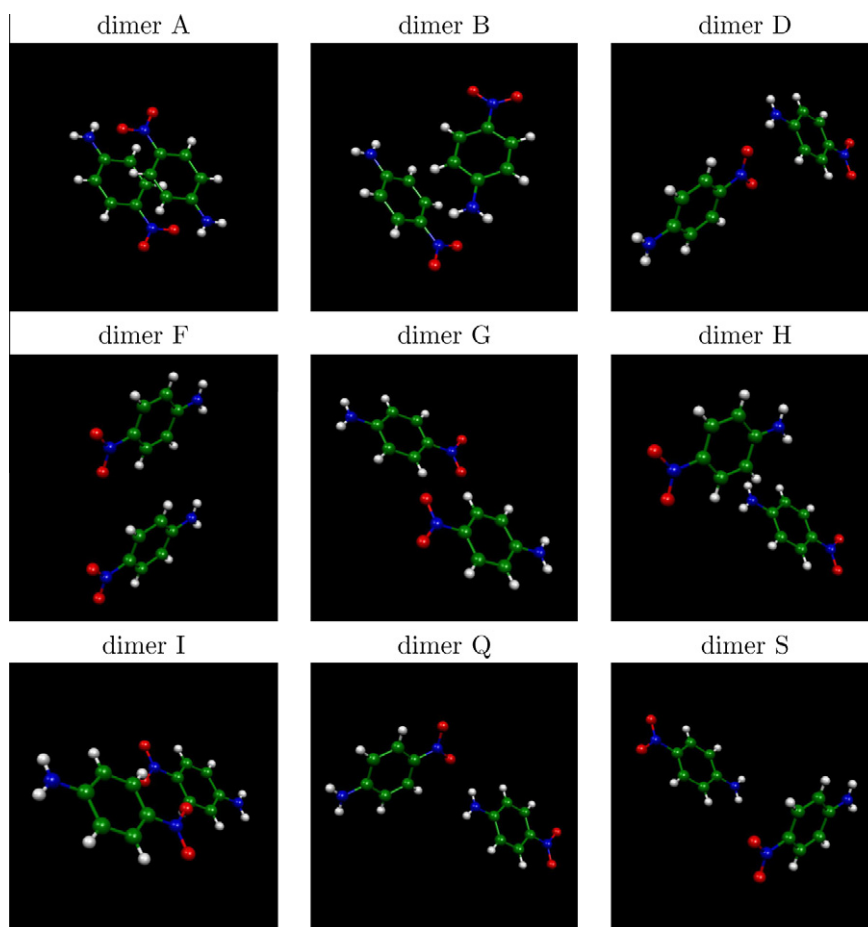


Fig. 2. Non-equivalent nearest neighbour dimers extracted from the crystal structure of PNA [12].

Table 1

Coefficients derived from the TDM projection procedure for dimer A; the dimer TDM ρ_{ab}^j is projected on the monomers one $\rho_{a/b}^j$. Coefficients lower than 0.01 are not reported.

	ρ_a^1	ρ_b^1	ρ_a^2	ρ_b^2	ρ_a^3	ρ_b^3	ρ_a^4	ρ_b^4	ρ_a^5	ρ_b^5	ρ_a^6	ρ_b^6
ρ_{ab}^1	1.00	0.04	–	–	–	–	–	–	–	–	–	–
ρ_{ab}^2	0.04	–1.00	–	–	–	–	–	–	–	–	–	–
ρ_{ab}^3	–	–	1.00	–0.09	–	–	–	–	–	–	–	–
ρ_{ab}^4	–	–	–0.09	–1.00	–	–	–	–	–	–	–	–
ρ_{ab}^5	–	–	–	–	0.70	0.69	0.04	0.04	–	–	–0.02	–0.02
ρ_{ab}^6	–	–	–	–	0.70	–0.71	–	–	–	–	–0.04	–0.04

ϕ_-) is the higher energy one. We observe that very small contributions from $S_{a/b}^4$ and $S_{a/b}^6$ states are also found. These minor contributions have been neglected in the forthcoming analysis since the associated coefficients in the excitonic wavefunction that describes states S_{ab}^5 and S_{ab}^6 are less than one order of magnitude smaller than those of $S_{a/b}^3$.

Finally, once the *in-phase* and *out-of-phase* excitons have been identified (S_{ab}^5 and S_{ab}^6 , respectively – see Table 1) we can evaluate in sign and modulus the exciton coupling for dimer A as:

$$J = \frac{E_{\phi_+} - E_{\phi_-}}{2} = \frac{S_{ab}^5 - S_{ab}^6}{2} = -0.13 \text{ eV.} \quad (14)$$

The validity of the TDM projection method has been tested further by comparing the transition dipole moment μ_{ab}^j computed for the dimer with that deduced from the coefficients obtained with the TDM method and the excitonic approach [2]:

$$\mu_{ab}^j = c_a \mu_a^j + c_b \mu_b^j \quad (15)$$

In Table 2 we report the cartesian components of the transition dipole moments for the Davydov split excited states of the dimer (S_{ab}^5 and S_{ab}^6) evaluated with (i) a direct ZINDO calculation on dimer A

Table 2

Cartesian components of transition dipole moment μ_{ab}^j for excited states S_{ab}^5 and S_{ab}^6 of dimer A, obtained by a ZINDO calculation on the dimer and the TDM projection method approach (Eq. (15) see text). Transition dipole moments are expressed in Debye.

	μ_{ab}^5			μ_{ab}^6		
	μ_x	μ_y	μ_z	μ_x	μ_y	μ_z
ZINDO	0.00	0.00	–0.02	–0.07	–0.11	–3.21
TDM	0.00	0.00	–0.03	–0.06	–0.07	–3.31

Table 3
Exciton couplings for all possible nearest neighbour PNA molecules in the crystal evaluated at ZINDO and TD-B3LYP/6-31G** levels. The distances between the centre of mass of the molecules in each dimer are reported together with the i, j labels of both molecules and their cell indexes within the crystal (see also Fig. 1). The i index is always referred to a molecule placed within the reference (0, 0, 0) cell. These J values have been used to write the **A** and **B** appearing in Eq. (7).

Dimer	ZINDO J (eV)	TD-DFT J (eV)	Mass centre distance (Å)	$i \in (0, 0, 0)$	$j \in (n_1, n_2, n_3)$	n_1	n_2	n_3
A	-0.1309	-0.0919	3.83	2	3	0	0	0
B	-0.0362	-0.0439	4.61	1	2	0	0	0
D	-0.0556	-0.0560	8.06	1	3	0	0	-1
F	0.0396	0.0328	6.03	1	1	0	1	0
G	-0.0478	-0.0305	6.94	1	4	-1	0	-1
H	0.0179	0.0177	7.32	1	2	0	1	-1
I	-0.0179	0.0017	7.70	1	4	-1	1	0
Q	-0.0295	-0.0381	8.23	1	3	0	1	-1
S	0.0135	0.0107	7.53	1	3	-1	1	-1

and (ii) the excitonic approach through TDMs (Eqs. (15) and (13)). We obtain a very good agreement between approach (i) and (ii) thus both demonstrating the validity of the TDM projection method and testing the known additivity of transition dipoles in Frenkel exciton aggregates.

With the help of the TDM projection method the results obtained with ZINDO on the dimer can be fully rationalized. Since molecules in dimer A are in an anti-parallel configuration, the *in-phase* combination of $\mu_{a/b}$ (state S_{ab}^5) gives a vanishing total μ_{ab} . On the opposite, in the *out-of-phase* combination (state S_{ab}^6) the transition dipole moments of monomers are cooperatively added together, giving rise to a net transition dipole μ_{ab} .

The procedure described above has been also applied for all the dimers extracted from the PNA crystal structure, evaluating all the exciton couplings required for the construction of the crystal exciton hamiltonian (see Eq. (7)). We list in Table 3 the exciton couplings for the PNA dimers shown in Fig. 2. Results from both ZINDO and TD-B3LYP/6-31G** are given. The two methods provide a very similar description: the couplings have the same order of magnitude and sign, except for dimer I. The exciton coupling associated to dimer A, in which the molecules are as close as possible in the crystal, is the largest. The other couplings have the same order of magnitude, therefore none of them can be neglected in the formulation of **H**.

Overall the evaluated exciton couplings (Table 3) nicely compare with values reported in literature for other organic crystals or molecular aggregates (e.g. $J = 0.012$ eV for nanotubes aggregates [24] or $J = 0.008$ eV for biological molecules [25]). Notably the exciton coupling for dimer A is rather large due to close dipole-dipole interaction. By symmetry the on-site transition energies are equivalent for all four molecules within the crystal cell and they have been approximated with the excitation energy of the molecule (with geometry given by the X-ray diffraction data) as: 3.48 eV (ZINDO) and 4.14 eV (TD-B3LYP/6-31G**).

4. Results and discussion

PNA has an intense UV-Vis absorption band centred around ~ 4.2 eV in gas phase with no resolved vibronic structure [13]. This absorption band red shifts in solution, with a strong solvatochromism behaviour by changing the solvent polarity, from 3.8 eV in cyclohexane to 3.3 eV in water [15].

Absorption UV-Vis spectra of solid crystalline PNA powders, to the best of the authors knowledge, have not been reported in the literature. Therefore we have proceeded with a measure in our laboratory (thanks to Dr. A. Lucotti). The UV-Vis absorption spectrum has been recorded by depositing a few drops of ethanol solution of PNA on a QS SUPRASIL quartz slide (from Hellma, spectral range 200–2500 nm) and letting them dry completely. A thin polycrystal-

line deposit was obtained suitable for measurement with an integrating sphere setup on a JASCO 570 V UV-Vis NIR spectrometer.

We show in the upper panel of Fig. 3 the UV-Vis absorption spectrum of crystalline PNA powders at room temperature: the main absorption band peaks around 3.0 eV, with a band-width of ~ 1.8 eV (from 2.55 to 4.35 eV) and a satellite peak around 4.1 eV. Comparing the solid state absorption with the main intense absorption band of PNA in gas phase [13] and in solution [15], we observe an aggregation induced effect (crystal effect) which causes an overall red shift and a broadening of the main exciton band (from 4.2 eV in gas phase down to 3.0 eV in crystalline powders).

ZINDO (and also TD-DFT) simulations carried out on the isolated PNA unit cell (containing four molecules) are not able to describe the absorption spectrum of crystalline PNA. In particular ZINDO predicts two dipole allowed excited states, positioned at 3.34 eV ($f = 0.43$) and at 3.45 eV ($f = 1.18$). These states do not describe the correct red shift and overall, can not account for the observed broadening (see Fig. 3).

The experimental solid state absorption spectrum can be rationalised in the framework of Frenkel exciton theory and the previous theoretical analysis (Section 3). Starting from the knowledge of the exciton couplings J_{pq} (see Table 3) and of the on-site excitation energy Ω_p , we can write the crystal hamiltonian of Eq. (7) for the PNA crystal. The PNA unit cell contains four molecules, hence the

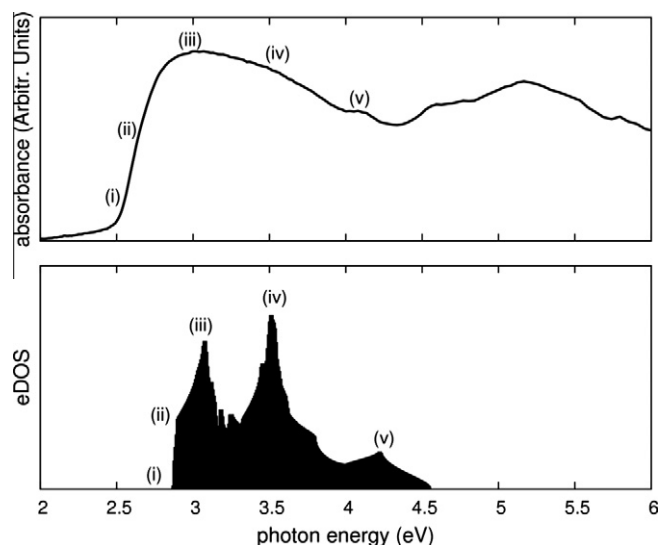


Fig. 3. UV-Vis absorption spectrum of PNA crystalline powders at room temperature (upper panel) and density of exciton states (eDOS) for the PNA crystal from ZINDO simulations (lower panel). Labels are placed in correspondence of characteristic features of the experimental spectrum which are also recognisable in the calculated eDOS. See text for details.

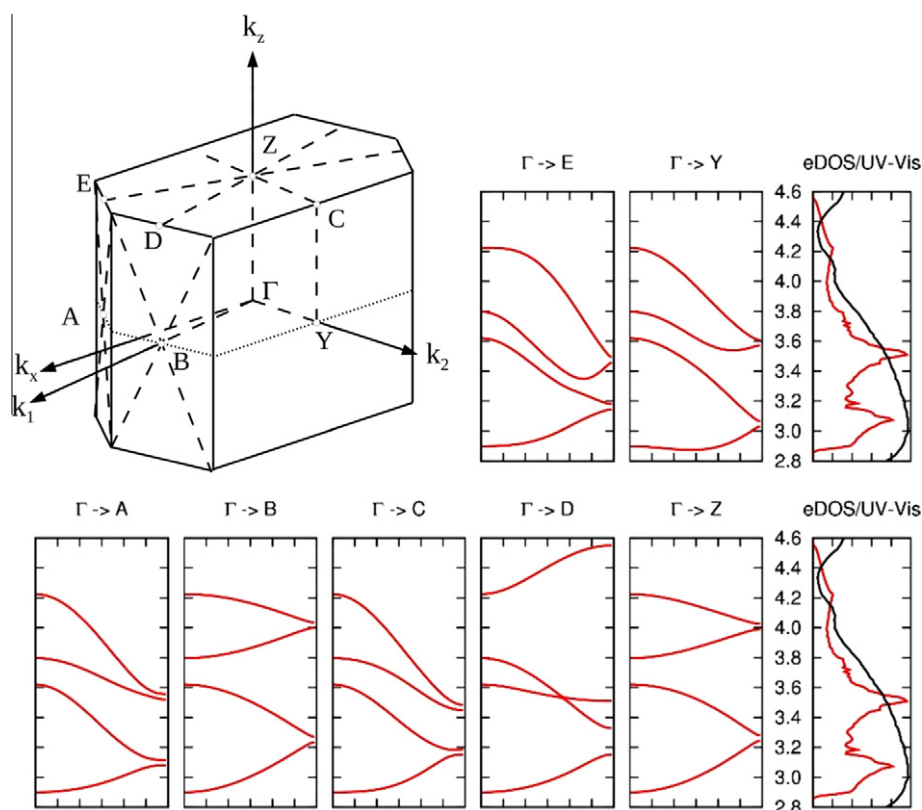


Fig. 4. Exciton dispersion bands of the PNA crystal as calculated from diagonalisation of the crystal exciton hamiltonian along specific directions of the reciprocal lattice reported in the first top panel.

crystal exciton states originated from the first dipole-allowed excited state of PNA ($S^3 = 3.47$ eV, ZINDO) will result in four bands.

Rashba's theory [2,9,16,26] asserts that, assuming a little bandwidth of the phonon dispersion band, the absorption spectrum of an organic solid turns to be proportional to the exciton density of states eDOS (E):

$$I_{abs} \propto \text{eDOS}(E) \quad (16)$$

Excitons in PNA crystal can be optically created far from the Γ point ($\mathbf{k} = \mathbf{0}$) since the formation of an exciton with wave vector \mathbf{k} can be assisted by a coupled phonon with wave vector $\mathbf{q} = -\mathbf{k}$. In this way the conservation of momentum is guaranteed and excitations can occur all over the first Brillouin zone (BZ) ($-\pi < \theta_i < \pi$, $i = 1, 2, 3$).

The exciton density of states obtained by diagonalising \mathbf{H} (Eq. (7)) within the first BZ is reported in Fig. 3 (bottom panel) and compared with the experimental UV-Vis absorption spectrum, recorded on PNA powders. This eDOS is related to the four exciton bands associated to the first optically allowed excited state of PNA (S^3). Thus the absorption band experimentally observed around 5.0 eV is not accounted for by our calculations since it is originated from higher excited states which have not been considered here.

From the comparison between the eDOS and the absorption spectrum of PNA powders, we can observe that the eDOS is overall centered on the main absorption band and that the eDOS width nicely spans over the experimental band-width. Moreover, many characteristic peaks of the eDOS are found in correspondence or close to features of the experimental spectrum (see labels (i)–(v) in Fig. 3). The absence of any absorption band below 3.0 eV (i), the main band around 3.0 eV (iii) and the low intensity peak around 4.1 eV (v) are well accounted for by the computed eDOS.

Also slight changes in the slope of the absorption, (ii) and (iv) can be related with corresponding features of the eDOS.

Further insights on the description of excitons in PNA crystals can be obtained from the analysis of the exciton band dispersion in the first BZ. These have been obtained by diagonalising \mathbf{H} along high symmetry directions starting from the Γ point. The exciton bands are reported in Fig. 4 together with the eDOS. We observe that there are some directions along which exciton bands are highly dispersive ($\Gamma \rightarrow E$, $\Gamma \rightarrow Y$, $\Gamma \rightarrow D$) and directions along which the bands are less dispersive ($\Gamma \rightarrow Z$, $\Gamma \rightarrow B$). The analysis of exciton bands dispersion, which can be easily obtained with the present approach, could be of use for the evaluation of exciton mobility in organic crystals.

5. Conclusions

Molecular exciton theory, within the Frenkel approximation, has been applied to describe the UV-Vis absorption spectrum of PNA in its crystalline state. A method based on the evaluation of the transition density matrix has been conceived in order to classify the excited states of molecular aggregates (specifically dimers) on the basis of those of the single molecules, as extracted from the aggregate. This method provides a detailed and satisfactory description of excitons in the aggregate.

The crystal hamiltonian of PNA has been evaluated by determining all exciton couplings between nearest neighbours. The resulting exciton density of states has been successfully used within Rashba theory to analyse the features observed in the UV-Vis absorption of PNA crystalline powders.

This demonstrates the applicability of both the TDM projection method and the molecular exciton theory even in the description of non-weakly interacting molecular crystal as the PNA crystal

(characterised by dipole–dipole interactions and hydrogen bonding).

Acknowledgments

This work was supported by the Italian Ministry of Education, University and Research (MIUR) through PRIN Project 2008 JKBBK4 ‘Tracking Ultrafast photoinduced intra- and intermolecular processes in natural and artificial photosensors’. The authors gratefully acknowledge Dr. A. Lucotti (Politecnico di Milano) for UV–Vis absorption spectrum of PNA crystalline powders. One of the authors (M.T.) wishes to express his gratitude to Prof. Shaul Mukamel for introducing him to the use of density matrices.

References

- [1] J.L. Brédas, D. Beljonne, V. Coropceanu, J. Cornil, *Chem. Rev.* 104 (2004) 4971.
- [2] M. Pope, C.E. Swenberg, *Electronic Process in Organic Crystals*, Oxford University Press, New York, 1982.
- [3] A.S. Davydov, *Theory of Molecular Exciton*, McGraw-Hill, New York, 1962.
- [4] J. Frenkel, *Phys. Rev.* 37 (1931) 17.
- [5] T. Holstein, *Ann. Phys.* 8 (1959) 325.
- [6] S.H. Lim, T.G. Bjorklund, F.C. Spano, C.J. Bardeen, *Phys. Rev. Lett.* 92 (2004) 107402.
- [7] F.C. Spano, *Annu. Rev. Phys. Chem.* 57 (2006) 217.
- [8] S. Athanasopoulos, E.V. Emelianova, A.B. Walker, D. Beljonne, *Phys. Rev. B* 80 (2009) 195209.
- [9] W. Gebauer, A. Langner, M. Schneider, M. Sokolowski, E. Umbach, *Phys. Rev. B* 69 (2004) 125420.
- [10] J. Cornil, D.A. dos Santos, X. Crispin, R. Silbey, J.L. Brédas, *J. Am. Chem. Soc.* 120 (1998) 1289.
- [11] J. Cornil, D. Beljonne, R. Silbey, P. Millié, J.L. Brédas, *J. Chem. Phys.* 112 (2000) 4749.
- [12] M. Tonogaki, T. Kawata, S. Ohba, Y. Iwata, I. Shibuya, *Acta Crystallogr.* 49 (1993) 1031.
- [13] S. Millefiori, G. Favini, A. Millefiori, D. Grasso, *Spectrochim. Acta* 33 (1977) 21.
- [14] T.P. Carsey, G.L. Findley, S.P. McGlynn, *J. Am. Chem. Soc.* 101 (1979) 4502.
- [15] V.M. Farztdinov, R. Schanz, S.A. Kovalenko, N.P. Ernsting, *J. Phys. Chem. A* 104 (2000) 11486.
- [16] E.I. Rashba, *Soviet. Phys. Solid State* 5 (1963) 757.
- [17] S. Mukamel, S. Tretiak, *Chem. Rev.* 102 (2002) 3171.
- [18] C. Curuchet, B. Mennucci, *J. Am. Chem. Soc.* 127 (2005) 16733.
- [19] We note that the definition given by Eq. (12) slightly differs from the definition of scalar product given in [17] for CEO transition density matrices. This is due in this work to the use of transition density matrices obtained from calculations different from CEO ones.
- [20] M. Ottonelli, G. Musso, G. Dellepiane, *J. Phys. Chem. A* 112 (2008) 3991.
- [21] M.J. Frisch et al., *Gaussian 03, Revision C.02*, Gaussian Inc., Wallingford, CT, 2004.
- [22] D. Chemla, J. Zyss, in: D. Chemla, J. Zyss (Eds.), *Nonlinear Optical Properties of Organic Molecules and Crystals*, vol. 1, Academic Press, New York, 1987, p. 23.
- [23] R. Cammi, L. Frediani, B. Mennucci, K. Ruud, *J. Chem. Phys.* 119 (2003) 5818.
- [24] C.Y. Wong, C. Curuchet, S. Tretiak, G.D. Scholes, *J. Chem. Phys.* 130 (2009) 081104.
- [25] C. Curuchet, G.D. Scholes, B. Mennucci, R. Cammi, *J. Phys. Chem. B* 111 (2007) 13253.
- [26] R. Totoki, T. Aoki-Matsumoto, K. Mizuno, *J. Luminescence* 112 (2005) 308.

2.3.2 attachment b

Cite this: *Phys. Chem. Chem. Phys.*, 2011, **13**, 18615–18625

www.rsc.org/pccp

PAPER

A computational investigation on singlet and triplet exciton couplings in acene molecular crystals†

Claudio Quarti,^{ab} Daniele Fazzi^{*c} and Mirella Del Zoppo^{ab}

Received 19th April 2011, Accepted 30th August 2011

DOI: 10.1039/c1cp21246j

Quantum chemical calculations (DFT, TDDFT and ZINDO/S) of singlet and triplet exciton couplings are presented and discussed for some acene derivatives (such as anthracene, tetracene, 9,10-di(phenyl)anthracene and 9,10-bis(phenylethynyl)anthracene). An accurate excited state single molecule characterization has been carried out followed by an analysis of the inter-molecular excitonic interactions, taking place in the crystalline phase. These have been correlated to exciton coupling terms obtaining guidelines for the choice of molecular materials with large exciton couplings. Such organic systems are likely to show multiexciton processes such as singlet fission (SF) and triplet–triplet annihilation (TTA) which are useful in energy conversion phenomena to be exploited in photonic and optoelectronic devices.

Introduction

Organic conjugated materials have become the centre of an ever growing interest in the field of energy conversion and storage.^{1–10} Organic photovoltaic (OPVC) solar cells are indeed currently produced and available on the worldwide market.^{6–8} In organic materials the conversion of the incoming solar energy into electric current takes place in several steps that occur inside the cell, namely: (i) exciton formation, (ii) transport (*i.e.* diffusion), (iii) exciton dissociation (separation of electron–hole pairs), (iv) transport of the carriers to the

electrodes and (v) extraction of the charges to the external circuit.¹¹ Every step has to be optimized in order to obtain a good yield in the overall photoinduced process.^{1–4,11} Many studies, both theoretical and experimental, have been carried out during these years to find, for organic materials, structure–property relationships which can help in the optimization of solar energy conversion efficiency.^{1–4}

One of the factors limiting the efficiency of conventional single-stage OPVC solar cells having a single light-absorbing phase is that part of the energy of the absorbed photons is converted into heat and only the photons with energy close to the energy gap of the absorbing medium can be used for energy production.¹² One way to improve the efficiency is that of taking advantage of exciton multiplication processes such as singlet fission (SF).^{12–17} In this process, an excited singlet state of a chromophore (a) shares its energy with a nearby molecule (b) in its ground state, producing a triplet excited state for both a and b. If the two triplets are sufficiently independent from each other to produce separated charge carriers, the photocurrent per photon would pass from 1/3, for an ideal single stage solar cell, to nearly 1/2 for SF cells.^{12,15–17}

SF can be considered a special kind of internal conversion and, like many other internal conversion processes, it can be very fast particularly in molecular crystals. SF is closely related to the inverse phenomenon, namely, triplet–triplet annihilation (TTA), where two triplet states on two neighboring chromophores (a and b) annihilate promoting one molecule (a) in an excited singlet state, leaving the other one (b) in its ground state.^{15–18} Both SF and TTA require that excitons, either singlet or triplet, be easily excited, diffuse and interact. In the case of molecular crystals, singlet excitons are short-lived (\sim ns timescale) and may be delocalized over more than one site, whereas triplet excitons are long-lived (\sim μ s) and tend

^a Politecnico di Milano, Dipartimento di Chimica, Materiali e Ing. Chimica CMIC “G. Natta”, p.za Leonardo da Vinci 32, 20133, Milano, Italy

^b INSTM, Udr Milano, Italy

^c Center for Nano Science and Technology @PoliMi, Istituto Italiano di Tecnologia, via Giovanni Pascoli, 70/3, 20133 Milano. E-mail: daniele.fazzi@iit.it

† Electronic supplementary information (ESI) available: Exciton couplings of the most interacting dimers, by using the IEFPCM method (Table S1) TD-DFT singlet and triplet excitation energies of BPEA evaluated with different functionals (Table S2). Atom numbering of anthracene, tetracene, DPA and BPEA (Fig. S1). Unit cells of anthracene, tetracene, DPA and BPEA (Fig. S2–S5). Molecular dimers found in the experimental crystal structures (Fig. S6–S9). TDDFT exciton couplings evaluated with the PDA (Table S3). Transition density matrix projections for singlet excited states evaluated at the ZINDO/S level (Table S4–S7). Properties of the singlet excited states of the molecular dimers evaluated at TD B3LYP/6-31G**: excitation energies, oscillator strength, molecular orbitals involved in the main transitions, TD-DFT eigenvector of the main transitions (Table S7–S10). High density planes for anthracene, tetracene and BPEA (Fig. S10–S12). Singlet excited states of the molecular dimers evaluated with TD-B3LYP/6-31G** (Fig. S13). Singlet excited states evaluated with TD-CAM-B3LYP/6-31G** (Fig. S14). Triplet excited states of the molecular dimers evaluated with TD-B3LYP/6-31G** (Fig. S15). Triplet excited states evaluated with TD-CAM-B3LYP/6-31G** (Fig. S16). See DOI: 10.1039/c1cp21246j

to be localized on a single site.¹⁵ In a perfect molecular crystal, both types of excitons can move by random hopping.^{18–26} The diffusion length is normally much smaller for singlet excitons (~ 10 nm) than for triplet excitons (~ 10 μm) because of the different lifetimes. The ability of excitons to diffuse, by following a Förster or a Dexter like energy transfer process, depends primarily on the magnitude of the exciton coupling (V), *i.e.* the interaction energy between nearest neighbor molecules in their excited states (in other words how the two molecules share their energy). The larger the exciton coupling, the easier the exciton transport and diffusion. Generally, for molecular crystals, exciton couplings are large so that exciton diffusion can be efficient, thus increasing the probability of exciton–exciton interactions leading to SF or TTA processes.^{15,27,28}

SF and TTA processes are highly affected both by intra- (single molecule) and inter-molecular (supramolecular) properties. In SF, for instance, one necessary single molecule property is that the excited state energy levels of singlets and triplets satisfy the relation $E(S_1) \geq 2E(T_1)$.^{12,15} As for supramolecular properties, SF (and also TTA) is affected by the molecular organization (*e.g.* molecular packing in crystals, the amount of ordered phases in blends), by the purity of the crystalline phases, by the presence of defects (dislocations, vacancies) or multiphases and also by temperature (that determines the exciton hopping rate) and pressure.¹⁵

Within a molecular engineering approach, which has the purpose of identifying the most performing molecular system, one of the most important parameters which needs a thorough study and optimization, is the exciton coupling (or resonance transfer integral) V , which strongly depends on both the electronic excited state structure and on the supramolecular organization and packing, as widely discussed in the literature.^{26–38}

Multi exciton generation in acene molecular crystals had already been detected in 1965³⁹ for anthracene, and in 1968⁴⁰ for tetracene; SF mechanism has been indeed demonstrated on the basis of delayed fluorescence measurements. In the case of 9,10-di(phenyl)anthracene (DPA) and 9,10-bis(phenylethynyl)anthracene (BPEA), TTA has been observed up to date in solution with the presence of a sensitizer, such as an organometallic complex. The heavy atom of the sensitizer enhances the intersystem crossing rate ($S_n \rightarrow T_n$) thus producing a large number of triplet states from which the energy transfer to the triplet state of BPEA or DPA occurs.^{41–43}

In this paper we focus on the evaluation of exciton coupling terms, for both singlet and triplet excitons, for different molecular crystals belonging to the class of acenes such as anthracene (**1**), tetracene (**2**) and two anthracene derivatives namely, DPA (**3**) and BPEA (**4**) (molecular structures sketched in Fig. 1).

We have calculated both intra- and inter-molecular properties for compounds **1–4**, by using quantum chemical calculations both at the semiempirical ZINDO/S and *ab initio* DFT and TDDFT levels. Singlet and triplet excited state energies and transition dipole moment orientations have been evaluated upon both DFT optimized structures and experimental geometries from X-ray structures.^{44–49} For the calculation of inter-molecular properties, on the basis of the experimental X-ray structures, we have identified all the possible inter-molecular interactions between pairs of nearest neighbor

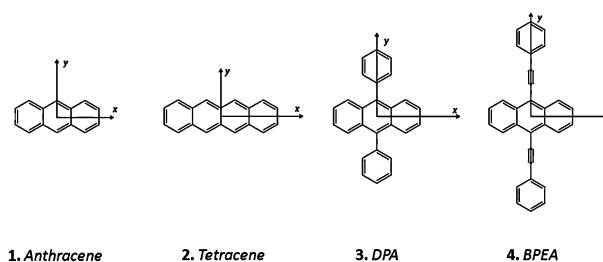


Fig. 1 Chemical structures of anthracene (**1**), tetracene (**2**), 9,10-di(phenyl)anthracene (DPA, **3**) and 9,10-bis(phenylethynyl)anthracene (BPEA, **4**). Long (x) and short (y) axes are also reported.

molecules (dimers) and, in the frame of ZINDO/S and TDDFT methods, we have evaluated the new excited state electronic structures and properties for all molecular crystals considered. For ZINDO/S calculations the classification of the excited states of molecular aggregates and crystals has been carried out on the basis of the transition density matrix (TDM) projection method, as reported in a previous work.⁵⁰ Both ZINDO/S and TDDFT exciton couplings have been evaluated in the frame of the so called supramolecular approach.^{29,51}

Purposes of this work are:

(i) to screen exciton properties of molecular crystals of some acenes widely used and studied for many optoelectronic and OPVC applications;

(ii) to correlate the effect of different chemical substituents (phenyl in DPA, and phenyl-ethynyl groups in BPEA) in the anthracene core with the excited state energies and structures, for both single molecules and crystals;

(iii) to provide useful guidelines for the development of new materials with improved exciton interactions (in particular for generating SF and TTA processes), thus providing enhanced performances in the field of solar energy conversion;

(iv) to compare the reliability of different methods (ZINDO/S *vs.* TDDFT) and functionals (B3LYP *vs.* CAM-B3LYP), in associating each single molecule excited state with the corresponding pair of dimer excited states present in the molecular crystal.

Methods

Excited state properties for **1–4** (see Fig. 1) molecular crystals have been studied in the framework of molecular exciton theory,^{30,52–54} thus assuming that the excited state wave functions in molecular aggregates are weakly influenced by inter-molecular forces. Under this hypothesis, they can be approximated by a linear combination of the excited state wave functions of the isolated molecules. In particular for a molecular dimer (ab) the Frenkel exciton Hamiltonian^{30,52,55} is given by:

$$H = H_a + H_b + V_{ab} \quad (1)$$

with H_a and H_b the Hamiltonian of the single molecules composing the dimer and V_{ab} the interaction term. Due to the presence of the V_{ab} term a generic excited state of the isolated molecule is split into two dimer states whose wavefunctions, approximated eigenfunctions of the Hamiltonian in eqn (1), are given as an in phase ($\phi_+ = c_a\psi'_a\psi_b + c_b\psi_a\psi'_b$) and

an out-of-phase ($\varphi_- = c_a\psi'_a\psi'_b - c_b\psi_a\psi'_b$) combination of the product between the ground ($\psi_{a/b}$) and the excited state wavefunctions ($\psi'_{a/b}$) of the isolated a/b molecules.^{30,54}

The energy splitting of states φ_+ and φ_- is $2V$ where V is the exciton coupling or resonance coupling integral, which is a measure of how easily the excitation energy can be transferred between molecules a and b.³⁰

Optical and energy transport properties of a molecular crystal or aggregate depend primarily on the magnitude of the exciton coupling V .^{56–58}

The exciton coupling V (that is the out of diagonal term of eqn (1)) can be expressed as:³²

$$V \approx V^{\text{Coul}} + V^{\text{exch}} \approx V^{\text{Coul}} + V^{\text{short}} \quad (2)$$

V^{Coul} takes into account the Coulomb interaction terms ($aa'|bb'$ integrals) and is long range, while V^{exch} (approximated as V^{short})³³ contains the exchange interactions term (e.g. Dexter like contribution ($a'b'|ba$) integrals).

V has been expressed *via* different approximations:²⁹

(i) point dipole approximation (PDA), that is dipole–dipole interactions between the two molecules:

$$V = \frac{1}{n^2} \left(\frac{\boldsymbol{\mu}_a \cdot \boldsymbol{\mu}_b}{R^3} - 3 \frac{(\boldsymbol{\mu}_a \cdot \mathbf{R})(\boldsymbol{\mu}_b \cdot \mathbf{R})}{R^5} \right) \quad (3)$$

where $\mu_{a/b}$ are the transition dipole moment vectors of the a/b molecules, n is the refractive index of the medium and R is the center of mass distance vector.

(ii) supramolecular method which consists in: (a) calculating excitation energies of molecular dimers, (b) identifying the dimer's states φ_+ and φ_- associated to each excited state of the isolated molecules and (c) evaluating the exciton coupling V as:

$$V = \frac{|\omega_+ - \omega_-|}{2} \quad (4)$$

for symmetric systems ($\omega_a = \omega_b$)

$$V = \frac{1}{2} \sqrt{(\omega_+ - \omega_-)^2 - (\omega_a - \omega_b)^2} \quad (5)$$

for asymmetric systems ($\omega_a \neq \omega_b$), where $\omega_{+/-}$ are the energies of the dimer excited states, $\varphi_{+/-}$ and $\omega_{a/b}$ are the on-site excitation energies of the single molecule (a/b).

V^{exch} is proportional to the square of the inter-molecular orbital overlap integral^{32,33} and it turns out to be important at short inter-molecular distances.

In a supramolecular approach we do not discriminate between these two terms (V^{Coul} vs. V^{exch}) but we globally evaluate the total exciton coupling V .²⁹ However, it will be important to consider eqn (2) when comparing singlet and triplet resonance integrals, in which the exchange contribution plays a different role^{53,54,56–59} (see later).

In this paper we calculate exciton couplings V for **1–4**, by considering nearest neighbor molecular pairs. The dimers have been studied in vacuum (gas phase). However, we have evaluated V , for the most interacting molecular dimers of each class of compounds **1–4** (see Table 3 and Fig. 3), also within the integral equation formalism (IEF) version of the polarizable continuum model (PCM)^{60,61} in order to check if there is a significant effect due to the crystalline field.

Both isotropic and anisotropic dielectric tensor constants⁶² have been considered, with dielectric constants $\epsilon_x = 4.0$ and $\epsilon_y = 2.5$ (anisotropic case),⁶² and $\epsilon = 3.0$ for the isotropic one,⁶³ as reported in the ESI.† For compounds **1–3** the calculated exciton couplings in PCM (both anisotropic and isotropic cases), evaluated for centro-symmetric dimers (those with maximum V , see Table 3), are not greatly affected by the environment (see data in Table S1, ESI†). Only in the case of compound **4** (BPEA) for the PCM isotropic dielectric tensor, we observe a large decrease of V (see data in Table S1, ESI†).⁶⁴ However, it must be noted that in this case the choice of the appropriate dielectric constants is particularly delicate since the “conjugation” state of the molecule is different from that of the other three cases and no experimental data are available. In all cases, we have verified (see Table S1, ESI†) that the physico-chemical description of the excited states remains the same both in vacuum and in the PCM formalism.

For the above reasons we prefer to focus our discussion only on the results obtained in vacuum.

Singlet and triplet excited state calculations on isolated molecules and molecular dimers have been performed with both semiempirical ZINDO and *ab initio* TDDFT methods. From eqn (4) and (5) it is evident that the correct evaluation of the exciton couplings relies on a correct assignment of the φ_+ and φ_- dimer states. To set the proper correspondence between the excited states of the isolated a and b molecules and those of the molecular dimers, we have proposed a direct method for the classification of excited states in organic crystals (or aggregates), based on the transition density matrix (TDM) analysis (TDM projection method).⁵⁰ Details are reported in ref. 50; here we only recall the definition of the TDM between the ground g and a generic excited state j :⁶⁵

$$\rho^j = \langle g | c_n^\dagger c_m | j \rangle \quad (6)$$

where c_n^\dagger and c_m are, respectively, the creation and the annihilation operators for the n th and m th atomic orbitals (usually assumed to be orthonormal) and g and j are, respectively, the wavefunctions of the ground and the j th excited state. ρ^j describes the $g \rightarrow j$ excitation process in terms of changes in the electronic density.⁶⁵ The TDM projection method for singlet excited states has been used only in the frame of ZINDO/S calculations.

Transition density matrixes have been evaluated also at the TDDFT level, but the TDM projection method has not yet been extended to this case. In this latter case the correspondence between the excited states of the isolated molecules and those of the dimers has been established on the basis of a detailed analysis of the excitation energies, molecular orbitals and coefficients involved in the transitions and the criterion choice is that of the closest similarity.

The choice of DFT exchange-correlation functional is fundamental in order to obtain a reliable description of the excited state properties. For this reason we have carried out a preliminary screening; BPEA has been taken as a test case since no DFT calculations have been performed up to date. We considered PBEPBE, B3LYP, PBE0, BHandH functionals.^{66–69} Double (Pople, 6-31G**) and triple zeta (correlation consistent cc-pVTZ) basis sets have been used in

order to determine the effect of the basis set extension. BPEA geometry optimization (ground state singlet S_0) and excited state energies (singlets S_n and triplets T_n) have been evaluated for each combination of functional and basis set. Results are reported in Table S2 (ESI[†]). B3LYP provides the best compromise for an accurate description (according to experimental data) of both S_1 and T_1 states. To correctly evaluate the effect of intruder states⁵¹ and long range interactions, especially in the description of molecular aggregates (dimers),⁷⁰ we considered also the long range corrected (Coulomb Attenuated Method) CAM-B3LYP functional,⁷¹ both for isolated molecules and all the dimers of **1–4**. All calculations have been performed with the Gaussian09 code.⁷²

Results and discussion

Study of singlets and triplets of isolated molecules

As already mentioned in the Introduction, exciton couplings (V) are affected by both intra- and inter-molecular properties. For this reason, before evaluating and discussing V , we have carried out a thorough characterization of the excited state (singlet S_1 and triplet T_1) properties of the isolated molecules **1–4**.

Singlets. Molecular structures of **1–4** have been optimized both at B3LYP and CAM-B3LYP levels with 6-31G** basis set. Excited states have been calculated at ZINDO/S and TDDFT levels on optimized DFT geometries. Excited state calculations have been performed also on X-ray experimental geometries.

In Table 1 we report the calculated excitation energies, oscillator strength (f) and transition dipole moment ($\mu^{0 \rightarrow 1}$) for the $S_0 \rightarrow S_1$ singlet transitions on both DFT optimized and X-ray geometries.

Anthracene, tetracene and BPEA optimized molecular structures belong to the D_{2h} point group; their S_1 excited state is of B_{2u} symmetry and it is polarized along the y molecular axis (transverse axis with respect to the anthracene core, see Fig. 1). DFT optimized DPA belongs to the C_2 point group;

S_1 is of A symmetry, polarized along the y axis. For all molecules the S_1 state has a prevalent HOMO–LUMO character (see Fig. 2).

Even if the limits of the TDDFT method in predicting the excitation energies of charge transfer states in π electron conjugated systems are well known,^{71,73} our results are in good agreement with the experimental data reported in Table 1; TD CAM-B3LYP calculations are known to overestimate excited state vertical energies.

From Table 1 we can observe that both ZINDO/S and TDDFT S_1 calculated vertical energies of DPA and BPEA shift downwards with respect to that of anthracene. In the case of DPA the down shift is of the order of 1000–1500 cm^{-1} (both TDDFT and ZINDO/S) while for BPEA, ZINDO/S predicts a red shift of 4600 cm^{-1} and TDDFT of 6000 cm^{-1} . The lowest lying S_1 state is predicted by TDDFT calculations for BPEA while, in ZINDO/S calculations, the lowest lying S_1 state is found for tetracene, as is experimentally observed.

The addition to the anthracene core of phenyl (DPA) or phenyl-ethynyl groups (BPEA) in 9,10-positions brings in a global increment of the transverse (y axis) π -electron conjugation, which reduces the $S_0 \rightarrow S_1$ optical gap.

In DPA the S_1 down-shift is small because the DFT (both B3LYP and CAM-B3LYP) optimized structure is non-planar, with phenyl rings almost normal to the acene plane (dihedral angle $\approx 89^\circ$), hence only a small increase of the π -electron conjugation is expected. This is confirmed also by the analysis of the calculated ZINDO/S transition density matrix (TDM) and by the molecular orbitals (see Fig. 2) involved in the $S_0 \rightarrow S_1$ transition. The charge density variation occurring during the $S_0 \rightarrow S_1$ excitation is indeed very localized upon the carbon atoms of the acene core (see bottom panel of Fig. 2), without involving the lateral phenyl groups.

In contrast, in BPEA the triple bonds between the anthracene core and the phenyl rings extend the π conjugation transverse to the acene long axis inducing the planarization of the phenyl rings and the S_1 state is further down shifted. The analysis of the TDM and of the molecular orbitals

Table 1 Vertical excitation energy (E), oscillator strength (f), transition dipole moment ($\mu^{0 \rightarrow 1}$) of the $S_0 \rightarrow S_1$ transition evaluated at ZINDO/S, TD-B3LYP and TD-CAM-B3LYP/6-31G** levels. S_1 properties evaluated on both DFT optimized geometries (B3LYP and CAM-B3LYP) and on X-ray crystalline structures are reported

	ZINDO/S			TD-B3LYP			TD-CAM-B3LYP			$E_{\text{expt}}/\text{cm}^{-1}$
	$E(S_0 \rightarrow S_1)/\text{cm}^{-1}$	f	$\mu^{0 \rightarrow 1}/\text{D}$	$E(S_0 \rightarrow S_1)/\text{cm}^{-1}$	f	$\mu^{0 \rightarrow 1}/\text{D}$	$E(S_0 \rightarrow S_1)/\text{cm}^{-1}$	f	$\mu^{0 \rightarrow 1}/\text{D}$	
	B3LYP/6-31G** opt geom.									
Anthracene	26 878	0.22	1.65	26 406	0.06	0.86	29 807	0.09	0.98	26 730 ^a
Tetracene	20 446	0.25	1.93	20 102	0.05	0.91	23 654	0.08	1.14	21 130 ^a 19 357 ^b 18 712 ^b
DPA	25 350	0.38	2.21	25 548	0.15	1.37	28 811	0.2	1.56	24 950 ^c
BPEA	22 247	1.02	4.05	19 871	0.84	3.73	23 159	0.9	3.58	22 180 ^c
	X-ray geom.									
Anthracene	26 673	0.23	1.70	26 203	0.06	0.87	29 056	0.09	1.01	
Tetracene	$\omega_a = 22 111$ $\omega_b = 21 111$	0.37	2.36	$\omega_a = 20 008$ $\omega_b = 19 316$	0.09	1.21	$\omega_a = 22 936$ $\omega_b = 21 808$	0.14	1.42	
DPA	28 544	0.27	1.77	29 088	0.15	1.31	32 017	0.19	1.40	
BPEA	21 093	0.96	3.87	20 568	0.79	3.55	22 971	0.88	3.54	

^a Experimental values (E_{expt}) of λ_{max} in *n*-heptane.⁷⁴ ^b Experimental values (E_{expt}) of λ_{max} in solid state from ref. 15. ^c Experimental values (E_{expt}) of λ_{max} in dimethylformamide (DMF).^{41,75}

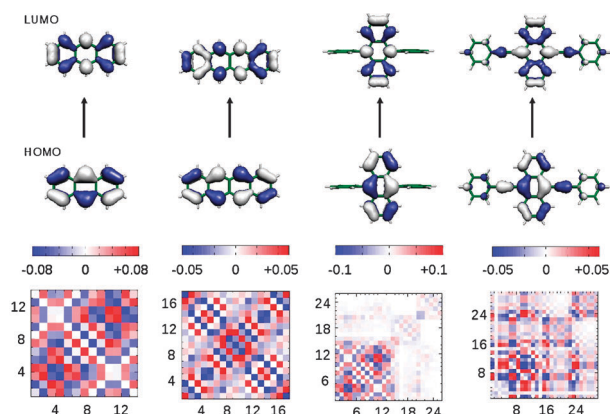


Fig. 2 (Top) Molecular orbitals (HOMO–LUMO) mostly involved in the $S_0 \rightarrow S_1$ transition for anthracene, tetracene, DPA and BPEA. (Bottom) ZINDO/S TDM associated to the $S_0 \rightarrow S_1$ excitation. Numbers label the carbon atoms (as reported on the top panel). For numbering see also Fig. S1 (ESI†). For DPA, numbers 15–20 and 21–26 refer to the carbon atoms of the phenyl groups. For BPEA, 15–16 and 23–24 refer to the triple bonds, while 17–22 and 25–30 to the phenyl groups.

involved in $S_0 \rightarrow S_1$ (see Fig. 2) shows that the excitation is delocalized across the whole molecular structure with large contributions to ρ^j also from the lateral groups (triple bonds and phenyl rings) (see the ZINDO/S TDM map, Fig. 2 bottom).⁷⁶

It is interesting to note that the increase of π conjugation along the short anthracene axis (BPEA) produces the same effect (red shift of the first dipole allowed transition) of an increase of conjugation along the acene backbone, as indeed observed for tetracene.

In tetracene the S_1 excited state is calculated to be 6300 cm^{-1} lower than that of anthracene.

It is interesting to observe that notwithstanding the large red shift of S_1 obtained in going from anthracene to tetracene, the molecular transition dipole moment ($\mu^{0 \rightarrow 1}$) related to the $S_0 \rightarrow S_1$ excitation is only slightly increased (both for ZINDO/S and TDDFT, see Table 1). In contrast, in the case of BPEA (**4**) $\mu^{0 \rightarrow 1}$ is more than twice the value of anthracene (**1**) or tetracene (**2**) ($\mu_4^{0 \rightarrow 1} = 4.05 \text{ D}$ vs. $\mu_2^{0 \rightarrow 1} = 1.93 \text{ D}$ at

ZINDO/S and $\mu_4^{0 \rightarrow 1} = 3.73 \text{ D}$ vs. $\mu_2^{0 \rightarrow 1} = 0.91 \text{ D}$ at TD-B3LYP levels). The reason why this happens is related to the presence of the lateral phenyl-ethynyl groups which open a *transversal conjugation channel* in the direction of the transition dipole moment (y axis). (Note that this observation will be important also for the rationalization of the calculated singlet exciton couplings, see next section.)

In Table 1 we also report the properties of the $S_0 \rightarrow S_1$ transition evaluated on experimental geometries both at ZINDO/S and TDDFT levels. For anthracene and BPEA only small differences in the S_1 vertical excitation energy and transition dipole moment are observed between DFT optimized and X-ray experimental geometries. In the crystal, compounds **1** and **4** retain an almost planar structure, and small variations between calculated and experimental geometries have been found.

Crystalline tetracene has two roto-translationally inequivalent molecules per cell,^{46,47} thus producing two different on-site singlet excitation energies (ω_a and ω_b , see eqn (4) and (5)). The differences in the on-site energies of tetracene calculated on optimized DFT or experimental X-ray structures have been evaluated to be about 1000 cm^{-1} , 700 cm^{-1} and 1100 cm^{-1} at ZINDO/S, TD-B3LYP and TD-CAM-B3LYP levels respectively. Also in this case differences are not too large.

In contrast, in the case of DPA, the difference between the S_1 excited state energy, evaluated on the optimized or experimental structures, is large ($\sim 3000 \text{ cm}^{-1}$ for ZINDO/S, $\sim 3500 \text{ cm}^{-1}$ for TD-B3LYP and $\sim 3200 \text{ cm}^{-1}$ for TD-CAM-B3LYP). This overestimate can be ascribed to rather different theoretical and experimental values for bond lengths and angles.⁴⁸ However, we expect that this discrepancy should not affect the inter-molecular organization, preserving the analysis carried out on the exciton coupling terms V that are mainly dependent on inter-molecular distances and orientation.

Triplets. Triplet excited states have been evaluated with the same procedure adopted for singlets. Calculated T_1 energies are reported in Table 2.

In this case we observe that TD-UB3LYP provides the best agreement with experimental values. Both TD-UCAM-B3LYP and ZINDO/S underestimate T_1 energy, the latter predicting energies about half the experimental values.

Table 2 Energy of triplet state T_1 , evaluated at ZINDO/S, TD-UB3LYP/6-31G** and TD-UCAM-B3LYP/6-31G** levels. T_1 excitation energies are reported for both optimized (B3LYP/6-31G** and CAM-B3LYP/6-31G**) and experimental geometries

	ZINDO/S/ cm^{-1}	TD-UB3LYP/ cm^{-1}	TD-UCAM-B3LYP/ cm^{-1}	$E_{\text{expt.}}/\text{cm}^{-1}$
	S_0 optimized structures (B3LYP/6-31G**)		S_0 optimized structures (CAM-B3LYP/6-31G**)	
Anthracene	8899	14 546	13 372	14 850 ^a
Tetracene	5576	9088	6951	10 250 ^b
				10 082 ^c
DPA	8035	14 023	12 841	14 275 ^d
BPEA	6401	10 057	8922	12 340 ^d
	As extracted from X-ray data			
Anthracene	8669	14 335	12 269	
Tetracene	$\omega_a = 5525$ $\omega_b = 4349$	$\omega_a = 8914$ $\omega_b = 7708$	$\omega_a = 5454$ $\omega_b = 1611$	
DPA	11 850	18 754	17 483	
BPEA	6867	10 704	8378	

^a Experimental values in *n*-heptane.⁷⁷ ^b Experimental values in DMF,⁴¹ ^c Experimental values in solid state from ref. 15. ^d Experimental values in DMF.⁷⁸

Compounds **2–4** exhibit red-shifts (with respect to anthracene) of T_1 similar to those observed for S_1 . DPA and BPEA are red shifted, respectively, by about 500 cm^{-1} (in ZINDO/S) and 4500 cm^{-1} (in TDUDFT). Among the molecules considered, the lowest lying T_1 level is that of tetracene, in agreement with the experimental findings.

As already observed in the case of singlets, the largest discrepancy ($\sim 4000\text{ cm}^{-1}$) between the T_1 energy evaluated on the experimental structure and that on UDFT optimized geometry has been found for DPA.

Our interest in the evaluation of T_1 energy, both at the single molecule and the crystal level (exciton splitting), is justified by the fact that its position determines the mechanism for its population, which is the first step in multiexciton processes (e.g. SF or TTA). In particular, two population mechanisms are possible: (i) direct population, using a laser in resonance with T_1 or (ii) excitation to higher singlet states able to give rise to singlet fission.

The theoretical screening carried out in this work can help in the choice of acene derivatives different from those already studied in the literature such as anthracene or tetracene, suitable for multiexciton processes in the solid state.

By recalling the energetic requirement for an efficient SF ($E(S_1) > 2E(T_1)$) or TTA ($E(S_1) < 2E(T_1)$), one can note from the data reported in Tables 1 and 2 that tetracene can exhibit both up- and down-conversion mechanisms, as experimentally revealed.¹⁵

Our calculations show that BPEA can, in principle, satisfy the TTA requirement, being $E(S_1) = 19870\text{ cm}^{-1} < 2E(T_1) = 20100\text{ cm}^{-1}$. Provided that (i) an efficient T_1 population (e.g. by resonant laser energy) is obtained and (ii) large triplet–triplet exciton couplings are present, it is likely that TTA phenomena can take place in BPEA molecular crystals.

Analysis of singlet and triplet exciton couplings

Once the properties of the first singlet (S_1) and triplet (T_1) excited states of compounds **1–4** have been analyzed, we can study how they are modified (crystal splitting) in the molecular aggregates.

This study has been carried out by analyzing the crystalline structure of **1–4**^{44–49} and by determining, for each crystal, all possible nearest neighbor pairs of molecules in order to map the inter-molecular interactions taking place inside the crystals.

There are four non-equivalent dimers (A, B, C, D) in crystalline anthracene; eight dimers (A, A1, B, B1, C, C1, D, D1) in tetracene⁷⁹ and, in both DPA and BPEA crystals, 5 dimers (A, B, C, D, E/F). Their structures are reported in Fig. S6–S9 (ESI†).

Each dimer has been analyzed in the framework of molecular exciton theory³⁰ as discussed in Methods section; we have evaluated exciton couplings V for both singlet and triplet states, according to the supramolecular approach (see eqn (4) and (5)). The exciton coupling has been evaluated also according to the PDA approximation (see eqn (3)), using the transition dipole moments calculated at the TDDFT level (see Table S3, ESI†). Even though it is well known that the PDA approximation in the intermolecular distance regime we are dealing with is not accurate,²⁹ we refer to PDA because it is

useful to qualitatively rationalize the trends we obtain in terms of transition dipole moments and molecular orientation.

Within the ZINDO/S approach we have obtained, for all the 22 dimers considered, the TDM ρ^i for both the dimer (ab) and the constituting molecules (a and b) in order to establish the correct correspondence between their excited states. Once the dimer excited states (φ_+ and φ_-) have been correlated to those of the single molecules (see Table S4–S7 (ESI†) for exciton coefficients and assignment), we obtained the exciton couplings V by using eqn (4) and (5).

Regarding TDDFT calculations, to set the proper correspondence between dimer and single molecule excited states, energies, molecular orbital coefficients involved in the excited state determinant and oscillator strengths have been used as guidelines⁸⁰ (see Table S7–S10, ESI†). The same kind of approaches has been used in the case of triplet states.

Singlet and triplet couplings V are collected in Table 3 together with the mass center distance (R) between the two molecules constituting the dimer.

The calculated singlet exciton couplings are in good agreement with the values reported in the literature for similar molecular aggregates;⁵¹ in particular ZINDO/S calculations on anthracene crystals agree very well with those reported by Philpott and Spano.^{81,82}

Considering the couplings evaluated at the ZINDO/S level we can observe that in anthracene, tetracene and DPA molecular crystals there is only one dimer with a large singlet exciton coupling (i.e. dimer B (230 cm^{-1}) for anthracene, B1 (137 cm^{-1}) for tetracene and D (107 cm^{-1}) for DPA); in contrast, in BPEA all dimers show large singlet couplings (A: 353 cm^{-1} , B: 135 cm^{-1} , C: 188 cm^{-1} , D: 244 cm^{-1} , F: 200 cm^{-1}) with absolute values higher than those evaluated for anthracene or tetracene crystals. This behavior can be qualitatively explained, as mentioned in the single molecule analysis (see previous section), with the presence in BPEA of a large transition dipole moment ($\mu^{0\rightarrow 1} = 4.05\text{ D}$, ZINDO/S) transverse (y axis) to the acene long axis (x axis). Since $\mu^{0\rightarrow 1}$ is twice that of anthracene/tetracene ($\mu^{0\rightarrow 1} = 1.65\text{ D}/1.93\text{ D}$, see Table 1), in the frame of the PDA approximation (see eqn (3)), we should expect an exciton coupling four times that of anthracene/tetracene (considering the same dimer geometry). Since the actual dimer local geometry (distances and relative orientations) is different from that of the isolated molecule, BPEA exciton couplings are less than four times those of anthracene or tetracene.

TDDFT exciton couplings evaluated with the PDA according to eqn (3) (see Table S3, ESI†) nicely correlate with those obtained in the supramolecular approach, even if absolute values are strongly overestimated because of the small intermolecular distances. For further details and the numerical values for the case of PDA, we refer to the ESI† data.

Another peculiar feature of the BPEA crystal is that, due to the presence of lateral phenyl-ethynyl groups, even if the distance between mass centers is significant (e.g. dimers B or C with $R = 18.9\text{ \AA}$), the singlet exciton coupling can be substantial. This effect can be qualitatively rationalized again by using the transition dipole moment approximation relationship (see ESI†) for V (e.g. $V \approx \mu_a \cdot \mu_b / R^3$): in BPEA μ_a and μ_b are transverse to the core, pointing in the direction of the

Table 3 Singlet and triplet exciton couplings V (cm^{-1}) evaluated with the supramolecular approach at the ZINDO/S and TDDFT (B3LYP and CAM-B3LYP/6-31G**) levels; mass centre distances R (\AA) between molecules constituting each dimer are reported. The largest (singlet and triplet) exciton couplings are highlighted in bold

$R/\text{\AA}$	Singlet			Triplet			
	ZINDO/S V/cm^{-1}	TD-B3LYP V/cm^{-1}	TD-CAM-B3LYP V/cm^{-1}	ZINDO/S V/cm^{-1}	TD-UB3LYP V/cm^{-1}	TD-UCAM-B3LYP V/cm^{-1}	
Anthracene							
A	5.2	76	121	29	4	23	29
B	6.0	230	157	256	6	20	15
C	9.9	34	12	27	4	25	27
D	11.2	44	15	21	0	0	0
Tetracene							
A	4.8	88	<i>a</i>	<i>a</i>	87	146	425
A1	5.1	46	369	<i>a</i>	<i>a</i>	<i>a</i>	<i>a</i>
B	6.1	49	8	13	5	7	12
B1	6.1	137	107	134	1	0	3
C	12.3	<i>a</i>	247	83	31	109	125
C1	13.4	<i>a</i>	<i>a</i>	<i>a</i>	38	<i>a</i>	<i>a</i>
D	13.6	20	113	25	0	0	1
D1	13.6	11	80	2	0	0	0
DPA							
A	10.7	35	29	23	0	0	0
B	8.6	32	313	50	0	2	2
C	8.6	66	48	61	0	0	0
D	8.1	107	80	96	0	0	0
E	8.1	54	265	25	1	0	0
BPEA							
A	5.6	353	754	221	120	171	183
B	18.9	135	165	160	0	0.0	0
C	18.9	188	291	231	0	2	1
D	10.0	244	255	262	0	7	7
F	8.5	200	212	215	0	0	1

^a In the case of tetracene, some of the calculations on a few dimers yield an imaginary value for V . This is due to the fact that $\Delta\omega_{+/-}$ and $\Delta\omega_{a/b}$ (evaluated on experimental geometries) (see eqn (5)) are very similar so that their difference is practically zero (either $0+$ or $0-$).

external phenyl groups and, even if R is relevant, the scalar product ($\mu_a \cdot \mu_b$) is so large (dipoles being perfectly aligned in the same direction (see Fig. 3)), that a noticeable exciton coupling (A dimer: $V = 353 \text{ cm}^{-1}$) is obtained.

The most interacting (ZINDO/S) dimers of compounds 1–4 are sketched in Fig. 3. For both anthracene (1) and tetracene (2) these dimers lie onto the highest packing plane ($\{0,0,1\}$ see Fig. S10–S11, ESI†) with molecules shifted along the b crystal axis. In this configuration, the transition dipole moments of both molecules (a and b) of each dimer point in the same direction, giving rise, as a proof of concept, to a large scalar product ($\mu_a \cdot \mu_b$) hence a high exciton coupling ($V_1 = 230 \text{ cm}^{-1}$ and $V_2 = 137 \text{ cm}^{-1}$).

In crystalline DPA (3), molecules are arranged in a herringbone fashion (see Fig. S4 and S8, ESI†). Phenyls, as previously observed (see Fig. 2), are not involved in the electronic transitions and act as spacers keeping the molecules far apart and screening exciton interactions. Dimer D is the only one where a direct interaction between molecules can take place resulting in a moderate value of V (D dimer: $V_3 = 107 \text{ cm}^{-1}$).

Finally, in dimer A of BPEA (4), the two molecules are nearly superimposed, thus resulting in a very strong exciton interaction, of 353 cm^{-1} (large Coulomb and exchange contribution, see eqn (2)). In Fig. 3 for BPEA we also report dimer B which, notwithstanding a large R (18.9 \AA), presents a relevant exciton coupling (135 cm^{-1}).

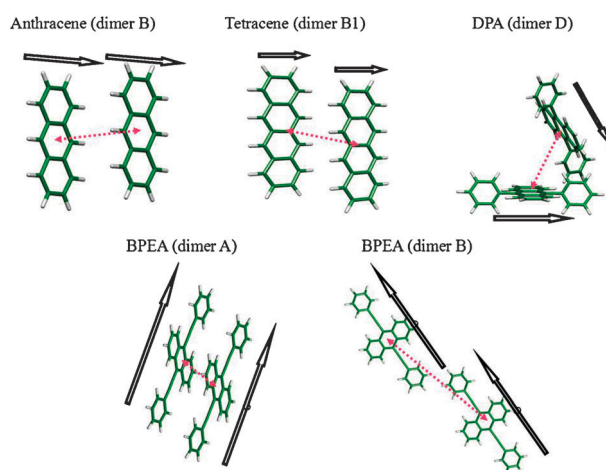


Fig. 3 Molecular dimers with the largest (ZINDO/S) singlet exciton coupling. Black arrows indicate the direction of the transition dipole moment μ_a and μ_b . Red arrows indicate the center of mass distance between pair of molecules.

In conclusion, laterally substituted anthracene derivatives exhibiting a large *transverse* π -electron conjugation with a close packed crystalline structure are good candidates for having organic systems with large exciton couplings and, probably, good coherent energy transport (if spectral overlap is good enough).^{26,36}

The same analysis has been carried out at the TD-B3LYP/6-31G** level. As it can be seen from Table 3, TDDFT couplings are of the same order of magnitude of the ZINDO/S ones (see the case of anthracene). In some cases (e.g. DPA and especially BPEA) TDDFT couplings are larger than ZINDO/S's. This overestimate has been justified in recent works by Mennucci and Curutchet.⁵¹ Usually the overestimate of TDDFT couplings is due to an unbalanced description of the excited states involved in the molecular aggregate. In some instances, the lowest state is too low and, generally, at the TD-B3LYP level there are fictitious low-lying excited states^{51,80} that make the evaluation of the couplings very difficult or incorrect. For many dimers, especially those of tetracene, we find intruder states lower in energy than the first real split dimer state. Moreover, it is also known that in molecular complexes with excitation-energy transfer the TD-B3LYP intruder low-lying state has a marked charge-transfer (CT) character. The error in the evaluation of the excitation energies of these TD-B3LYP CT excited states usually leads to an underestimated optical energy gap.⁸³ To gain a better understanding and to correctly predict the character of the low lying dimer excited states we have performed calculations also with the long range corrected Coulomb Attenuated Method, TD-CAM-B3LYP. With TD-CAM-B3LYP most of the intruder low lying singlet states have been removed (see Fig. S13–S16, ESI†) and the calculated singlet exciton couplings are now in a much better agreement with those predicted by ZINDO/S.

In any case, it is interesting to note that for BPEA also TDDFT calculations (both B3LYP and CAM-B3LYP) yield large/moderate singlet exciton couplings for all the dimers. This means that for BPEA, contrary to the other compounds (1–3), exciton interactions are non-directional at all levels of calculation.

From the above discussion on singlet exciton couplings, we can derive some useful (both intra- and inter-molecular) structure–property relationships:

(1) in the case of anthracene and tetracene, there are only few large exciton couplings which are indicative of anisotropic exciton interactions in the crystal resulting, probably, in exciton propagation along well defined directions (identified by dimers B and B1 for anthracene and tetracene, respectively). Furthermore, for both crystals, we calculate strong singlet exciton interactions in the {0,0,1} crystal plane and small interactions between planes (see Fig. S10–S11, ESI†);⁸¹

(2) in the case of DPA small singlet exciton couplings have been predicted at both ZINDO/S and TD-CAMB3LYP levels, because phenyl rings prevent an efficient crystal packing (DPA is indeed the only molecule with a non-planar geometry);

(3) BPEA is the only molecule that presents large singlet exciton couplings for all the dimers considered, thus showing isotropic inter-molecular singlet exciton interactions.

From the above three points we can conclude that the introduction of the π -conjugated chemical groups (phenyl-ethynyl) along the direction of the transition dipole moment of the anthracene core (9,10 positions, y axis) enables a good crystal packing, where molecules can arrange themselves in an efficient π - π stacking structure, thus resulting in large inter-planar interactions (in spite of rather large inter-molecular distances).

As in the case of singlets, we have calculated also triplet exciton couplings at both ZINDO/S and TDDFT levels (see values reported in Table 3), for all the 22 dimers considered.

For the calculation of triplet exciton couplings we have used the supramolecular approach verifying, in every case, that the low lying triplet state of the dimer is well separated in energy from the other states (see Fig. S15–S16, ESI†) so that it is possible to rule out excited state mixing.

From the values reported in Table 3 we can observe that triplet exciton couplings are always smaller (in some cases also by one or two orders of magnitudes) than the singlet counterpart; this effect can be explained recalling eqn (2) reported in Methods section.

The exciton coupling V is calculated as a sum between a Coulomb and an exchange term; the latter depends on the square of the inter-molecular overlap integral that is large at short distances and adds a negative contribution to V (see eqn (15)–(17) in ref. 55). Jortner *et al.*⁵⁹ have evaluated triplet exciton couplings in molecular crystals of naphthalene, anthracene and biphenyl, finding values around 5–10 cm^{-1} , in very good agreement with our results on anthracene (4–6 cm^{-1} at ZINDO/S and $\sim 20 \text{ cm}^{-1}$ at TDDFT levels).

Contrary to singlet exciton couplings we find that triplet interactions are more selective. In BPEA, for instance, only the dimer with the largest singlet exciton coupling (A) presents also a large triplet coupling ($V^{\text{singlet}} = 353 \text{ cm}^{-1}$ vs. $V^{\text{triplet}} = 120 \text{ cm}^{-1}$ (ZINDO/S) or $V^{\text{singlet}} = 221 \text{ cm}^{-1}$ vs. $V^{\text{triplet}} = 183 \text{ cm}^{-1}$ (TD-CAMB3LYP), see Table 3). All the other dimers have vanishing or small triplet exciton couplings (few cm^{-1}). The rationale behind this behavior is the following: in the case of dimer A both molecules are superimposed with a small inter-molecular distance ($R = 5.6 \text{ \AA}$), thus favoring a good inter-molecular wavefunction overlap; in all the other BPEA dimers instead, molecules are far apart (large R) resulting in a small (or null) wavefunction overlap.

Also triplet couplings in DPA can be rationalized; in this framework all DPA dimers have a small wavefunction overlap (large inter-molecular distance and/or unfavorable relative orientation) so that very small triplet exciton couplings are expected (see values in Table 3). As already seen in the case of singlet exciton couplings, TDDFT slightly overestimates triplet couplings, especially in the case of anthracene dimers.

For the case of tetracene instead, ZINDO/S predicts a relatively large triplet exciton coupling for dimer A ($V = 87 \text{ cm}^{-1}$); TDDFT, in particular TDCAM-B3LYP, overestimates the triplet exciton coupling and this behavior is probably related to the erroneous evaluation of the site energy (ω_a and ω_b). It is to be mentioned that dimer A is the only dimer in which both ZINDO/S and TDDFT methods predict a large triplet exciton coupling.

From the above analysis carried out on both singlet and triplet exciton couplings at ZINDO/S and TDDFT levels, we conclude that:

(1) by increasing the transverse (y axis) π -electron conjugation, *i.e.* from anthracene to BPEA, both singlet and triplet exciton couplings increase;

(2) BPEA, thanks to the high crystalline packing and the large transition dipole moment along the y axis, presents relevant singlet exciton couplings along each crystal direction,

both inside a crystallographic plane and between planes (see Fig. S11, ESI†).

(3) DPA, because of the perpendicular phenyl rings, exhibits a less dense crystalline structure, thus resulting in small singlet and triplet exciton couplings.

(4) triplet exciton couplings, heavily affected by the intermolecular wavefunction overlap, are smaller than singlet exciton couplings and are non-vanishing only for specific dimer geometries (*i.e.* crystallographic direction).

(5) BPEA, which exhibits the largest *transverse* π -electron conjugation and transition dipole moment, shows the most relevant singlet and triplet exciton couplings among the anthracene derivatives considered in this study.

As mentioned in the Introduction both in anthracene and tetracene crystals, multiexciton generation phenomena such as SF and TTA have been observed.¹⁵ These results seem in agreement with our findings, indeed both anthracene and tetracene have large singlet and triplet exciton couplings ($V^{\text{singlet}} \approx$ hundred of cm^{-1} and $V^{\text{triplet}} \approx$ tens of cm^{-1}) thus favoring, in the frame of Förster (singlet) or Dexter (triplet) theories, efficient diffusion and/or interaction mechanisms. The larger the exciton coupling the higher the interaction and hence, with a favorable spectral overlap, the longer the length travelled (*i.e.* diffusion mechanism) by the exciton. As the distances travelled increase, exciton–exciton interactions become more probable and multiexciton processes such as SF and TTA should take place.

To the authors' knowledge, either SF or TTA processes have not yet been measured in BPEA single crystals. In this quantum chemical investigation we suggest BPEA as a good candidate for having efficient multiexciton phenomena in the solid state.

The following criteria can be suggested as guidelines for the choice of the most suitable acene derivatives for SF and/or TTA processes: (i) large *transverse* π -electron conjugation and transition dipole moment (intra-molecular properties); (ii) planar molecular structure and (iii) efficient molecular packing and supramolecular organization (inter-molecular properties).

Conclusions

In this paper we have presented a comprehensive study on exciton properties of molecular crystals of anthracene (**1**), tetracene (**2**) and some acene derivatives (**3–4**, Fig. 1). The effect of extended π -electron conjugated groups, attached to the anthracene core, on electronic and optical properties, has been investigated for both single molecules and molecular aggregates, with semiempirical (ZINDO/S) and *ab initio* (TDDFT) calculations. In particular, focusing on the single molecule properties, we have shown that the first dipole allowed excited state S_1 and the triplet state T_1 down shift in energy by increasing the *transverse* π -electron conjugation (*e.g.* in BPEA). Furthermore, in BPEA the transition dipole moment μ , related to the $S_0 \rightarrow S_1$ transition (along the *transverse*, y axis), is more than twice that of anthracene and tetracene. This property is fundamental in determining singlet exciton inter-molecular interactions (singlet exciton couplings) in molecular crystals with an efficient packing.

In the frame of exciton theory and by using the supra-molecular approach singlet and triplet exciton couplings for

1–4 molecular crystals have been evaluated. The transition density matrix projection method has been used together with ZINDO/S theory to properly assign each dimer excited state on the basis of single molecule states. In the TDDFT study of the excited states of molecular aggregates both B3LYP and CAM-B3LYP functionals have been tested.

Among the molecular crystals studied, BPEA presents the largest singlet and triplet exciton couplings (both at the ZINDO/S and the TDDFT level). In the case of singlets we have found that: BPEA shows for all dimers, representative of different crystallographic directions, large singlet exciton couplings (hundreds of cm^{-1}), while anthracene, tetracene and DPA present only few dimers with large couplings. The behavior can be qualitatively rationalized in the frame of the point dipole approximation (Förster theory).

Triplet exciton couplings are, for compounds (**1–4**), smaller than the corresponding singlet couplings and are more sensitive to the relative molecular orientation and position (intermolecular wavefunction overlap). Also in this case, BPEA has the largest coupling which has been obtained for the dimer with maximum inter-molecular wavefunction overlap. More accurate quantum chemical calculations, such as multi-configurational MCSCF, coupled clusters single/double CCSD or Moller–Plesset methods (MPn), better describe the singlet/triplet wavefunction overlap, giving a more reliable description of the excited state properties and exciton coupling, as reported in some works.^{84–87} In addition, also DFT-D functionals, as those implemented by Grimme *et al.*,^{88,89} can be considered for a better description of the dispersion/correlation contributions affecting the exact calculation of the exciton coupling. However, these methods are too demanding for our purposes or are out of the scope of this work. Our quantum chemical study can be considered as a preliminary investigation for finding guidelines to design molecules to be used for optoelectronic devices, which present, in the solid state, multiexciton generation phenomena (as SF and TTA). In particular we found that, for the class of anthracene derivatives, the increment of the *transverse* π -electron conjugation can have two major effects on the intra-molecular properties: (i) the decrease of both S_1 and T_1 energies and (ii) the increase of the transition dipole moment $\mu^{0 \rightarrow 1}$.

The effect of the *transverse* π -electron conjugation on intermolecular properties is twofold: (i) large singlet exciton couplings in all crystallographic directions (isotropic), and (ii) large triplet exciton couplings.

In conclusion BPEA can be proposed as a good candidate for SF and/or TTA processes since it has low lying singlet and triplet excited states (efficient population) and large exciton couplings (efficient exciton diffusion).

Acknowledgements

This work was supported partly by PRIN Project 2008 JKBBK4 “Tracking ultrafast photoinduced intra- and intermolecular processes in natural and artificial photosensors” and partly by Fondazione CARIPLO 2010 “Nanostrutture organiche ed ibride per la conversione dell'energia solare (SOLCO)”. The authors thank Dr Luigi Brambilla and Dr Matteo Tommasini for the useful discussions.

Notes and references

- 1 J. L. Brédas, J. E. Norton, J. Cornil and V. Coropceanu, *Acc. Chem. Res.*, 2009, **42**, 1691–1699.
- 2 T. M. Clarke and J. R. Durrant, *Chem. Rev.*, 2010, **110**, 6736–6767.
- 3 J. L. Brédas, D. Beljonne, V. Coropceanu and J. Cornil, *Chem. Rev.*, 2004, **104**, 4971–5003.
- 4 V. Coropceanu, J. Cornil, D. A. da Silva Filho, Y. Olivier, R. Silbey and J. L. Brédas, *Chem. Rev.*, 2007, **107**, 926–952.
- 5 S. Gunes, H. Neugebauer and N. S. Sariciftci, *Chem. Rev.*, 2007, **107**, 1324–1338.
- 6 A. C. Mayer, S. R. Scully, B. E. Hardin, M. W. Rowell and M. D. McGehee, *Mater. Today (Oxford, UK)*, 2007, **10**, 28–33.
- 7 B. Kippelen and J. L. Brédas, *Energy Environ. Sci.*, 2009, **2**, 251–261.
- 8 J. Y. Kim, K. Lee, N. E. Coates, D. Moses, T. Q. Nguyen, M. Dante and A. J. Heeger, *Science*, 2007, **317**, 222–225.
- 9 N. Martsinovich, D. R. Jones and A. Troisi, *J. Phys. Chem. C*, 2010, **114**, 22659–22670.
- 10 J. S. Kim, L. Lu, P. Sreearunothai, A. Seeley, K.-H. Yim, A. Petrozza, C. E. Murphy, D. Beljonne, J. Cornil and R. H. Friend, *J. Am. Chem. Soc.*, 2008, **130**, 13120–13131.
- 11 V. Lemaur, M. Steel, D. Beljonne, J. L. Brédas and J. Cornil, *J. Am. Chem. Soc.*, 2005, **127**, 6077–6086.
- 12 I. Paci, J. C. Johnson, X. Chen, G. Rana, D. Popović, D. E. David, A. J. Nozik, M. A. Ratner and J. Michl, *J. Am. Chem. Soc.*, 2006, **128**, 16546–16553.
- 13 M. R. Antognazza, L. Lüer, D. Polli, R. L. Christensen, R. R. Schrock, G. Lanzani and G. Cerullo, *Chem. Phys.*, 2010, **373**, 115–121.
- 14 G. Lanzani, G. Cerullo, M. Zavelani-Rossi, S. De Silvestri, D. Comoretto, G. Musso and G. Dellepiane, *Phys. Rev. Lett.*, 2001, **87**, 187402.
- 15 M. B. Smith and J. Michl, *Chem. Rev.*, 2010, **110**, 6891–6936.
- 16 A. F. Schwerin, J. C. Johnson, M. B. Smith, P. Sreearunothai, D. Popović, J. Černý, Z. Havlas, I. Paci, A. Akdag, M. K. MacLeod, X. Chen, D. E. David, M. A. Ratner, J. R. Miller, A. J. Nozik and J. Michl, *J. Phys. Chem. A*, 2010, **114**, 1457–1473.
- 17 L. D. A. Siebbeles, *Nat. Chem.*, 2010, **2**, 608–609.
- 18 H. Sternlicht, G. Nieman and G. W. Robinson, *J. Chem. Phys.*, 1963, **38**, 1326–1335.
- 19 T. Förster, *Ann. Phys. (Leipzig)*, 1948, **2**, 55–75.
- 20 H. Kallmann and F. Z. London, *Phys. Chem.*, 1929, **2**, 207–243.
- 21 G. D. Scholes, *Annu. Rev. Phys. Chem.*, 2003, **54**, 57–87.
- 22 D. Beljonne, C. Curutchet, G. D. Scholes and R. J. Silbey, *J. Phys. Chem. B*, 2009, **113**, 6583–6599.
- 23 C. Curutchet, B. Mennucci, G. D. Scholes and D. Beljonne, *J. Phys. Chem. B*, 2008, **112**, 3759–3766.
- 24 S. E. Braslavsky, E. Fron, H. B. Rodriguez, E. S. Román, G. D. Scholes, G. Schweitzer, B. Valeur and J. Wirz, *Photochem. Photobiol. Sci.*, 2008, **7**, 1444–1448.
- 25 D. L. Andrews, *Chem. Phys.*, 1989, **135**, 195–201.
- 26 C. P. Hsu, *Acc. Chem. Res.*, 2009, **4**, 509–518.
- 27 E. C. Greyson, B. R. Stepp, X. Chen, A. F. Schwerin, I. Paci, M. B. Smith, A. Akdag, J. C. Johnson, A. J. Nozik, J. Michl and M. A. Ratner, *J. Phys. Chem. B*, 2010, **114**, 14223–14232.
- 28 E. C. Greyson, J. Vura-Weis, J. Michl and M. A. Ratner, *J. Phys. Chem. B*, 2010, **114**, 14168–14177.
- 29 D. Beljonne, J. Cornil, R. Silbey, P. Millié and J. L. Brédas, *J. Chem. Phys.*, 2000, **112**, 4749–4758.
- 30 M. Pope and C. E. Swenberg, *Electronic Processes in Organic Crystals*, Oxford University Press, New York, 1982.
- 31 J. Cornil, D. A. dos Santos, X. Crispin, R. Silbey and J. L. Brédas, *J. Am. Chem. Soc.*, 1998, **120**, 1289.
- 32 G. D. Scholes and K. P. Ghiggino, *J. Phys. Chem.*, 1994, **98**, 4580–4590.
- 33 D. L. Andrews and G. Juzeliunas, *J. Chem. Phys.*, 1991, **95**, 5513.
- 34 R. McWeeny, *Methods of Molecular Quantum Mechanics*, 2nd edn, Academic Press, New York, 1992.
- 35 F. Donati, A. Pucci, C. Cappelli, B. Mennucci and G. Ruggeri, *J. Phys. Chem. B*, 2008, **112**, 3668–3679.
- 36 D. Beljonne, E. Hennebicq, C. Daniel, L. M. Herz, C. Silva, G. D. Scholes, F. J. M. Hoeben, P. Jonkheijm, A. P. H. J. Schenning, S. C. J. Meskers, R. T. Phillips, R. H. Friend and E. W. Meijer, *J. Phys. Chem. B*, 2005, **109**, 10594–10604.
- 37 A. Datta, S. Mohakud and S. K. Pati, *J. Chem. Phys.*, 2007, **126**, 144710.
- 38 A. Datta, S. Mohakud and S. K. Pati, *J. Mater. Chem.*, 2007, **17**, 1933–1938.
- 39 S. Singh, W. J. Jones, W. Siebrand, B. P. Stoicheff and W. G. Schneider, *J. Chem. Phys.*, 1965, **42**, 330.
- 40 C. E. Swenberg and W. T. Stacy, *Chem. Phys. Lett.*, 1968, **2**, 327.
- 41 A. Monguzzi, R. Tubino and F. Meinardi, *J. Phys. Chem. A*, 2009, **113**, 1171.
- 42 A. Monguzzi, J. Mezyk, F. Scotognella, R. Tubino and F. Meinardi, *Phys. Rev. B: Condens. Matter*, 2008, **78**, 195112.
- 43 A. Monguzzi, R. Tubino and F. Meinardi, *Int. J. Photoenergy*, 2008, 684196.
- 44 A. McL. Mathieson, J. M. Robertson and V. C. Sinclair, *Acta Crystallogr.*, 1950, **3**, 245.
- 45 V. C. Sinclair, J. M. Robertson and A. McL. Mathieson, *Acta Crystallogr.*, 1950, **3**, 251.
- 46 R. B. Campbell, J. M. Robertson and J. Trotter, *Acta Crystallogr.*, 1961, **14**, 705.
- 47 R. B. Campbell, J. M. Robertson and J. Trotter, *Acta Crystallogr.*, 1962, **15**, 289.
- 48 J. M. Adams and R. Ramdas, *Acta Crystallogr.*, 1979, **B35**, 679–683.
- 49 M. Maekawa, Y. Suenaga, T. Kuroda-Sowa and M. Munakata, *Sci. Technol.*, 2000, **12**, 27–30.
- 50 C. Quarti, D. Fazzi and M. Tommasini, *Chem. Phys. Lett.*, 2010, **496**, 284.
- 51 C. Curutchet and B. Mennucci, *J. Am. Chem. Soc.*, 2005, **127**, 16733–16744.
- 52 A. S. Davydov, *Theory of Molecular Excitations*, Mc-Graw-Hill, New York, 1962.
- 53 A. Datta and S. K. Pati, *Chem. Soc. Rev.*, 2006, **35**, 1305–1323.
- 54 Z. Shuai, D. Beljonne, R. J. Silbey and J. L. Brédas, *Phys. Rev. Lett.*, 2000, **84**, 131.
- 55 J. Frenkel, *Phys. Rev.*, 1931, **37**, 17.
- 56 Z. Shuai, J. L. Bredas, S. K. Pati and S. Ramasesha, *Phys. Rev. B: Condens. Matter*, 1998, **58**, 15329.
- 57 S. K. Pati, S. Ramasesha, Z. Shuai and J. L. Bredas, *Phys. Rev. B: Condens. Matter*, 1999, **59**, 14827.
- 58 S. Ramasesha, S. K. Pati, H. R. Krishnamurthy, Z. Shuai and J. L. Bredas, *Synth. Met.*, 1997, **85**, 1019.
- 59 J. Jortner, S. A. Rice and J. L. Katz, *J. Chem. Phys.*, 1965, **42**, 309–323.
- 60 J. Tomasi, B. Mennucci and R. Cammi, *Chem. Rev.*, 2005, **105**, 2999.
- 61 *Continuum solvation models in chemical physics, from theory to applications*, ed. B. Mennucci and R. Cammi, Wiley, Chichester, UK, 2007.
- 62 F. Lipparini and B. Mennucci, *J. Chem. Phys.*, 2007, **127**, 144706.
- 63 Z. G. Soos, E. V. Tsiper and A. Painelli, *J. Lumin.*, 2004, **110**, 332.
- 64 It has to be mentioned that no experimental values of ϵ tensor are available in the literature for DPA and BPEA crystals. For this reason we used for all the compounds the ϵ value of anthracene. This might be a source of error in our calculations for DPA and BPEA crystals.
- 65 S. Tretiak and S. Mukamel, *Chem. Rev.*, 2002, **102**, 3171.
- 66 J. P. Perdew, K. Burke and M. Ernzerhof, *Phys. Rev. Lett.*, 1996, **77**, 3865.
- 67 A. D. Becke, *J. Chem. Phys.*, 1993, **98**, 1372–1376.
- 68 C. Adamo and V. Barone, *J. Chem. Phys.*, 1999, **110**, 6158.
- 69 A. D. Becke, *J. Chem. Phys.*, 1993, **98**, 1372.
- 70 J. Neugebauer, C. Curutchet, A. Muñoz-Losa and B. Mennucci, *J. Chem. Theor. Comput.*, 2010, **6**, 1843.
- 71 T. Yanai, D. Tew and N. Handy, *Chem. Phys. Lett.*, 2004, **393**, 51.
- 72 M. J. Frisch, G. W. Trucks, H. B. Schlegel, G. E. Scuseria, M. A. Robb, J. R. Cheeseman, G. Scalmani, V. Barone, B. Mennucci, G. A. Petersson, H. Nakatsuji, M. Caricato, X. Li, H. P. Hratchian, A. F. Izmaylov, J. Bloino, G. Zheng, J. L. Sonnenberg, M. Hada, M. Ehara, K. Toyota, R. Fukuda, J. Hasegawa, M. Ishida, T. Nakajima, Y. Honda, O. Kitao, H. Nakai, T. Vreven, J. A. Montgomery Jr., J. E. Peralta, F. Ogliaro, M. Bearpark, J. J. Heyd, E. Brothers, K. N. Kudin, V. N. Staroverov, R. Kobayashi, J. Normand, K. Raghavachari, A. Rendell, J. C. Burant, S. S. Iyengar, J. Tomasi, M. Cossi, N. Rega, J. M. Millam, M. Klene, J. E. Knox, J. B. Cross, V. Bakken, C. Adamo, J. Jaramillo, R. Gomperts,

- R. E. Stratmann, O. Yazyev, A. J. Austin, R. Cammi, C. Pomelli, J. W. Ochterski, R. L. Martin, K. Morokuma, V. G. Zakrzewski, G. A. Voth, P. Salvador, J. J. Dannenberg, S. Dapprich, A. D. Daniels, Ö. Farkas, J. B. Foresman, J. V. Ortiz, J. Cioslowski and D. J. Fox, *Gaussian 09, Revision A.1*, Gaussian, Inc., Wallingford, CT, 2009.
- 73 A. Dreuw and M. Head-Gordon, *Chem. Rev.*, 2005, **105**, 4009.
- 74 H. B. Kleven and J. R. Platt, *Chem. Phys.*, 1949, **17**, 470.
- 75 R. R. Islangulov, J. Lott, C. Weder and F. N. Castellano, *J. Am. Chem. Soc.*, 2007, **129**, 12652.
- 76 We verified, by means of a conformational study carried out at the B3LYP/6-31G** level, that the BPEA planar conformer is the most stable. Indeed conformers with both phenyl rings normal to the acene plane or with one normal and one parallel to the plane are 2.87 and 1.24 kcal mol⁻¹ higher than the fully planar one.
- 77 S. P. McGlynn, M. R. Padhye and M. Kasha, *J. Chem. Phys.*, 1955, **23**, 593.
- 78 S. Balushev, V. Yakutkin, T. Miteva, G. Wegner, T. Roberts, G. Nelles, A. Yasuda, S. Chernov, S. Aleshchenkov and A. Cheprakov, *New J. Phys.*, 2008, **10**, 013007.
- 79 Notice that in tetracene due to the presence of two non-equivalent molecules in the unit cell, there are two dimers (X and X1) similar to the X dimer of anthracene.
- 80 L. Yang, S. Caprasecca, B. Mennucci and S. Jang, *J. Am. Chem. Soc.*, 2010, **132**, 16911–16921.
- 81 D. W. Schlosser and M. R. Philpott, *J. Chem. Phys.*, 1982, **77**, 1969.
- 82 F. C. Spano, *Acc. Chem. Res.*, 2010, **43**, 429–439.
- 83 B. Mennucci, C. Cappelli, C. A. Guido, R. Cammi and J. Tomasi, *J. Phys. Chem. A*, 2009, **113**, 3009–3020.
- 84 S. Ramasesha, S. K. Pati, H. R. Krishnamurthy, Z. Shuai and J. L. Bredas, *Phys. Rev. B: Condens. Matter*, 1996, **54**, 7598–7601.
- 85 Z. Shuai, S. K. Pati, W. P. Su, J. L. Bredas and S. Ramasesha, *Phys. Rev. B: Condens. Matter*, 1997, **55**, 15368–15371.
- 86 Z. Shuai, J. L. Bredas, S. K. Pati and S. Ramasesha, *Phys. Rev. B: Condens. Matter*, 1997, **56**, 9298–9301.
- 87 Z. Shuai, J. L. Bredas, S. K. Pati and S. Ramasesha, *Phys. Rev. B: Condens. Matter*, 1998, **58**, 15329–15332.
- 88 S. Grimme, *J. Comput. Chem.*, 2006, **27**, 1787–1799.
- 89 S. Grimme and M. Parac, *ChemPhysChem*, 2003, **4**, 292–295.

Chapter 3

Vibrational spectroscopy of polymeric crystals

3.1 Introduction

Polymeric materials find application in several fields and they are practically ubiquitous in our everyday life. Moreover, new possible applications can be forecast thanks to the development of new polymer based nanomaterials [70, 71] or to the development of innovative production techniques, that allow to obtain more and more complex morphologies [72, 73]. Thanks to these advances, the use of polymers in innovative fields, like nanomedicine [3], biomaterials, optics [74], electronics [75] and energy conversion [76] have currently become promising fields of research.

From a more fundamental point of view, the development of new and more performing materials requires an adequate knowledge of *structure-properties* relationships. In this regard, vibrational spectroscopy techniques, namely Infrared (IR) and Raman spectroscopies, have been very important tools for the characterization of polymers and for the study of their physico-chemical properties and they have been widely used in the past [77, 78]. IR and Raman spectroscopy have been fruitfully used to study the conformation of molecular chains in semicrystalline polymers, to determine the structure of conformational defects and to follow their evolution with temperature [79, 80]. They have given also important contributions to the study of the intermolecular forces that held together the polymer chains in the solid phase and that are responsible for the mechanical properties of these materials [81]. Moreover, since the vibrational problem is strictly connected with the electronic structure of the material, Zerbi and co-workers have used Raman spectroscopy to study the connection between structural, vibrational and electronic properties of semiconducting polymers and polyconjugated materials [4, 5].

In spite of the amount of information accessible by means of vibrational

spectroscopy, the interpretation and the assignment of the vibrational spectra of polymeric systems is not an easy task, because of the presence of different contributions in the spectrum of the material, arising from *i*) defects, *ii*) polymorphism, *iii*) interfaces and, obviously, *iv*) contributions from the crystalline and *v*) from the amorphous phase, that is always present for this class of materials. As a consequence, it is not unusual to find ambiguities and debates in the literature on the interpretation of the IR and Raman spectroscopic data and on the assignment of the spectral features. In this sense, the possibility to adopt computational techniques able to predict the structure and the spectroscopic response of polymeric materials has always been considered with interest, in order to ease the analysis and to support the assignments of the experimental data. However, the application of molecular simulations of the spectroscopic response to complex systems as polymeric materials has been quite limited in the past, because of the lacking of computational resources and codes. Molecular dynamics calculations based on classical force fields have been presented in the past [82] but these methods do not allow to predict the vibrational spectra. On the other side, *ab-initio* simulations are effective in predicting the vibrational spectrum but, due to their high computational cost, they have been used in the past only considering very small models as molecular fragments (oligomeric approach) or isolated infinite polymeric chains [83], that are not always suitable for the prediction of the properties of polymer materials in the solid phase. However, thanks to the recent increase of the computational resources and to the development of computational codes, it has been possible to extend the use of quantum chemical tools to large systems and some new investigations on the structural and spectroscopic properties of polymers by means of *ab-initio* methods have been presented in the last years [84, 85, 86, 87, 88, 12]. As an example, the current implementation of the CRYSTAL09 [89] code allows to carry out DFT simulations on periodic systems characterized by a large unit cell (i. e. containing a few hundreds of atoms) and to simulate their IR spectrum. CRYSTAL09 makes use of atomic gaussian basis sets according to the MO-LCAO procedure and it exploits the full symmetry of the system. Moreover, the recent implementation of the interatomic pairwise potential method for the description of the van der Waals forces (see Section 3.2.1) and of the Berry phase approach for the calculation of the IR intensities of periodic systems make the CRYSTAL09 code the ideal tool for the study of the structure and spectroscopic response of semi-crystalline polymers.

In this chapter, we carry out *Density Functional Theory* (DFT) calculations (performed with both CRYSTAL09 [89] and GAUSSIAN09 [90] codes), to study the structure and the IR response of some polymeric systems, for which some debates and ambiguities in the assignment of the vibrational spectra have been raised in the past: the α crystalline form of *nylon 6,6*, the α and γ forms of *nylon 6* and the conformation of polymeric chains of *poly(tetrafluoroethylene)* in the crystalline phase. The recent development

of new polyamide based nanoclays [70] and nanofibres [72, 73] have renewed the interest of scientists on this class of polymers but, for an in-depth characterization of their properties by means of IR spectroscopy, a revision of the vibrational assignments is mandatory, due to the several open questions that are still present in the literature. The simulation and the revision of the IR spectrum of crystalline nylon 6,6 is the issue of the paper in attachment **c**. (D. Galimberti, C. Quarti, A. Milani, L. Brambilla, B. Civalleri and C. Castiglioni; “IR spectroscopy of crystalline polymers from ab-initio calculations: nylon 6,6”, *Vib. Spectroscop.* in press).

Besides, polymorphism represents another source of complication in the case of single-numbered polyamides (nylon n , with n even). In these systems, two main stable crystalline structures can be found: the α form, characterized by a planar conformation of the chains and stable for $n \leq 6$, and the γ form, with a gauche conformation of the bonds close to the amide groups and stable for $n > 6$. Polyamide 6 is a very peculiar case for both fundamental and practical applications, since the two polymorphs are quasi-isoenergetics, with estimated energy differences for the two forms of the order of 1 kcal/mol, such that they can occur simultaneously in the sample. The calculation of the IR spectrum of the α and γ polymorphs of polyamide 6 and their assignment are presented in attachment **d** (C. Quarti, A. Milani, B. Civalleri, R. Orlando and C. Castiglioni; “Ab initio calculation of the crystalline structure and IR spectrum of polymers: nylon 6 polymorphs”; *J. Phys. Chem. B*, 116:8299-8311, 2012).

In attachment **e** (C. Quarti, A. Milani and C. Castiglioni; “Ab initio calculation of the IR spectrum of PTFE: helical symmetry and defects”; *J. Phys. Chem. B*, 117:706-718, 2013) we carry out a revision of the IR spectrum of crystalline PTFE, with the support of DFT calculations. The structural characterization of PTFE by means of IR spectroscopy is quite complex because its IR spectrum is characterized by few, broad bands, typical of systems containing a large concentration of conformational defects. In attachment **e** we adopt models of regular chain (treated as 1-D crystal) as well as models of chain segments carrying conformational defects, in order to address the contributions from the ordered phase and from defects to the IR spectrum. In particular, we focus on the assignment of the doublet falling at 638-626 cm^{-1} , which is the only spectral feature showing an evolution with the temperature and which interpretation has been subject of a long debate in the literature.

In our studies, we consider both oligomeric models, infinite polymer chains and polymer crystals for the study of the structure and spectroscopic response of polymeric materials. To the best of the author’s knowledge, it is the first time that the IR spectroscopic response of polymeric materials is studied with ab-initio techniques, considering the whole 3-dimensional crystal (see attachment **c** and **d**), thus taking into account explicitly also the effects of the intermolecular interactions.

Van der Waals interactions are crucial for the stabilization of polymers in the solid phase but the description of these interactions by means of standard ab-initio techniques is inadequate. The origin of the difficulty in the description of the van der Waals interactions by means of DFT is briefly described in section 3.2.1. A list of the methods that are effective in describing these interactions is presented and the *interatomic pairwise vdW potential* method, used in the present work, is discussed. Advantages and limitations of this approach are highlighted and its main parameters are explained (see section 3.2.1).

In order to properly analyze the effects of the intermolecular interactions on the vibrational spectra of highly crystalline polymers and to distinguish between markers of **crystallinity** and markers of **regularity**¹, we developed an “*ad-hoc*” method, named the *eigenvectors projection* method. This method is conceptually similar to the *density matrix projection* method presented in the previous chapter and it consists in comparing mathematically the normal modes of the crystal with those of the isolated infinite regular polymer chain, in order to establish a correspondence between IR bands of the crystal with those of the isolated chain. This method is a valid alternative to the procedure of visualization of the eigenvectors, which can be cumbersome for the case of crystals containing more than one chain per unit cell and that is always characterized by a large degree of arbitrariness. A detailed description of the eigenvector projection method is reported in Section 3.2.2.

3.2 Methods

3.2.1 Description of the van der Waals interactions

The correct description of Van der Waals (vdW) interactions is among the most important challenges for electronic structure based methods. We now discuss briefly on the origin of these interactions. An expression for the van der Waals interaction between two non overlapping atoms or molecular fragments is represented by the well known Lennard-Jones potential:

$$V_{vdW}(r) = \frac{C_{12}}{r^{12}} - \frac{C_6}{r^6} \quad (3.1)$$

where r is the inter-atomic distance and the C_{12} and C_6 coefficients fix the position and the depth of the potential minimum. The repulsion part of

¹**Regularity** markers are those bands that are not actually markers of a specific packing motif but they can be found on polymer chains with a given regular conformation as well as in all 3-D crystals characterized by the same regular conformation of the chains belonging to the original cell. At the opposite, **crystallinity** markers are peculiar of a specific packing motif; thus they arise from the intermolecular interactions taking place between different chains and they cannot be found in other crystalline structures as well in the isolated chain [91].

the potential in Eq. 3.1 is consequence of the Pauli exclusion principle, while the attraction part arises from quantum fluctuations of the electronic densities of the two fragments: the fluctuating electronic density of the fragment n°1 interacts with the fluctuating electronic density of the fragment n°2 through long range electronic correlation. Such interaction can be described as an induced dipole/induced dipole interaction that results in a stabilizing contribution which decays as r^{-6} [15], as shown in Eq. 3.1. Since correlation is the main ingredient of the van der Waals interactions, their description falls naturally in the field of the correlated wave-function based methods. In this framework, coupled cluster with singles, doubles and perturbative triple excitations (CCSD(T)) and second order Möller-Plesset perturbation theory (MP2) are the typical methods used for the description of the intermolecular interactions [92, 93, 94, 95]. However, these methods are computationally demanding and they are not suitable for large systems. On the other side, DFT is a cheaper method that can, in principle, manage with these interactions but the standard, widely used LDA, GGA and hybrid *exchange-correlations* functionals provide a wrong description of the attractive part of the potential or they do not predict the correct minimum energy (see the left panel of Figure 3.1). This happens because these functionals are based on “local” or “semilocal” approximations, that are clearly unsuitable for describing the long range correlation.

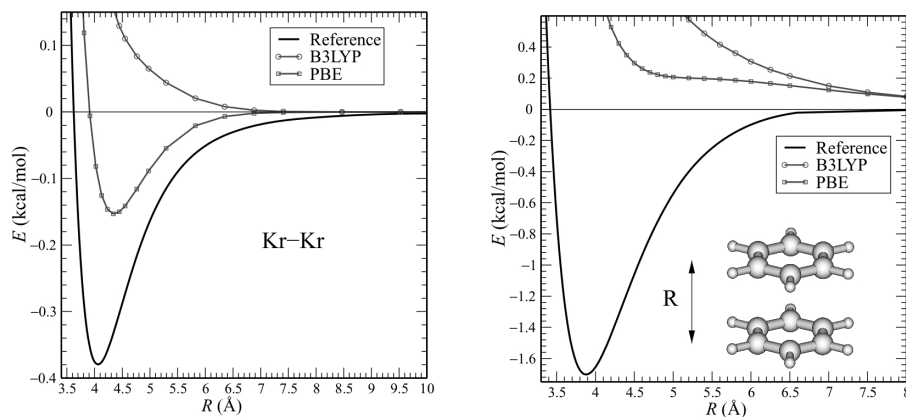


Figure 3.1: Performance of widely used PBE and B3LYP exchange correlation functionals in describing van der Waals intermolecular interactions for the Kr₂ and the benzene dimer. Reference potential energy surface is calculated at CCSD(T) level of theory. Figure taken from REF [96].

A great effort has been therefore devoted to the development of models for the *exchange-correlation* functionals that express the long range dispersion as explicit functional of the electron density [97, 98, 99, 100]. Calculations with these methods revealed computationally efficient and they have

been successfully applied to study the crystalline structure of polyethylene [99].

In this work of thesis we use a more pragmatic approach, often referred in the literature as *interatomic pairwise vdW potential* method. It consists in adding an attraction contribution E_{vdW} of the form C_6/r^6 “*a posteriori*” to the energy obtained from the Self Consistent Field (SCF) calculation E_{SCF} :

$$E = E_{SCF} + E_{vdW} \quad (3.2)$$

with the following form for the van der Waals interactions:

$$E_{vdW} = -s_6 \sum_{i=1}^{n_{at}-1} \sum_{j=i+1}^{n_{at}} \frac{C_6^{ij}}{r_{ij}^6} f_{dmp}(r_{ij}) \quad (3.3)$$

where n_{at} is the number of atoms in the system. Eq. 3.3 thus considers the vdW interactions between all the couples of atoms of the systems. The term s_6 is a scaling factor that depends on the level of the SCF calculation. The damping function f_{dmp} instead has the following meaning: since the repulsive part of the van der Waals interactions, due to the Pauli exclusion principle, is already taken into account correctly in the SCF calculation, the damping function guarantees that the van der Waals correction of Eq. 3.3 goes to zero at interatomic distances that are much shorter than the true equilibrium position and it becomes effective at medium and large distance. Many forms of the damping function have been proposed in the literature [101, 102, 103, 104, 105] but the most used one is given by:

$$f_{dmp}(r_{ij}) = \frac{1}{1 + e^{-\alpha(r_{ij}/r_0 - 1)}} \quad (3.4)$$

where r_0 is the sum of the atomic van der Waals radii. Eq. 3.4 guarantees that the correction in eq. 3.3 decays to zero fast enough to avoid spurious effects in the description of the covalent and ionic interactions.

The present approach tracks back to the seventies [101] and it has the advantage of being computationally cheap and accurate, thus it is the best choice for treating very large systems (i.e. systems with hundreds of atoms). In addition, this approach has been recently implemented in the new version of the CRYSTAL code [106]. Nevertheless, the use of empirical parameters to fit the intermolecular potential makes the present approach more similar to “force field” based methods rather than to an *ab-initio* treatment; the transferability of the empirical parameters indeed is a matter of investigation. About the choice of the C_6^{ij} parameters, two approaches are reported in the literature: Grimme uses constant parameters that fit the results of calculations carried out at higher levels of theory [107, 108, 109], while Tkatchenko determines them from first-principle calculations [110]. Clearly, the second approach is more flexible since it takes into account the

effect of the environment and of the hybridization state of the atoms in the systems under investigation. However, according to Grimme: “changing the C_6 values by $\pm 10\%$ has only a small impact on the results when compared to other theoretical or experimental data, which show, in general, relatively large scattering” [107]. In our work we consider the C_6 parameters with values fixed at 0.14, 1.75, 1.23 and 0.70 J nm⁶ mol⁻¹ respectively for H, C, N and O (taken from ref. [108]). On the opposite, the van der Waals radii, r_0 , affect heavily the results of the calculation. In order to address the effects of this set of parameters on the equilibrium geometry and on the energetics of crystalline polymers, we made use of three different sets of van der Waals radii:

set 1) parameters proposed by Grimme in REF [108]

set 2) parameters proposed by Civalleri in REF [106]

set 3) parameters proposed by Bondi in REF [111] for C, N and O atoms and that proposed by Civalleri in REF [106] for the H atom.

The numerical values for these sets of parameters are reported in Table 3.1.

The remaining parameters are taken from the original work of Civalleri: $s_6=1.00$ for the B3LYP method and $\alpha = 20$. Summation in Eq. 3.3 is carried out for all the couples of atoms within a cutoff distance of 25 Å (default in CRYSTAL09).

Table 3.1: sets of van der Waals radii in Eq. 3.4 for the description of the van der Waals interactions used in attachment **c** and **d**.

reference	H (Å)	C (Å)	N (Å)	O (Å)
grimme 2006 [108]	1.0010	1.6100	1.3970	1.3420
civalleri 2008 [106]	1.3013	1.5246	1.4668	1.4091
our works [111]	1.3013	1.7000	1.5500	1.5200

3.2.2 Eigenvector projection method

The advantage of ab-initio methods for the simulation of the (IR) spectroscopic response resides in the fact that they provide a complete solution of the vibrational problem: vibrational frequencies, IR intensities and atomic displacements from the equilibrium positions for each normal mode are indeed provided. In addition, they allow to investigate systems that are hardly accessible to experiments, like the infinite polymeric chain with regular conformation. All this information can be used properly to address the effect of intermolecular interactions on the IR spectroscopic response of crystalline polymers: by comparing the spectrum of the isolated, infinite regular chain

with that of the crystal, it is possible to address the effect of the intermolecular interactions in terms of band splitting and shifting and in terms of the enhancement and redistribution of IR intensities. In this ground, a methodologic problem is the development of an unambiguous and unarbitrary connection between the spectral features of the isolated chain and those of the crystal. Is there the possibility to establish a rigorous mapping between the normal modes of the isolated chain with those of the crystal?

For this task, we developed a method that is conceptually similar to the *transition density projection* method used for studying exciton in organic crystal (see Section 2.2.3). The present method is named *eigenvector projection method* and it consists in projecting the eigenvector associated to the i -th normal mode of the crystal on the eigenvector associated to the j -th normal mode of the chain. The detailed procedure of the *eigenvector projection method* used in attachments **c** and **d** is the following:

- i) starting from the hessian matrices of the infinite chains, \mathbf{F}^{chain} , and of the 3D crystal, \mathbf{F}^{cry} , we re-diagonalize the vibrational problem expressed in the mass weighed cartesian coordinates:

$$\begin{aligned} (\mathbf{M}^{cry})^{-1/2} \mathbf{F}^{cry} (\mathbf{M}^{cry})^{-1/2} \mathcal{L}^{cry} &= \omega^2 \mathcal{L}^{cry} \\ (\mathbf{M}^{chain})^{-1/2} \mathbf{F}^{chain} (\mathbf{M}^{chain})^{-1/2} \mathcal{L}^{chain} &= \omega^2 \mathcal{L}^{chain} \end{aligned} \quad (3.5)$$

where $\mathbf{M}^{cry/chain}$ are respectively the matrix of the masses for the crystal and for the isolated chain.

- ii) we decompose the generic i -th eigenvector associated to the crystal in the contributions from the first, the second, ... the α -th chain of the crystals, $\mathcal{L}_i^1, \mathcal{L}_i^2 \dots \mathcal{L}_i^\alpha$;
- iii) we ensure that the numbering of the atoms of the isolated chain is the same of the atoms of the chain extracted from the crystal and that the eigenvectors of the two systems are referred to the same reference system. This step often requires to re-arrange the order of the components of the \mathcal{L} vector and/or to suitably rotate the cartesian reference system;
- iv) we project the portion of the i -th eigenvector associated to the α -th chain of the crystal, \mathcal{L}_i^α , on the j -th eigenvector of the isolated chain \mathcal{L}_j^{chain} with a simple scalar product:

$$(\mathcal{L}_i^\alpha, \mathcal{L}_j^{chain}) = \sum_h (\mathcal{L}_i^\alpha)_h (\mathcal{L}_j^{chain})_h \quad (3.6)$$

In this way, we describe the normal modes of the whole crystal in terms of the normal modes of the isolated chain. The advantage of using the vibrational problem in the mass weighted coordinates (see Eq. 3.5) is that

it becomes hermitian, thus we can take advantage of the orthonormality of both the crystal and the single chain eigenvectors.

The eigenvector projection method gets back to the methodology of describing the normal modes of complex systems on simpler or physically meaningful basis sets, for instance, on the basis of maximally localized modes or on the basis of the single constituents of complex systems [112]. When a given normal mode of the crystal shows a large projection on a specific normal mode of the isolated chain and negligible projection all the others, then we can state that the two normal modes coincident; we are thus able to establish the effects of the intermolecular interactions by measuring the frequency shift and the variation of the IR intensity from the isolated chain to the crystal.

The present method allows also to distinguish the IR marker bands of the crystal as **regularity** or **crystallinity** bands. When a normal mode of the crystal is associated to a normal mode of the isolated chain and the two show close frequency values and comparable intensity, we can state that the mode is peculiar of the regular conformation but it is quite insensitive to the crystal packing. In this case, the associated band is defined **regularity** band. At the opposite, when a normal mode of the crystal is associated to a normal mode of the isolated chain showing a different frequency and/or remarkable intensity change, this means that the normal mode in the crystal is affected by specific intermolecular interactions and also by charge fluxes associated to them [113]. In this case, the associated band is defined **crystallinity** band.

3.3 Publications

In this section the results of our investigations on the structure and IR spectroscopic response of crystalline polymers are briefly presented and discussed. Attachments **c** and **d** deal with the structural investigation and the revision of the assignment of IR spectra of two polyamide systems. In attachment **e** a critical discussion on the IR spectrum of *poly(tetrafluoroethylene)*, PTFE, is presented.

Attachment **c**)

“IR spectroscopy of crystalline polymers from ab-initio calculations: nylon 6,6” D. Galimberti, C. Quarti, A. Milani, L. Brambilla, B. Civalleri and C. Castiglioni; *Vib. Spectroscop.* accepted for publication.

In the first work on the structure and IR spectroscopic response of polyamides, we have applied DFT method to study the crystalline α phase of nylon 6,6. This system represents an interesting test case for the application of electronic structure calculations for several reasons. On the one hand, its

crystal structure is characterized by just one polymer chain per unit cell and thus it requires a limited computational effort. Moreover, this system is not affected significantly by polymorphism effects and thus the interpretation of the IR spectrum of crystalline samples should be quite straightforward. In addition, even if the IR spectrum of nylon 6,6 has been studied since long time, there are still some ambiguities and debates on some assignments that need to be solved.

At first, we have carried out a geometry optimization of the crystalline structure of nylon 6,6 with DFT method, at the B3LYP/6-31G(d,p) level of theory, with periodic boundary conditions (PBC) along the three crystalline axis and imposing the space group symmetry determined from X-ray diffraction experiments ($P\bar{1}$ space group). Van der Waals interactions have been described with the interatomic pairwise vdW potential method presented in section 3.2.1. The same calculation has been carried out on the isolated, infinite chain by imposing the PBC along the chain axis. For the description of the van der Waals interactions we used only the Grimme parameters of the set 3 reported in Table 3.1. The computed cell parameters are reported in Table 2 of attachment **c** and they show good agreement with the experimental one, obtained from X-ray diffraction.

The IR spectrum has been calculated on the optimized structure of both the crystal and the infinite polymer chain. The resulting spectra are reported in Figure 2 of the attachment **c** and they are compared with the experimental IR spectrum of a crystalline sample of nylon 6,6. A very good agreement between the theoretical spectrum of the crystal and the experimental data is found, while the spectrum of the polymer chain does not parallel the general experimental pattern. The fact that the isolated chain model is not adequate for reproducing the IR spectrum is meaningful and it points out the importance of intermolecular interactions in affecting the spectroscopic response of nylon 6,6, as expected because of the presence of strong hydrogen-bond interactions. A revision of the marker bands previously proposed in the literature has been carried out on the basis of our theoretical results: the ambiguities related to the assignments found in the literature are solved and new markers are proposed.

A further analysis has been carried out to describe more in detail the marker bands previously confirmed, as well as the most intense IR bands. In particular, we were interested in classifying all these bands as **crystallinity** or **regularity** bands [91]. To this aim, we have compared the IR spectrum of the crystal with that of the polymer chain and we have used the eigenvector projection method illustrated in Section 3.2.2, in order to establish a rigorous correspondence between the normal modes of the former and those of the latter. Through this analysis it has been possible to associate each normal mode of the crystal to its “parent” mode of the polymer chain, whenever possible. The results of our revision on the assignment of the IR spectrum of nylon 6,6 are summarized in Table 6 of attachment **c**.

The successful prediction of the IR spectrum of nylon 6,6 in the crystalline phase demonstrates that our approach is effective in describing the spectroscopic response of complex systems as polyamides, whose structure is dictated by a detailed balance of intramolecular forces, van der Waals interactions and hydrogen bonding. The novelty of our approach resides in considering the whole crystal as a model and not adopting only the isolated polymer chain model with regular conformation or even simpler oligomeric models [83, 84, 85, 86]. The results obtained demonstrate that quantum chemical calculations have currently reached the maturity to tackle complex systems as crystalline polymers. We expect that, in the next future, these methods will be successfully applied not only for the spectroscopic characterization of polymeric systems but also for the study of a variety of problems dealing with their physico-chemical properties.

Attachment d)

“Ab initio calculation of the crystalline structure and IR spectrum of polymers: nylon 6 polymorphs” C. Quarti, A. Milani, B. Civalleri, R. Orlando and C. Castiglioni; *J. Phys. Chem. B* 116:8299-8311, 2012.

In a second paper, we have investigated polymorphism effects in nylon 6 by means of DFT calculations. Polymorphism is very common in molecular based materials and it is one of the key features ruling their properties, both at the nanoscale and at the macroscale. Nylon 6 is a very peculiar case, since it presents two stable crystalline forms, namely the α and the γ form, that are quasi-isoenergetic. Thus, real samples can present simultaneously both the forms and they can undergo phase transition as result of the processing or external conditions. The possibility to characterize real samples of nylon 6 with vibrational spectroscopy techniques is therefore highly coveted; unfortunately there have been some debates and contradictions in the literature on the assignments of some IR marker bands of the two polymorphs. Here, we use the CRYSTAL09 code to compute the IR spectra of both the α and γ polymorphs of nylon 6 and to propose a revision of the previous assignments.

We have first carried out a geometry optimization of both the α and the γ crystalline forms, at the B3LYP/6-31G(d,p) level of theory, using periodic boundary conditions and imposing the space group symmetry obtained from X-ray diffraction studies ($P2_1$ and $P2_1/a$ respectively for the α and the γ form). Also in this case, we used the interatomic pairwise potential method (see Section 3.2.1) to describe van der Waals interactions, with all the three sets of van der Waals radii reported in Table 3.1. We have optimized also the structure of the infinite, isolated chains “extracted” from the two crystalline forms, which are characterized by two different regular conformations. The cell parameters of the two polymorphs have been computed with all the three

sets of van der Waals radii and they are reported Table 3.1. A general good agreement between theory and experiments is found, with the set 3 that provides the best estimate of the cell parameters (see Table 2 of attachment **d**).

For both the α and γ polymorphs, we have then carried out the calculation of the IR spectra on the optimized structure of both the infinite chains and the crystals and we compared them with the experimental spectra. Also in this case, the theoretical spectra of the crystals nicely reproduce the pattern shown by the experimental spectra, especially in the region between 1500-900 cm^{-1} , where the marker bands of the two polymorphs are found. On the opposite, the IR spectra calculated on the isolated infinite chains do not reproduce the experimental IR data and this points out again the influence of intermolecular interactions on the (IR) spectroscopic response of polyamides. A deeper analysis of the region between 1500-900 cm^{-1} allowed to solve the ambiguities found in the literature on the assignment of the marker bands of the two polymorphs, confirming the validity of some marker bands and proposing some new one. The marker bands of the two polymorphs are summarized in Table 7 of attachment **d**. A more exhaustive analysis about the effect of intermolecular interactions on the IR spectra of nylon 6 polymers has been done by comparing the IR spectrum calculated for the crystal with that of the polymer chain. We used the eigenvector projection method, presented in Section 3.2.2, to establish the correspondence between the normal modes of the crystal and those of the polymer chain. The results of this analysis for both the α and γ polymorphs are reported respectively in Table 4 and 5 of attachment **d**. The revision of the assignments of the marker bands of the two polymorphs are summarized in Table 6, together with the classification of the most intense IR bands into **crystallinity/regularity** bands.

As in the previous paper on nylon 6,6, this work demonstrates that ab-initio computational techniques are now viable to predict the structure and the vibrational spectroscopic response of polymer crystals. In the present case, our approach proved to be effective for studying a complex phenomenon such as polymorphism. In fact, both the α and the γ structures have been predicted to be stable in nylon 6 and their calculated IR spectra showed a good correspondence with the experimental data. We expect therefore that these methods can be fruitfully employed for more comprehensive studies of polymorphism in polyamides.

Attachment e)

“*Ab initio* calculation of the IR spectrum of PTFE: helical symmetry and defects” C. Quarti, A. Milani and C. Castiglioni; *J. Phys. Chem. B* 117:706-718, 2013.

In this paper we use DFT calculations to shed light on the debated assignment of the IR spectrum of crystalline *poly(tetrafluoroethylene)*, PTFE. The structural characterization of PTFE is not an easy task, because of the presence of two phase transitions at room temperature, at 19 °C and 30 °C, in which disorder in the crystalline phase is observed, in addition to the usual presence of fully amorphous regions. During the first phase transition, at 19 °C, the conformation of the chains changes from a 13_6 helix to a 15_7 one [114], while at the second transition the chains keep the 15_7 regular conformation but the supramolecular crystal packing slightly modifies [115]. In addition, also a crystal phase with all-trans conformation of the chains has been observed at high pressure [116]. IR spectra of PTFE recorded at different temperature do not show any marked change that can be related to the phase transition; only the relative intensity of the doublet at $638\text{-}626\text{ cm}^{-1}$ evolves with the temperature, within a range that exceeds the temperatures of the phase transitions, going from 19 °C to about 50 °C. The higher component of this doublet $638\text{-}626\text{ cm}^{-1}$ has been associated to the regular PTFE chains with 15_7 and 13_6 helical conformation, while two assignments for the lower component were proposed in the literature: *i*) Brown assigned it to a conformational defect, consisting in the reversal of the helical direction, i. e. a helical reversal defect. Such defect should not be hindered by the supramolecular packing, since the chains can hold their axis (i.e. they do not change direction); *ii*) Zerbi instead, on the basis of calculations with an empirical force field carried out on infinite isolated chain models with 15_7 , 10_3 , 4_1 and 2_1 helical conformation, assigned the lower component of the doublet to chain segments with an all-trans (2_1) conformation.

In this work, we revise the assignment of the IR spectrum of semicrystalline PTFE by means of DFT calculations. We have first performed again the calculations proposed by Zerbi on systems with 15_7 , 10_3 , 4_1 and 2_1 helical structures, by using the state-of-the-art B3LYP/Ahlrichs-TZVP method. In addition, we considered also the 13_6 conformation, in order to investigate on the phase transition. These calculations have been performed on both infinite chains and finite oligomers, respectively with the CRYSTAL09 and GAUSSIAN 09 code. Calculations show that no clear IR markers associated to the phase transition from the 13_6 to the 15_7 conformation can be found. Moreover, they show that no active IR bands associated to the 2_1 helical conformation can be found in correspondence with the doublet $638\text{-}626\text{ cm}^{-1}$. Thus, based on our calculations, the assignment proposed by Zerbi should be reconsidered.

We considered then the effects of conformational defects on the IR spectrum of PTFE. A model for the helix-reversal defect has been taken from

REF [117] and it has been re-optimized at B3LYP/Ahlich-TZVP level of theory on two oligomeric models: $C_{16}F_{34}$ and $C_{28}F_{58}$. Our calculations demonstrated that the helix-reversal defect is actually a local minimum conformation for both the $C_{16}F_{34}$ and the $C_{28}F_{58}$ oligomers. Calculated IR spectra of both the $C_{16}F_{34}$ and the $C_{28}F_{58}$ oligomers with helix-reversal defects present a IR band at 628 cm^{-1} (frequency not rescaled), in good correspondence with the lower component of the $638\text{-}626\text{ cm}^{-1}$ doublet. These results confirm the assignment proposed by Brown, that the 626 cm^{-1} is due to the formation of helix-reversal defects. In addition, we have carried out a conformational analysis on the C_8F_{18} oligomer, in order to address the effect of the amorphous phase on the $638\text{-}626\text{ cm}^{-1}$ doublet and on the $1000\text{-}700\text{ cm}^{-1}$ frequency region, traditionally associated to the amorphous component.

The conclusion reached concerning the assignment of the lower component of the $638\text{-}626\text{ cm}^{-1}$ doublet clarifies the nature and the behaviour of PTFE at the molecular scale. The small signal from the 626 cm^{-1} band of the IR spectrum of PTFE at temperature well below the first phase transition demonstrates that this material is characterized by a large concentration of helix-reversal defects already at low temperature and the steadily increase of the intensity of this band between 19 and $30\text{ }^\circ\text{C}$ shows that the phase transition is accompanied by a large increase of the concentration of these defects. These findings support the suggestion of Kimmig et Al. that the phase transitions in PTFE are transitions from a state where intermolecular interactions are dominant to a state where intramolecular interactions prevail [118].

3.3.1 attachment c

IR spectroscopy of crystalline polymers from ab-initio calculations: Nylon 6,6

Daria Galimberti¹, Claudio Quarti¹, Alberto Milani^{1*}, Luigi Brambilla¹, Bartolomeo Civalleri², Chiara Castiglioni¹

¹*Politecnico di Milano – Dip. Chimica, Materiali e Ing. Chimica “G. Natta”,
P.zza Leonardo da Vinci 32, I-20133 Milano, Italy*

²*Università di Torino – Dip. Chimica e Centro di Eccellenza NIS
Via P. Giuria 7, I-10125 Torino, Italy*

Abstract

The IR spectrum of Nylon 6,6 in the crystalline α phase is computed by means of dispersion-corrected Density Functional Theory calculations carried out with periodic boundary conditions on the crystal. The results are carefully compared to experimental spectra through a detailed analysis of different frequency regions and focusing on the spectroscopic markers of crystallinity or regularity (i. e. of the regular conformation of the polymer chain). The previous assignments, based exclusively on experimental or semi-empirical investigations, are critically revised, demonstrating that state of the art computational methods in solid state chemistry can provide tools to obtain an unambiguous description of the vibrational properties of the crystalline phases of macromolecular materials. In particular, the ambiguities related to the assignment of some debated bands of crystallinity/regularity are solved. The structural and vibrational properties are interpreted on the basis of the peculiar intra and intermolecular interactions occurring in polyamides.

Keywords: polyamides; hydrogen bonding; density functional theory calculations; crystallinity bands

* Corresponding Author: Dr. Alberto Milani, Dip. Chimica, Materiali, Ing. Chimica “G. Natta” – Politecnico di Milano – P.zza Leonardo da Vinci, 32 – 20133, Milano, Italy.
e-mail: alberto.milani@polimi.it
phone-+39-0223993383

1. Introduction

Despite the widely spread application of vibrational spectroscopy methods for polymer systems [1-4] also in the industrial environment, the study of polymers structure and of their vibrational properties by means of quantum chemical approaches is only at its early stages. While molecular dynamics simulations and periodic first principles calculation encountered a large success for the investigation of the crystal structure of macromolecules, few calculations have been carried out for the accurate prediction of the vibrational spectra of polymers, due to the fact that quantum chemical calculations of a suitable level of theory are required to this aim. The investigation of the vibrational properties of polymers and the assignments of the IR spectra for practical and analytical purposes have been based mainly on experimental works or semiempirical calculations. It is thus not rare to find contrasting assignments, different interpretations and also some ambiguities in the past literature. More recently, ab-initio calculations have been often carried out by taking into account small molecular models (i.e. short oligomers), according to the so-called “oligomer approach” [5-9] but only in the last years, ab initio calculations of IR spectra of polymers explicitly exploiting the translational symmetry have been presented [10-19], thanks in particular to the new computational tools that have been implemented and that are now routinely available. Furthermore, accurate computational models for a correct description of intermolecular interactions in the framework of density functional theory became available only recently [20-23] and they are mandatory for a reliable study of molecular crystals, especially in the case of soft materials such as polymers.

In this class of materials, polyamides are well recognized and widespread in our everyday life. Furthermore, the development of new systems such as nanocomposites [24,25], electrospun nanofibers [26-34] and their application in the field of biomaterial and nanomedicine are currently promising fields of research. However, some fundamental chemical/physical phenomena related to the interplay between intra- and inter-molecular interactions are currently investigated both experimentally and theoretically aiming at the development of structure/property relationships based on a molecular approach, in connection with related characterization techniques. Furthermore, the complexity of these interactions has been the main responsible of the ambiguities which are present in the literature, lacking the support of a suitable computational investigation.

In this paper, we want to explore the application of the new computational tools now available for the description of polymeric materials in the crystalline state, presenting a computational study based on Density Functional Theory (DFT) calculations augmented with an empirical dispersion correction (DFT-D) [20,21] of the IR spectra of NY6,6 by using the CRYSTAL09 code [35,36]. The calculations take into account the space group symmetry for the accurate simulation of the vibrational properties of crystalline molecular materials. In the case of vibrational spectroscopy of

polymers, this code has been successfully applied to few cases, namely to the case of syndiotactic polystyrene [10-12], polyglycine [13], nylon 6 polymorphs [18] and polytetrafluoroethylene [19]. In Section 3.2 the DFT-D computed crystal structure of the α form of NY6,6 will be compared with the experimental structure and the predicted IR spectra will be used to give an interpretation of the experimental spectra in the different frequency ranges. Their interpretation and the detailed assignment of the spectroscopic markers of crystallinity or regularity are reported in Section 3.3.

2. Materials and Methods

The present computational study has been carried out by applying the same procedure adopted in our previous work on Nylon 6 polymorphs [18]. Full geometry optimization of the structure and the calculation of the IR spectra of the NY6,6 chain in its regular conformation (1D model chain, rod symmetry group $P\bar{1}$, isomorphous to the C_i point group) and of the crystal (triclinic cell, $P\bar{1}$ space group) have been carried out by means of the CRYSTAL09 code [35,36], in the framework of DFT and adopting periodic boundary conditions (PBC). We chose dispersion-corrected B3LYP [37,38] exchange-correlation functional together with the 6-31G(d,p) basis set. As starting guess structures for the calculations, we considered the experimentally determined crystal parameters and atomic coordinates reported by Bunn et al. [39] for the α form of NY6,6, sketched in Fig. 1.

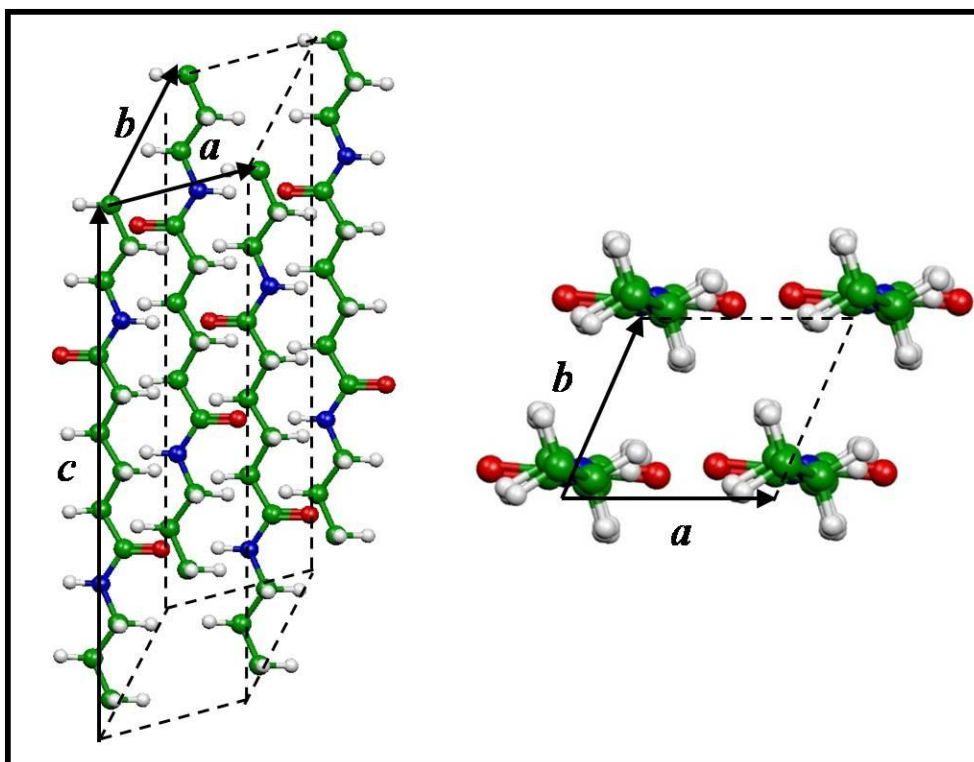


Fig. 1: Sketch of the crystalline structure of the NY6,6 crystal, α phase.

The geometry optimization and frequency calculation on the infinite polymer chain, required to discuss the spectroscopic markers of regularity vs. crystallinity, have been carried out by using as a starting guess the chain structure extracted from the crystal, according to the point group C_i .

Vibrational frequencies and eigenvectors obtained for the 1D model chains have been used for the interpretation of normal modes of vibration observed in the crystal, according to the procedure presented in Ref. [18] and summarized in the Supplementary Data.

All the DFT calculations included the Grimme's correction for dispersion interactions [20-23] (DFT-D), using the parameters adopted for Nylon 6 and reported in Table 1.

Table 1: List of the numerical values adopted in calculations for the parameters C_6 and R_{vdW} occurring in Grimme's correction E_{Disp} for dispersion interactions [20,21]

$$(E_{Disp} = -s_6 \sum_g \sum_{ij} \frac{1}{1 + e^{-d(R_{ij,g}/R_{vdW}-1)}} \frac{C_6^{ij}}{R_{ij,g}^6}).$$

A cutoff distance of 25.0 Å was used to truncate direct lattice summation. C_6 are in units of $\text{J nm}^6 \text{mol}^{-1}$ and their values have been taken from Ref. [20,21] while R_{vdW} are in unit of Å. For the "d" parameter a standard value of 20 has been chosen and for s_6 parameter a value of 1.00 [23].

Atom	C_6 ($\text{J nm}^6 \text{mol}^{-1}$)	R_{vdW} (Å)
H	0.14	1.3013 [23]
C	1.75	1.70 [40]
O	0.70	1.52 [40]
N	1.23	1.55 [40]

In all calculations, the atomic positions and the lattice parameters were fully optimized while normal frequencies calculations (at Γ point) have been carried out on the optimized geometries by diagonalization of the (numerically computed) Hessian matrix.

To compare the computed and the experimental data, the calculated frequencies were scaled by 0.97. This value has been determined in order to match the Amide I band computed for the crystal with the corresponding one in the experimental spectrum.

In this paper, the computational parameters adopted have been selected on the basis of the results obtained in the cases of NY6 [18], for which the comparison of different parameters has been made: future works should be carried out to investigate systematically the effect of the choice of

DFT functional, of the basis set and of the the parameters used for Grimme’s correction on the final crystal structure and IR spectra.

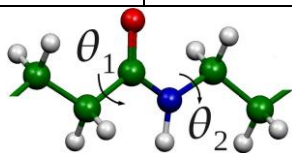
NY6,6 samples were prepared as self-standing thin film, with thickness ranging from few to tenths μm , by means of Doctor Blade technique using a formic acid solution of NY6,6 pellets (5% in weight kept under magnetic stirring for 1 hour) deposited on glass. All the samples were heated at 50°C in a oven for 1 hour in order to remove the formic acid and then detached from the glass. IR absorption spectra of the polymer films have been recorded with a FT-IR Nicolet Nexus Spectrometer (resolution 1 cm^{-1} , 128 scans).

3. Results and Discussion

3.1 Prediction of NY6,6 crystal structure

In Tab. 2 we report the DFT-D computed values for the cell parameters of NY6,6 α crystal, compared with the experimental values. The \mathbf{c} vector coincides with the chains axis, \mathbf{a} lies in the plane which contains hydrogen bonds while vdW packing occurs along \mathbf{b} direction. Hydrogen bonded distances, intra and inter-sheet distances between the axis of adjacent chains (respectively $a \sin\beta$ and $b \sin\alpha$) are also compared.

Table 2: Experimental [39] and DFT-D computed cell parameters for α NY6,6. Distances are in Å, angles in degrees. Experimental values are also reported for comparison. Intra and intersheet distances between the axis of adjacent chains ($a \sin\beta$ and $b \sin\alpha$) and torsional angles θ_i (referred to the backbone atoms) next to the amide group are reported. In the last column the absolute and percentage Δ between experimental and DFT-D values are reported.

	Experimental [39]	B3LYP/6-31G(d,p)	Δ (exp-DFT-D)
a	4.90	4.98	-0.08/-1.63%
b	5.40	5.29	+0.11/+2.04%
c	17.20	17.48	-0.28/-1.63%
α	48.50	45.37	+3.13/+6.45%
β	77.00	74.14	+2.86/+3.71%
γ	63.50	62.37	+1.13/+1.78%
$R_{O\dots N}$	2.8	2.89	-0.09/-3.21%
$a \sin\beta$	4.77	4.79	-0.02/-0.42%
$b \sin\alpha$	4.04	3.76	+0.28/+6.93%
			
θ_1	174	167	+7/+4.02%
θ_2	169	166	+3/+1.78%

A satisfactory agreement is found between experimental and DFT-D values and only minor discrepancies are observed. As observed also in the case of Nylon 6 [18], these discrepancies are dependent on the parameters used for Grimme's correction and by using different choices for van der Waals radii, non negligible variations can be observed for the cell parameters, in particular for those directions dominated by weak packing forces (b parameter). Furthermore, it should be noted that thermal effects can have an important role in modulating cell parameters in polyamides crystals, as reported by Itoh [42]. Any comparison with DFT values (obtained by a full geometry optimization i.e. at 0 K) should be thus carried out carefully. Considering in particular the intramolecular torsional angles around the amide group (θ value in Table 2), a larger deviation from transplanarity is predicted by calculations with respect to the experimental values.

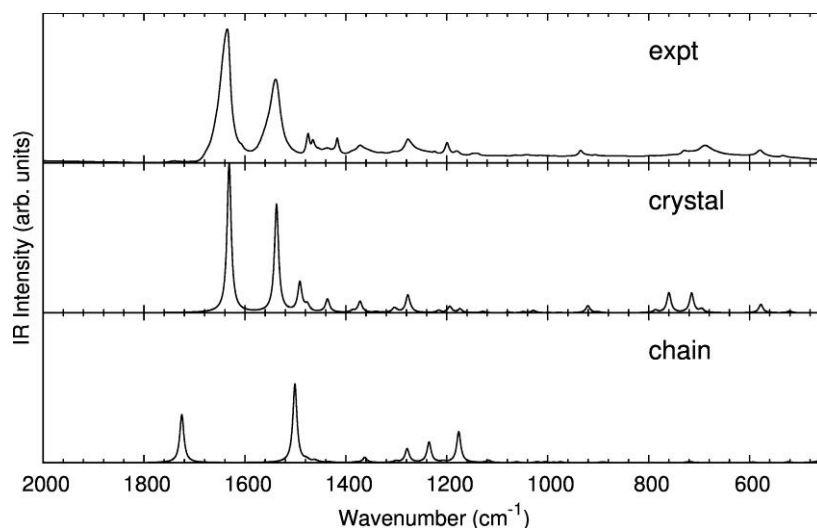


Fig. 2: Comparison between experimental and DFT-D computed IR spectra (crystal and single chain model) in the frequency range below 2000 cm^{-1} (scaling factor 0.97).

3.2 IR spectra of NY6,6

In Fig. 2 we report the comparison between the experimental and DFT computed IR spectra of NY6,6 in the frequency range $2000\text{-}500\text{ cm}^{-1}$ which is the most important for practical application. The spectra computed both for the infinite polymer chain and the crystal are reported: as expected, in the case of polyamides, the occurrence of hydrogen bonding prevents the interpretation of the experimental spectra on the basis of a single, infinite chain model but the whole crystal needs to be considered. This is particularly true in the case of Amide I and Amide II bands, whose frequencies and intensities are significantly influenced by hydrogen bonding. As described in Section 3.3, the comparison between the IR spectra of the infinite chain and the crystal is anyway useful, since it gives the possibility to assign the marker bands sensitive to the crystal packing (e.g. crystallinity bands) or mainly due to the existence of a regular conformation of the chains (e.g. regularity bands).

This issue is particularly important in the case of NY6,6 since many of the discrepancies found in the literature [43-64] concern the assignments of some bands as marker of crystallinity or regularity, thus affecting their use in practical applications.

Table 3: Wavenumbers of the most important experimentally determined IR marker bands of NY6,6 proposed in the literature by different authors [43-64].

	wavenumber (cm ⁻¹) of marker bands in the IR spectra
Crystallinity	906, 936, 1200, 1466, 1460, 2946
Regularity	1474, 1417
Amorphous	924, 1136, 1140
Reference	1630
Uncertain	1180, 1144, 1224, 1329

The spectrum computed for the crystal in Fig. 2 reproduces accurately the experimental spectrum even in minor details and the pattern in both frequencies and relative intensities shows a very good agreement. In the following, the different frequency ranges will be analyzed in detail, focusing in particular on the marker bands previously proposed in the literature and which are summarized in Table 3.

3.2.1. 800-1100 cm⁻¹ frequency range

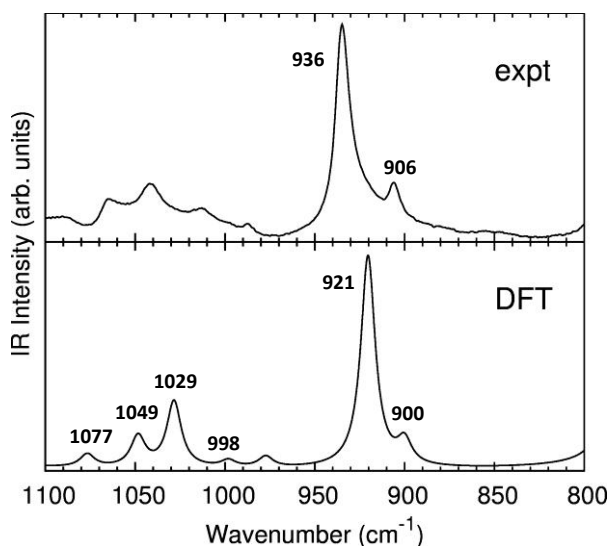


Fig. 3: Comparison between experimental and DFT-D computed IR spectra for α -NY6,6 in the wavenumber range 1100-800 cm⁻¹ (scaling factor: 0.97).

In this frequency region, important marker bands are found for polyamides crystals: also in the case of NY6,6, the two bands observed at 936 and 906 cm⁻¹ are usually assigned as marker of crystallinity [43-53]. However, a significant discrepancy is present in the literature: based on

previous observations [54], Quintanilla et al. [50] state that the band at 936 cm^{-1} is a marker of the trans conformation of the chain, independently of the presence of a crystal phase (i.e. it is a regularity band). Such assignment would prevent a diagnosis of crystallinity in real samples based on the detection this band, as well as its quantitative determination through the measured absorption intensity. In Section 3.3 we will show that DFT-D calculations carried out on the isolated chain (1D model chain) can unravel this ambiguity and confirm that both these bands (predicted at 921 and 900 cm^{-1} , scaled values) are markers for the NY6,6 crystal. In addition to these two bands, Fig. 3 shows that the pattern of the four main bands observed between 1080 and 980 cm^{-1} in the experimental spectrum is reproduced by the calculations, where four bands are indeed predicted.

3.2.2. $1100\text{-}1500\text{ cm}^{-1}$ frequency range

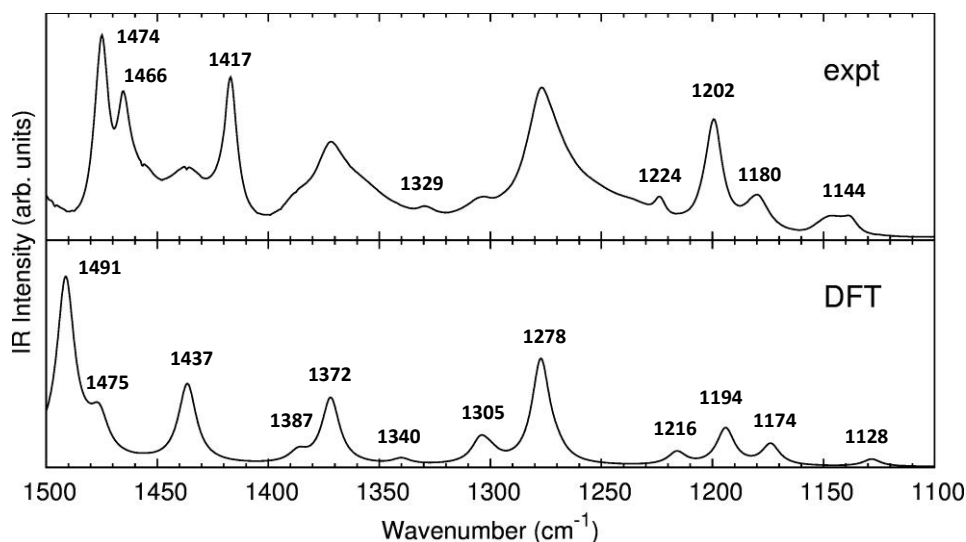


Fig. 4: Comparison between experimental and DFT-D computed IR spectra for α -NY6,6 in the frequency range $1500\text{-}1100\text{ cm}^{-1}$ (scaling factor: 0.97).

In the frequency range below 1500 cm^{-1} many bands are observed having medium/weak intensity if compared with the strong amide I and II bands. The comparison with DFT-D computed spectra is reported in Fig. 4 and a good agreement is again found both in frequencies and intensities, even for the minor features. Also in this range, a lot of discrepancies are present in the previous literature.

The weak and broad band observed at 1144 cm^{-1} has been previously assigned to the amorphous phase and in Refs. [50,55] it has been assigned to chain defects involving gauche conformations. DFT-D calculations predict a very weak band at 1128 cm^{-1} (scaled value) which can be related to the experimental band at 1144 cm^{-1} and thus they support the conclusions of Vasanthan [45,46] who indicated that also a contribution of the crystalline phase to this feature can be present. In any case, even if such a contribution is present, it is not strong enough to ascribe the observed transition to

the effect of the crystal phase only and we can definitely confirm the assignment of the 1144 cm^{-1} band as a marker of the amorphous phase. In the case of the band observed at 1180 cm^{-1} , some authors assigned it as a marker of the amorphous phase [56], while Vasanthan [45,46] and Cooper [55] demonstrated that it gets a contribution due to the crystalline phase: DFT-D calculations predict a band at 1174 cm^{-1} (scaled value) thus confirming that it is due to the NY6,6 crystal. The crystallinity band falling at 1202 cm^{-1} [45,46] is also confirmed (computed band at 1194 cm^{-1}).

The weak bands observed at 1329 and 1224 cm^{-1} have been previously attributed to folded chains in the crystal [47,48] and should be thus absent in DFT-D computed spectra due to the periodic boundary conditions adopted to describe the (ideal) crystal. However, two bands are predicted at 1340 cm^{-1} (weak intensity) and 1216 cm^{-1} , demonstrating that the two bands are present in the bulk crystal and cannot be taken as evidence of chain folding, as also previously discussed by Cooper [55]. Further marker bands are those found between 1491 and 1437 cm^{-1} : computed spectra are still in general agreement with previous assignments [55] of the observed bands at 1474 , 1466 and 1417 cm^{-1} (predicted at 1437 cm^{-1}) to the crystal or to chains with regular conformation but a deeper investigation based also on the single chain model is required for a detailed assignment (see Section 3.3).

As a final comment, the calculations indicate the presence of four other possible marker bands at 1387 , 1372 , 1305 and 1278 cm^{-1} (computed values) for the crystal, not used in previous studies.

3.2.3. Other spectral regions

In Fig. 5a the experimental and DFT-D spectra are compared in the frequency range $800\text{-}400\text{ cm}^{-1}$. Again a close correspondence is found, in particular for the two bands at about 578 and 535 cm^{-1} whose pattern is accurately predicted. In the case of the broad, structured bands falling between 680 and 760 cm^{-1} DFT-D calculations are not able to reproduce the correct relative intensities: a similar behaviour was observed also in the case of NY6 [18] in the same spectral region and it could be due to the contribution of the amorphous in the experimental spectra.

In the frequency range $1700\text{-}1450\text{ cm}^{-1}$ (Fig. 5b) the intense amide I and II bands are observed and their pattern in frequencies and intensities is again nicely reproduced by the calculations, including the presence of the weak band observed at about 1475 cm^{-1} . As widely known [57], the amide bands, in addition to the NH stretching band observed at about 3300 cm^{-1} and reported in Fig. 5d, are very sensitive to hydrogen bonding and their correct prediction requires calculations on the whole crystal, making unreliable the 1D chain model for an interpretation of the spectra of crystalline samples.

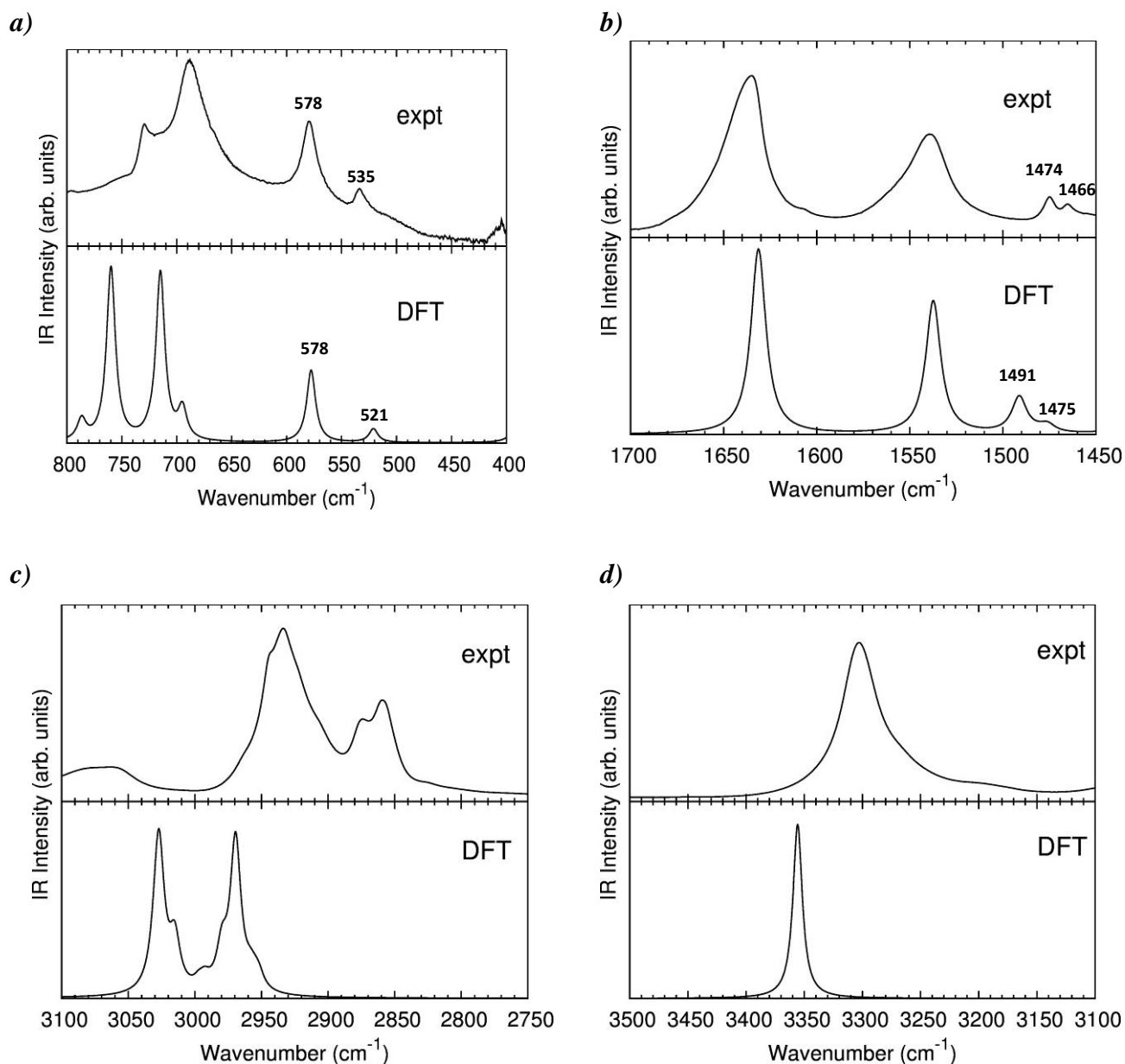


Fig. 5: Comparison between experimental and DFT-D computed IR spectra for α NY6,6 in the following wavenumbers ranges: (a) 800-400 cm^{-1} , (b) 1700-1450 cm^{-1} , (c) 3100-2750 cm^{-1} , (d) 3500-3100 cm^{-1} (scaling factor: 0.97)

Finally, in Fig. 5c the CH stretching region (3100-2800 cm^{-1}) is reported: as expected some discrepancies are found, in particular when relative intensities are analyzed; two main features are however predicted, both characterized by the presence of several components in agreement with the experimental spectrum. It is well-known that in this frequency range anharmonicity effects (overtone, Fermi resonances) can give an important contribution; furthermore, conformational effects (e.g. amorphous contribution) can introduce a modulation of the CH stretching bands [65]. Also the approximations introduced by the calculations (e.g. basis set superposition error, Grimme's

correction for dispersion interactions, etc) can originate discrepancies. In spite of this, we will show in the next section that also in this frequency range, DFT-D calculations are useful to obtain some further insights on the intramolecular interactions taking place for the polymer chain.

3.3. Comparison with 1D model chain spectra

Vibrational spectra of highly crystalline polymers [1,3] are often discussed in terms of *crystallinity* vs. *regularity* bands. This classification is based on the assumption that the $\mathbf{q} = \mathbf{0}$ phonons of the crystal can be described in terms of $\mathbf{q} = \mathbf{0}$ phonons of the single chains belonging to the 3-D unit cell, which are characterized by a regular conformation and then are described as 1-D crystal. If the inter-molecular interactions are weak, the perturbation by the 3-D crystal packing is small and the spectrum is reasonably predicted simply by the calculation of the phonons of the isolated chain: on this basis we can conclude that we are in presence of vibrations mainly sensitive to the regular structure of the single chain (*regularity bands*). Sometimes, as for instance in the case of polyethylene, some regularity bands show the so called crystal splitting, which is indeed the signature of the presence of a regular 3-D packing: in this case the band is classified as *crystallinity band*. Moreover the crystal splitting proves the presence of more than one chain in the unit cell [1,3].

In the case of NY6,6 (and in general for polymers characterized by strong intermolecular interactions (i.e. H bonds) the above description does not apply, since in this case the regular single chain represents an ideal model. Indeed a NY6,6 chain is expected to develop inter- and intramolecular hydrogen bonds in any phase of the matter (and in particular both in the amorphous and in the crystalline phases). It may be however interesting to exploit the comparison of the vibrational spectrum of the 3-D crystal with that calculated for the ideal 1-D model, in order to obtain a classification of the normal modes capable to get some information on the relevant interactions taking place in the solid state. On the basis of the comparison of the two computed infrared spectra and in analogy with the case of van der Waals polymers crystals, we will assign marker bands of crystallinity (i.e. of bands associated to normal vibrations which are sensitive to the 3-D crystal packing) or marker bands of regularity, the latter being simply predicted on the basis of the phonons of the 1-D infinite chain, i.e. related to the existence of a regular conformation of the chains, *independently* of their supramolecular arrangement.

An additional advantage of ab-initio calculations relies in the possibility to associate each frequency to the corresponding normal mode of vibration, allowing to propose a detailed vibrational assignment and gathering information on the dynamics of the system in terms of specific intra and intermolecular interactions. The analysis has been done by following the “projection method”

previously adopted in the case of Nylon 6 [18] and described in the Supplementary Data. According to this method, the normal modes of the crystal are described on the basis of the characteristic normal modes of the isolated chain. In this way a correspondence between the relevant IR active transitions of the crystal and of the 1D model can be established, enabling to capture the effects of the crystal packing and H bonds formation in terms of frequency shifts and IR intensity redistribution due to the “mixing” of chain modes induced by the intermolecular interactions.

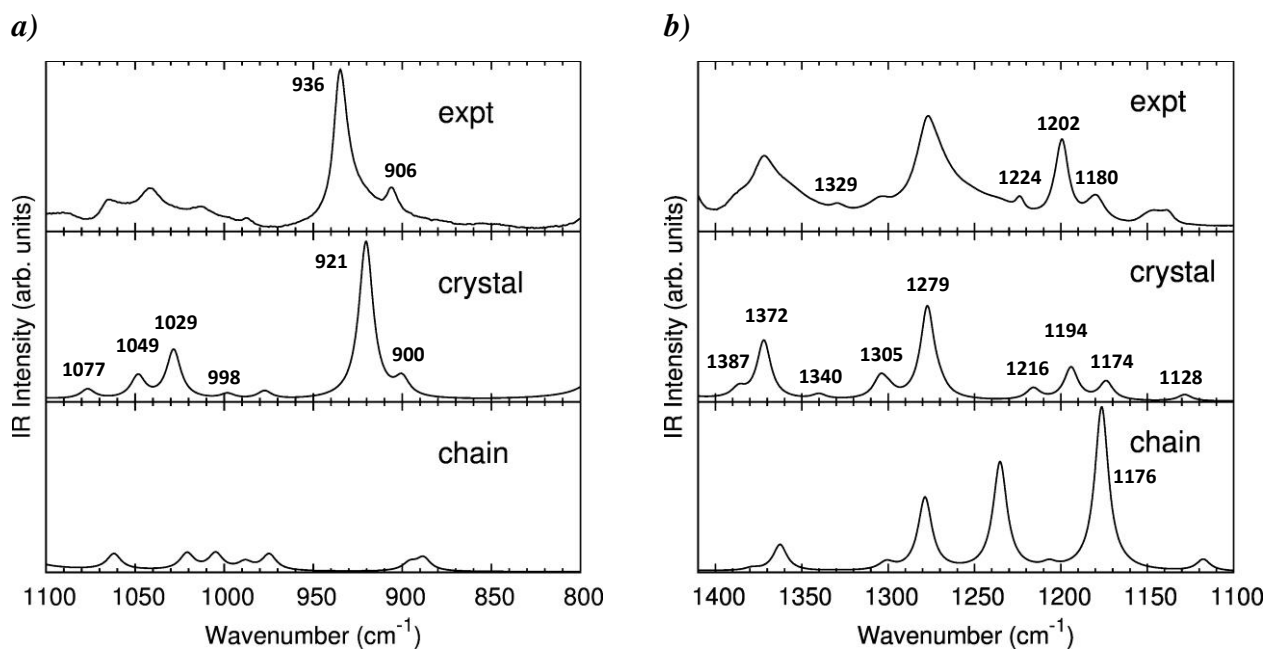


Fig. 6: Comparison between DFT-D computed IR spectra of the α crystal and 1D model chain of NY6,6 in the frequency range (a) 1100-800 cm^{-1} and (b) 1400-1100 cm^{-1} (frequency scaling factor: 0.97).

In Fig. 6a the frequency range 800-1100 cm^{-1} is shown. In the previous section we shown that the debated band at 936 cm^{-1} is nicely predicted by calculations carried out on the crystal; however this does not prove that the appearance of this band in the experimental spectrum should be taken as an evidence of the presence of a 3-D packing (i. e. it is a marker of crystallinity). Indeed it could be due only to the presence of chain segments showing trans-planar conformation (such as that observed in crystal), even if they are not packed in a crystal, characterized by a regular network of H bonds. The comparison with the spectrum computed for the 1D model chain definitely assigns both the band observed at 936 and 906 cm^{-1} as markers of crystallinity: indeed, their intensity would be much weaker for a regular isolated chain and the pattern recorded can be nicely reproduced only if a periodic tridimensional chain packing is present. On this basis the assignment of the band at 936 cm^{-1} as a marker band of trans regular conformation [50] is definitely discarded. As reported in

Table S1 of the Supplementary Data, the normal modes associated to the bands 936 and 906 cm^{-1} involve directly the amide groups and CH_2 deformation modes. It is thus quite straightforward to understand why, due to the high sensitivity to the intra/intermolecular environment of the CH bonds [65,66], these bands are significantly affected by the hydrogen bonding taking place in the crystal.

On the one hand, the four bands observed between 950 and 1080 cm^{-1} result to be slightly stronger according to the calculation on the crystal but the differences between 1D and 3D models are not so significant to consider them as reliable markers of the crystalline phase: for this reason it is reasonable to suggest that the bands predicted at 1077 and 998 cm^{-1} should be considered markers of regularity, as also confirmed by the analysis reported in the Supplementary Data. On the other hand, based on intensity arguments, the two bands at 1049 and 1029 cm^{-1} could be considered markers of crystallinity, even if they are not suitable for practical purposes.

In the case of 1400-1100 cm^{-1} range (Fig. 6b) a quite complex behaviour is observed: while the band at about 1174 cm^{-1} in the computed spectrum of the crystal (assigned to the experimental band at 1180 cm^{-1}) is a marker of crystallinity, the band predicted for the isolated chain at about 1176 cm^{-1} seems to lose intensity in the crystal; the same holds also for the bands predicted at about 1235 cm^{-1} and 1128 cm^{-1} †. It should be also noted that, in the case of the doublet of bands predicted at 1194 and 1174 cm^{-1} the projection method reveals that a significant coupling of different normal modes of the 1D chains is present and thus the trend in intensity cannot be simply interpreted carrying out a one-to-one correspondence with the bands of the 1D chain. Based on these results, it is appropriate to assign the bands observed at 1201 and 1180 cm^{-1} as markers of crystallinity, confirming the conclusions reported in previous papers [45,46]. On the opposite, it is possible to assign the bands predicted at about 1278 cm^{-1} and 1216 cm^{-1} in the crystal as markers of regularity while the bands predicted at 1372 cm^{-1} , 1387 cm^{-1} and 1305 cm^{-1} are enhanced in intensity in the crystal and are assigned as markers of crystallinity (see Table S1). As pointed out in the previous section, the two bands observed at 1224 and 1329 cm^{-1} cannot be considered as markers of chain folding [55] since they have two correspondent bands in the DFT-D computed spectrum at 1216 and 1340 cm^{-1} respectively.

On the basis of the previous investigation carried out on Nylon 6 [18], we can also conclude that the assignment of individual bands as markers of crystallinity/regularity is not trivial in this range since significant dynamical couplings take place because of the supramolecular arrangement. In particular the whole pattern of bands and their relative intensity in this region provide the evidence of crystallinity, as clearly shown in Fig. 6b.

† A similar behaviour in intensity has been found in the same frequency range also for Nylon 6 and it is due probably to subtle effects of hydrogen bonding in modulating non-principal charge fluxes [67-70] associated to these vibrations.

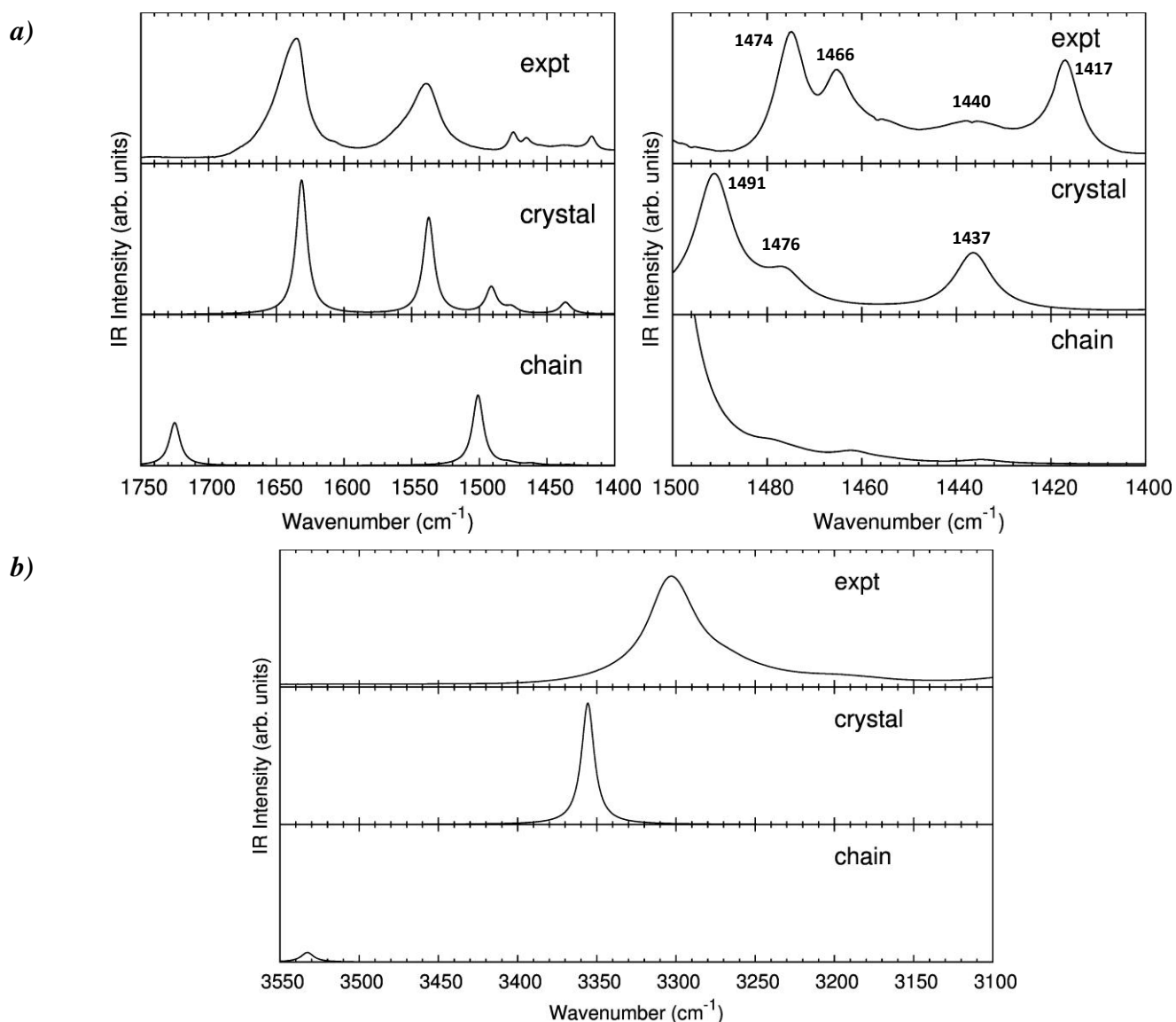


Fig. 7: Comparison between DFT-D computed IR spectra of the α crystal and 1D model chain of NY6,6 in the frequency range (a) 1750-1400 cm^{-1} and (b) 3550-3100 cm^{-1} (frequency scaling factor: 0.97). In panel b) the intensity for the 1D model chain have been multiplied for 5 for a better comparison.

In Fig. 7a the frequency range associated to Amide I and II bands is reported: the usual frequency downshift and intensification of Amide I band and the frequency upshift of Amide II bands when passing from the 1D chain to the crystal is observed, consistently with the occurrence of hydrogen bonding [57]. In addition to this standard and well-known behaviour, further insights can be obtained by inspection of the 1490-1400 cm^{-1} range. The bands observed at 1474 and 1466 cm^{-1} and predicted for the crystal at 1491 and 1476 cm^{-1} (scaled values) increase in intensity due to crystal packing and are thus markers of crystallinity. Finally, the other major band predicted at 1437 cm^{-1} for the crystal is clearly a marker of crystallinity. Our assignments in this region differ from those

previously proposed by some authors [55,58,59,64] who assigned the band at 1474 and 1417 cm^{-1} as regularity bands. On the contrary, the previous assignment of the band at 1440 cm^{-1} to a gauche conformation of the chain is assessed also by our calculations since we do not observe bands with significant intensity to be assigned to this experimental feature.

In Fig. 7 we report also the NH stretching region where the well-known significant redshift and intensification [57] originated by hydrogen bonding is clearly observed in the computed spectra.

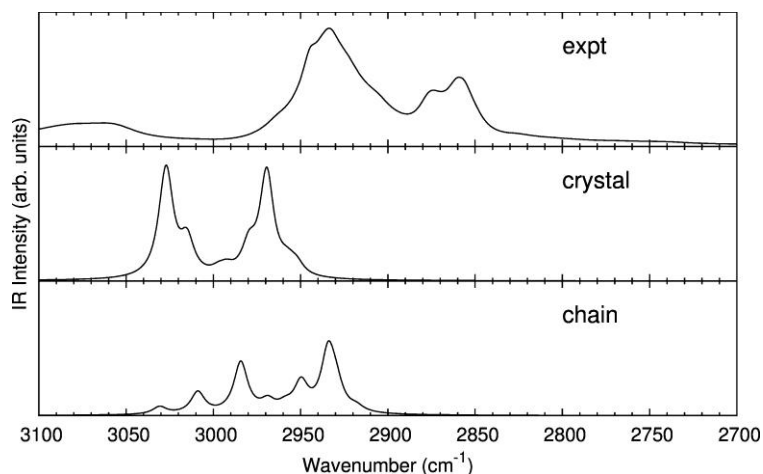


Fig. 8: Comparison between DFT-D computed IR spectra of the α crystal and 1D model chain of NY6,6 in the frequency range 3100-2700 cm^{-1} .

Lastly, we now analyze the comparison between experimental and DFT-D computed spectra in the CH stretching region, reported in Fig. 8. We already mentioned that this region should be analyzed with care, due to the presence of significant anharmonicity not taken into account in present calculations, carried out in harmonic approximation. As usual, this region is structured, due to the overlap of many contributions and it is difficult to detect markers of crystallinity/regularity in such a range. As a first observation, we can note that the pattern of bands of the crystal is blue-shifted with respect to that of the 1D chain, as also observed in the case of the α form of Nylon 6, probably due to the steric hindrance between CH_2 groups when packed in the crystal.

The analysis of CH stretching bands is particularly useful to study the intramolecular vibrational interactions taking place in NY6,6 chain. It is indeed well-known since the pioneering work by McKean [66] that CH stretching frequencies are sensitive to their molecular environment; furthermore, in a very recent paper [65], it is shown how CH_2 stretching frequencies are particularly sensitive to the neighbouring chemical groups, being influenced both by inductive effects by halogens and electronegative groups and by conformational effects. In the present case of NY6,6, the presence of the amide groups can modify the nature of the CH_2 in the alkyl chain depending on

their relative distance along the polymer. In particular, CH₂ groups immediately adjacent to the amide group are expected to be remarkably different from the other methylenic groups. Furthermore, since the creation of hydrogen bonding strongly modulates the electronic structure of the whole amide group, it can be expected that it results also in a modulation of the characteristic of the CH₂ groups closer to it and the bands associated to vibrations localized on these groups will be sensitive to the crystal packing. In Table 4 we report the assignment of the CH stretching bands: it is immediately evident that some bands are directly related to a normal mode localized only on one or two CH₂ groups adjacent to the NH or C=O bonds of the amide group, such as for example the bands calculated at 3027, 2997, 2993, 2980, 2956 and 2952 cm⁻¹. The extreme sensitivity of CH₂ vibrations to their environment is further highlighted by the fact that CH₂ groups adjacent to the NH bond have different stretching frequencies with respect to CH₂ groups adjacent to the C=O bond.

Thanks to the projection method, it seems correct to relate the experimental bands at 2946 and 2933 cm⁻¹ respectively to the convolution of the modes predicted in the range 3029-3027 cm⁻¹ and to the band at 3015 cm⁻¹. We agree with the assignment of Cooper [55] and Heidemann [58] of the band at 2946 cm⁻¹ to the antisymmetric stretching of the CH₂ mainly adjacent to the NH bond; in addition the contribution of the mode predicted at 3027 cm⁻¹ is related to normal modes associated also to the CH₂ groups adjacent to the C=O bond. Considering the band at 2970 cm⁻¹, this is associated to stretching modes on CH₂ groups adjacent to the N atom, as proposed by Zimba [60]. Finally, since no other bands are predicted above 3029 cm⁻¹ (corresponding to the experimental band at 2946 cm⁻¹), we confirm that the bands observed at 3195 cm⁻¹ and 3058 cm⁻¹ can be probably assigned to overtones, as proposed by Cannon [61].

As a summary to the whole discussion and in order to quantify the effect on IR intensities due to the hydrogen bonding in the crystal, we report in Table 5 the comparison between the computed intensity sums for the 1D model chain and the crystal in the different regions of the spectrum previously analyzed.

Table 4: Assignment of the CH stretching modes. In the last column the location of the CH₂ group with respect to the N-H or C=O bond of the amide group is indicated by greek letters (α : first neighbour, β : second neighbour...)

Crystal		Assignment	
DFT computed frequency (scaled) (cm ⁻¹)	IR intensity (km/mol)		
3029	35	CH ₂ Antisymmetric Stretching	collective
3027	226	CH ₂ Antisymmetric Stretching	β (CO)
			α (NH)
3015	81	CH ₂ Antisymmetric Stretching	β (NH)
			α (NH)
			γ (NH)
2997	12	CH ₂ Antisymmetric Stretching	β (NH)
			γ (NH)
2993	17	CH ₂ Antisymmetric Stretching	α (CO)
2980	65	CH ₂ Symmetric Stretching	β (CO)
2970	244	CH ₂ Symmetric Stretching	α (NH)
			β (NH)
			γ (NH)
2959	17	CH ₂ Symmetric Stretching	α (NH)
			β (NH)
			γ (NH)
2956	14	CH ₂ Symmetric Stretching	α (CO)
2952	23	CH ₂ Symmetric Stretching	β (NH)
			γ (NH)

As expected due to the presence of hydrogen bonding, the NH stretching region and the Amide I and II region are significantly enhanced in intensity; however, also in the 500-900 and 900-1150 regions, an enhancement in intensity characterizes the crystal, confirming again that many bands in this region are indeed important markers of crystallinity, which can be used also for practical purposes. On the other side, in the region 1150-1550 cm^{-1} , with the exception of the amide II band, such a remarkable effect is not observed and the projection method reveals that it is quite difficult to obtain a definite assignment of crystallinity/regularity bands in this region.

Based on the detailed analysis reported, we finally report in Table 6 our assignments for the IR spectrum of NY6,6 α crystal, also compared to previous assignments. In this Table we report only the relevant marker bands; the complete list of DFT-D computed frequencies and intensities for both the crystal and the chain can be found in the Supplementary Data.

Table 5: Intensity behavior of the infrared spectrum of 1D model chains (single chain) and crystals of NY6,6.

Frequency range (cm^{-1})	1D (CHAIN)	3D (CRYSTAL)
500-900	31	468
900-1150	27	103
1150-1550	1332	1731
Amide I and II	1061	2161
CH stret	492	733
NH stretc	28	1804

4. Conclusions

In this work, we have shown how recent developments in theoretical and computational solid-state offer valuable tools for the calculation of the infrared spectra and vibrational properties of soft crystalline materials. Polymers are a significant example of this kind of materials, since vibrational spectroscopy techniques are widely used also in the industrial environment, but their application relied almost exclusively on experimental and/or semiempirical approaches. It is thus not rare to find many discrepancies, ambiguities and open questions in the literature, also in relation to materials which are widely used in the everyday life. The CRYSTAL code is very powerful to predict the IR spectra of molecular crystals, due to the possibility to take into account the full space group symmetry (required for structural optimization, band assignment and description of the

polarization properties) and to include a suitable description of van der Waals interactions in the framework of density functional theory. Here, we have used CRYSTAL09 code to carry out DFT-D calculations of the IR spectra of Nylon 6,6 polymer, by considering both the crystalline structure (α form) and the infinite chain model. A good description of both the crystalline structure and of the experimental IR spectrum has been obtained. In particular, some ambiguities in the assignment of the marker bands, previously proposed on the basis of experimental investigations, have been unraveled and a better insight has been obtained.

As in our recent paper on vibrational properties of Nylon 6 polymorphs [18], the results here obtained demonstrate that accurate DFT-D calculations of the IR spectra of crystalline polymers are possible and can be applied to discuss a wide range of problems, providing answers to several open questions. Their importance is not restricted to the interpretation of the chemical/physical properties of material but they are a valuable tool to support experimental techniques in the development and characterization of innovative polymeric systems.

References

- [1] P. C. Painter, M. M. Coleman, J. L. Koenig, *The theory of vibrational spectroscopy and its application to polymeric materials*, Wiley, Chichester, 1982.
- [2] G. Zerbi, in: R. J. G. Clark, R. R. Hester (Ed.), *Advances in Infrared and Raman spectroscopy*, Wiley, Heyden, 1984; Vol. 11, pp. 301
- [3] C. Castiglioni, in: N. J. Everall, L. M. Chalmers, P. R. Griffiths (Ed.), *Vibrational Spectroscopy of Polymers: Principles and Practices*, Wiley: Chichester, 2007; pp. 455.
- [4] R. Zbinden, *Infrared spectroscopy of high polymers*, Academic Press, 1964
- [5] E. Koglin, R. J. Meier, *Comput. Theor. Polym. Sci.* 9 (1999) 327-333.
- [6] R. J. Meier, *Polymer* 43 (2002) 517-522.
- [7] A. Tarazona, E. Koglin, B. B. Coussens, R. J. Meier, *Vib. Spectrosc.* 14 (1997) 159-170.
- [8] A. Milani, C. Castiglioni, E. Di Dedda, S. Radice, G. Canil, A. Di Meo, R. Picozzi, C. Tonelli, *Polymer* 51 (2010) 2597-2610.
- [9] A. Milani, M. Tommasini, C. Castiglioni, G. Zerbi, S. Radice, G. Canil, P. Toniolo, F. Triulzi, P. Colaianna, *Polymer* 49 (2008) 1812-1822.
- [10] F. Javier Torres, B. Civalleri, A. Meyer, P. Musto, A. R. Albuñia, P. Rizzo, G. Guerra, *J. Phys. Chem. B* 113 (2009) 5059-5071.
- [11] F. Javier Torres, B. Civalleri, C. Pisani, P. Musto, A. R. Albuñia, G. Guerra, *J. Phys. Chem. B* 111 (2007) 6327-6335.

- [12] A. R. Alburnia, P. Rizzo, G. Guerra, F. Javier Torres, B. Civalleri, C. M. Zicovich-Wilson, *Macromolecules* 40 (2007) 3895-3897.
- [13] A. M. Ferrari, B. Civalleri, R. Dovesi, *J. Comput. Chem.* 31 (2010) 1777-1784.
- [14] S. M. Nakhmanson, R. Korlacki, J. Travis Johnston, S. Ducharme, Z. Ge, J. M. Takacs, *Phys. Rev. B* 81 (2010) 174120.
- [15] J. Kleis, B. I. Lundqvist, D. C. Langreth, E. Schroder, *Phys. Rev. B* 761 (2007) 100201.
- [16] N. J. Ramer, T. Marrone, K. A. Stiso, *Polymer* 47 (2006) 7160-7165.
- [17] N. J. Ramer, C. M. Raynor, K. A. Stiso, *Polymer* 47 (2006) 424-428.
- [18] C. Quarti, A. Milani, B. Civalleri, R. Orlando, C. Castiglioni, *J. Phys. Chem. B* 116 (2012) 8299-8311.
- [19] C. Quarti, A. Milani, C. Castiglioni, *J. Phys. Chem. B* in press doi: 10.1021/jp3102145
- [20] S. Grimme, *J. Comput. Chem.* 25 (2004) 1463-1473.
- [21] S. Grimme, *J. Comput. Chem.* 27 (2006) 1787-1795.
- [22] C. S. Liu, G. Pilania, C. Wang, R. Ramprasad, *J. Phys. Chem. A* 116 (2012) 9347-9352.
- [23] B. Civalleri, C. M. Zicovich-Wilson, L. Valenzano, P. Ugliengo, *CrystEngComm* 10 (2008) 405-410.
- [24] L. S. Loo, K. K. Gleason, *Macromolecules* 36 (2003) 2587-2590.
- [25] G. Chen, D. Shen, M. Feng, M. Yang, *Macromol. Rapid Commun.* 25 (2004) 1121-1124.
- [26] Song, K.; Rabolt, J. F. *Macromolecules* **2001**, 34, 1650-1654
- [27] K. H. Lee, K. W. Kim, A. Pesapane, H. Y. Kim, J. F. Rabolt, *Macromolecules* 41 (2004) 1494-1498.
- [28] F. Granato, A. Bianco, C. Bertarelli, G. Zerbi, *Macromol. Rapid Commun.* 30 (2009) 453-458.
- [29] A. Bianco, G. Iardino, A. Manuelli, C. Bertarelli, G. Zerbi, *Chem Phys Chem.* 8 (2007) 510-514
- [30] J. S. Stephens, D. B. Chase, J. F. Rabolt, *Macromolecules* 37 (2004) 877-881.
- [31] Y. Liu, L. Qi, F. Guan, N. E. Hedin, L. Zhu, L.; H. Fong, *Macromolecules* 40 (2007) 6283-6290.
- [32] E. Zussman, N. Burman, A. L. Yarin, R. Khalfin, Y. Cohen, *J. Polym. Sci. Part B: Polym. Phys.* 44 (2006) 1482-1489.
- [33] U. Stachewicz, A. H. Barber, *Langmuir* 27 (2011) 3024-3029.
- [34] A. Milani, M. Casalegno, C. Castiglioni, G. Raos, *Macromol. Theory Simul.* 20 (2011) 305-319.

- [35] R. Dovesi, V. R. Saunders, C. Roetti, R. Orlando, C. M. Zicovich-Wilson, F. Pascale, B. Civalleri, K. Doll, N. M. Harrison, I. J. Bush, P. D'Arco, M. Llunell, CRYSTAL09 User's Manual. University of Torino, Torino, 2009.
- [36] R. Dovesi, R. Orlando, B. Civalleri, C. Roetti, V. R. Saunders, C. M. Zicovich-Wilson, F. Pascale, *Zeit. Kristallogr.* 220 (2005) 571-573.
- [37] A. D. Becke, *J. Chem. Phys.* 98 (1993) 5648-5652.
- [38] C. Lee, W. Yang, R. G. Parr, *Phys. Rev. B* 37 (1988) 785-789.
- [39] C. W. Bunn, E. V. Garner, *Proc. Roy Soc.* 39 (1947) 39-68
- [40] A. Bondi, *J. Phys. Chem.* 68 (1964) 441-451.
- [41] R. Scott Rowland, R. Taylor, *J. Phys. Chem.* 100 (1996) 7384-7391.
- [42] T. Itho, *Jpn. J. Appl. Phys.* 15 (1976) 2295-2306.
- [43] H. Arimoto, *J. Polym Sci Part A 2* (1964) 2283
- [44] N. S. Murthy, R. Bray, S. Curran, M. McDonald, in: J. P. Sibilio (Ed.) *A Guide to Material Characterization and Analysis*, VCH, New York, 1994, pp. 84.
- [45] N. Vasanthan, D. R. Salem, *J. Polym. Sci. B: Polym. Phys.* 38 (2000) 516-52.
- [46] N. Vasanthan, D. R. Salem, *Mat. Res. Innovat.* 38 (2001) 155-160.
- [47] J. L. Koenig, M. Itoga, *J. Macromol. Sci. Phys. B* 6 (1972) 309.
- [48] J. L. Koenig, M. C. Agboatwalla, *J. Macromol. Sci. Phys. B* 2 (1968) 391
- [49] J. Jakes, S. Krimm, *Spectrochim. Acta A* 27 (1971) 19
- [50] L. Quintanilla, J. C. Rodriguez-Cabello, J. M. Pastor, *Polymer* 35 (1994) 2321-2328.
- [51] S. J. Cooper, E. D. T. Atkins, M. J. Hill, *Macromolecules* 31 (1998) 5032-5042.
- [52] S. J. Cooper, E. D. T. Atkins, M. J. Hill, *J. Polym. Sci. B: Polym. Phys. Edn.* 36 (1998) 2849-2863.
- [53] S. J. Cooper, E. D. T. Atkins M. J. Hill, *Macromolecules* 31 (1998) 8947-8956.
- [54] D. Garcia, H. W. Starkweather, *J. Polym. Sci.: Polym. Phys. Edn.* 23 (1985) 537.
- [55] S. J. Cooper, M. Coogan, N. Everall, I. Priestnall, *Polymer* 42 (2001) 10119-10132.
- [56] E. M. Murty, T. W. Yehl, *Polym. Eng. Sci.* 30 (1990) 1595.
- [57] G. C. Pimentel, A. L. McClellan, *The hydrogen bond*, W.H. Freeman, S. Francisco, 1960.
- [58] G. Heidemann, H. Zahn, *Makromol. Chem.* 62 (1963) 123.
- [59] I. Matsubara, J. H. Magill, *Polymer* , 7 (1966) 199-215.
- [60] C. G. Zimba, J. F. Rabolt, A. D. English, *Macromolecules* 22 (1989) 2863-2867.
- [61] C. G. Cannon, *Spectrochim. Acta* 16 (1960) 302-319.
- [62] A. Anton, *J. Appl. Polym. Sci.* 12 (1968) 2117.
- [63] H. W. Starkweather, R. E. Moynihan, *J. Polym. Sci.* 19 (1956) 363.

- [64] A. Miyake, *J. Polym. Sci.* 44 (1963) 223.
- [65] A. Milani, C. Castiglioni, L. Brambilla, G. Zerbi, *J. Mol. Struct.* 1009 (2012) 130-140.
- [66] D. C. McKean, *Chem. Soc. Rev.* 7 (1978) 399.
- [67] M. Gussoni, C. Castiglioni, G. Zerbi, G. in: J. Chalmers, P. Griffiths (Ed.), *Handbook of Vibrational Spectroscopy*, John Wiley & Sons, Chichester, 2001.
- [68] A. Milani, C. Castiglioni, *J. Phys. Chem. A* 114 (2010) 624-632.
- [69] A. Milani, D. Galimberti, C. Castiglioni, G. Zerbi, *J. Mol. Struct.* 976 (2010) 342-349.
- [70] A. Milani, M. Tommasini, C. Castiglioni, *Theor. Chem. Acc.* 131 (2012) 1139.

3.3.2 attachment d

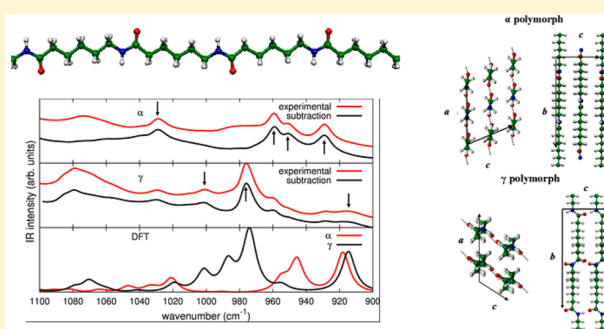
Ab Initio Calculation of the Crystalline Structure and IR Spectrum of Polymers: Nylon 6 Polymorphs

Claudio Quarti,[†] Alberto Milani,^{*†} Bartolomeo Civalleri,[‡] Roberto Orlando,[‡] and Chiara Castiglioni[†][†]Dipartimento di Chimica, Materiali e Ingegneria Chimica "G. Natta", Politecnico di Milano, Piazza Leonardo da Vinci 32, I-20133 Milano, Italy[‡]Dipartimento di Chimica e Centro di Eccellenza NIS, Università di Torino, Via P. Giuria 7, I-10125 Torino, Italy

Supporting Information

ABSTRACT: State-of-the-art computational methods in solid-state chemistry were applied to predict the structural and spectroscopic properties of the α and γ crystalline polymorphs of nylon 6. Density functional theory calculations augmented with an empirical dispersion correction (DFT-D) were used for the optimization of the two different crystal structures and of the isolated chains, characterized by a different regular conformation and described as one-dimensional infinite chains. The structural parameters of both crystalline polymorphs were correctly predicted, and new insight into the interplay of conformational effects, hydrogen bonding, and van der Waals interactions in affecting the properties of the crystal structures of polyamides was obtained.

The calculated infrared spectra were compared to experimental data; based on computed vibrational eigenvectors, assignment of the infrared absorptions of the two nylon 6 polymorphs was carried out and critically analyzed in light of previous investigations. On the basis of a comparison of the computed and experimental IR spectra, a set of marker bands was identified and proposed as a tool for detecting and quantifying the presence of a given polymorph in a real sample: several marker bands employed in the past were confirmed, whereas some of the previous assignments are criticized. In addition, some new marker bands are proposed. The results obtained demonstrate that accurate computational techniques are now affordable for polymers characterization, opening the way to several applications of ab initio modeling to the study of many families of polymeric materials.



I. INTRODUCTION

Polyamides, commonly known by the commercial name nylon, are well-recognized polymeric materials, because of their wide occurrence in everyday life. Despite their well-assessed applications, scientific and technological research on this class of polymers is far from having reached a plateau: The development of nanocomposites based on nylons,¹ the application of new techniques of production such as electrospinning,² and even the application of polyamides in the field of biomaterials and nanomedicine are currently active and promising fields of investigation.

From a more basic, physicochemical point of view, the development of structure/property relationships based on a molecular approach and the understanding of the origin of the polymorphism that arises in several semicrystalline polyamides are currently being deeply investigated both experimentally^{2f,3} and theoretically;⁴ in particular, thanks to the development of molecular simulations and related computational techniques, ab initio theoretical modeling can be exploited to this aim.

Polymorphism is one of the key features ruling, at the nanoscale, the properties of polyamides; however, despite its importance, the control and experimental recognition of the crystalline structure of nylons are issues that have not been

completely solved. The existence of metastable phases, the peculiar behavior observed upon thermal or mechanical stresses, the phenomena ruling the stability of one phase or another, and the understanding of phase transitions from a molecular perspective are just a few topics about which many questions are still unanswered. The complexity of this matter arises from the peculiar balance between intra- and intermolecular interactions taking place in these systems. For instance, in the case of single-numbered nylons (nylon n , where n is even), the stability of the α crystalline form with respect to the γ form depends on the length of the monomer chain (i.e., on the number of $-\text{CH}_2-$ units). Indeed, the balance between intermolecular H-bonding and van der Waals (vdW) interactions among $-\text{CH}_2-$ units belonging to adjacent chains in the crystal determines the predominance of one form or the other.^{4a} In particular, the α form is more stable for $n \leq 6$, whereas the γ form is more stable for $n \geq 8$. The case of nylon 6 (NY6) is most peculiar because it presents both crystal forms, often occurring simultaneously in the same sample, because of

Received: April 18, 2012

Revised: May 29, 2012

Published: June 14, 2012

the small difference in energy between them, with the α form being more stable. In addition, this polymer can easily undergo a phase transition from the α to the γ form as a result of external stimuli or processing.^{2b,3e,i,5}

Because the setting of a given crystal structure implies peculiar trends of the macroscopic properties (e.g., melting temperatures, densities, mechanical properties), a careful determination of the crystal structure is mandatory and has been widely carried out by means of X-ray diffraction and IR spectroscopy.^{2b,3i,5,6}

In parallel, calculations based on molecular dynamics^{4a,7} have been used to investigate the structural properties of nylons, together with quantum chemical simulations carried out on feasible small molecular models.^{4b} However, because of the limited computational resources and the lack of standard codes, any accurate quantum chemical calculations of infinite polymer chains and their crystal structures were unaffordable in the past. Even if a very good computational description of the molecular structure could be obtained by means of classical molecular dynamics,⁷ these methods do not allow the prediction of reliable vibrational spectra. On the other hand, *ab initio* molecular dynamics techniques can, in principle, give a very good description of the vibrational force field and spectra of quite large molecular systems, provided that the simulations are long enough for reliable statistics to be obtained. Anharmonic effects can be automatically included in these calculations, but on the other hand, a description of the vibrational properties in terms of normal modes is not straightforward. Recently, these methods have been applied successfully to different molecular systems,⁸ but they have not found application yet in the case of polymeric materials, which are still too computationally expensive. So far, indeed, very few works have been published on the computational vibrational spectroscopy of polyamides, and they were all based on semiempirical force fields.⁹

Because of this lack, the characterization of nylons by means of vibrational spectroscopy has always relied on band assignments based on purely experimental works.^{5,6,9} The diagnostic tools so developed are now routinely used for the spectroscopic characterization of new systems such as nanocomposites or electrospun nanofibers as well. Unfortunately, the reliability of these assignments has not been confirmed through accurate molecular modeling.

In this article, we present a computational study based on density functional theory (DFT) calculations of the IR spectra of the α and γ crystalline forms of NY6 using state-of-the-art computational techniques in solid-state chemistry. Indeed, in the current implementation of the CRYSTAL09 code,¹⁰ accurate simulation of the vibrational properties of crystalline molecular materials is possible, explicitly taking into account the space group symmetry of the systems. In the case of polymeric materials, accurate calculations using this code have recently been presented and applied with success to the case of a single chain of syndiotactic polystyrene,¹¹ polyglycine,¹² and a few polyconjugated polymers.¹³ To our knowledge, however, no other application of this code to the study of polymer materials has been presented so far.

The work is organized as follows: In section III.1, the DFT-computed equilibrium structures of the two α and γ crystalline forms of NY6 are compared with experimental determinations, focusing in particular on the importance of van der Waals interactions and the effects of their correction by means of Grimme's procedure. The structural results obtained were then used in the simulation of the IR spectra described in section

III.2. The interpretation of the IR spectra and the assignment of the spectroscopic markers of α and γ polymorphs of NY6 are reported in section IV.

II. COMPUTATIONAL AND EXPERIMENTAL DETAILS

Full geometry optimization of the crystal structures and calculation of the IR spectra of the α and γ polymorphs of NY6 were carried out by means of the CRYSTAL09 code¹⁰ within the framework of density functional theory (DFT). We employed the B3LYP¹⁴ hybrid exchange-correlation functional together with the 6-31G(d,p) basis set. (The dimensions of the basis set are reported in the Supporting Information, together with the atoms and fractional coordinates of the asymmetric unit of the optimized structures.)

All B3LYP calculations included the empirical correction for dispersion interactions proposed by Grimme¹⁵ and implemented in CRYSTAL09. Three different sets of empirical parameters were used and compared because it has been demonstrated in previous works¹⁶ that the results could be significantly affected by different choices. The numerical values of the parameters finally chosen in this work are reported in Table 1. Further details and comments about this choice are reported in the Supporting Information.

Table 1. Summary of the C_6 and R_{vdW} Parameters Employed in the Present Work for the Grimme Correction^{15,α,β}

atom	C_6^{15} (J nm ⁶ mol ⁻¹)	R_{vdW} (Å)
H	0.14	1.3013 ¹⁶
C	1.75	1.70 ¹⁷
O	0.70	1.52 ¹⁷
N	1.23	1.55 ¹⁷

^αCutoff distance of 25.0 Å used to truncate direct lattice summation.

^βStandard values of $d = 20$ and $s_6 = 1.00$ used.¹⁶

In all calculations, the atomic positions and the lattice parameters were fully optimized; default optimization algorithms and convergence criteria were employed.^{10a}

As starting guess structures for the calculations, we considered the experimentally determined crystal parameters and atomic coordinates reported by Holmes et al.^{18a} and Simon et al.^{18b} for the α form ($P2_1$ space group) and by Arimoto et al. for the γ form ($P2_1/a$).¹⁹ To detect the spectroscopic markers of regularity/crystallinity,²⁰ we carried out geometry optimizations and frequency calculation on the infinite polymer chain characterized by a regular conformation (one-dimensional model chain), taking as starting structures the two different conformations shown by the chains in the two polymorphs: The " α -type" chain belongs to $P2_1am$ line group and is characterized by a transplanar structure, whereas the " γ -type" chain belongs to the $P2_111$ line group and shows a nonplanar arrangement of the backbone atoms, determined by the skew conformation of the CH₂ units adjacent to the amide group.

The two crystal structures, showing the two different conformations of the polymer chains, are sketched in Figure 1.

Calculations of normal frequencies (at the Γ point) were carried out on the optimized geometries as obtained by diagonalization of the (numerically calculated) Hessian matrix.

Vibrational frequencies and eigenvectors obtained for the one-dimensional model chains were used for the interpretation of the normal modes of vibration observed in the crystal, according to a "projection" procedure reported in section IV.

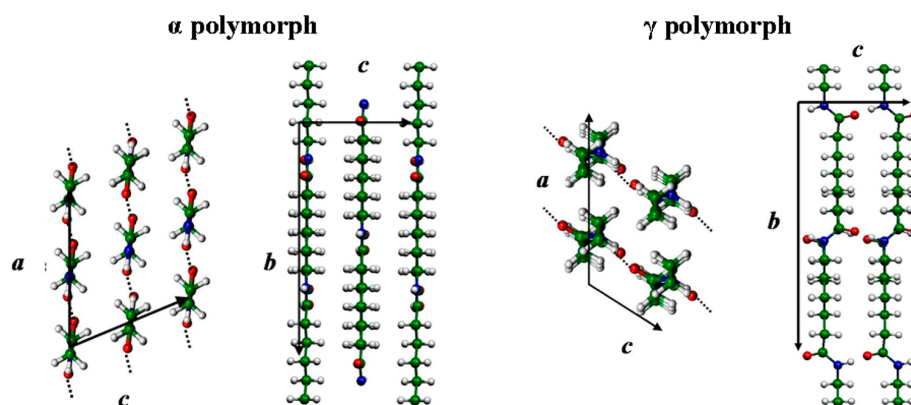


Figure 1. Sketches of the crystalline structures of the α and γ polymorphs of NY6. Carbon atoms are in green; hydrogen atoms, white; oxygen atoms, red; and nitrogen atoms, blue.

To compare the computed and experimental data, the calculated frequencies were scaled by 0.9614²¹ in the frequency range of 4000–1100 cm^{-1} and by 0.975 below 1100 cm^{-1} . Different scaling factors were used here to obtain the best fit between the experimental and computed IR spectra.

The DFT-D-computed spectra were compared with experimental IR spectra of two different NY6 samples showing large excess contents of the α and γ crystalline polymorphs and with an amorphous sample.²² Samples of α crystals with a thickness suitable for IR analysis were prepared starting from formic acid solution of NY6 and coating a film by means of the Doctor Blade technique. Samples of the γ form were prepared following the procedure previously reported in the literature.^{3i,22,23} IR spectra were recorded using an FT-IR Nicolet Nexus Spectrometer (resolution 1 cm^{-1} , 128 scans). Amorphous samples were obtained by rapid quenching of the melt in liquid nitrogen. All experimental spectra reported showed good agreement with the experimental spectra previously published in the literature and can be used for a reliable validation and discussion of the DFT-D-predicted spectra. In the case of the γ form, the IR spectra show very weak bands, which can be associated to the presence of slight impurities of the α form. Anyway, their content is very limited and does not affect the comparison with the predicted spectra.

III. RESULTS

III.1. Prediction of the Crystal Structures. The correct prediction of the crystal structure and of the cohesive energy of NY6 polymorphs is a computationally difficult task. As already mentioned, the intermolecular properties of single-numbered nylons are ruled by the interplay between hydrogen-bonding and vdW interactions among $>\text{CH}_2$ groups, stabilizing the α or the γ crystalline form depending on the length of the monomer chain. The computational description of these interactions is currently one of the weaknesses of the DFT method in the case of small molecules as well, but it can be corrected by the empirical procedure proposed by Grimme,¹⁵ employed herein. Furthermore, the computational difficulties parallel the experimental problems related to the existence (or coexistence) of other polymorphs in addition to the α and γ phases and of the unavoidable presence of the amorphous phase, as always occurs for any semicrystalline polymer. These facts add further uncertainties in the interpretation of experimental measures, as documented by the wide debate on the crystalline structures of NY6 that took place in the past literature.^{5,6}

In this work, we restrict ourselves to the modeling of the structures of the two main (α and γ) crystalline forms of NY6, by comparing them to the experimental structures reported by Holmes et al. and Simon and Argay¹⁸ and by Arimoto et al.¹⁹ these structures are indeed referred to by most of the scientific articles dealing with NY6.

In Table 2, we report a comparison between the experimental cell parameters and those computed using the

Table 2. Experimental^{18,19} and DFT-D-Computed Cell Parameters for α and γ Forms of NY6

	α polymorph ($P2_1$)		γ polymorph ($P2_1/a$)	
	expt ¹⁸	DFT-D	expt ¹⁹	DFT-D
a (Å)	9.56	9.57	9.33	8.99
b (Å)	17.24	17.48	16.88	16.85
c (Å)	8.01	7.53	4.78	4.75
β (deg)	67.5	68.64	121.0	123.3

set of parameters for the Grimme correction reported in Table 1. A complete discussion of the results obtained using other different sets of parameters is provided in the Supporting Information.

Considering first the results for the α form, good predictions were found for the β angle and b parameter (chain axis direction), consistent with the fact that the latter cell parameter depends on the good computational description of the intramolecular degrees of freedom. The a parameter is related to the packing between neighboring hydrogen-bonded chains forming a sheet (see Figure 1). Very good agreement with experimental data was obtained in this case as well, indicating that hydrogen-bonding effects are described properly by the computational method employed. The largest discrepancy with the experimental data was found for the c parameter, related to the packing of “sheets” (formed by H-bonded chains) interacting through vdW forces: The set of parameters employed (Table 1) was the one giving the best agreement (see the Supporting Information), even though a non-negligible difference from the experimental determination was still present. For the γ form, a very similar situation was found: The b parameter (chain axis), the β angle, and the c parameter (H-bonded chains in pleated sheets) were described accurately, and a good description was obtained for the a parameter (stacking of sheets through vdW interactions), even though a

non-negligible difference was still found with respect to the experimental value.

However, on one hand, in the case of molecular solids, thermal effects can have a non-negligible role in modulating this cell parameter,²⁴ and a comparison with the result of a complete cell optimization by means of *ab initio* calculations should be undertaken with care because no thermal effects are included in the latter. On the other hand, the slight underestimation can be due to a basis set incompleteness that causes a spurious extra-binding due to basis set superposition error (BSSE) that adds to the genuine attractive dispersion correction. The employed set of parameters, in particular the use of Bondi's van der Waals radii, probably leads to an error cancellation between the two contributions that provides the best prediction of the lattice parameters (see the Supporting Information).

One can thus conclude that a reasonably good description of the crystal structure of NY6 polymorphs can be obtained by using the selected parameters employed for the Grimme correction (see Table 1), justifying their use also for the computation of the IR spectra of the two polymorphs.

A very important feature for the comprehension of the polymorphism in NY6 is the relative stability of one crystalline form with respect to the other. To date, very few works based on molecular mechanics⁷ or quantum chemical calculations applied to small molecular models^{4b} have been used for this purpose, and the general conclusion was that the α form is more stable than the γ form, showing an energy difference of 0.5–1.5 kcal/mol per monomer unit, depending on the computational method employed. Because in the present work our aim is a detailed description and discussion of structure and vibrational features of the two polymorphs, a complete investigation of the energetics behind nylon's polymorphism is planned for the near future. We just briefly summarize some preliminary results here.

It is interesting to compare the energy differences between the two isolated polymer chains (one-dimensional model chains), exhibiting conformations very similar to those observed when forming the crystal, to determine the contribution of the conformational potential energy for the two different chains. Grimme's correction has also been used in this case to guarantee the best description of the interactions between nonbonded atoms, playing a significant role in determining the shape of the torsional potential surface.

If one uses the molecular structure of a single polymer chain "extracted" from the experimental crystal structures as a guess geometry and carries out a complete geometry optimization (no constraints except for the choice of symmetry rod group, which does not affect the final value of the torsional angles), the two starting conformations are kept (except for an expected and small geometry relaxation). This is a first very interesting result: it suggests that the two chain conformations characteristic of the α and γ forms are not driven by the intermolecular interactions but also satisfy equilibrium requirements for the isolated chain (i.e., they correspond to minima of the torsional potential energy surface of the single polymer chain). The energy difference between the two conformations of the isolated chains (normalized on the monomer units) demonstrates that the γ -type conformation is slightly more stable (1.073 kcal/mol) than the α -type conformation whereas, in the crystals, the two polymorphs are practically isoenergetic (energy difference of 0.045 kcal/mol per monomer unit). On the other hand, the α form is slightly more stable (up to a

maximum of 1.5 kcal/mol per monomer unit) if other sets of parameters for Grimme's correction are used (see Table S3 of the Supporting Information). These preliminary and qualitative results are particularly interesting because they show how polymorphism in nylon 6 results from a subtle balance of both intra- and intermolecular interactions, requiring an accurate computational description of both of these types of interactions.

III.2. IR Spectra of NY6 Polymorphs. In this section, the IR spectra obtained by DFT-D calculations are presented and compared to the experimental spectra of the two polymorphs. In Figure 2, the computed and experimental spectra for the two

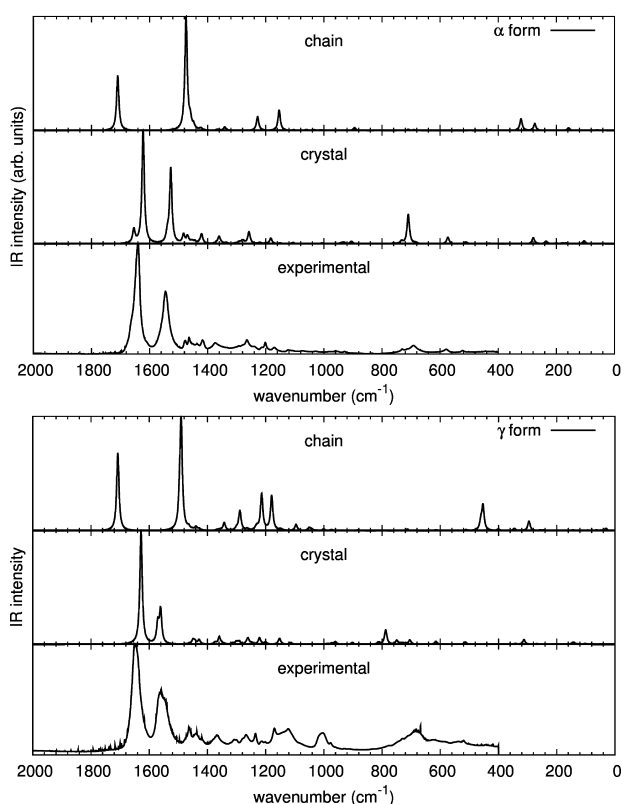


Figure 2. Comparison between experimental and DFT-D-computed IR spectra (crystal and single-chain model) for α (top) and γ (bottom) polymorphs of NY6 in the frequency range below 2000 cm^{-1} (scaling factor of 0.9614 for the whole range of frequencies).

polymorphs are shown in the range below 2000 cm^{-1} ; in the same figure, IR spectra calculated for the two isolated chains, characterized by the regular conformations of the α and γ forms, are also reported for comparison. The general pattern of the experimental spectra, dominated by the so-called amide I and amide II bands in the range between 1700 and 1500 cm^{-1} , is well reproduced by DFT-D predictions on crystals. Moreover, as expected, it is immediately clear that calculations on the isolated chains are inadequate even to give a qualitative prediction of the most relevant spectral features.

Below 1500 cm^{-1} , the experimental spectra show several weaker transitions that were found to be very sensitive to the polymorph structure: These IR bands have been indeed proposed in the past as spectroscopic markers to recognize the presence of the different crystalline forms in real samples (see a list of the experimental frequencies of the most widely

used markers, proposed or employed by several authors, in Table 3).

Table 3. Frequencies of the Most Important Experimentally Determined IR Marker Bands of the α and γ Polymorphs of NY6 Previously Proposed in the Literature^{3i,5,6}

	frequencies (cm ⁻¹)
α form	930, 950, 960, 1030, 1200
γ form	915, 970, 1002
amorphous	985, 1124
reference	1170, 1630

In the following sections (see Figures 3 and 4), a detailed discussion of the marker bands is carried out focusing on each

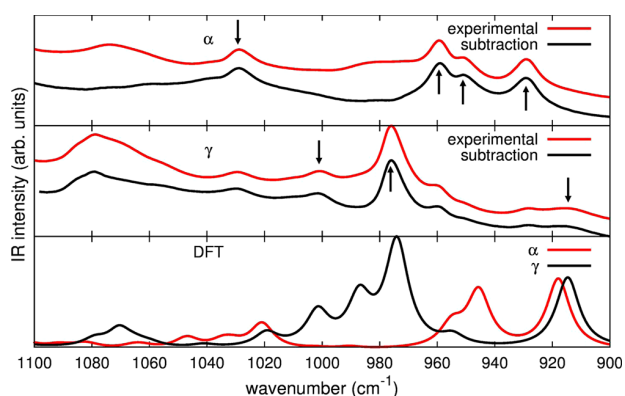


Figure 3. Comparison between experimental and DFT-D-computed IR spectra for α and γ polymorphs of NY6 in the wavenumber range 1100–900 cm⁻¹ (scaling factor = 0.975). For the experimental spectra, the spectra obtained upon subtraction of the spectrum of an amorphous sample are also reported.

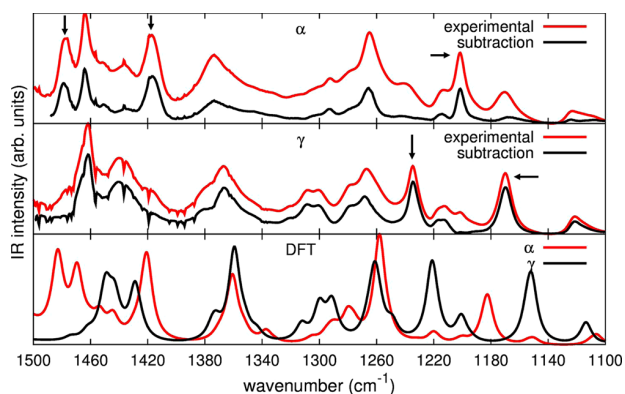


Figure 4. Comparison between experimental and DFT-D-computed IR spectra for α and γ polymorphs of NY6 in the frequency range 1500–1100 cm⁻¹ (scaling factor = 0.9614). For the experimental spectra, the spectra obtained upon subtraction of the spectrum of an amorphous sample are also reported.

specific spectral region, where transitions sensitive to the crystal structure of NY6 occur. (In the Supporting Information, similar figures are reported comparing experimental spectra with DFT-computed spectra obtained using different sets of parameters for Grimme's correction.) To ease the comparison between calculations and experiments, a suitable scaling factor was employed for each spectral range; for the same reason, in the

text, we refer to calculated peak frequencies, reporting values after scaling.

900–1100 cm⁻¹ Frequency Range. In Figure 3, we report a comparison between experimental and DFT-D-computed spectra for the α and γ polymorphs in the 900–1100 cm⁻¹ range. This is probably the most important range because of the presence of very popular marker bands of the two polymorphs.

Indeed, according to Table 3, there are three strong marker bands for the α form at 930, 960, and 1030 cm⁻¹ and two marker bands for the γ form at about 970 and 1000 cm⁻¹. Minor markers are the bands at 950 and 915 cm⁻¹ for the α and γ forms, respectively.

By inspection of Figure 3, one can verify that DFT-D-computed spectra show a good agreement with the experimental ones: In particular, calculations confirm that the previously reported bands are all characteristic markers of the α and γ polymorphs of NY6.

Despite the general agreement between theory and experiments, there are several discrepancies in the description of some details: In the case of the α crystal, the predicted intensity ratios between the three bands at 930, 950, and 960 cm⁻¹ do not exactly parallel the experimental ones. It should be noted that the experimental spectrum is affected by the presence of non-negligible contributions from the amorphous phase, which is indeed responsible for a broad band peaked at about 985 cm⁻¹. To obtain spectra free from the amorphous contribution, a spectral subtraction of this contribution was carried out (Figure 3) to determine whether the intensities of the two bands, in particular the 960 cm⁻¹ band, could be affected. No changes were observed, and thus one can conclude that DFT-D calculations are not sufficiently accurate in this case to satisfactorily reproduce the experimental intensities and intensity ratio of the two bands.

A similar situation was found in the case of the IR spectra of the γ form (Figure 3): A good description was obtained for the bands at 970 and 1000 cm⁻¹, but an additional absorption feature was calculated between these two features. This extra transition probably falls under the main band (occurring at 970 cm⁻¹ in the experimental spectrum) or shows a negligible intensity in the experiment, whereas its relative position and/or intensity are differently predicted by DFT-D calculations. It should be noted that the calculations correctly predict the existence of a third band (experimental frequency = 915 cm⁻¹), although it is again too intense with respect to the experimental (broad) band.

Despite the discrepancies underlined above, the overall agreement between the experimental and DFT-D-computed spectra is good and confirms the assignments (reported in Table 3), based on purely experimental investigations. In particular, the selectivity of this spectral region for the recognition of the two different crystalline polymorphs is well reproduced by calculations.

1100–1500 cm⁻¹ Frequency Range. In Figure 4, we report a comparison between the experimental and DFT-D-computed IR spectra in the frequency range of 1100–1500 cm⁻¹.

Vasanthan and co-workers^{5c,6f} proposed the band at 1200 cm⁻¹ as a marker of the α form, whereas no other marker bands of NY6 polymorphs have been discussed in this range so far. Based on the experimental spectra reported in Figure 4, one can see that the band falling at 1170 cm⁻¹ (usually taken as a reference band^{5c,e}) is predominant for the γ form, and a similar behavior was observed for the band at 1234 cm⁻¹. On this basis, we suggest that these two bands be considered as additional

markers of the γ polymorph. Moreover, in the case of the α form, in addition to the 1200 cm^{-1} absorption, two strong bands falling at 1416 and 1478 cm^{-1} were distinctly observed and can be thus proposed as further marker bands.

Considering DFT-D-computed spectra, the agreement with the experimental spectra was very good also in minor details. Considering first the γ form, we confirm that the experimental band at 1170 cm^{-1} (predicted at lower frequency by the calculations, i.e., 1152 cm^{-1}) is indeed a marker of this form. This finding allows us to solve one of the discrepancies found in the literature: Indeed, the 1170 cm^{-1} band was taken by some authors as a marker of the amorphous phase, whereas Vasanthan and Salem^{5c,e} demonstrated that this band was somehow dependent on the crystal morphology of the system and proposed it as a reference band. Our results further suggest that the 1170 cm^{-1} band can indeed be associated with the γ polymorph. Also, in the case of the band at 1234 cm^{-1} , the calculations (predicted band frequency at 1222 cm^{-1}) support its assignment to the γ form: To our knowledge, this band has not yet been proposed as a marker of the γ form. Moreover, computed data predict a further marker for this form at about 1380 cm^{-1} , where a band is clearly detected. However, in this range, the experimental spectra are quite broad and structureless, and thus, this marker band seems to be unsuitable for practical applications.

Considering the α form, DFT-D calculations confirm again that the band at 1200 cm^{-1} is a marker band of this polymorph; moreover, calculations indicate that the two bands at 1416 and 1478 cm^{-1} are additional markers of α form, although they have not been used for practical purposes. In addition to the main features described above, the calculations also reproduce minor details quite well, such as the pattern of bands observed between 1400 and 1500 cm^{-1} for both forms or the pattern observed at about 1300 cm^{-1} for the γ form.

Other Spectral Regions. In the previous section, the most relevant spectral regions for the application of IR spectroscopy to the characterization of materials based on NY6 were analyzed. In this section, we briefly discuss other different frequency ranges, where some additional information can be obtained. All of the related figures can be found in the Supporting Information.

Between 1500 and 1800 cm^{-1} (upper panel of Figure S7, Supporting Information), the most intense vibrations of polyamides can be found, namely, the amide I and amide II bands. The relative positions observed in the experimental spectra for the two bands were reproduced correctly by DFT-D calculations. In particular, the amide I band of the α form exhibited a lower frequency than the γ form, indicating that, in the former case, there is a more efficient hydrogen-bond network, characterized by stronger bonds.

Another feature directly related to hydrogen bonding is the NH stretching band falling at about 3300 cm^{-1} (see the lower panel of Figure S7, Supporting Information). Whereas the experimental spectra of the two polymorphs show very similar peak positions for these broad bands, DFT-D calculations predict a slightly lower frequency for the γ form, thus suggesting that stronger hydrogen bonds are present. This finding is in contrast with what is observed for the amide I band, in both the experimental and DFT-D-computed spectra. However, the fact that, considering the experimental spectra, no significant differences between the two polymorphs were found in the NH stretching region suggests that the trend given by the present calculations should be ascribed to some weaknesses of

the theoretical modeling, such as the influence of basis set superposition error or of the Grimme corrections in the description of hydrogen bonding. Furthermore, anharmonicities can have a non-negligible effect in this frequency range but were not taken into account in the present (harmonic) calculations.

Below 900 cm^{-1} , no important features were observed except for an intense and broad band at about 690 cm^{-1} for both forms (see Figure S8, Supporting Information). Also, in this range, DFT-D calculations reproduce the experimental pattern, and in particular, they describe well the weak bands occurring between 500 and 650 cm^{-1} . However, considering the intense absorption feature falling at about 690 cm^{-1} in both the experimental spectra, a too-large frequency splitting between the absorption peaks of the two crystalline forms is predicted by the calculations. To better clarify the origin of this discrepancy, further experimental investigations are required to clearly distinguish the contribution due to the amorphous domains in this frequency range.

Finally, in the CH stretching frequency region (Figure S9, Supporting Information), an overall agreement was found again with DFT-D calculations, despite the fact that anharmonic effects, overtones, Fermi resonances, and so on, usually significantly affect the spectral pattern. In particular, the two main broad bands of the γ form were found at lower frequencies than the two broad bands of the α form, as reproduced by DFT-D calculations. A qualitative interpretation of this fact can be proposed: It is indeed believed that, in the α form, the best geometrical arrangement for the hydrogen bonds is obtained at the expense of a less favorable packing of the $>\text{CH}_2$ groups of adjacent chains, whereas the opposite situation is found in the case of the γ form. The fact that the CH stretchings of the α form show higher frequencies can be ascribed to repulsive intermolecular interactions originating in the tight contact of nonbonded H atoms of the methylene units of adjacent chains. By comparing the calculated IR spectra of the crystals with those of the single chains, we verify in section IV that this behavior is indeed uniquely related to the intermolecular interactions between closely packed chains in the crystal.

IV. DISCUSSION

An additional advantage of ab initio calculations of vibrational spectra relies on the possibility to associate with each frequency (i.e., eigenvalue) the related eigenvector describing the normal mode of vibration, to carry out a band assignment. In the case of polyamides, the vibrational assignment was derived in the past only on the basis of empirical correlations or considering the eigenvectors obtained through semiempirical calculations on small oligomers.^{8a,b}

In addition to the identification of characteristic group frequencies, the analysis of the computed vibrational eigenvectors allows information to be gathered on the dynamics of the system in terms of relevant intramolecular interactions and provides a tool to estimate the effect of the intermolecular interactions between different molecules. However, in the case under study, the eigenvector analysis carried out by means of a visual inspection of the Cartesian atom displacements associated with the vibrational modes of the crystal is rather difficult, because of the presence of more than one molecule per unit cell.

In this case, a useful technique for the analysis of eigenvectors is the comparison between the vibrational

Table 4. Correspondence between the Normal Modes Associated with the Main IR Transitions of the α Polymorph of NY6 and Normal Modes of the One-Dimensional Model Chain in α -Type Conformation^{a,b}

crystal			isolated chain (1D model chain)				crystal			isolated chain (1D model chain)			
Freq. (cm ⁻¹)	IR intens. (km/mol)	Symm. species	Freq. (cm ⁻¹)	IR intens. (km/mol)	Symm. species	Eigenvector	Freq. (cm ⁻¹)	IR intens. (km/mol)	Symm. species	Freq. (cm ⁻¹)	IR intens. (km/mol)	Symm. species	Eigenvector
918 (M) ^c	96 [24]	A	907	22	A ₁		1337	48 [12]	B	1316	2	B ₁	
946 (M)	70 [18]	B	931	1	B ₁		1361	274 [69]	A	1341	26	A ₁	
955 (M)	21[7]	B	948	3	B ₂					1352	0 (0.2)	A ₁	
1021 (M)	35 [9]	B	1009	0 (0.06)	B ₁		1421 (M)	326 [81]	B	1424	7	B ₁	
1106	42 [14]	A	1104	6	A ₁					1444	81[20]	A	1441
1182 (M)	179 [45]	A	1155	153	A ₁		1454	73[18]	B	1441	1	B ₁	
1185	45 [11]												
1258	462 [115]	A	1228	105	A ₁		1482	57 [14]	A	1479	13	A ₁	
1276	48[12]	A	1259	0	A ₂		1482	43 [11]	B	1479	5	B ₁	
1280	100[25]	A	1261	0 (0.5)	A ₁		1484	60 [15]					

^aFrequencies scaled by 0.9614 (above 1100 cm⁻¹) and 0.975 (below 1100 cm⁻¹). ^bIR intensity values normalized to the number of chains in the unit cell of the crystal in brackets. ^cMarker bands are indicated by (M).

modes calculated for the single, regular chain (one-dimensional model chain) and the vibrational modes of the crystal. In this way, it is possible to establish a correspondence between the latter and the former, which provides a description of the vibrational problem of the crystal on the basis of the vibrational modes of the isolated chain. Moreover, it allows the effects of the intermolecular interactions in terms of frequency shifts and IR intensity redistributions driven by the different vibrational couplings occurring in the single chain with respect to the crystal to be captured. Indeed, in the presence of strong intermolecular interactions, the description (in terms of atomic displacements) of the vibrational modes of the crystal can markedly deviate from that of any mode of the isolated chain. This behavior is often found in the case of NY6 and explains the impressive change of the spectral pattern when intermolecular interactions are taken into account.

The detailed analytical procedure followed to carry out this analysis is reported in the Supporting Information.

The method was applied to the analysis of the marker bands discussed in the previous sections: the correlation established between the normal modes of the crystal and those of the one-dimensional model chain is illustrated in Tables 4 and 5, where frequencies and IR intensities of selected transitions of the α and γ crystals are shown. The data here reported were extracted

from the output of the DFT-D calculations according to the following criteria:

- All IR transitions previously identified as markers (or potential markers) for the detection of the crystal polymorphs are reported.
- Strong IR features (even if not recognized as marker bands) in the characteristic range 1500–900 cm⁻¹ are included in the tables. In this case, a quite drastic threshold intensity value of 40 km/mol was defined, corresponding to about 10% of the strongest IR transition of the α form in this frequency range.
- For any given selected transition of the crystal, we report the computed (scaled) frequency and intensity of the corresponding (i.e., similar) IR transition of the isolated chain (one-dimensional model chain). This normal mode of the single chain is the one showing the higher similarity to the normal mode of the crystal considered (i.e., it shows the highest scores $s_{kt}^{(i)}$; see the Supporting Information). A sketch of the eigenvector (single-chain mode) is also reported, thus providing an indication useful for the vibrational assignment.

According to the symmetry rules dictated by the site symmetry, the vibrations of the crystal showing correspondence with vibrations of the one-dimensional model chain must obey the following symmetry relationships:

Table 5. Correspondence between the Normal Modes Associated with the Main IR Transitions of the γ Polymorph of NY6 and the Normal Modes of the One-Dimensional Model Chain in γ -Type Conformation^{a,b}

crystal			isolated chain (1D model chain)				crystal			isolated chain (1D model chain)			
Freq (cm ⁻¹)	IR intens. (km/mol)	Symm. species	Freq (cm ⁻¹)	IR intens. (km/mol)	Symm. species	eigenvector	Freq (cm ⁻¹)	IR intens. (km/mol)	Symm. species	Freq (cm ⁻¹)	IR intens. (km/mol)	Symm. species	eigenvector
915 (M) ^c	49 [25]	B _u	893	4	B		1291 1300	51 [26] 74 [37]	A _u	1288	89	A	
974 (M)	73 [37]	B _u	962	1	B					1291	12	A	
1002 (M)	23 [12]	B _u	996	1	B		1360	192 [96]	A _u	1342	39	A	
1113	48 [20]	A _u	1096	30	A					1354	4	A	
1152 (M)	121 [61]	B _u	1150	7	B		1429	116 [58]	B _u	1438	13	B	
1155	51 [26]	A _u	1142	1	A					1443	81 [41]	B _u	1444
1201	55 [28]	B _u	1197	3	B		1449	102 [61]	B _u	1465	11	B	
1222 (M)	153 [77]	A _u	1214	183	A								
1262	135 [68]	A _u	1229	14	A								

^aFrequencies scaled by 0.9614 and 0.975 above and below 1100 cm⁻¹, respectively. ^bIR intensity values normalized to the number of chains in the unit cell of the crystal in brackets. ^cMarker bands are indicated by (M).

- For the α form, the A and B modes can be obtained as mixing of A₁, A₂ and B₁, B₂ modes, respectively, of the α -type isolated chain.
- For the γ form, the A_u and B_u modes are obtained from A and B modes, respectively, of the γ -type chain.

Notice that, to make a correct comparison between IR band intensities obtained for crystals and one-dimensional model chains, the IR intensity values of the crystals must be divided by the number of chains in the unit cell (values in brackets in Tables 4 and 5).

IV.1. IR Spectra of Crystals and Isolated Chains. Before performing a detailed analysis of the data reported in Tables 4 and 5, it is instructive to compare the predicted IR features of the isolated chains and of crystals, reported in Figure 5. To carry out a correct comparison, the intensity relative to crystals must be normalized to the number of chains belonging to the crystal cell.

Considering the 1100–800 cm⁻¹ range, the most impressive effect due to the three-dimensional arrangement of the chains is a marked increase of the global intensity. In particular, in the case of the α form, the IR spectrum of the isolated chain presents just one strong infrared active band (at 907 cm⁻¹), whereas in the spectrum of the crystal, at least two strong features appear with comparable intensity. Interestingly, a frequency correlation seems to exist between the band of the one-dimensional model chain at 907 cm⁻¹ and the lower-frequency band of the crystal (918 cm⁻¹), which moreover

shows a very similar intensity. The situation is even more dramatic for the γ form, where several relevant features appear in the crystal, whereas the single chain shows only two features (at 1056 and 1096 cm⁻¹) of medium intensity.

In the range of 1500–1100 cm⁻¹, neglecting the strong amide II transition that appears between 1400 and 1500 cm⁻¹ for the isolated chains and is affected by a marked blue shift in the crystal (see Figure 2) due to the occurrence of H bonding, it is very difficult to establish a correspondence between the IR bands of the crystals and those of the isolated chains. It seems that, in this range, the global intensity is only slightly enhanced by the crystal packing, but it is redistributed over a larger number of vibrational modes, giving rise to very structured spectra.

The data reported in Tables 4 and 5 are useful to rationalize these trends.

By considering the sketches of the eigenvectors of the single isolated chains (last column of Tables 4 and 5), all of the vibrational modes can be labeled as collective normal modes, because they involve cooperative angular deformations of all the CH₂ units and, in most cases, also contain a non-negligible contribution by bending of the amide groups. The “delocalization” of these modes over all of the chemical groups of the polymer chains does not allow a classification in terms of characteristic group vibrations. On the other hand, this clearly explains why the spectral ranges considered are so sensitive both to the chain conformation and to the crystal packing: It is

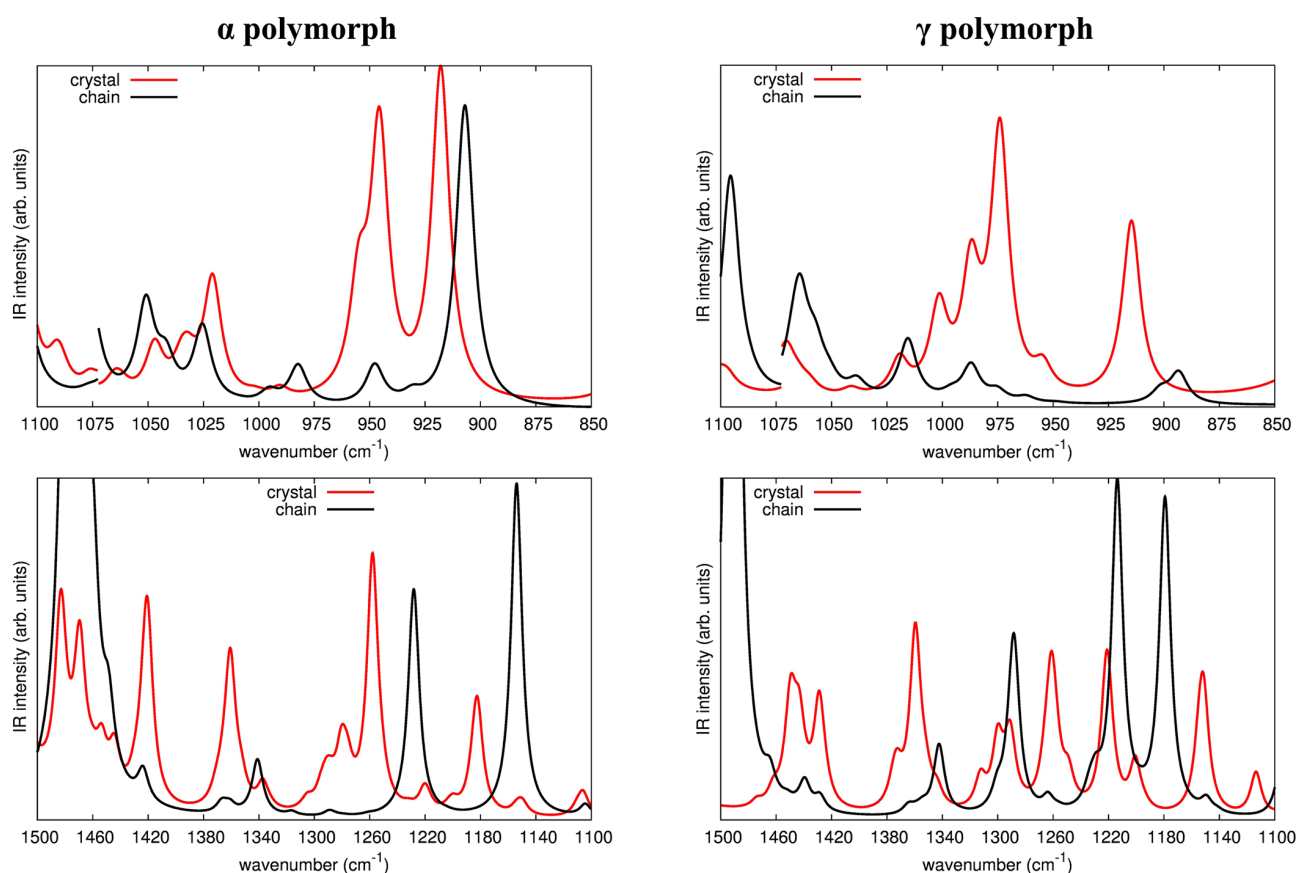


Figure 5. Comparison between DFT-D-computed IR spectra of the crystal and one-dimensional model chain of the α (left) and γ (right) polymorphs of NY6 in the frequency ranges 900–1100 cm^{-1} (frequency scaling factor = 0.975) and 1500–1100 cm^{-1} (frequency scaling factor = 0.9614). For a correct comparison, the intensities of the crystals were divided by the number of chains in the unit cell. The discontinuities at about 1075 cm^{-1} are due to the use of different scaling factors.

indeed well-known that frequencies of collective normal modes are usually strongly affected by the specific molecular shape, that is, by the architecture of the molecule as a whole.

Another remark can be made about the calculated frequencies of the crystal and the corresponding ones of the isolated chain: Frequencies of the two similar modes are quite close, and in most cases, the relative shifts do not exceed 20 cm^{-1} . Nevertheless, there is a remarkable remixing of the single-chain modes considering the vibrations of the crystal structures. This is especially true in the higher frequency range, where the analysis of the score values demonstrates that many vibrations of the crystal take comparable contributions (i.e., comparable score values) from many vibrations of the isolated chain.

Considering the IR intensity values reported in Tables 4 and 5, it can be seen that totally symmetric vibrations (i.e., modes invariant under the symmetry operation associated with the 2-fold screw axis) show a different behavior than vibrations belonging to the B species. Indeed, the transitions of the one-dimensional model chains associated with totally symmetric modes show the highest IR intensities, whereas those of B species are usually very weak. In the crystal, there is a general increase of the intensity associated with B-symmetry normal modes, which in several cases, show an intensity enhancement of about 1 order of magnitude with respect to the corresponding transition (similar normal mode) of the isolated chain. On the other hand, normal modes of A-symmetry species can show the following different behaviors:

- The IR intensity of the normal mode of the chain can be almost “transferred” to the similar mode of the crystal (consider, for instance, the modes of the α crystal at 918, 1258, and 1482 cm^{-1}).
- The IR intensity of the normal modes of the isolated chain can show a non-negligible decrease while going to the similar ones of the crystal; in this case, the intensity decrease seems to be compensated by an intensity enhancement of other normal modes of the crystal, just belonging to the A species. As an example, the 1182 and 1185 cm^{-1} bands of the α crystal show a total IR intensity of 56 km/mol (per chain) to be compared with the intensity (153 km/mol) of the similar mode of the single chain at 1155 cm^{-1} . This intensity depletion in the crystal is partially compensated by the occurrence of the 1280 cm^{-1} band (25 km/mol), correlated with a weakly IR-active A_1 mode of the single chain (0.5 km/mol) at 1261 cm^{-1} . This last feature can be simply ascribed to the effect of mode remixing occurring in the crystal, as confirmed by considering the whole set of scores obtained.

As a further support for the above conclusions, some summary data are reported in Table 6, where the intensity behavior of the infrared spectrum of one-dimensional model chains and crystals of NY6 (α and γ forms) is illustrated on the basis of global IR intensity values, obtained as sums of the

Table 6. Intensity Behavior of the Infrared Spectra of One-Dimensional Model Chains (Single Chains) and Crystals of NY6 in the α and γ Forms^{a,b}

α Form of NY6					
frequency range (cm ⁻¹)	modes selected	IR intensity (km/mol)			
		A		B	
		1-D (chain)	3-D (crystal) ^c	1-D (chain)	3-D (crystal) ^c
900–1150	most intense + markers	28	138 [35]	4	125 [31]
	all	45	181 [45]	12	169 [42]
1150–1550	most intense + markers	296	1247 [311]	17	1013 [253]
	all	402	1550 [388]	23	1240 [310]

γ Form of NY6					
frequency range (cm ⁻¹)	modes selected	IR intensity (km/mol)			
		A _u		B _u	
		1-D (chain)	3-D (crystal) ^c	1-D (chain)	3-D (crystal) ^c
900–1150	most intense + markers	30	48 [24]	6	145 [72]
	all	59	83 [41]	20	189 [95]
1150–1550	most intense + markers	341	657 [328]	34	475 [238]
	all	511	784 [392]	91	692 [346]

^aData refer to sum of the IR intensities of selected transitions belonging to given spectral ranges (see text for details). ^bContributions from normal modes of symmetry species A and B presented separately. ^cIR intensity values normalized to the number of chains in the unit cell of the crystal in brackets.

intensities of the selected transitions analyzed in Tables 4 and 5. In Table 6, contributions from normal modes of the symmetry species A and B are presented separately. It can immediately be realized that the total intensity associated with the totally symmetric vibrations of the single chain is practically kept unaltered in the crystal, whereas B modes undergo to a marked intensity enhancement in the crystal. To confirm that this peculiar behavior is related neither to the (quite arbitrary) selection of bands made in Tables 4 and 5 nor to the selection of the normal modes of the one-dimensional model chain (based on the similarity criterion), we show in Table 6 IR intensity data obtained by summing over the whole spectral ranges analyzed in Tables 4 and 5, without any preliminary selection of bands for crystals and one-dimensional model chains. These data confirm the trends already described, for both the α and γ polymorphs.

Accordingly, it seems quite clear that the strong intermolecular interactions arising from the formation of interchain H bonds selectively affect the IR intensity of normal vibrations transverse with respect to the chain axis (i.e., B normal modes), as expected because of the geometrical arrangement of the H bonds. An extended and deeper analysis based on internal and Cartesian intensity parameters²⁵ would be required to give further insights into this behavior.

IV.2. Classification of the Marker Bands: Crystallinity and Regularity Bands. Tables 4 and 5 demonstrate that most of the marker bands of both polymorphs are true markers of crystallinity: they are indeed associated with modes that show negligible intensities for the single one-dimensional models but gain intensity due to the interactions occurring in the crystal.

On the other hand, some bands (e.g., the bands at 918 and 1182 cm⁻¹ for the α form and those at 1113 and 1222 cm⁻¹ for the γ form, all of A species) show similar or even lower (normalized) intensities in the crystal than in the polymer chain. These bands can be considered specific markers of the presence of a regular chain having a transplanar α -type or a nonplanar γ -type conformation: On one hand, they are well correlated (frequency and intensity) with vibrations of the single chain, and on the other hand, they are not affected by the characteristic intensity enhancement associated with the formation of the H bonds between the chains. For this reason, we prefer to label the above IR absorptions as “regularity bands” instead of “crystallinity bands”. Notice that the experimental marker band of the α form at 930 cm⁻¹ (computed frequency of 918 cm⁻¹) found wide application in the literature for the characterization of NY6 polymorphism by means of IR spectroscopy, and its classification as a conformation-sensitive regularity band is particularly meaningful in this respect.

In Table 7, the full list of marker bands of NY6 crystal polymorphs (including the markers newly proposed in this work) is summarized.

Table 7. Classification of Marker Bands of NY6 Crystal Polymorphs

experimental frequency (cm ⁻¹)	ref(s)	DFT-D-computed frequency (scaled) (cm ⁻¹)	IR intensity (km/mol)	regularity/crystallinity assignment
α Form				
930	1b, 5, 6	918	96	regularity
950	Sb, e	946	70	crystallinity
960	Sa, e, b, 1b, 6e, 5f	955	21	crystallinity
1030	Se, 6e, 5f	1021	35	crystallinity
1200	Se	1182	179	regularity
1416		1421	326	crystallinity
1478		1483	157	crystallinity
γ Form				
915	Sa, 6e, 5f	915	49	crystallinity
970	1b, 5, 6a–d, f	974	73	crystallinity
1000	6e, 5f	1002	23	crystallinity
1170	Se	1152	121	crystallinity
1234		1222	153	regularity

IV.3. CH Stretching Region. Further insight into the role of intermolecular interactions in affecting the vibrational properties of NY6 can be obtained by comparing the IR spectra of the one-dimensional model chain and the crystal in the CH stretching region. In Figure 6, we report the computed IR spectra of the crystal and the single polymer chain for both polymorphs. The α -type and γ -type one-dimensional model chains have CH stretching bands in the same frequency range, whereas the situation is markedly different for the two crystals. This behavior was already outlined in the previous section concerning the experimental spectra, and it was attributed to the different extents of interactions between >CH₂ groups of adjacent chains in the two cases.

Figure 6 shows that, in the case of the γ form, the shape and intensity of the IR spectrum changes in going from the isolated chain to the crystal but, overall, there is not a significant frequency shift. On the contrary, in the case of the α crystal, a

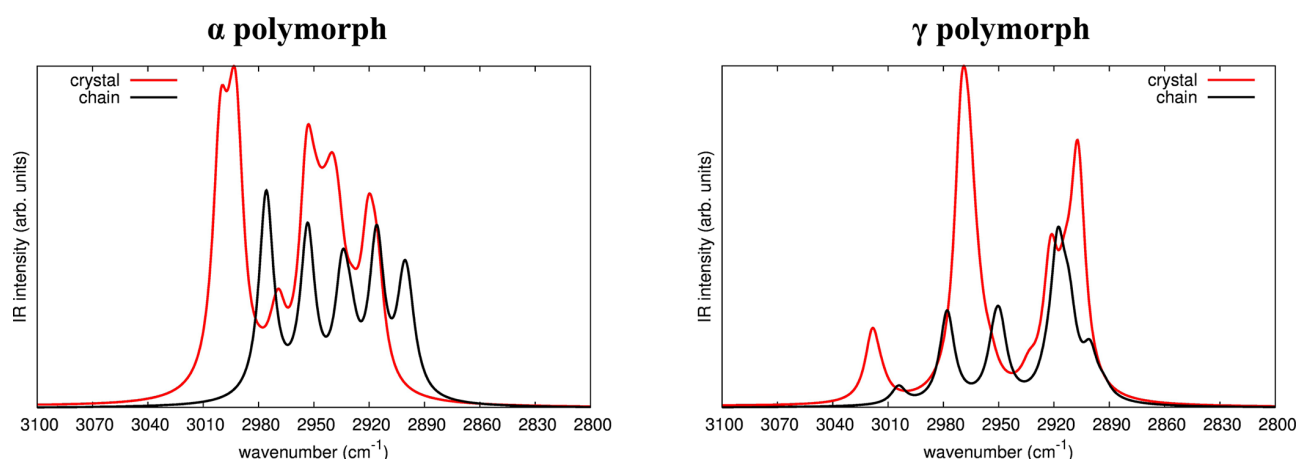


Figure 6. Comparison between DFT-D-computed IR spectra of the crystal and one-dimensional model chain of the α (left) and γ (right) polymorphs of NY6 in the frequency range 2800–3100 cm^{-1} (frequency scaling factor = 0.9614). For a correct comparison, the intensities of the crystal were divided by the number of chains in the unit cell.

non-negligible frequency blue shift of the main peak is observed with respect to the one-dimensional model chain, thus revealing a stronger intermolecular interaction between $>\text{CH}_2$ groups of the adjacent chains in this form.

V. CONCLUSIONS

The characterization of polymer structures and of their vibrational properties by means of high-level quantum chemical approaches is only at its early stages. Whereas molecular dynamics simulations and periodic first-principles calculation have been used to investigate the crystal structures of macromolecules, very few calculations have been carried out for the determination of the vibrational spectra of polymers, because of the fact that quantum chemical calculations are required for a reliable determination of the vibrational force field. So far, DFT or ab initio calculations have been carried out by taking into account small molecular models (i.e., short oligomers), according to the so-called “oligomer approach”.²⁶ Because of these limitations, the investigation of the vibrational properties of polymers and also the vibrational assignments of the IR spectra for practical and analytical purposes have been based so far only on purely experimental works or semi-empirical calculations, and a confirmation based on a reliable theoretical investigation is still lacking. Indeed, contrasting assignments, interpretations, and also some ambiguities are often present in the literature. Only recently, periodic ab initio calculations of IR spectra of polymers have been presented,^{10,12,27} thanks in particular to the new computational tools that have been implemented and that are now routinely available in a few packages.

In this work, we used CRYSTAL09 to carry out DFT-D calculations of the IR spectra of two nylon 6 polymorphs (α and γ forms). The CRYSTAL code is particularly powerful for this purpose because of the possibility of taking into account the full symmetry of the crystal, as required for a reliable band assignment and for the subsequent investigation of the polarization properties of the system. Furthermore, van der Waals interactions can be taken into account by including Grimme’s correction in DFT functionals.^{15,16} The use of a Gaussian basis set further allows a quantum description of the system that is more “molecule-based” than other approaches, such as the pseudopotential plane-wave method. A good

description of the crystalline structures was obtained for both the α and γ polymorphs of NY6, and the comparison between DFT-D-computed and experimental IR spectra of the two forms supports the reliability of the method. Some marker bands previously found from experimental investigations have been confirmed and assigned. Some other assignments have been revised on the basis of the comparison between the calculated spectrum of the crystal and that of the single chain. In particular, the widely used marker bands at 930 and 1200 cm^{-1} of the α form have been confirmed to be markers of a regular transplanar conformation, not necessarily related to the occurrence of a crystal packing. We found that the band at 1170 cm^{-1} , assigned ambiguously in the literature, is peculiar of the γ form. Moreover, we have proposed some new marker bands at 1416 and 1478 cm^{-1} for the α form and at 1234 cm^{-1} for the γ form.

The results obtained demonstrate that quantum chemical calculations of the IR spectra of polymers are now viable; they can be applied to a very wide range of problems and can open the way for new applications of the modeling. Indeed, in addition to the straightforward review of the experimental assignments of the vibrational spectra of many classes of polymer, they can provide answers to several open questions. In the case of nylons, the study of the relative stability of the α or γ forms with varying length of the monomer chemical unit, the characterization of other stable crystalline forms, and the determination of the crystalline structure of nylons that have not been precisely refined based on XRD experiments are just few examples where the state-of-the-art computational techniques exploited herein could make a significant contribution.

Furthermore, an increasingly deep insight into the molecular phenomena ruling the physicochemical and mechanical performances of polymer materials is expected to be the direct outcome of these computational methodologies. In particular, these approaches can support standard characterization techniques in the study of new polymeric system, such as nanocomposites, electrospun nanofibers, and nanostructured polymer materials currently being developed for a wide number of innovative applications in many different fields.

■ ASSOCIATED CONTENT

● Supporting Information

Additional computational details, tables, and discussion of the predictions of the crystal structure. Description of the procedure for eigenvector analysis. Figures reporting comparisons between experimental and DFT-D-computed IR spectra for both the α and γ polymorphs of nylon 6 in all of the different frequency ranges and different sets of parameters for Grimme's correction. Tables of DFT-D-computed frequencies and intensities of α/γ crystals and α -type/ γ -type one-dimensional model chains obtained for different sets of parameters in Grimme's correction. Tables of DFT-D-computed cell parameters and fractional coordinates of α and γ crystals obtained for different sets of parameters in Grimme's correction. Table of score values for the eigenvector analysis of the vibrational modes of the two NY6 polymorphs. This material is available free of charge via the Internet at <http://pubs.acs.org>.

■ AUTHOR INFORMATION

Corresponding Author

*E-mail: alberto.milani@polimi.it.

Notes

The authors declare no competing financial interest.

■ REFERENCES

- (1) (a) Loo, L. S.; Gleason, K. K. *Macromolecules* **2003**, *36*, 2587–2590. (b) Chen, G.; Shen, D.; Feng, M.; Yang, M. *Macromol. Rapid Commun.* **2004**, *25*, 1121–1124.
- (2) (a) Song, K.; Rabolt, J. F. *Macromolecules* **2001**, *34*, 1650–1654. (b) Lee, K. H.; Kim, K. W.; Pesapane, A.; Kim, H. Y.; Rabolt, J. F. *Macromolecules* **2008**, *41*, 1494–1498. (c) Granato, F.; Bianco, A.; Bertarelli, C.; Zerbi, G. *Macromol. Rapid Commun.* **2009**, *30*, 453–458. (d) Bianco, A.; Iardino, G.; Manuelli, A.; Bertarelli, C.; Zerbi, G. *Chem Phys Chem.* **2007**, *8*, 510–514. (e) Stephens, J. S.; Chase, D. B.; Rabolt, J. F. *Macromolecules* **2004**, *37*, 877–881. (f) Liu, Y.; Qi, L.; Guan, F.; Hedin, N. E.; Zhu, L.; Fong, H. *Macromolecules* **2007**, *40*, 6283–6290. (g) Zussman, E.; Burman, N.; Yarin, A. L.; Khalifin, R.; Cohen, Y. *J. Polym. Sci. B: Polym. Phys.* **2006**, *44*, 1482–1489. (h) Stachewicz, U.; Barber, A. H. *Langmuir* **2011**, *27*, 3024–3029. (i) Milani, A.; Casalegno, M.; Castiglioni, C.; Raos, G. *Macromol. Theory Simul.* **2011**, *20*, 305–319.
- (3) (a) Kohan, M. I. *Nylon Plastics Handbook*; Hanser: New York, 1995. (b) Kinoshita, Y. *Makromol. Chem.* **1959**, *33*, 1–19. (c) Slichter, W. P. *J. Polym. Sci.* **1959**, *36*, 259–266. (d) Ramesh, C. *Macromolecules* **1999**, *32*, 3721–3726. (e) Ramesh, C.; Gowd, E. B. *Macromolecules* **2001**, *34*, 3308–3313. (f) Murthy, N. S. *Polym. Commun.* **1991**, *32*, 301–305. (g) Salem, D. R.; Weigmann, H. D. *Polym. Commun.* **1989**, *30*, 336–338. (h) Murthy, N. S.; Minor, H. *Polym. Commun.* **1991**, *32*, 297–300. (i) Arimoto, H. *J. Polym. Sci.* **1964**, *2*, 2283–2295.
- (4) (a) Aleman, C.; Casanovas, J. *Colloid Polym. Sci.* **2004**, *282*, 535–543. (b) Bernadò, P.; Aleman, C.; Puiggali, J. *Eur. Polym. J.* **1999**, *35*, 835–847. (c) Len, S.; Aleman, C.; Munoz-Guerra, S. *Macromolecules* **2000**, *33*, 5754–5756.
- (5) (a) Murthy, N. S.; Bray, R. G.; Correale, S. T.; Moore, R. A. F. *Polymer* **1995**, *36*, 3863–3873. (b) Loo, L. S.; Gleason, K. K. *Macromolecules* **2003**, *36*, 6114–6126. (c) Vasanthan, N.; Salem, D. R. *J. Polym. Sci. B: Polym. Phys.* **2001**, *39*, 536–547. (d) Na, B.; Lv, R.; Tian, N.; Xu, W.; Li, Z.; Fu, Q. *J. Polym. Sci. B: Polym. Phys.* **2009**, *47*, 898–902. (e) Vasanthan, N. *J. Polym. Sci. B: Polym. Phys.* **2003**, *41*, 2870–2877. (f) Miri, V.; Persyn, O.; Lefebvre, J. M.; Segula, R.; Stroeks, A. *Polymer* **2007**, *48*, 5080–5087.
- (6) (a) Miyake, A. *J. Polym. Sci.* **1960**, *44*, 223–232. (b) Sandeman, I.; Keller, A. *J. Polym. Sci.* **1956**, *19*, 401–435. (c) Rotter, G.; Ishida, H. *J. Polym. Sci. B: Polym. Phys.* **1992**, *30*, 489–495. (d) Vasanthan, N. *Appl. Spectrosc.* **2005**, *59*, 897–903. (e) Persyn, O.; Miri, V.; Lefebvre, J. M.; Depecker, C.; Gors, C.; Stroeks, A. *Polym. Eng. Sci.* **2004**, *44*, 261–271. (f) Vasanthan, N.; Murthy, N. S.; Bray, R. G. *Macromolecules* **1998**, *31*, 8433–8435.
- (7) (a) Dasgupta, S.; Hammond, W. B.; Goddard, W. A. *J. Am. Chem. Soc.* **1996**, *118*, 12291–12301. (b) Li, Y.; Goddard, W. A. *Macromolecules* **2002**, *35*, 8440–8455.
- (8) (a) Gaigeot, M. P. *Phys. Chem. Chem. Phys.* **2010**, *12*, 3336–3359. (b) Brauer, B.; Pincu, M.; Buch, V.; Bar, I.; Smons, J. P.; Gerber, R. B. *J. Phys. Chem. A* **2011**, *115*, 5859–5872. (c) Pagliai, M.; Cavazzoni, C.; Cardini, G.; Erbacci, G.; Parrinello, M.; Schettino, V. *J. Chem. Phys.* **2008**, *128*, 224514.
- (9) (a) Jakes, J.; Krimm, S. *Spectrochim. Acta A* **1971**, *27*, 19–34. (b) Jakes, J.; Krimm, S. *Spectrochim. Acta A* **1971**, *27*, 35–63. (c) Shukla, S. K.; Kumar, N.; Tandom, P.; Gupta, V. D. *J. Appl. Polym. Sci.* **2010**, *116*, 3202–3211.
- (10) (a) Dovesi, R.; Saunders, V. R.; Roetti, C.; Orlando, R.; Zicovich-Wilson, C. M.; Pascale, F.; Civalleri, B.; Doll, K.; Harrison, N. M.; Bush, I. J.; D'Arco, P.; Llunell, M. *CRYSTAL09 User's Manual*; University of Torino: Torino, Italy, 2009. (b) Dovesi, R.; Orlando, R.; Civalleri, B.; Roetti, C.; Saunders, V. R.; Zicovich-Wilson, C. M.; Pascale, F.; Civalleri, B. *Z. Kristallogr.* **2005**, *220*, 571–573.
- (11) (a) Javier Torres, F.; Civalleri, B.; Meyer, A.; Musto, P.; Albonia, A. R.; Rizzo, P.; Guerra, G. *J. Phys. Chem. B* **2009**, *113*, 5059–5071. (b) Javier Torres, F.; Civalleri, B.; Pisani, C.; Musto, P.; Albonia, A. R.; Guerra, G. *J. Phys. Chem. B* **2007**, *111*, 6327–6335. (c) Albonia, A. R.; Rizzo, P.; Guerra, G.; Javier Torres, F.; Civalleri, B.; Zicovich-Wilson, C. M. *Macromolecules* **2007**, *40*, 3895–3897.
- (12) Ferrari, A. M.; Civalleri, B.; Dovesi, R. *J. Comput. Chem.* **2010**, *31*, 1777–1784.
- (13) (a) Noel, Y.; D'Arco, P.; Demichelis, R.; Zicovich-Wilson, C. M.; Dovesi, R. *J. Comput. Chem.* **2010**, *31*, 855–862. (b) Zicovich-Wilson, C. M.; Kirtman, B.; Civalleri, B.; Ramirez-Solis, A. *Phys. Chem. Chem. Phys.* **2010**, *12*, 3289–3293. (c) Colle, R.; Grosso, G.; Ronzani, A.; Zicovich-Wilson, C. *Phys. Status Solidi B* **2011**, *6*, 1360–1368.
- (14) (a) Becke, A. D. *J. Chem. Phys.* **1993**, *98*, 5648–5652. (b) Lee, C.; Yang, W.; Parr, R. G. *Phys. Rev. B* **1988**, *37*, 785–789.
- (15) (a) Grimme, S. *J. Comput. Chem.* **2004**, *25*, 1463–1473. (b) Grimme, S. *J. Comput. Chem.* **2006**, *27*, 1787–1795.
- (16) Civalleri, B.; Zicovich-Wilson, C. M.; Valenzano, L.; Ugliengo, P. *CrystEngComm* **2008**, *10*, 405–410.
- (17) (a) Bondi, A. *J. Phys. Chem.* **1964**, *68*, 441–451. (b) Rowland, R. S.; Taylor, R. *J. Phys. Chem.* **1996**, *100*, 7384–7391.
- (18) (a) Holmes, D. R.; Bunn, C. W.; Smith, D. J. *J. Polym. Sci.* **1955**, *17*, 159–177. (b) Simon, P.; Argay, G. Y. *J. Polym. Sci. B: Polym. Phys.* **1978**, *16*, 935–937.
- (19) Arimoto, H.; Ishibashi, M.; Hirai, M. *J. Polym. Sci. A: Polym. Chem.* **1965**, *3*, 317–326.
- (20) (a) Painter, P. C.; Coleman, M. M.; Koenig, J. L. *The Theory of Vibrational Spectroscopy and Its Application to Polymeric Materials*; Wiley: Chichester, U.K., 1982. (b) Zerbi, G. In *Advances in Infrared and Raman Spectroscopy*; Clark, R. J. H., Hester, R. R., Eds.; Wiley: New York, 1984; Vol. 11, p 301. (c) Castiglioni, C. In *Vibrational Spectroscopy of Polymers: Principles and Practices*; Everall, N. J., Chalmers, J. M., Griffiths, P. R., Eds.; Wiley: Chichester, U.K., 2007; p 455.
- (21) Merrick, J. P.; Moran, D.; Radom, L. *J. Phys. Chem. A* **2007**, *111*, 11683–11700.
- (22) Dendena, M. *Master's Thesis*, Politecnico di Milano, Milano, Italy, 2010.
- (23) Abu-Isa, I. A. *J. Appl. Polym. Sci.* **1971**, *15*, 2865–2876.
- (24) Itho, T. *Jpn. J. Appl. Phys.* **1976**, *15*, 2295–2306.
- (25) (a) Gussoni, M.; Castiglioni, C.; Zerbi, G. In *Handbook of Vibrational Spectroscopy*; Chalmers, J., Griffiths, P., Eds.; John Wiley & Sons: Chichester, U.K., 2001; pp 2040–2077. (b) Milani, A.; Castiglioni, C. *J. Phys. Chem. A* **2010**, *114*, 624–632. (c) Milani, A.; Galimberti, D.; Castiglioni, C.; Zerbi, G. *J. Mol. Struct.* **2010**, *976*, 342–349. (d) Milani, A.; Tommasini, M.; Castiglioni, C. *Theor. Chem. Acc.* **2012**, *131*, 1139.

- (26) (a) Koglin, E.; Meier, R. J. *Comput. Theor. Polym. Sci.* **1999**, *9*, 327–333. (b) Meier, R. J. *Polymer* **2002**, *43*, 517–522. (c) Tarazona, A.; Koglin, E.; Coussens, B. B.; Meier, R. J. *Vib. Spectrosc.* **1997**, *14*, 159–170. (d) Milani, A.; Castiglioni, C.; Di Dedda, E.; Radice, S.; Canil, G.; Di Meo, A.; Picozzi, R.; Tonelli, C. *Polymer* **2010**, *51*, 2597–2610. (e) Milani, A.; Tommasini, M.; Castiglioni, C.; Zerbi, G.; Radice, S.; Canil, G.; Toniolo, P.; Triulzi, F.; Colaianna, P. *Polymer* **2008**, *49*, 1812–1822. (f) Milani, A.; Zanetti, J.; Castiglioni, C.; Di Dedda, E.; Radice, S.; Canil, G.; Tonelli, C. *Eur. Polym. J.* **2012**, *48*, 391–403.
- (27) (a) Nakhmanson, S. M.; Korlacki, R.; Travis Johnston, J.; Ducharme, S.; Ge, Z.; Takacs, J. M. *Phys. Rev. B* **2010**, *81*, 174120. (b) Kleis, J.; Lundqvist, B. I.; Langreth, D. C.; Schroder, E. *Phys. Rev. B* **2007**, *76*, 100201. (c) Ramer, N. J.; Marrone, T.; Stiso, K. A. *Polymer* **2006**, *47*, 7160–7165. (d) Ramer, N. J.; Raynor, C. M.; Stiso, K. A. *Polymer* **2006**, *47*, 424–428.

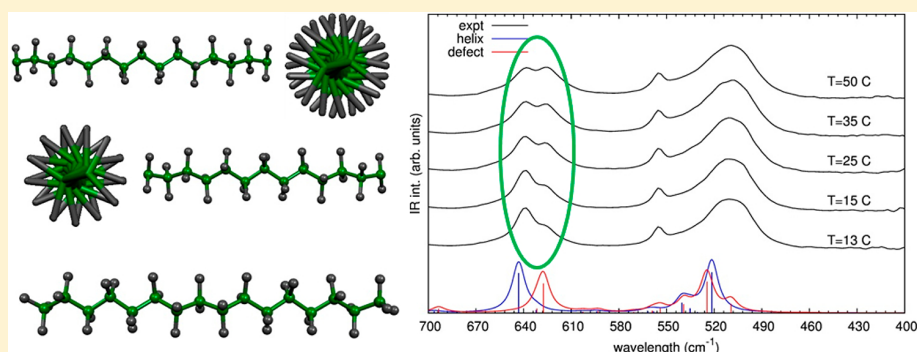
3.3.3 attachment e

Ab Initio Calculation of the IR Spectrum of PTFE: Helical Symmetry and Defects

Claudio Quarti,* Alberto Milani, and Chiara Castiglioni

Politecnico di Milano – Dip. Chimica, Materiali e Ing. Chimica “G. Natta”, P.zza Leonardo da Vinci 32, I-20133 Milano, Italy

Supporting Information



ABSTRACT: A detailed analysis of the structure and vibrational properties of PTFE and the assignment of its IR spectrum are carried out by means of density functional theory simulations on infinite, one-dimensional chains. Calculations take into consideration regular polymer chains with different conformations (15_7 , 13_6 , 10_3 , 4_1 , and 2_1) in order to investigate the main features due to the peculiar helical structures in the IR spectra. In addition, also the helix-reversal defect and effects related to conformational disorder are considered, to analyze the contributions in the spectrum due to defects and to the amorphous phase. The present study solves the ambiguities in the interpretation of the 638 – 626 cm^{-1} doublet, assigning the lower frequency component to a normal mode of the helix-reversal defect. This interpretation is consistent with the general belief that the PTFE crystal contains a large concentration of defects already at low temperature and that the two crystalline transitions at room temperatures (19 and 30 $^\circ\text{C}$) are accompanied by an order–disorder transition. As an additional result, the 788 cm^{-1} band, previously adopted to measure the amount of amorphous material in real samples, is confirmed as a marker of this phase.

1. INTRODUCTION

In spite of the wide range of applications and the large amount of scientific literature dealing with the fundamental and technological properties of poly(tetrafluoroethylene) (PTFE), this polymer still presents some debated issues concerning its structural and spectroscopic characterization. Furthermore, a thorough understanding of its molecular properties is desirable, since PTFE is the simplest fluorinated polymer and it is often considered as a model in structural and spectroscopic studies of the many new advanced fluorinated materials.¹

The difficulty encountered in the definition of the PTFE structure is related to the occurrence of several phase transitions in a rather small range of temperatures (0 – 50 $^\circ\text{C}$), in which conformational disorder is observed in the crystalline phase, coexistent with fully amorphous regions. The different crystalline phases are characterized by a different chain conformation and/or by a different three-dimensional arrangement of the polymer chains in the crystal cell. Two regular conformations of the chain have been identified, namely, a 13_6 helix found in form II, stable below 19 $^\circ\text{C}$, and a 15_7 helix at temperatures higher than 19 $^\circ\text{C}$.^{2a} Between 19 and 30 $^\circ\text{C}$, the 15_7 chains are packed in a hexagonal structure (form IV) which goes through a transition to a

pseudo-hexagonal structure above 30 $^\circ\text{C}$ (form I).^{2b} Another crystalline form (form III) is reported for samples obtained by crystallization under high pressure and is characterized by the transplanar conformation of the polymer chains.^{3,4} The smearing of the XRD peaks going from form II to IV to I has been interpreted as due to an increase of the structural disorder in the higher temperature phases. According to the early paper of Rigby and Bunn, “there is an evident change of crystal structure; it is, however, not a change from one precise arrangement to another, but a change from a 3-dimensional (fully crystalline) order below 20 $^\circ\text{C}$ to a lower degree of order above 20 $^\circ\text{C}$ ”.^{5a} However, DSC measures on PTFE demonstrated that the observed phase transitions happen at well-defined temperatures.⁶

In addition to X-ray diffraction studies,^{2,5,7} also vibrational spectroscopy^{4,8–13} has been used for the structure characterization of PTFE, providing in some cases contrasting interpretations of the few, often broad and overlapped vibrational features. Krimm and Liang carried out a first assignment of the IR

Received: October 16, 2012

Revised: December 14, 2012

Published: December 17, 2012

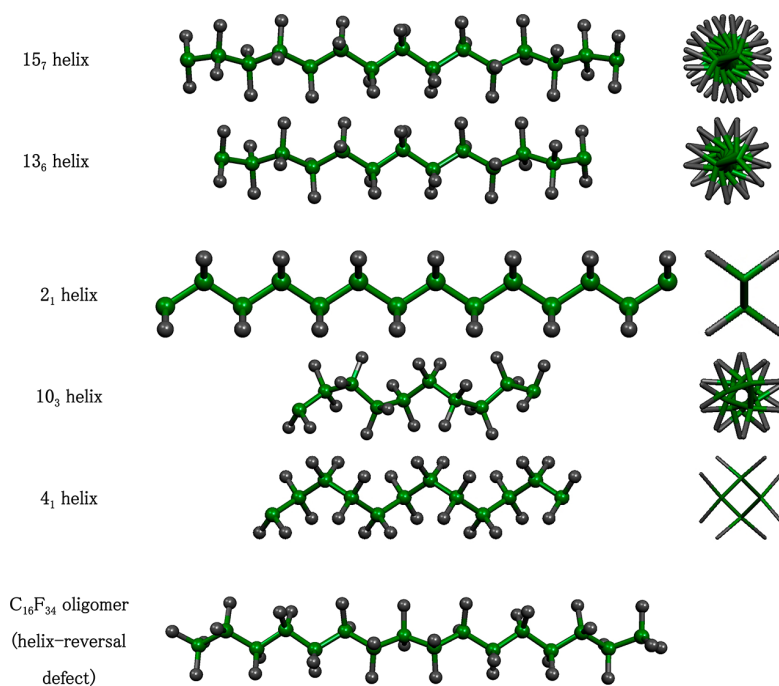


Figure 1. Sketches of the infinite and finite length model systems adopted in the computational study. The helix models have been investigated by means of the CRYSTAL09 code²⁰ taking into account explicitly the helical symmetry; the helix-reversal defect has been investigated by means of GAUSSIAN09 code²¹ by considering $C_{16}F_{34}$ and $C_{28}F_{58}$ oligomers. Only the $C_{16}F_{34}$ model is drawn. Carbon atoms are painted in green and fluorine atoms in gray.

spectrum of PTFE on the basis of the 13_6 helical structure of the chain.⁸ Successively, Moynihan revised the assignment of a few bands; moreover, he suggested that the intensity ratio between the 778 and 2367 cm^{-1} bands could be used for a measure of the degree of crystallinity of PTFE samples⁹ and this method finds practical application still nowadays.¹⁴

The relative IR intensity of the $638\text{--}626\text{ cm}^{-1}$ doublet is the only spectral feature that shows a significant evolution with the temperature. In correspondence of the crystal transitions, going from 19 to $30\text{ }^\circ\text{C}$, the 638 cm^{-1} component decreases in intensity, while the 626 cm^{-1} component increases. Moynihan associated this variation to the transition between the crystalline form, showing a 13_6 (form II) conformation of the chain and the phases characterized by the 15_7 helix (forms IV and I).⁹ Accordingly, the peak at 638 cm^{-1} was associated to the former phase and the peak at 626 cm^{-1} to the latter. Subsequently, this interpretation was debated by Brown,⁴ who noticed that the change of the intensity ratio in the $638\text{--}626\text{ cm}^{-1}$ doublet is not limited to the temperature ranges characteristic of the phase transformations: indeed, an absorption feature at 626 cm^{-1} is also present well below $19\text{ }^\circ\text{C}$, and its intensity steadily increases until $50\text{ }^\circ\text{C}$. On this basis, Brown assigned the 626 cm^{-1} band to the formation of a helix-reversal defect,⁴ which can be easily arranged in the crystal.

In the same period, De Sanctis et al. carried out a theoretical study on the conformation potential of PTFE, as a function of the torsional angle (θ) around the CC bond. On the basis of molecular mechanics (empirical potential energy functions), they obtained a symmetric potential curve with global minima at about $\pm 165^\circ$ and local minima around ± 90 and $\pm 60^\circ$. Only one flat minimum was found around 165° ; thus, the presence of two stable conformations (the 15_7 and 13_6 conformations) cannot be taken into account on the basis of the conformational potential of

PTFE. In addition, the trans-planar conformation ($\theta = 180^\circ$) was found to be a maximum of the potential surface.¹⁵

In the 1970s, Koenig and co-workers carried out an extensive investigation on PTFE by means of Raman spectroscopy and they developed a specific empirical force field for the prediction of the vibrational frequencies.¹⁰ These authors concluded that no (Raman) spectroscopic markers associated to the phase transition at room temperature exist and they claimed for evidence of crystal splitting.^{10e} It is still not clear whether the low temperature phase (form II) contains one chain per cell^{5b} or two chains with different chirality;¹⁶ thus, the presence of crystal splitting cannot be ruled out.

A deep revision of the IR spectrum of PTFE was carried out by Zerbi and co-workers,¹³ by means of calculations based on the force field developed by Koenig et al.^{10c} Zerbi calculated $k = 0$ phonons and phonon dispersion curves of different helical structures. In connection with the results of De Sanctis,¹⁵ he considered the 15_7 , 10_3 , 4_1 , and planar 2_1 helical conformations. Accordingly, he predicted a band at 619 cm^{-1} for the planar 2_1 conformation. The assignment of this theoretical band to the observed feature at 626 cm^{-1} brought the hypothesis of the occurrence in the crystal of long sequences of CF_2 units in transplanar conformation. In addition, bands calculated for the PTFE helices characterized by the 10_3 and 4_1 conformations found a correspondence with the experimental bands at 288 and 778 cm^{-1} .

However, the question of the correct assignment of the lower frequency component of the IR doublet at $638\text{--}626\text{ cm}^{-1}$ remained unsettled until now, due to the lack of theoretical methods suitable for a deeper investigation of the problem. Nowadays, the availability of theoretical methods and computational quantum chemical codes suitable for the prediction and the interpretation of the vibrational spectroscopic features of crystalline polymers is well assessed.^{17,18} On this basis, in this

work, we revise the assignment of the IR spectrum of PTFE, thus settling the controversial issue on the assignment of the 626 cm^{-1} band and giving a deeper comprehension of the spectroscopic behavior of PTFE. Our calculations confirm the interpretation of Brown on the formation of the helix-reversal defects in PTFE. Moreover, they support the belief that the vibrational properties of PTFE are related to a transition to a more disordered crystalline phase at room temperature.^{7c}

The manuscript is organized as follows. In section 2, the models and the computational methods employed are presented. In section 3, we show the results of the calculations concerning both the molecular structures and the IR spectra of PTFE. In particular, in section 3.1, we revisit the work of Zerbi on polymer chains with different helical structures. Both infinite and finite model systems have been considered, respectively, in sections 3.1.1 and 3.1.2. In section 3.2, we discuss the helix-reversal defects. In section 3.3, we carry out a conformational analysis on PTFE oligomers, to discuss the contribution (in the IR spectrum) of the amorphous phase. Discussions and conclusions are reported, respectively, in sections 4 and 5.

2. COMPUTATIONAL DETAILS

Calculations of the equilibrium structures and of the IR spectra of PTFE are carried out in the framework of the density functional theory (DFT). PTFE is described as a single, isolated polymeric chain in regular conformation, similarly to a previous study on polystyrene.¹⁸ The choice of neglecting the supra-molecular arrangement is dictated by the fact that the structures on the 3-D crystal phases are still debated¹⁶ and intermolecular effects are expected to have small or negligible effects on the IR spectrum. In fact, if on one side the intermolecular interactions would give place to crystal splitting of some $k = 0$ bands in systems with more chains per unit cell, on the other side, the splitting can be hardly detected in the IR spectra of semicrystalline polymers, characterized by broad absorption bands, as is indeed the case of PTFE. On the opposite, the effects due to the intramolecular structure usually show clear signatures in the IR spectrum. Indeed, several examples are reported of studies where the presence of different conformers is observed by IR spectroscopy and the evolution of their relative population with temperature is monitored by IR intensity analysis;^{1a} moreover, the detection of conformational defects in polymeric materials has been successfully carried out for a long time through IR analysis.¹⁹ For the above reasons, we believe that the models adopted here (namely, single PTFE chains *in vacuo*) are reliable for the detailed investigation on the IR spectrum of PTFE.

DFT calculations are carried out on both infinite and finite models, sketched in Figure 1: calculations on the infinite polymeric chains are performed with CRYSTAL09 code,²⁰ which allows the helical symmetry to be taken into account explicitly. Calculations on finite oligomers are carried out with GAUSSIAN09 code.²¹

The hybrid B3LYP functional²² and Ahlrichs-TZVP basis set²³ were adopted. Calculations on both infinite and finite chains were repeated also with the widely used and cheaper B3LYP/6-31G(d,p)²⁴ method, in order to investigate the effect of the basis set; these results are reported in the Supporting Information. Since intramolecular dispersion effects can be important in different helices, we carried out calculations also by introducing the D2 semiempirical corrections developed by Grimme.²⁵ The effects on relative energies and spectra prediction are however completely negligible, as proven by the results reported in the Supporting Information.

Thin films of PTFE were kindly provided by Solvay Solexis; temperature controlled infrared absorption spectra were recorded with a Nicolet Nexus FT-IR spectrometer (resolution 1 cm^{-1} and 128 scans) on PTFE film placed in a Mettler FP82 Hot Stage cell.

3.1. RESULTS

3.1.1. IR Spectra of Infinite Polymeric Chains with Different Helical Structure. Calculations on infinite polymer chains of PTFE with different helical structures, proposed by Zerbi in the 1970s, are revisited here by using *state-of-the-art* electronic structure calculations (B3LYP/TZVP). In ref 13, the following helical structures, 15_7 , 10_3 , 4_1 , and the trans-planar 2_1 , were taken into account. Here, in addition to the above conformations, we consider also the 13_6 helical conformation, in order to investigate the transition from the low temperature 13_6 phase to the higher temperature 15_7 one. The different regular helix conformations of the infinite chain were selected by a symmetry constraint, which in turn determines the order of the rototranslational axis. The structural parameters were optimized for the various conformations, and they are reported in Table 1

Table 1. Equilibrium Repeating Distance, Torsional Angles, and Relative Energies of the 15_7 , 13_6 , 10_3 , 4_1 , and 2_1 Helical Structures of an Infinite PTFE Chain^a

helix	repeating distance (Å)	dihedral angle (deg)	energy (kcal/mol per CF ₂ unit)
15_7	19.71	165.6	0.07
13_6	17.06	163.4	0.00
10_3	11.93	91.7	1.85
4_1	4.68	72.4	2.97
2_1	2.65	180.0	0.41

^aCalculations (B3LYP/TZVP) have been carried out with the CRYSTAL09 package by imposing PBC along the chain direction, with constrained helical symmetry.

together with the respective energies. Computed optimized geometries adequately reproduce the experimental data available for crystals showing the 15_7 and 13_6 conformation of the chains, characterized by a cell parameter along the polymer axis, respectively, of 19.5 and 16.88 Å and torsional angle around the CC bond of 165.8 and 163.5°.³

Considering the relative stability of the 15_7 and 13_6 helices, they are predicted to be quasi-isoenergetic, the latter being more stable than the former of less than 0.1 kcal/mol. However, calculations at a different level of theory (B3LYP/6-31G(d,p)) show the opposite trend, with the 15_7 more stable than the 13_6 by 0.04 kcal/mol (see Table S11, Supporting Information).²⁶ Because of the small energy difference obtained for the two conformations, it is hard to discuss the relative stability of the 13_6 (phase II) and 15_7 forms (phases IV and I) on the basis of our theoretical predictions. However, we notice that the energy difference found between the two conformations is certainly comparable to the dispersion interactions between the different chains packed in the crystal. This fact is somehow consistent with the interpretation of Strobl, who suggested that the low temperature 13_6 phase is dominated by intermolecular interactions, while the high temperature 15_7 phase is dominated by intramolecular interactions.^{7c}

Our calculations show that helices with the 10_3 or 4_1 conformation lie higher in energy; namely, the formation of a single helical turn requires more than 10 kcal/mol. Finally, the 2_1

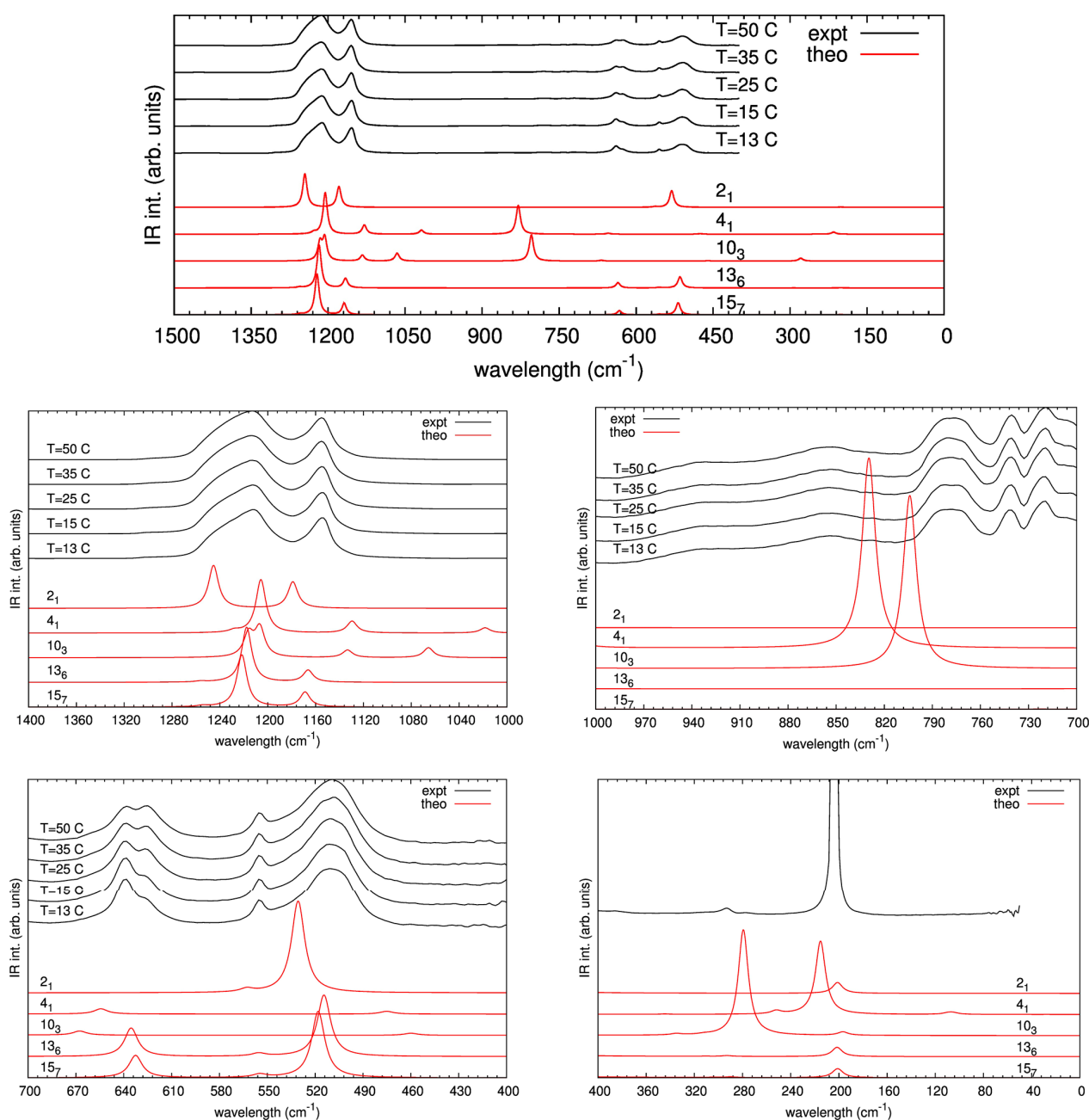


Figure 2. Comparison of the experimental spectra of PTFE recorded at various temperatures and the theoretical spectra calculated on the 15_7 , 13_6 , 10_3 , 4_1 , and 2_1 helical structures for the infinite chains. The B3LYP/TZVP functional/basis set is used. No scaling factor for the frequencies is used. Theoretical intensities are normalized to one CF_2 group and different intensity scales are adopted in the different spectral range, for a better visualization.

helical conformation is associated to a local maximum in the potential energy surface for symmetry reasons,^{15,27,28} and its energy determines the energetic barrier between the left and right 13_6 helical conformations, which results in being of the order of $k_B T$ (at room temperature), thus supporting the possibility of the formation of helical reversal defects, as proposed by Brown.⁴

In Figure 2, we compare the IR spectra calculated for the various helix models (15_7 , 13_6 , 10_3 , 4_1 , 2_1) with experimental spectra recorded at different temperatures (from 13 to 50 °C); for a correct comparison, the IR intensities of the theoretical spectra are normalized to one CF_2 group, while the intensity scale

adopted for the experimental spectra is arbitrary. The choice of the basis set does not affect the general pattern of the spectra, even if the use of the 6-31G(d,p) basis set red-shifts slightly the frequency of the bands in the CF stretching region (see Figure S11, Supporting Information). IR spectra computed for the 15_7 and 13_6 conformations are very similar and nicely reproduce the experimental features in the whole spectral region, with the exception of the region between 1000 and 700 cm^{-1} , that is traditionally associated to the amorphous phase (in this region, the experimental spectra have been magnified in order to clearly show the absorption features). Frequency differences between

the IR spectra calculated for the 15_7 and 13_6 conformations are in general very small, amounting to 5 cm^{-1} in the worst case.

Focusing on the region of the doublet at $638\text{--}626\text{ cm}^{-1}$, we notice that, going from the 13_6 to 15_7 conformation, the calculated band actually red-shifts from 636 to 632 cm^{-1} . Even if the predicted frequency shift (4 cm^{-1}) is small with respect to the splitting of the doublet experimentally observed (12 cm^{-1}), one could tentatively assign the two peaks of the experimental spectra to the different crystalline phases (forms II and IV), characterized by a change in chain conformation. However, the assignment of the two peaks to the 13_6 and 15_7 helices has already been rejected by many authors,^{4,13} since the variation of the relative IR intensity of the two components of the doublet extends well outside the range of temperatures characteristic of the phase transition. Accordingly, we state that, also on the basis of our theoretical predictions, no IR markers of transition from 13_6 to 15_7 helices of PTFE can be proposed.

In ref 13, the band at 626 cm^{-1} was assigned to a planar 2_1 helical structure: as shown in Figure 2 (region $700\text{--}400\text{ cm}^{-1}$), no IR active bands are present for the 2_1 conformation in this suitable spectral range. One vibrational mode associated to such a conformation is predicted by our calculations in this region (615 cm^{-1}), but it is not IR active, since it belongs to B_{1g} symmetry. Thus, the previous assignment should be revised according to the present DFT results.

On the other hand, in agreement with previous assignments,¹³ we find that some bands calculated for the 10_3 and 4_1 conformations nicely reproduce the 740 and 778 cm^{-1} experimental absorptions in a spectral region assigned to the amorphous phase. Also, the original assignment of the IR band at 288 cm^{-1} to the 10_3 conformation finds a parallel in our calculations. It is difficult, at this stage of our investigation, to state whether the occurrence of some absorption bands in the $1000\text{--}700\text{ cm}^{-1}$ range reveals the presence of long chain sequences in a peculiar regular helix conformation (namely, 10_3 or 4_1 helices) or can be better explained as originated by disordered conformations occurring in the amorphous phase, containing isolated gauche defects (i.e., with some torsional angle close to $\pm 60^\circ$). Since this point deserves a deeper investigation, an analysis of the absorption features in the $1000\text{--}700\text{ cm}^{-1}$ region will be done in the section 3.3, by means of a conformational analysis of PTFE oligomers.

3.1.2. IR Spectra of Finite Oligomers with Different Helical Structures. In parallel with the previous calculations on infinite systems, we carried out geometry optimization and calculation of the IR spectrum also on some oligomeric models of PTFE, characterized by the same helical structures adopted for the study of the 1-D crystal. This analysis was done in order (i) to make a comparison with the results previously obtained on infinite systems to check the consistency of the two computational approaches adopted and (ii) to provide information about the effect of the confinement due to the finite size of molecules. The issues described in (i) and (ii) are particularly important in the perspective of the subsequent studies on finite size models and aimed to identify spectroscopic markers of structural defects, such as the helix-reversal defect and conformational disorder typical of the amorphous phase.

As in the works of Barone and co-workers,²⁹ the oligomer $C_{16}F_{34}$ was taken as a model: five relevant helical conformations, namely, 15_7 , 13_6 , 10_3 , 4_1 , and 2_1 helices, were constrained by fixing the torsional angles of the oligomer to the values found for the infinite models, reported in Table 1. Then, the molecular geometry has been optimized by keeping fixed all the torsional

angles of the polymer backbone. In addition, a full molecular optimization without constraints on torsional angles was carried out, using as a guess structure the most stable helical conformation, i.e., the 13_6 helix.

Calculations on the five $C_{16}F_{34}$ oligomers obtained according to the different helical structures considered show relative energies that follow the same trend found in the case of the infinite helices, as reported in Table 2. This is an indication that

Table 2. Equilibrium Dihedral Angles and Relative Energies per CF_2 Group of the Fully Optimized (OPT) and of the 15_7 , 13_6 , 10_3 , 4_1 , and 2_1 Helical Structures of the Finite $C_{16}F_{32}$ Oligomer^a

helix	dihedral angle (deg)	energy (kcal/mol per CF_2 unit)
OPT	161.8	
15_7	165.6	0.20
13_6	163.4	0.07
10_3	91.7	1.47
4_1	72.4	2.16
2_1	180.0	0.48

^aCalculations were carried out with the GAUSSIAN09 package (B3LYP/TZVP).

results obtained for the $C_{16}F_{34}$ model can be considered consistent with those obtained on the infinite chain. The fully optimized structure shows a geometry very similar to the 13_6 conformation, with torsional angles of about 162° .

IR spectra of the $C_{16}F_{34}$ oligomer constrained in the five different helical structures were calculated and are reported in Figure 3, where a comparison with spectra calculated for the infinite chains is also shown. A procedure used in some of our previous works,^{1b} that consists of computing vibrational spectra for molecules carrying fictitious heavy masses at the terminal CF_3 groups, allows one to avoid spurious features due to terminal CF_3 groups and to obtain a spectrum which can be compared with that of the infinite chain straightforwardly. The results of the calculations on the finite $C_{16}F_{34}$ system parallel those of the infinite systems, especially in the region of the doublet $638\text{--}626\text{ cm}^{-1}$. On the opposite, the weak bands calculated at 740 and 720 cm^{-1} for the 13_6 and 15_7 conformations of the oligomer do not parallel any feature of the corresponding infinite chain. On this basis, the experimental bands at 740 and 720 cm^{-1} could be associated to finite chain effects.

While the spectra calculated with the two approaches (on infinite and finite systems) do not match perfectly in frequency, calculations on longer oligomers (30 CF_2 units), carried out with the B3LYP/6-31G(d,p) (Figure S12, Supporting Information) basis set, reproduce very well the results obtained for the infinite systems at the same level of theory. This suggests that the frequency mismatch shown by the spectra reported in Figure 3 has to be ascribed exclusively to effects due to the finite length of the chain.

In light of the calculations on the oligomers, we can confirm the relevant conclusion of section 3.1.1. No intense IR bands associated to sequences in all trans conformation are predicted in correspondence of the doublet at $638\text{--}626\text{ cm}^{-1}$; moreover, in this region, also in the case of the oligomer the 2_1 helical structure shows just one, IR inactive (B_{1g}) band.

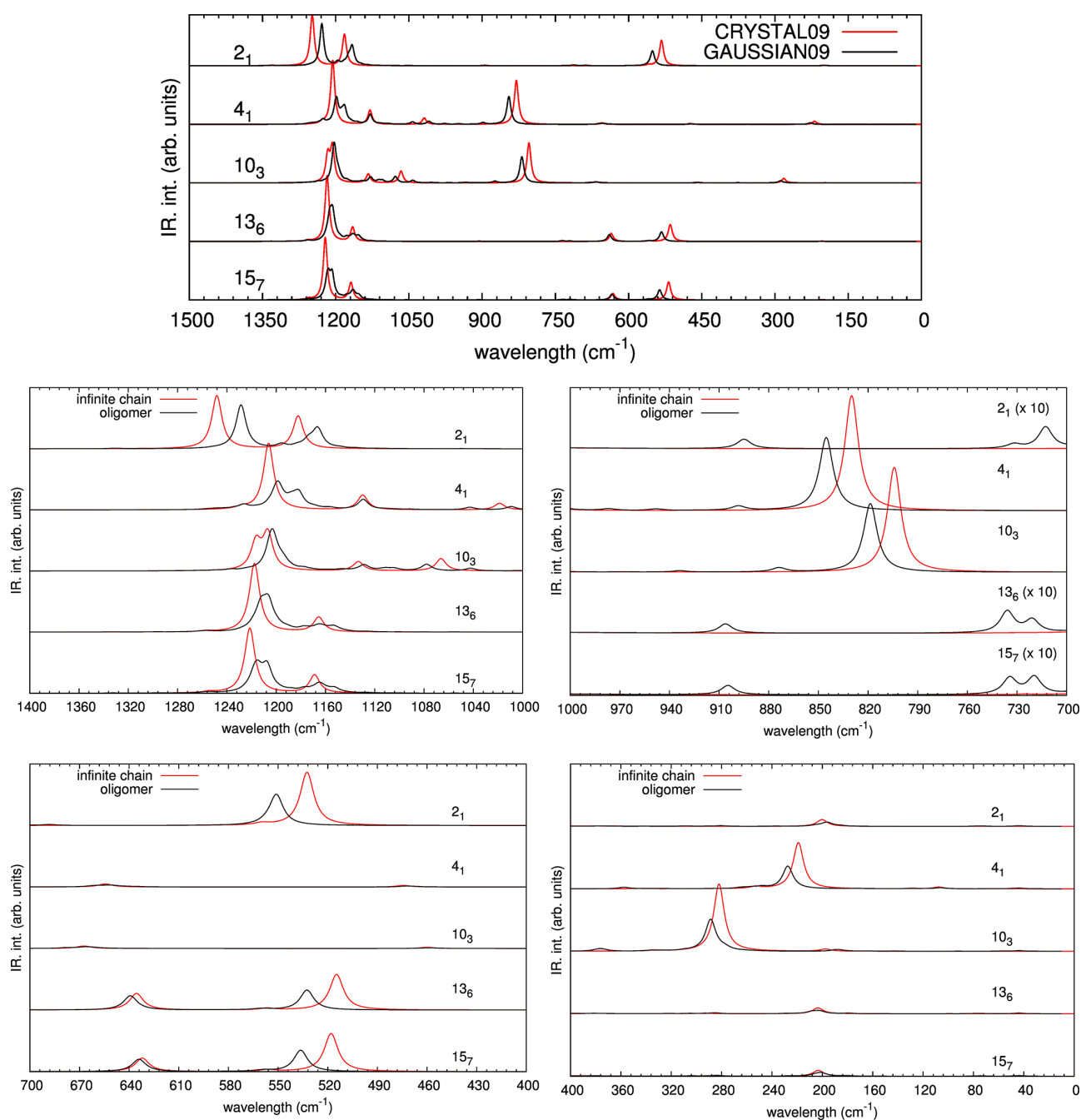


Figure 3. Comparison between the spectra calculated on infinite PTFE chains (CRYSTAL09) and on the $C_{16}F_{34}$ oligomer (GAUSSIAN09), for the 15_7 , 13_6 , 10_3 , 4_1 , and planar 2_1 helical structures (B3LYP/TZVP). No scaling factors for frequencies are used. Theoretical intensities are normalized to one CF_2 group (except for the region $1000\text{--}700\text{ cm}^{-1}$, where the intensities for the 15_7 , 13_6 , and 2_1 helical structures have been amplified by a factor of 10) and different intensity scales are adopted in the different spectral range, for a better visualization.

3.2. HELICAL REVERSE DEFECT

In this section, we will take into consideration the interpretation of Brown, according to which the 626 cm^{-1} band is associated to the formation of a helix-reversal defect.⁴

A model for the helix-reversal defect has been proposed recently by Barone and co-workers, based on DFT calculations.²⁹ They considered the $C_{16}F_{34}$ oligomer as representative of the PTFE chain, and they obtained a stable conformation of the type $\dots t^+ t^+ (t^+)^* (t^-)^* t^- t^- \dots$, where $t^\pm = \pm 162.4^\circ$ and $(t^\pm)^* = \pm 172.2^\circ$

(optimization performed with GAUSSIAN09 at the PBE0/6-31G(d) level). In the present work, in addition to the $C_{16}F_{34}$ oligomer, we consider also the longer oligomer $C_{28}F_{58}$, in order to investigate the effect of increasing chain lengths on the IR spectrum of the PTFE helix with the reversal defect.³⁰

For both oligomers, we started with a similar guess geometry: $\dots t^+ t^+ t^+ t^- t^- t^- \dots$ (where $t^\pm = \pm 160^\circ$). Then, we performed a full optimization at the B3LYP/TZVP level. The helical reversal is preserved during the optimization, and the system finally converged to a conformation very similar to that obtained by

Table 3. Torsional Angles Obtained for (i) the Fully Optimized Helical Structure (Helix) and (ii) the Helix-Reversal Defect (Defect) Model in $C_{16}F_{34}$ and $C_{28}F_{58}$ Oligomers^a

		$C_{16}F_{34}$							
		θ_1	θ_2	θ_3	θ_4	θ_5	θ_6	θ_7	θ_8
helix		169.2	162.6	161.8	161.8	161.8	161.8	161.8	161.8
defect		169.2	163.0	161.7	161.7	161.5	160.6	169.2	-173.6
		θ_9	θ_{10}	θ_{11}	θ_{12}	θ_{13}	θ_{14}	θ_{15}	
helix		161.8	161.8	161.8	161.8	161.8	162.6	169.2	
defect		-161.6	-161.3	-161.7	-161.8	-161.8	-162.6	-169.2	
		$C_{28}F_{58}$							
		θ_1	θ_2	θ_3	θ_4	θ_5	θ_6	θ_7	θ_8
helix		169.2	162.6	161.8	161.8	161.8	161.8	161.8	161.8
defect		169.2	162.6	161.8	161.8	161.8	161.8	161.8	161.9
		θ_9	θ_{10}	θ_{11}	θ_{12}	θ_{13}	θ_{14}	θ_{15}	θ_{16}
helix		161.8	161.8	161.7	161.9	161.7	161.9	161.7	161.9
defect		161.7	161.8	161.6	161.7	160.9	171.2	-171.5	-161.0
		θ_{17}	θ_{18}	θ_{19}	θ_{20}	θ_{21}	θ_{22}	θ_{23}	θ_{24}
helix		161.7	161.8	161.7	161.8	161.8	161.8	161.8	161.8
defect		-161.4	-161.7	-161.8	-161.8	-161.9	-161.8	-161.8	-161.8
			θ_{25}		θ_{26}		θ_{27}		
helix			161.8		162.6		169.2		
defect			-161.8		-162.6		-169.2		

^aDihedral angles are labeled by increasing integer numbers starting from one end group and moving toward the other (B3LYP/TZVP).

Barone and co-workers. Thus, we can confirm that the helix-reversal defect is actually a local minimum of the potential energy surface of both the $C_{16}F_{34}$ and $C_{28}F_{58}$ oligomers.

In Table 3, we compare the values of the torsional angles calculated for the “regular” oligomers and for the same oligomers carrying the helix-reversal defect, as obtained through geometry optimization of $C_{16}F_{34}$ and $C_{28}F_{58}$. Notice that, with the exception of the end torsional angles, the fully optimized “regular” structures show a geometry closer to that of the 13_6 conformation ($\theta = 163.4^\circ$) than that of the 15_7 one ($\theta = 165.6^\circ$). In the molecules showing helix-reversal, the defect is quite localized and only two dihedral angles in the middle of the helix are markedly different from the optimum value characteristic of the regular structure. In particular, these angles relax to values (about $\pm 170^\circ$) close to 180° , which is the torsional angle characteristic of the trans-planar conformation (helix 2_1). The computed relative energy of the molecule with the helix-reversal defect is found to be 1.50 kcal/mol larger than that of the fully optimized regular chain, for both $C_{16}F_{34}$ and $C_{28}F_{58}$ oligomers. This result is in agreement with the value of 1.25 kcal/mol obtained empirically by Brown from the analysis of the IR spectra⁴ and with the value of 1.14 kcal/mol found by Barone et al. by means of DFT calculations at the PBE0/6-31G(d) level.²⁹

In Figures 4 and 5, we compare the IR spectrum calculated for the regular helical structure and for the helix-reversal defect, respectively, in the case of $C_{16}F_{34}$ and $C_{28}F_{58}$. In the same figures, the experimental spectrum of PTFE is shown, for the sake of comparison. The IR spectra computed for the helix-reversal defect and for the regular helical structure are quite similar in the CF stretching region: indeed, both $C_{16}F_{34}$ and $C_{28}F_{58}$ show a slight change in the intensity pattern, but no spectroscopic markers clearly associated to the helix-reversal defect can be found in this region. The two bands at 740 and 720 cm^{-1} (absent for the infinite model) find correspondence both in the spectrum computed for the helix-reversal defect and in that of the regular helical structure. As noted in the previous section, such bands can be attributed to finite chain effects, thanks to the activation of

phonons at $k \neq 0$ due to the breaking of the translational symmetry. Notice moreover that also the presence of a helix-reversal defect breaks the translational symmetry of a polymeric chain; i.e., it might induce the occurrence of transitions typical of chains of finite size, also for a long chain.

Similar arguments hold for the band at 288 cm^{-1} , which is not present in the spectrum of the infinite 13_6 chain, but it appears both in the spectrum of the finite regular chains and in that of molecules characterized by the helix-reversal defect. However, we must recall that in section 3.1.1 we showed that the 740, 720, and 288 cm^{-1} experimental bands find a correspondence also with some bands for the 10_3 and 4_1 helical structures. Thus, two assignments can be proposed for these features: (i) finite size effects, due to the presence of short chains in the sample or simply induced by conformational defects (as for instance the helix-reversal one), and (ii) formation of helical segments with 10_3 or 4_1 conformations. Because of the large energy associated to the formation of helical segments characterized by the 10_3 and 4_1 conformations, we think that the mechanism related to the activation of phonons at $k \neq 0$ in short regular CF_2 sequences with 13_6 helix structure is more likely.

In the region between 700 and 400 cm^{-1} , we see that the IR band calculated at 520 cm^{-1} actually decreases its intensity when the helical defect is formed. Also, this effect, due to the occurrence of additional transitions in the same spectral region, over which the IR intensity is redistributed resulting in a broader absorption band, can be considered a marker of the helix-reversal defect. It is pleasant to notice that a continuous decrease of the peak height of the corresponding experimental feature (at 520 cm^{-1}) has been observed while increasing the sample temperature in the range between 13 and 50 $^\circ\text{C}$.

In the region of the doublet 638–626 cm^{-1} , a band characteristic of the helix-reversal defect of the $C_{16}F_{34}$ oligomer appears (see Figure 4), in very good correspondence with the lower component of the doublet. Similar results are found for the $C_{28}F_{58}$ oligomer (see Figure 5), where, in the case of the defected

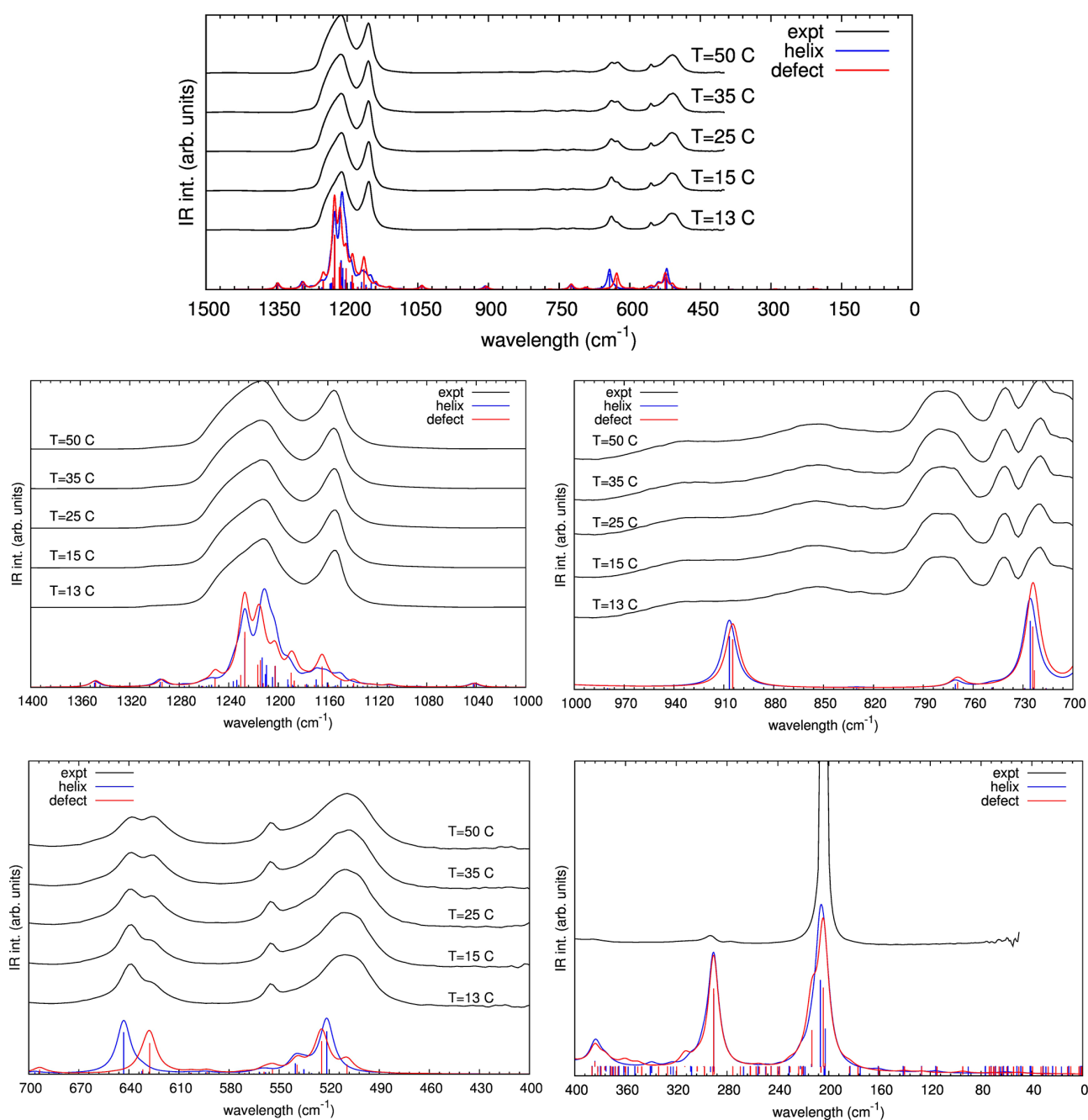


Figure 4. Comparison of the IR spectrum of $C_{16}F_{34}$ oligomer in two different optimized conformations: (i) regular helical structure; (ii) helix-reversal defect. Experimental spectra of PTFE at different temperatures are also shown. Calculations carried out with the GAUSSIAN09 package (B3LYP/TZVP). No scaling factor for the frequencies is used. Different intensity scales are adopted in the different spectral range, for a better visualization. Theoretical spectra have been obtained by assuming a Lorentzian band shape with a full width at half-maximum of 10 cm^{-1} .

molecule, two bands are predicted in correspondence of the observed doublet at $638\text{--}626\text{ cm}^{-1}$.

These results on oligomers strongly support the interpretation of Brown, namely, that the variation of the relative IR intensity of the doublet $638\text{--}626\text{ cm}^{-1}$ is due to the formation of a helix-reversal defect, whose population in the crystal increases as the temperature increases. Considering the short $C_{16}F_{34}$ chain, the lower component at 626 cm^{-1} is indeed definitely assigned to the helix-reversal defect and the higher component at 638 cm^{-1} is attributed to the regular helix. Notice instead that, in the case of

the longer $C_{28}F_{58}$ oligomer, the 638 cm^{-1} component gains intensity both from the chain in regular conformation and from the defected chain.

A further investigation, based on eigenvectors analysis, was carried out in order to better understand the behavior of the doublet. First, we report in Figure 6 the eigenvector of the band associated to the lower component of the $638\text{--}626\text{ cm}^{-1}$ doublet. As shown in Figure 6, this mode can be described mainly as CF_2 wagging vibration and it is quite localized on the

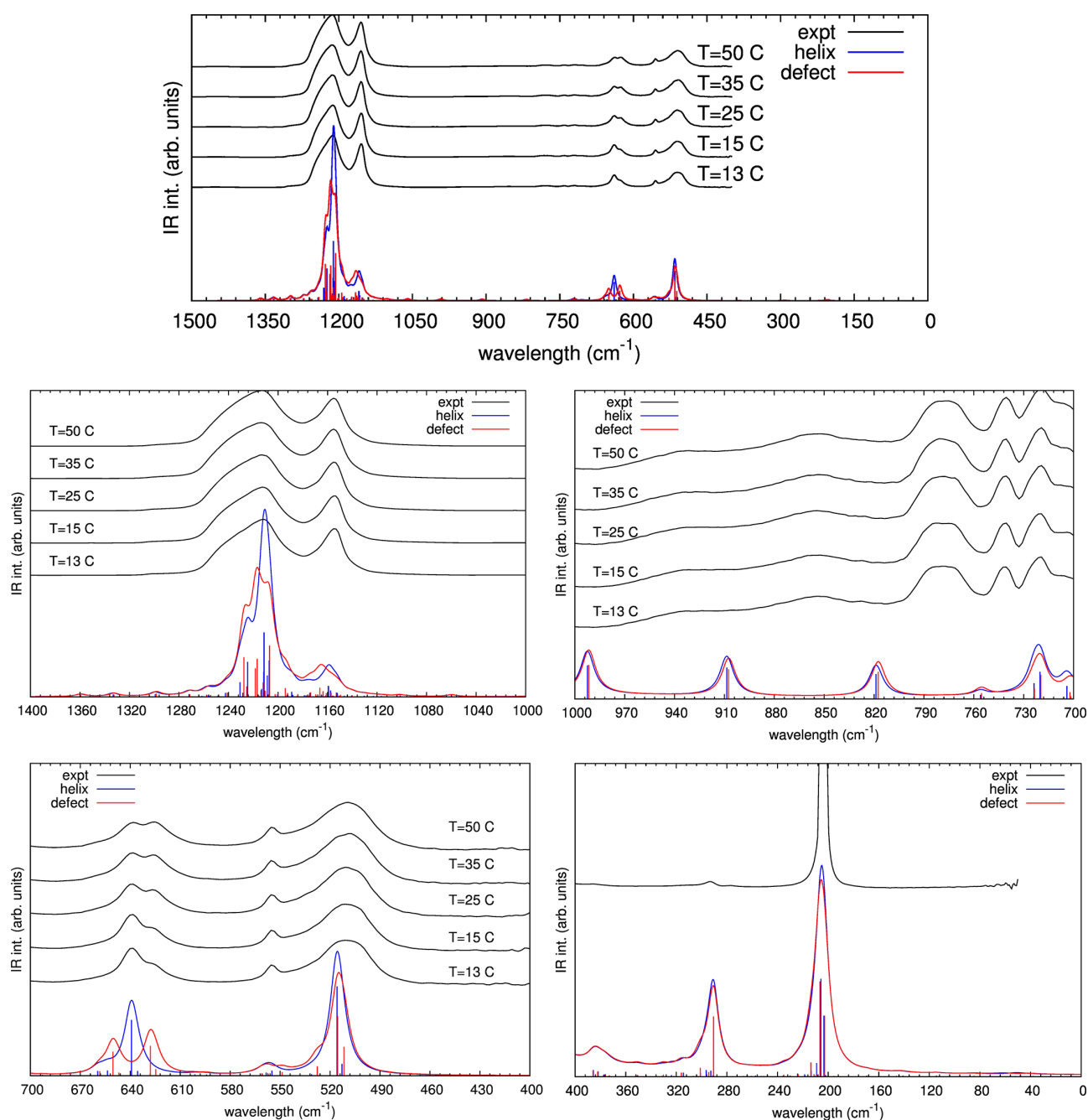


Figure 5. Comparison of the IR spectrum of $C_{28}F_{58}$ oligomer in two different optimized conformations: (i) regular helical structure; (ii) helix-reversal defect. Experimental spectra of PTFE at different temperatures are also shown. Calculations carried out with the GAUSSIAN09 package (B3LYP/TZVP). No scaling factor for the frequencies is used. Different intensity scales are adopted in the different spectral range, for a better visualization. Theoretical spectra have been obtained by assuming a Lorentzian band shape with a full width at half-maximum of 10 cm^{-1} .

seventh or eighth chemical units around the helix-reversal defect for both $C_{16}F_{34}$ and $C_{28}F_{58}$.

In Figure 7, we report the eigenvector associated to the high component of the doublet, for $C_{28}F_{58}$. A similar normal mode is found for the transition at 724 cm^{-1} predicted for $C_{16}F_{34}$, as shown in the same figure. The two normal modes sketched in Figure 7 can be described mainly as scissoring vibration of the CF_2 units, and they involve the whole chain and especially chemical units near the ends; their remarkable frequency shift can be ascribed to the different number of units involved, forming

a sequence with a regular helical conformation. On these grounds, we can argue that the 638 cm^{-1} band provides information about the coherence length of regular helical segments in real polymeric chains of PTFE. In Figure S13 (Supporting Information), the IR spectrum calculated for oligomers of increasing length and containing helix-reversal defect is reported and the bands associated to vibrational modes with eigenvector similar to those reported in Figure 7 are highlighted.

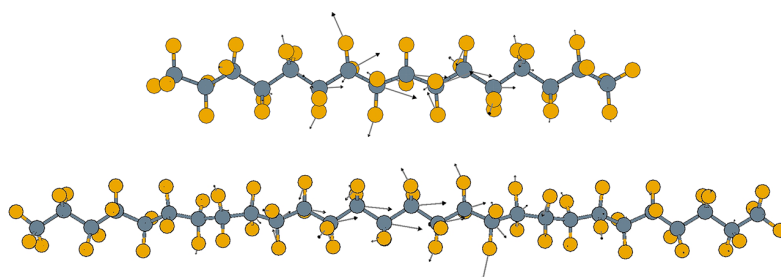


Figure 6. Eigenvectors associated with the band at 626 cm^{-1} as obtained from DFT calculations (B3LYP/TZVP) on $\text{C}_{16}\text{F}_{34}$ oligomer (upper panel) and on $\text{C}_{28}\text{F}_{58}$ (lower panel).

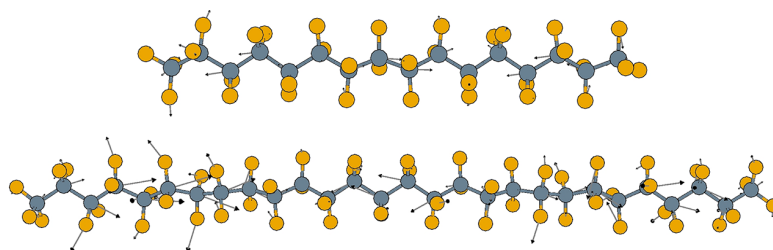


Figure 7. Eigenvectors associated with the band at 638 cm^{-1} as obtained from DFT calculations (B3LYP/TZVP) on $\text{C}_{16}\text{F}_{34}$ oligomer (upper panel) and on $\text{C}_{28}\text{F}_{58}$ (lower panel).

The selectivity of the helix-reversal defect (and that of its infrared marker band at 626 cm^{-1}) for a given kind of helix is another intriguing issue. In order to obtain some insight on this point, we studied the spectroscopic behavior of a helix-reversal defect on a chain characterized by both the 13_6 and 15_7 structures. Since a full optimization of a short chain always determines its relaxation into a structure with torsional angles of about 162° , it is necessary that all the torsional angles are kept fixed to the characteristic values reported in Table 1 for the 13_6 and 15_7 helices. For the two regular conformations, we calculated IR spectra for (i) the regular helical configuration and (ii) the chain carrying a helix-reversal defect in the middle, described as two segments characterized by the torsional angles of the 13_6 and 15_7 helices with opposite chirality and joined together. In other words, no relaxation for the torsional angles close to the helix-reversal defect was allowed. Calculations are carried out on the $\text{C}_{16}\text{F}_{34}$ oligomer. In Figure 8, the IR spectra of both (i) the regular helical configuration and (ii) the chain carrying a helix-reversal defect are compared in the region $700\text{--}400\text{ cm}^{-1}$. For each chain model, we found that the formation of the helix-reversal defect down-shifts the band at 640 cm^{-1} . The value of the frequency for the mode characteristic of the regular chain and of the defect band depends on the specific chain model adopted, but the computed frequencies always fall in the region of interest. Thus, we can conclude that the band at 626 cm^{-1} is not peculiar neither of the 13_6 nor of the 15_7 conformation.

3.3. CONFORMATIONAL STUDY

In order to evaluate the contributions of the amorphous phase to the IR spectrum of PTFE, we carried out a conformational study on a short oligomer. To this aim, we considered the C_8F_{18} oligomer as the best compromise between computational effort and accuracy needed to carry out a systematic investigation of the conformational space. The procedure for this analysis was the following. We constructed all the conformers which can be obtained by selecting, for each torsional angle, one of the following values: $0, 60, 120, 180, 240, 300^\circ$. In this way, we

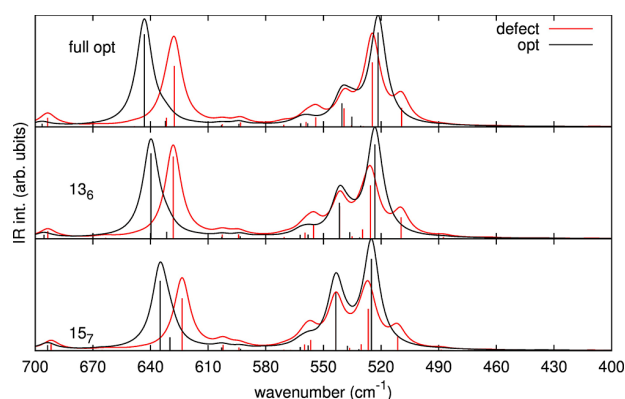


Figure 8. Comparison between the computed (B3LYP/TZVP) IR spectra for the $\text{C}_{16}\text{F}_{34}$ oligomer in its regular conformation (black line) and with a helix-reversal defect (red line). The molecular geometries are obtained according to three different ways: (i, top panel) fully optimized structure; (ii, middle panel) constrained 13_6 conformation; (iii, bottom panel) constrained 15_7 conformation.

collected 5^6 conformers. The conformation of each of them was optimized at a low theoretical level, namely, RHF/3-21G(d). Among the different conformers obtained, we selected only those characterized by a relative energy which does not exceed more than 5 kcal/mol the energy of the most stable structure, namely, that showing a structure similar to the 13_6 helix. Starting from the geometries so selected, a more accurate optimization and the calculation of the IR spectrum were carried out at the B3LYP/TZVP level.

The conformational analysis highlighted the presence of 49 conformers within the energy range of interest, whose energies and conformations are reported in Table S12 (Supporting Information). The theoretical IR spectrum characteristic of the amorphous phase reported in Figure 9 was obtained by summing the contribution from each conformer, weighted for its respective Boltzmann population at a given temperature, similarly to

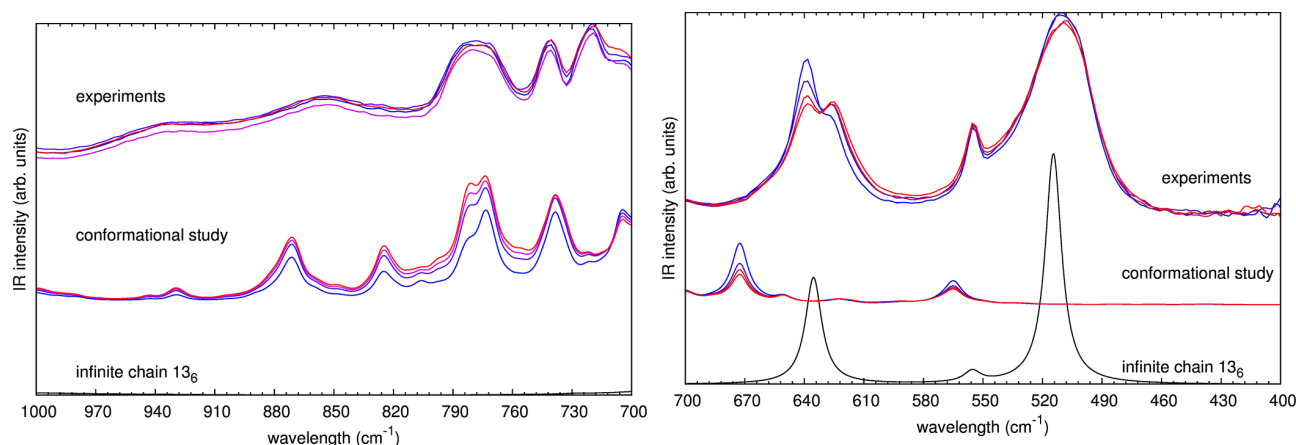


Figure 9. Comparison of the experimental IR spectra at various temperatures with those obtained by means of the conformational analysis of C_8F_{18} : the theoretical IR spectra are obtained by weighting the IR spectrum of each conformer with its corresponding Boltzmann statistical weight at different temperatures. The spectrum obtained for the infinite chain model 13_6 is also reported for the sake of comparison (B3LYP/TZVP).

previous studies.^{1a,31} We focus on the IR spectra of these conformers in the region between 1000 and 400 cm^{-1} in order (i) to discuss the possible contribution of the amorphous phase to the 638–626 cm^{-1} doublet and (ii) to analyze the region 900–700 cm^{-1} , traditionally associated to the amorphous phase. All the computed spectra are reported in Table S13 (Supporting Information).

Dealing with the first point (see Figure 9, region 700–400 cm^{-1}), we observe that only a few conformers show IR bands in the region of the 638–626 cm^{-1} doublet, namely, conformer nos. 108, 138, 58, 46, 21, 61, and 55. All of these conformers are characterized by two gauche-like torsional angles at about 60 or 90°, excluding no. 55 that shows three torsional angles around 90°. However, all of these conformers lie at higher energy than that of the helix-reversal defect (at least 2 kcal/mol above the most stable 13_6 helix-like geometry), to be compared with 1.5 kcal/mol, corresponding to the energy needed to make the helix-reversal defect. Moreover, the computed intensity of the transitions which can be put in correspondence with the 626 cm^{-1} band are generally very weak. Only conformer no. 58 shows a band with IR intensity comparable to that shown by the helix-reversal model (43 vs 238 kcal/mol). In addition, a contribution of the amorphous phase to the steep increase observed for the 626 cm^{-1} band above 19 °C should be excluded because it would require a fast increase in the concentration of gauche-like defects in correspondence of the crystalline phase transitions (between 19 and 30 °C).^{7c} Such defects can be hardly hosted in a crystalline phase, characterized by parallel, well packed chains. Molecular dynamic simulations, made by Sprik and co-workers, showed that formation of gauche defects within ordered regions of PTFE occurs only at very high temperatures (hundreds of °C), that is, in a temperature range in proximity of melting.³² For all of these reasons, we believe that the contribution of the amorphous phase to the IR intensity of the 638–626 cm^{-1} doublet is negligible (see Figure 9, region 700–400 cm^{-1}).

Dealing with the second point (see Figure 9, region 1000–700 cm^{-1}), from the inspection of the IR spectra collected in Table S13 (Supporting Information), we find many conformers that show intense bands in this spectral region. In particular, some predicted bands fall in correspondence with the experimental 740 and 720 cm^{-1} features, which were previously associated to phonons at $k \neq 0$. We believe that these bands get their intensity both from finite chain effects and from a truly amorphous phase.

In addition, many conformers show bands in correspondence with the 778 cm^{-1} broad band (conformer nos. 10, 26, 121, 113, 119, 79, 106, 38, 41, 115, 74, 7, 9, 68, 44, 61, 89, 99, 111, 32, and 34), that was associated by Moynihan⁹ to the amorphous phase; this interpretation is now confirmed by our present investigation.

4. DISCUSSION

The analysis presented in this paper allows to settle the assignment of the 638–626 cm^{-1} doublet in the IR spectrum of PTFE. The assignment of the 626 cm^{-1} band to the formation of trans-planar sequences¹³ can be definitely rejected because no IR active bands have been calculated for the 2_1 helical conformation in the spectral region of interest. The assignment proposed by Brown, who argued that the 626 cm^{-1} band is associated to the helix-reversal defect,⁴ is instead confirmed by our theoretical investigation. In fact, our calculations show that a stable structure associated to the helix-reversal defect exists, with energy of 1.5 kcal/mol above the energy of the most stable conformation (the 13_6 helix), in good agreement with the estimate from IR intensity measurements.⁴ In addition, the IR spectrum of this structure presents an IR active marker in correspondence to the lower component of the 638–626 cm^{-1} doublet.

This result confirms previous interpretations of the infrared features of PTFE, which have been attributed to the presence of structural disorder in crystalline PTFE, even at temperatures well below the melting point. In particular, based on the assignment of the 626 cm^{-1} feature to the helix-reversal defect, Kimmig and Strobl suggested that the transition from the 13_6 to the 15_7 helical conformation in PTFE is a transition from a state where intermolecular interactions are dominant to a state where intramolecular interactions prevail.^{7c} At low temperatures (lower than 19 °C), effective intermolecular interactions oppose the formation of helix-reversal and the concentration of these defects remains small. At the form II–form IV transition, the intermolecular interactions become less effective and thus the helix-reversal defects can easily develop, increasing in concentration until the thermodynamic equilibrium for the (quasi) isolated chain is reached. Accordingly, the transition at room temperature is better described as an order–disorder transition than as a true transition between different crystalline phases. This interpretation is consistent with the fact that crystal packing goes

from a triclinic structure in the 13_6 helix, that maximizes the intermolecular interactions of helical systems, to a hexagonal one for 15_7 helices.³ This structure indeed maximizes the packing of perfectly cylindrical objects, that is, for helices free to rotate.

Note that this interpretation is based on the assumption that the 13_6 conformation is stabilized by intermolecular interactions, while the 15_7 conformation is the true stable one, from a conformational point of view. Our calculations predict very small energy differences for these conformations (see Table 1), comparable with intermolecular interactions, but unfortunately, they cannot give a definitive validation to such an interpretation.

5. CONCLUSIONS

This work reanalyzes critically the interpretation of the IR spectrum of PTFE. Calculations with state-of-the-art methods for the prediction of the electronic and molecular structure are carried out at the aim of interpreting the experimental spectral features. Our calculations definitively settle the assignment of the $638\text{--}626\text{ cm}^{-1}$ doublet of PTFE as due to the formation of a helix-reversal defect, as proposed by Brown.⁴

The assignment of the bands at 740 , 720 , and 288 cm^{-1} to segments of helices with 10_3 and 4_1 conformation⁴ could be acceptable, but it seems not to be the main contribution because of the high energetic cost of these conformations (greater than 10 kcal/mol for helix turn). In fact, the experimental bands at 740 , 720 , and 288 cm^{-1} fall in correspondence with some transitions calculated for finite size chains (oligomers), with both helical structure and helix-reversal defects. On these grounds, the presence of such bands, showing constant IR intensity between 13 and $50\text{ }^\circ\text{C}$, can be taken as the evidence of the relatively low coherence length of the helix, already at low temperature.

As last useful result from a practical point of view, the assignment of the 778 cm^{-1} to the amorphous phase by Moynihan⁹ is confirmed by our analysis and then the use of the IR intensity of this band for a quantitative determination of the amount of amorphous material in real sample is supported by our theoretical results.

■ ASSOCIATED CONTENT

📄 Supporting Information

Table with DFT computed equilibrium torsional angles and minimum energies of the 15_7 , 13_6 , 10_3 , 4_1 , and 2_1 helical structures of infinite chains. B3LYP/6-31G(d,p) and B3LYP/TZVP IR spectra of the 15_7 , 13_6 , 10_3 , 4_1 , and planar 2_1 conformations calculated on infinite polymeric chains. Comparison between the spectra calculated on infinite polymeric chains and on finite oligomers of about 30 CF_2 units for the different helices. IR spectra calculated for a different helical reversal defect. Table with the energy and conformation of the 49 conformers obtained from the conformational analysis. IR spectra calculated on the 49 conformers selected from the conformational analysis in the region between 1000 and 400 cm^{-1} . Tables with the optimized geometries of the different helices and tables with their DFT computed frequencies and IR intensities. This material is available free of charge via the Internet at <http://pubs.acs.org>.

■ AUTHOR INFORMATION

Corresponding Author

*E-mail: claudio.quarti@mail.polimi.it.

Notes

The authors declare no competing financial interest.

■ ACKNOWLEDGMENTS

The authors are grateful to Dr. Andrea Lucotti (Politecnico di Milano) and Dr. Stefano Radice (R&D Analytical & Structural Characterization - Solvay Specialty Polymers Italy SpA) for providing the experimental IR spectra reported in the paper and to Solvay Specialty Polymers Italy SpA for providing the PTFE samples.

■ REFERENCES

- (1) (a) Tommasini, M.; Castiglioni, C.; Milani, A.; Zerbi, G.; Radice, S.; Toniolo, P.; Grozzi, C.; Picozzi, R.; Di Meo, A.; Tonelli, C. *J. Fluorine Chem.* **2006**, *127*, 320–329. (b) Milani, A.; Tommasini, M.; Castiglioni, C.; Zerbi, G.; Radice, S.; Canil, G.; Toniolo, P.; Triulzi, F.; Colaianna, P. *Polymer* **2008**, *49*, 1812–1822. (c) Milani, A.; Castiglioni, C.; Di Dedda, E.; Radice, S.; Canil, G.; Di Meo, A.; Picozzi, R.; Tonelli, C. *Polymer* **2010**, *51*, 2597–2610.
- (2) (a) Clark, E. S. *Polymer* **1999**, *40*, 4659–4665. (b) Clark, E. S. *J. Macromol. Sci., Part B: Phys.* **2006**, *45*, 201–213.
- (3) Tadokoro, H. *Structure of Crystalline Polymers*; John Wiley and Sons: New York, 1979.
- (4) Brown, R. G. *J. Chem. Phys.* **1964**, *40*, 2900–2908.
- (5) (a) Rigby, H. A.; Bunn, C. W. *Nature* **1949**, *164*, 583–583. (b) Bunn, C. W.; Howels, E. R. *Nature* **1954**, *174*, 549–551.
- (6) (a) Marx, P.; Dole, M. *J. Am. Chem. Soc.* **1955**, *77*, 4771–4774. (b) Villani, V. *Spectrochim. Acta* **1990**, *162*, 189–193.
- (7) (a) Corradini, G.; Guerra, G. *Macromolecules* **1977**, *10*, 1410–1413. (b) Farmer, B. L.; Eby, R. K. *Polymer* **1981**, *22*, 1480–1486. (c) Kimmig, M.; Strobl, G.; Stuhn, B. *Macromolecules* **1994**, *27*, 2481–2495.
- (8) Liang, C. Y.; Krimm, S. *J. Chem. Phys.* **1956**, *25*, 563–571.
- (9) Moynihan, R. E. *J. Am. Chem. Soc.* **1959**, *81*, 1045–1050.
- (10) (a) Koenig, J. L.; Boerio, F. J. *J. Chem. Phys.* **1969**, *50*, 2823–2829. (b) Hannon, M. J.; Koenig, J. L.; Boerio, F. J. *J. Chem. Phys.* **1969**, *50*, 2829–2836. (c) Koenig, J. L.; Boerio, F. J. *J. Chem. Phys.* **1970**, *52*, 4170–4171. (d) Boerio, F. J.; Koenig, J. L. *J. Chem. Phys.* **1970**, *52*, 4826–4829. (e) Boerio, F. J.; Koenig, J. L. *J. Chem. Phys.* **1971**, *54*, 3667–3677.
- (11) Peacock, C. J.; Hendra, P. J.; Willis, H. A.; Cudby, M. E. *J. Chem. Soc. A* **1970**, 2943–2947.
- (12) Piseri, L.; Powell, B. M.; Dolling, G. *Bull. Am. Phys. Soc.* **1971**, *16*, 311–?.
- (13) (a) Zerbi, G.; Sacchi, M. *Macromolecules* **1973**, *6*, 692–699. (b) Masetti, G.; Cabassi, F.; Morelli, G.; Zerbi, G. *Macromolecules* **1973**, *6*, 700–707.
- (14) Rae, P. J.; Dattelbaum, D. M. *Polymer* **2004**, *45*, 7615–7625.
- (15) De Santis, P.; Gliglio, E.; Liquori, A. M.; Ripamonti, A. *J. Polym. Sci., Part A* **1963**, *1*, 1383–1404.
- (16) Farmer, B. L.; Eby, R. K. *Polymer* **1985**, *26*, 1944–1952.
- (17) Quarti, C.; Milani, A.; Civalleri, B.; Orlando, R.; Castiglioni, C. *J. Phys. Chem. B* **2011**, *116*, 8299–8311.
- (18) (a) Javier Torres, F.; Civalleri, B.; Meyer, A.; Musto, P.; Albulnia, A. R.; Rizzo, P.; Guerra, G. *J. Phys. Chem. B* **2009**, *113*, 5059–5071. (b) Javier Torres, F.; Civalleri, B.; Pisani, C.; Musto, P.; Albulnia, A. R.; Guerra, G. *J. Phys. Chem. B* **2007**, *111*, 6327–6335. (c) Albulnia, A. R.; Rizzo, P.; Guerra, G.; Javier Torres, F.; Civalleri, B.; Zicovich-Wilson, C. M. *Macromolecules* **2007**, *40*, 3895–3897. (d) Ferrari, A. M.; Civalleri, B.; Dovesi, R. *J. Comput. Chem.* **2010**, *31*, 1777–1784.
- (19) (a) Zerbi, G.; Magni, R.; Gussoni, M.; Holland-Moritz, K.; Bigotto, A. B.; Dirlikov, S. *J. Chem. Phys.* **1981**, *75*, 3175–3194. (b) Zerbi, G.; Minoni, G.; Tulloch, M. P. *J. Chem. Phys.* **1983**, *78*, 5853–5862. (c) Piazza, R.; Zerbi, G. *Polymer* **1982**, *23*, 1921–1928. (d) Zerbi, G. *Vibrational spectroscopy of very large molecules*. In *Advances in Infrared and Raman spectroscopy*; Clark, R. J. H., Hester, R. E., Eds.; Heyden: New York, 1984; Vol. *11*, p 301. (e) *Modern Polymer Spectroscopy*; Zerbi, G., Ed.; Wiley-VCH: Weinheim, Germany, 1999.
- (20) Dovesi, R.; Orlando, R.; Civalleri, B.; Roetti, C.; Saunders, V. R.; Zicovich-Wilson, C. M. *Z. Kristallogr.* **2005**, *220*, 571–273.

(21) Frisch, M. J.; Trucks, G. W.; Schlegel, H. B.; Scuseria, G. E.; Robb, M. A.; Cheeseman, J. R.; Scalmani, G.; Barone, V.; Mennucci, B.; Petersson, G. A.; et al. *Gaussian 09*, revision A.02; Gaussian, Inc.: Wallingford, CT, 2009.

(22) Becke, A. D. *J. Chem. Phys.* **1996**, *104*, 1040–1046.

(23) Schafer, A.; Huber, C.; Ahlrichs, R. *J. Chem. Phys.* **1994**, *100*, 5829–5835.

(24) Hehre, W. J.; Ditchfield, R.; Pople, J. A. *J. Chem. Phys.* **1972**, *56*, 2257–2261.

(25) (a) Grimme, S. *J. Comput. Chem.* **2004**, *25*, 1463–1473.

(b) Grimme, S. *J. Comput. Chem.* **2006**, *27*, 1787–1795. (c) Civalleri, B.; Zicovich-Wilson, C. M.; Valenzano, L.; Ugliengo, P. *CrystEngComm* **2008**, *10*, 405–410.

(26) Since the different helical symmetries have been imposed in the calculations, we are not guaranteeing that the optimized chain structures correspond to true minima of the intramolecular potential energy surface. On the other hand, the full optimization of the geometry carried out on PTFE oligomers (see section 3.1.2) brings to the conclusion that the most stable conformation is characterized by torsional angles very close to the value of the 13_6 helix (163.4). In addition, an optimization with very small optimization steps and tight convergence criteria (“verytight” keyword used in the Gaussian input) from the starting geometry of the 15_7 helix (guess torsional angles fixed at $\theta = 165.6$) relaxes toward the most stable conformation (like the 13_6 helix).

(27) Smith, G. D.; Jaffe, R. L.; Yoon, D. Y. *Macromolecules* **1994**, *27*, 3166–3173.

(28) Rothlisberger, U.; Laasonen, K.; Klein, M. L.; Sprik, M. *J. Chem. Phys.* **1996**, *104*, 3692–3700.

(29) (a) D’Amore, M.; Auremma, F.; De Rosa, C.; Barone, V. *Macromolecules* **2004**, *37*, 9473–9480. (b) D’Amore, M.; Talarico, G.; Barone, V. *J. Am. Chem. Soc.* **2006**, *128*, 1099–1108.

(30) As an alternative strategy for the investigation of the structure and energetic properties of the helix-reversal defect, it is possible to carry out calculations also on a 1D periodic model of the defect. This study would require a further wide computational study which goes beyond the aims of the present paper, and it is left for future investigations. On the other hand, the molecular model of the defect here adopted is long enough to give a reliable description of the relevant dynamical couplings responsible for the spectroscopic response.

(31) Milani, A.; Zanetti, J.; Castiglioni, C.; Di Dedda, E.; Radice, S.; Canil, G.; Tonelli, C. *Eur. Polym. J.* **2012**, *48*, 391–403.

(32) Sprik, M.; Rothlisberger, U.; Klein, M. L. *J. Phys. Chem. B* **1997**, *101*, 2745–2749.

Appendix A

Organic and hybrid nanostructures for SOLar energy CONversion (SOLCO)

A.1 Introduction

In this chapter we present some preliminary results related to a project aimed to the development of innovative organic and hybrid nanostructures for the frequency conversion of the solar spectrum, in particular for the down-conversion from the UV and blue light to the red and Near InfraRed (NIR) region. The need for frequency conversion of light is strongly related to a more efficient use of the solar energy and systems that convert efficiently the light can find many applications in fields such as agriculture and photovoltaics. The photosynthetic process for instance has its maximum efficiency in the red-NIR (above 650 nm) and in the near UV (below 400 nm) part of the spectrum but the solar spectrum has its maximum intensity in correspondence of the yellow light (500 nm). The use of new cover materials for greenhouses which efficiently down-convert the visible light from the yellow to the red would increase the crop production and reduce water and soil contamination caused by the use of chemicals [119]. Similarly, silicon based photovoltaic cells have their maximum efficiency in a frequency range between 800 and 900 nm and the use of efficient luminescent solar concentrators, that absorb high energy sun light and re-emit it at longer wavelengths, would result in an increase of the efficiency of the photovoltaic process [120].

The central idea of this project is to recur to nanostructures composed by different chromophores. An *absorber/donor* chromophore absorbs large frequency photons and transfers its excitation energy by *resonance energy transfer* to an *acceptor/emitter* chromophore. The acceptor is chosen to have a smaller band gap than the donor. This cascade mechanism is depicted in

Figure A.1. The present design allows for a flexible tuning of the final emission wavelength, by properly choosing the number of chromophores and their energy levels.

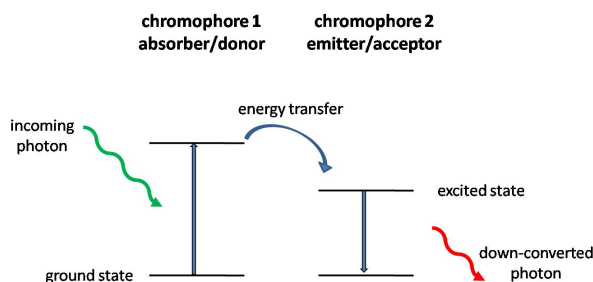


Figure A.1: Representation of the cascade mechanism proposed for the down-conversion of the solar light.

For the absorber/donor moiety, we have considered π -conjugated organic dyes, which absorb in the green and blue regions and which have large absorption cross sections. As emitter/acceptor moiety we have turned our attention to inorganic quantum dots (QD), which show efficient emission in the long wavelength portion of the Vis spectrum and in the NIR and whose emission wavelength can be properly tuned as function of the size and composition of the quantum dots. Hybrid donor/acceptor systems composed by organic dyes and inorganic quantum dots (QD) are not new and a plethora of studies where these systems are coupled together have been reported in the literature, mainly dedicated to the development of sensors [121, 122] and in photovoltaics [123]. These systems are also widely studied to investigate the resonance energy transfer process, because of the large chemical flexibility of these systems that allow to control the donor-acceptor separation [124, 125, 126, 127, 128, 129, 130].

The innovative idea of the present project is to couple the hybrid donor/acceptor design to that of the *host-guest* compound. In fact, we have chosen to include the organic dye in β -cyclodextrin (b-CD). This design provides different advantages. I) Intermolecular interactions taking place for organic dyes in the solid phase are in general detrimental for both the emission and the energy transfer processes since they introduce non radiative decay pathways that quench the exciton before it is emitted or it is transferred to the acceptor; the inclusion in β -cyclodextrin allows to avoid such interactions. II) At the same time, the inclusion in b-CD preserves a high density of the organic dye allowing to maximize the absorbed light, in a sort of *antenna complex*. III) Finally, it allows to tune the relative dye-QD distance and orientation to obtain the largest energy transfer efficiencies. After some introductory tests we have chosen a benzofurazan derivate,

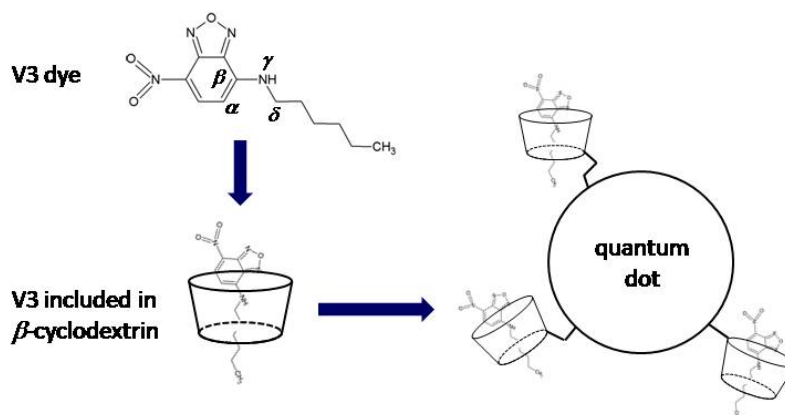


Figure A.2: Design of the nanostructure proposed for the frequency conversion of the solar spectrum. The V3 organic dye is included in β -cyclodextrin and various inclusion complex are attached to a single CdSe/ZnS.

the 4 - *hexylamino* - 7 - *nitro* - 2,1,3 - *benzoxadiazoles* (V3), as absorber/donor moiety. This chromophore absorbs the light at about 480 nm. As acceptor/emitter moiety, we have chosen a CdSe/ZnS core-shell QD, with a diameter of 6.3 nm and an emission wavelength declared by the producer around to be around 640 nm. The molecular structure of V3, V3 and b-CD inclusion complex and the whole nanostructure, are depicted in Figure A.2.

The nanostructures have been synthesized by the group of Prof. Paola del Buttero and the group of Prof. Giuseppe Di Silvestro (Univ. of Milano). The group of Dr. Chiara Botta (ISMAC-CNR) has carried out the UV-Vis characterization of the nanostructure. The author's group instead is involved in the theoretical modeling of the nanostructures.

The remaining part of this chapter is organized as follows. In Section A.2 we report some introductory results from the photophysical characterization of the V3 dye. These measurements demonstrate that specific intermolecular interactions between the V3 dye and the solvent have an important role on the optical properties of this chromophore. In Section A.3, we present and discuss some preliminary DFT and TD-DFT calculations, with the purpose of explaining the behavior of the V3 molecule in solution.

A.2 Experimental results

The optical properties of the V3 molecule have been investigated with UV-Vis and photoluminescence spectroscopy. The absorption and emission spectrum of the V3 molecule have been measured in solution with solvent of

different polarity: *ethyl acetate* (dielectric constant, $\epsilon=6.0$), *tetrahydrofuran* (THF, $\epsilon=7.5$), *dichloromethane* ($\epsilon=9.1$), *methanol* ($\epsilon=33.1$), *acetonitrile* ($\epsilon=36.2$) and *dimethylformamide* (DMF, $\epsilon=38.3$). The measured absorption and emission wavelength and the emission quantum yield (QD) are summarized in Table A.1.

Table A.1: Experimental absorption (λ_{abs}) and emission wavelength (λ_{emi}) of the V3 molecule in various solvents.

solvent	ϵ	λ_{abs} (nm)	λ_{emi} (nm)
ethyl acetate	6.02	460	525
THF	7.50	460	525
dichloromethane	9.10	455	515
methanol	33.10	475	540
acetonitrile	36.20	470	530
DMF	38.30	480	535

As showed in Table A.1, both the absorption and the emission wavelengths present a non monotonic behavior with the dielectric constant of the solvent. They are constant for the two solvents with smaller dielectric constant, then they decrease respectively to 455 and 515 nm in dichloromethane, they increase to 475 and 540 nm in methanol, decrease to 470 and 530 nm in acetonitrile and they increase again to 480 and 535 nm. Because of this non monotonic modulation of the optical properties of the V3 molecule, we cannot explain the solvent effects as due to the reciprocal polarization between dye and solvent. Instead, it is reasonable to assume that specific intermolecular interactions between the molecule and the solvent play an important role in determining the optical properties of this chromophore.

A.3 Theoretical calculations

DFT and TD-DFT calculations have been carried out with the B3LYP functional and the 6-31G(d,p) basis set. The present method generally provides accurate results with a limited computational cost. The optical properties of the isolated molecule have been investigated first in vacuum. Then we considered the interactions with the solvent by using both the *polarizable continuum model* (PCM) and specific interaction models, where the solvent molecules are considered explicitly.

A.3.1 Optical properties of the isolated molecule

The molecular structure of the V3 chromophore in the ground state has been optimized at DFT level. We have considered the V3 molecule in both the CIS

and TRANS conformation with respect to the atoms with label α , β , γ , δ in Figure A.2 and we have verified that the CIS conformer is actually the most stable. We carried out also the calculation of the vibrational frequencies to verify that the obtained molecular structure is a real minimum of the potential energy surface of the molecule. Singlet excited states have been calculated at the TD-DFT level on the optimized molecular structure, in order to compare the excitation energies with the experimental absorption energies. Our calculations show that the first excited state is dipole allowed, with an oscillator strength of 0.2444 and a transition dipole moment of about 1.77 atomic units oriented along the direction from the NO₂ group to the alkane chain. TD-B3LYP calculation considerably overestimates the excitation energy of about 0.50 eV, setting the vertical excitation energy at about 3.2 eV. However, such a large overestimation of the excitation energy is not unexpected. In fact, Jacquemine and co-workers found that the B3LYP functional applied to a large set of molecules, provides a mean absolute overestimation of the excitation energies of about 0.3 eV [131]. The transition from the ground state to the first excited state corresponds mainly to a transition from the HOMO to the LUMO orbitals, which are depicted in Figure A.3.

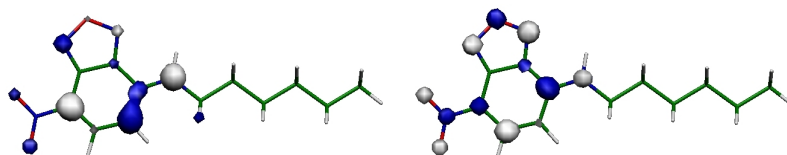


Figure A.3: Molecular orbitals mainly involved in the transition from the ground to the first singlet excited state of the V3 molecule in gas phase. Excited state calculations at TD-B3LYP/6-31G(d,p) level on the ground state obtained at B3LYP/6-31FG(d,p) optimized geometry

A.3.2 Calculations with PCM

Within PCM method the solute molecule is embedded into a cavity and the presence of the solvent is mimicked by point charges on the cavity surface, whose distribution depends on the relative polarization of the charges and of the electron density of the solute [132]. In this way the polarization effects can be evaluated but the effect due to specific interactions, such as hydrogen bonds, cannot be taken into consideration. Thus, we have carried out these calculations for sake of completeness and to estimate the strength of the polarization effects but we do not expect that they are able to reproduce the non monotonic pattern in the excitation and emission energies of the V3 molecule with the polarity of the solvent.

We first investigated the absorption properties of the V3 molecule. The molecular structure of the V3 dye has been optimized again in the ground state at DFT level with PCM, by setting the relative dielectric constant equal to the values reported in Table A.1 for the various solvents. Then, we have calculated the excited states of the obtained structure at the TD-DFT in PCM. The excitation energies from the ground to the first excited state for the various solvents are reported in Figure A.4 and compared with the experimental data. Also in this case the theoretical calculations overestimate the experimental excitation energies by about 0.4 eV. As shown in Figure A.4, with the increasing of the solvent polarity the excitation energy to the first excited state red-shifts of about 0.05 eV, reaching a plateau for dielectric constant greater than 30.

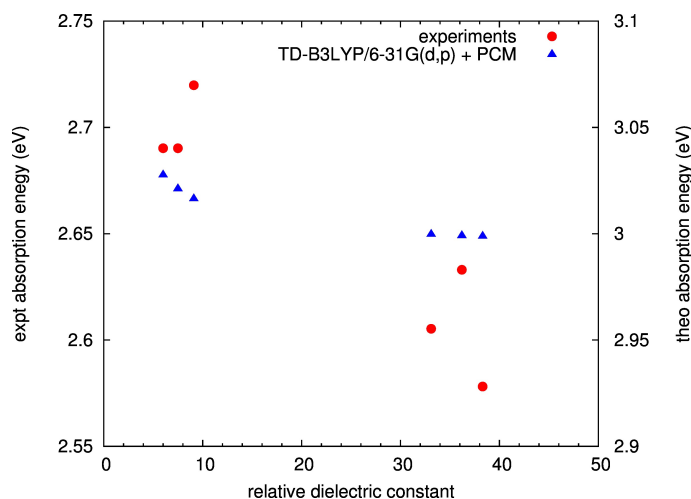


Figure A.4: Comparison between the UV-Vis experimental absorption energy and the theoretical excitation energy from the ground state to the first excited state of the molecule V3 calculated in different solvents. Excited states calculations carried out at TD-B3LYP/6-31G(d,p) on the B3LYP/6-31G(d,p) ground state geometry. Solvent effects modeled with the *polarizable continuum model* (PCM).

We have investigated also the emission properties of the V3 molecule. The molecular structure of the first excited state of the V3 molecule has been optimized at the TD-B3LYP/6-31G(d,p) level in PCM. The difference between the energy of the first excited state and the ground state in the equilibrium structure of the former (which corresponds to the emission from the first excited state) is depicted in Figure A.5 as a function of the solvent polarity and it is compared with the experimental emission energies data. As for the absorption, we observe a red-shift of the emission energy which reaches a plateau value of about 0.05 eV for dielectric constant greater than

30.

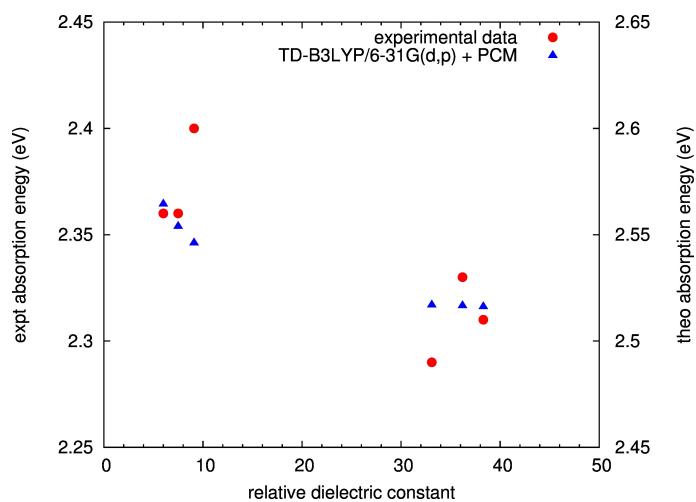


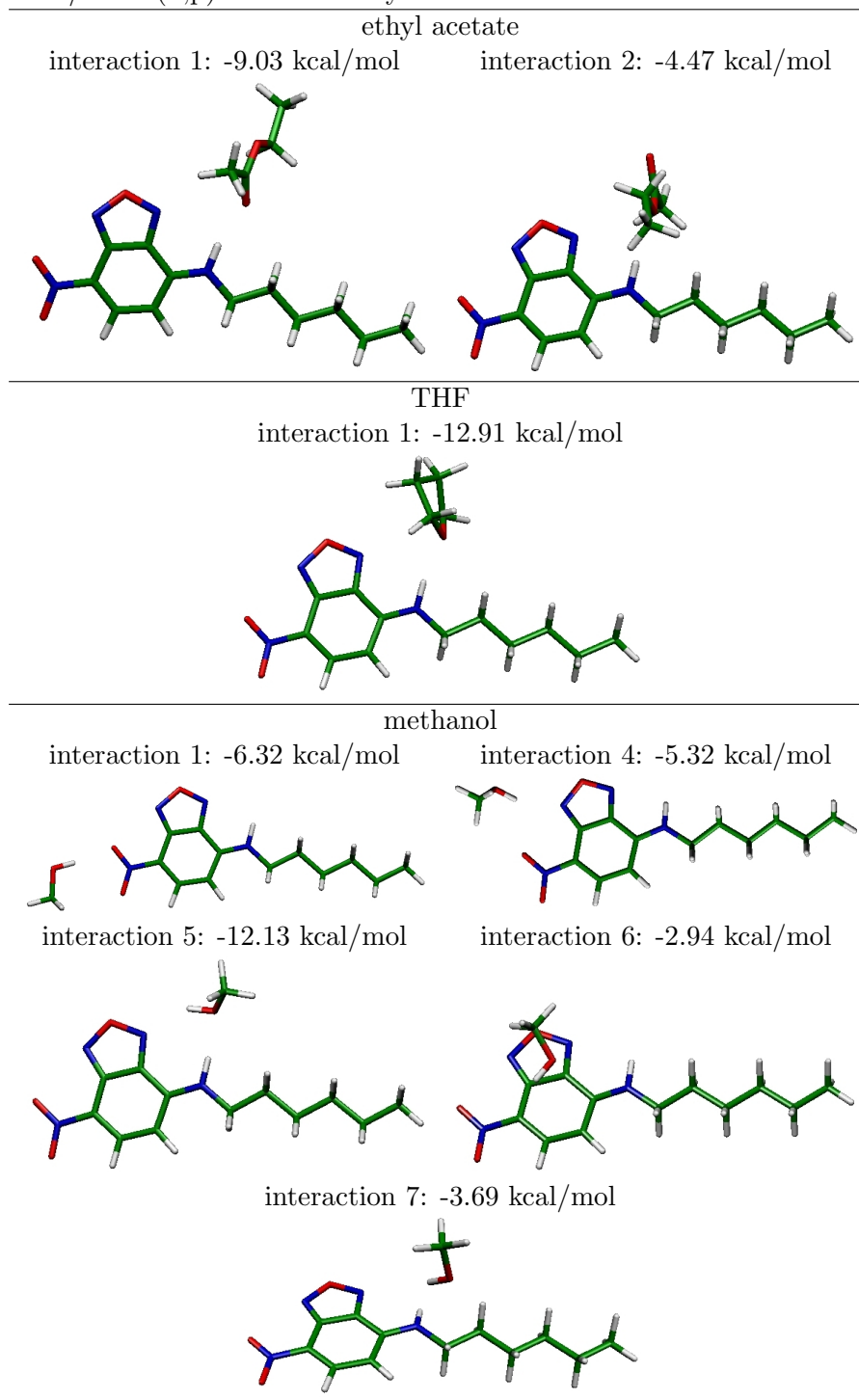
Figure A.5: Comparison between the experimental emission energy and the theoretical energy of the transition from the first excited state to the ground state in different solvents. Excited states calculations carried out at TD-B3LYP/6-31G(d,p) on the TD-B3LYP/6-31G(d,p) geometry of the first excited state. Solvent effects modeled with the *polarizable continuum model* (PCM).

A.3.3 Explicit interaction models

In order to study the effects of specific intermolecular interactions with the solvent on the optical properties of V3, we have developed some molecular models where these interactions are treated explicitly. We have considered molecular systems constituted by the V3 molecule and just one solvent molecule. We do not pretend that such simple models are sufficient to reproduce quantitatively the optical properties of the V3 molecule in solution but we expect that they provide some useful indication on the effect of the intermolecular interactions. Future studies could take into consideration more solvent molecules. The dimer configurations have been chosen on the basis of the possibility to form a hydrogen bond (H-bond) between the dye and the solvent molecule. For this study we have considered all the solvents reported in Table A.1 except dichloromethane, since halogen bonds are more difficult to be described accurately. Subsequently, each interaction model (referred to as dimer) has been optimized at the B3LYP/6-31G(d,p) theory level.

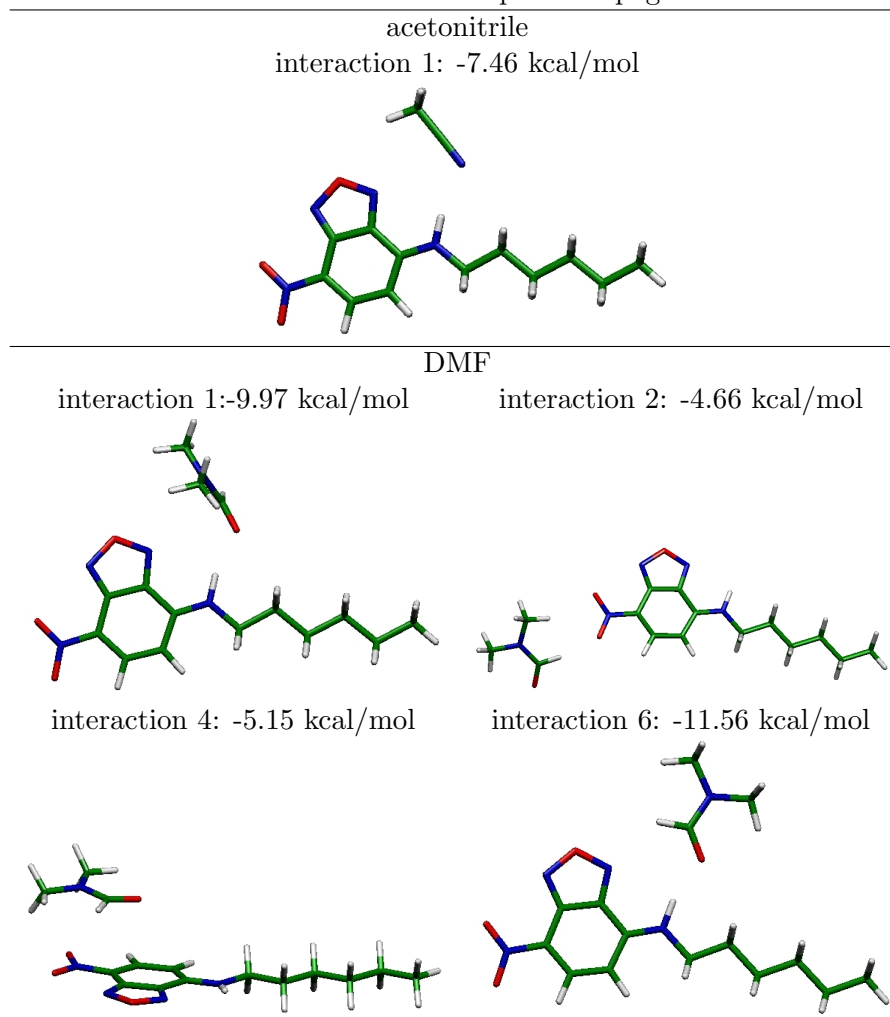
The interaction models obtained with this procedure are sketched in Figure A.2. We found *i*) two stable configurations for ethyl acetate, *ii*) one configuration for THF, *iii*) five for methanol, *iv*) one for acetonitrile and *v*) four for DMF. The interaction energies of all these model dimers, reported in Figure A.2, have been calculated without considering the basis set superposition error (BSSE). We have found that for all of the solvents, the most stable interaction takes place between the NH group of the dye and an electronegative atom of the solvent (nitrogen for acetonitrile and oxygen for all the other cases). The interaction energies estimated lie between 7 and 13 kcal/mol. The second most stable type of interaction is between the NO₂ group of the dye and a hydrogen bonded to an electronegative atom of the solvent, with an interaction energy between 4 and 7 kcal/mol. Interactions taking place outside the plane of the molecule are generally weaker, with interaction energies of the order of 2 or 3 kcal/mol, except interaction 4 of DMF. Further calculations have been carried out considering the BSSE but they provide very similar results.

Table A.2: Molecular geometries of the explicit interaction models between the V3 dye and one molecule of the solvent. Geometries optimized at the B3LYP/6-31G(d,p) level of theory.



Continues in the next page.

Continues from the previous page.



Then, we have calculated the excited state properties of the various dimers. Singlet excited states of all the interaction models have been calculated at the TD-DFT level. In Table A.3 we summarize the properties of the first excited state calculated for each interaction model. The orbitals mainly involved in the transitions from the ground to the first few excited states of all the interaction models are sketched in Table A.4. For the most stable interaction of each solvent, the transition from the ground to the low lying excited state is very similar to that in the gas phase in terms of orbitals involved (see Table A.4), transition dipole moment and oscillator strength. The excitation energies fall between 3.01 and 3.09 eV, very close to that of the isolated molecule (3.2 eV). In Figure A.6 the excitation energies from the ground to the first low lying excited state are reported for the most stable interaction model of each solvent, compared with the experimental absorp-

tion energy. As shown in Figure A.6, our interaction models qualitatively reproduce the non monotonic trend of the absorption energy with the solvent polarity. As in the case of the isolated molecule, TD-DFT calculations overestimate the experimental UV-Vis absorption energies of about 0.4 eV. These are still some small inconsistencies between theory and experiment but the use of more complex models, with many solvent molecules and using the PCM method to simulate polarization effects due to the second solvation shell, should result in a better agreement between theory and experiments but these investigation are out of the scope of this work.

Thus, we have demonstrated that specific interactions between dye and solvent actually take place and that our models of specific interaction are a good starting point to describe the optical properties of the V3 dye.

Table A.3: Properties of the first excited state of all the interaction models associated to each solvent. Interaction energies calculated at the B3LYP/6-31G(d,p) level. Excited state properties calculated at TD-B3LYP/6-31G(d,p) level. Calculations do not take into account the basis set superposition error.

solvent	interaction	interaction energy (kcal/mol)	excitation energy (eV)	excitation energy (nm)	oscillator strength
gas phase			3.1992	388	0.2444
ethyl acetate	1	-9.03	3.0992	400	0.2377
	2	-4.47	3.1425	395	0.2463
THF		-12.91	3.0841	402	0.2315
methanol	1	-6.32	2.4157	513	0.0001
	4	-5.32	2.4084	515	0.0018
	5	-12.13	3.0137	411	0.2057
	6	-2.94	3.2046	387	0.2524
	7	-3.69	3.2158	386	0.2532
acetonitrile		-7.46	3.0855	402	0.2216
DMF	1	-9.97	3.0690	404	0.2203
	2	-4.66	2.5057	495	0.0000
	4	-5.15	2.9751	417	0.0000
	6	-11.56	3.0663	404	0.0330

As reported in Table A.3, some dimers of methanol and DMF (interaction 1 and 4 of methanol and 2 and 4 of DMF) have a low lying excited state which is not dipole allowed (the oscillator strength goes from 0.0001 to 0.0018). The transition from the ground to this excited state of the molecular dimer lies between 2.4 eV and 2.5 eV with respect to the various interaction models, that is about 0.8 eV lower than the first dipole allowed excited state. The analysis of the orbitals (see Table A.4) shows that such

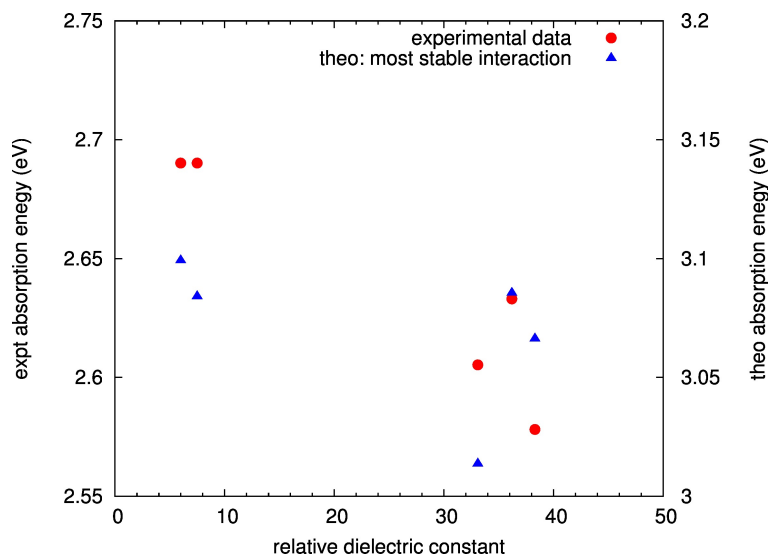
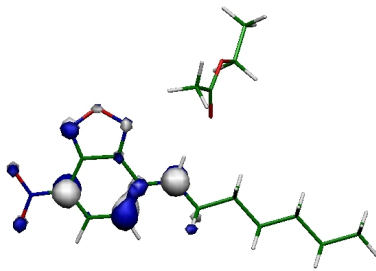
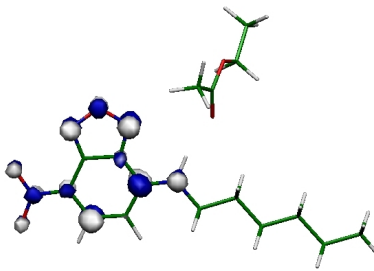
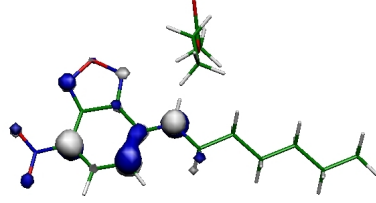
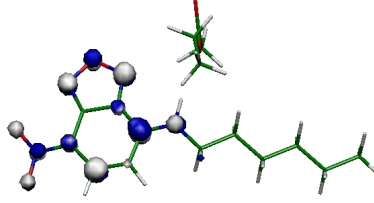
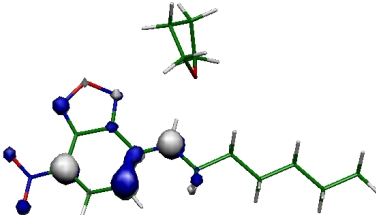
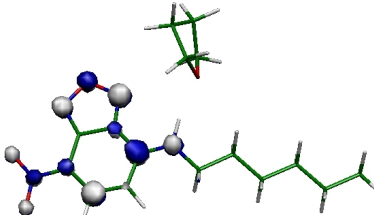


Figure A.6: Comparison between the experimental absorption energies of the V3 molecule in solution and those calculated for the most stable interaction model of Table A.2 for solvent. Excited states calculations carried out at TD-B3LYP/6-31G(d,p) on the B3LYP/6-31G(d,p) geometry of the first excited state.

a transition involves mainly the HOMO and LUMO orbitals of the dimer, where the former is mainly localized on the solvent and the latter on the V3 chromophore. Thus, this excited state has charge transfer character. We notice that the presence of this dipole forbidden excited state is selective with respect to the relative position of the solvent and of the dye. In all the dimers that present this charge transfer state, the NO_2 group of the V3 dye interacts with a hydrogen of the solvent.

The presence of such dipole forbidden state is very important since it introduces a possible mechanism for non radiative decay. However, the existence of such a charge transfer state and its actual energy position should be further investigated. In fact, the limitations of the theoretical method employed (TD-B3LYP and in general of TD-DFT methods with functionals containing a low exact exchange fraction) in describing charge transfer excited states are well known in the literature [133]. On the other hand, the prediction of a HOMO and LUMO orbitals fully localized respectively on the solvent and on the dye should be quite straightforward since the B3LYP functional generally provides a good description of the static properties of molecules. Moreover, a similar mechanism invoking a charge transfer dipole forbidden state has been reported recently in the literature on the basis of TD-DFT calculations for some organic dyes in solution [134, 135].

Table A.4: Properties of the low lying excited states of the interaction models between the V3 dye and the solvents (ethyl acetate, THF, methanol, acetonitrile and DMF). Calculations at the TD-B3LYP/6-31G(d,p) level on the B3LYP/6-31G(d,p) ground state optimized geometries.

state	excitation energy (eV)	oscillator strength	$\mu^{S^0 \rightarrow S^1}$ (atomic u.)	orbitals involved i → a	TD coeff.
ETHYL ACETATE					
Interaction 1					
S1	3.10	0.2377	1.77	HOMO LUMO	0.69
					
Interaction 2					
S1	3.14	0.2467	1.79	HOMO LUMO	0.69
					
THF					
Interaction 1					
S1	3.08	0.2315	1.75	HOMO LUMO	0.69
					

Continues in the next page


Continues from the previous page

state	excitation energy (eV)	oscillator strength	$\mu^{S^0 \rightarrow S^1}$ (atomic u.)	orbitals involved i \rightarrow a	TD coeff.
-------	------------------------	---------------------	--	--	-----------


METHANOL

Interaction 1

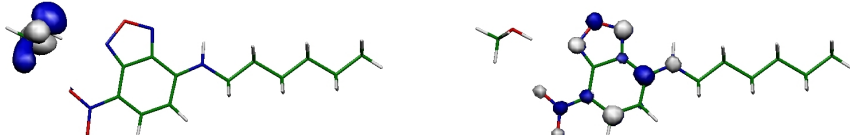
S1	2.42	0.0001	0.004	HOMO LUMO	0.69
----	------	--------	-------	-----------	------




S2	3.21	0.3000	1.95	HOMO-1 LUMO	0.69
----	------	--------	------	-------------	------


Interaction 4

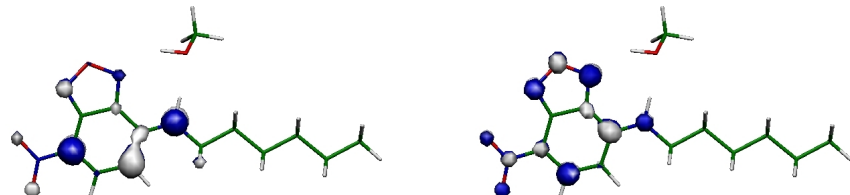
S1	2.41	0.0018	0.18	HOMO LUMO	0.69
----	------	--------	------	-----------	------



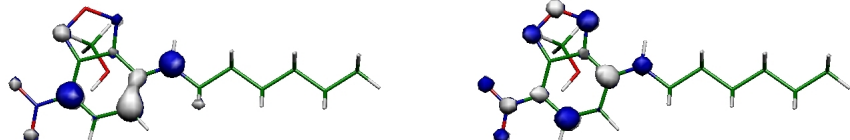
S2	3.16	0.2442	1.78	HOMO-1 LUMO	0.69
----	------	--------	------	-------------	------


Interaction 5

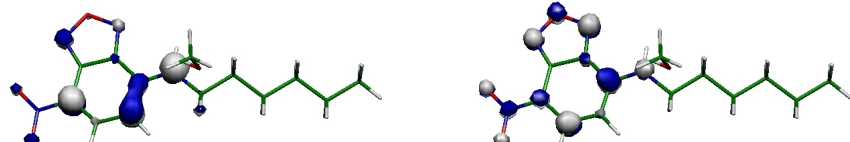
S1	3.01	0.2057	1.67	HOMO LUMO	0.69
----	------	--------	------	-----------	------


Interaction 6

S1	3.20	0.2524	1.79	HOMO LUMO	0.69
----	------	--------	------	-----------	------


Interaction 7

S1	3.22	0.2532	1.79	HOMO LUMO	0.69
----	------	--------	------	-----------	------



Continues in the next page

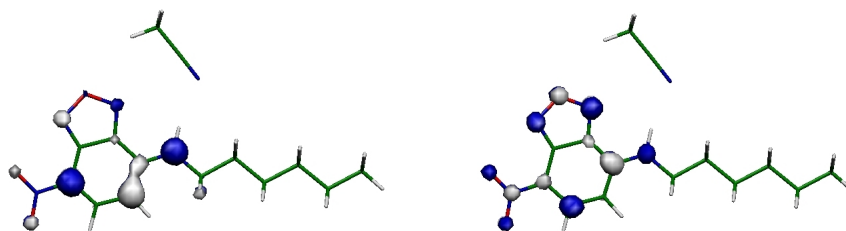
Continues from the previous page

state	excitation energy (eV)	oscillator strength	$\mu^{S^0 \rightarrow S^1}$ (atomic u.)	orbitals involved i \rightarrow a	TD coeff.
-------	------------------------	---------------------	--	--	-----------

ACETONITRILE

Interaction 1

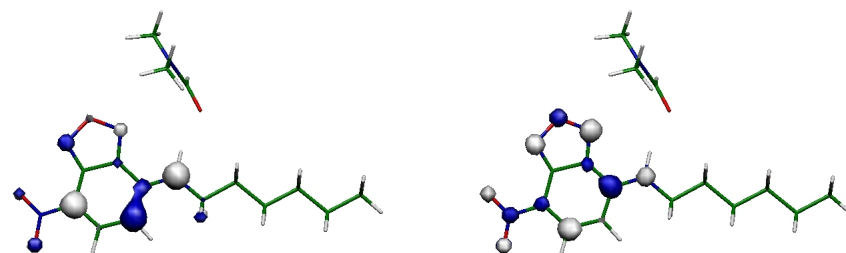
S1	3.09	0.2216	1.71	HOMO LUMO	0.69
----	------	--------	------	-----------	------



DMF

Interaction 1

S1	3.07	0.2203	1.71	HOMO LUMO	0.69
----	------	--------	------	-----------	------

**Interaction 2**

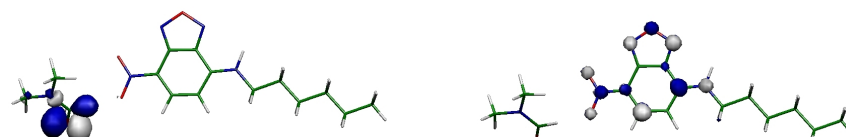
S1	2.51	0.0000	1.71	HOMO LUMO	0.69
----	------	--------	------	-----------	------



S2	2.72	0.0143	0.46	HOMO-1 LUMO	0.70
----	------	--------	------	-------------	------



S3	3.20	0.2897	1.92	HOMO-2 LUMO	0.70
----	------	--------	------	-------------	------



Continues in the next page

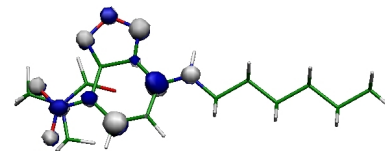
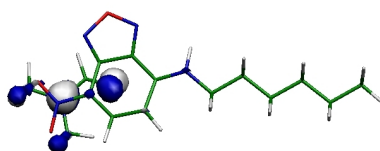
Continues from the previous page

state	excitation energy (eV)	oscillator strength	$\mu^{S^0 \rightarrow S^1}$ (atomic u.)	orbitals involved i \rightarrow a	TD coeff.
-------	---------------------------	------------------------	---	--	-----------

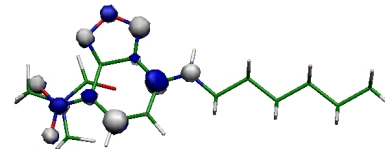
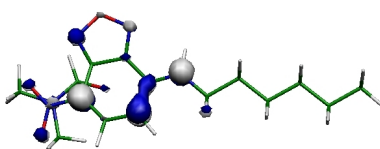
ACETONITRILE

Interaction 4

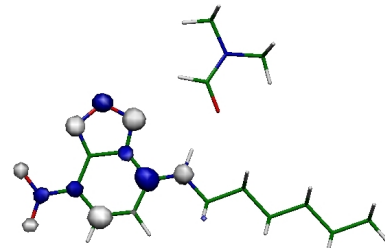
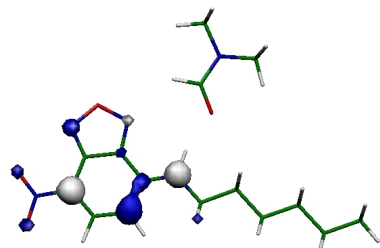
S1	2.98	0.0333	0.68	HOMO-1	LUMO	0.60
----	------	--------	------	--------	------	------



S2	3.18	0.2077	1.63	HOMO	LUMO	0.56
----	------	--------	------	------	------	------

**Interaction 6**

S1	3.07	0.2316	1.76	HOMO	LUMO	0.69
----	------	--------	------	------	------	------



Bibliography

- [1] J. S. Wu, W. Pisula, and K. Mullen. Graphenes as potential materials for electronics. *Chem. Rev.*, 2007:718–747, 2007.
- [2] S. R. Forrest. The path to ubiquitous and low-cost organic electronic appliance on plastic. *Nature*, 428:911–918, 2004.
- [3] J. Khandare, M. Calderón, N. M. Dagia, and R. Haag. Multifunctional dendritic polymers in nanomedicine: opportunities and challenges. *Chem. Soc. Rev.*, 41:2824–2848, 2012.
- [4] C. Castiglioni, M. Gussoni, J. T. Lopez-Navarrete, and G. Zerbi. A simple interpretation of the vibrational spectra of undoped, doped and photoexcited polyacetylene: Amplitude mode theory in the gf formalism. *Solid State Commun.*, 65:625–630, 1988.
- [5] M. Gussoni, C. Castiglioni, and G. Zerbi. *Spectroscopy of advanced materials*. John Wiley and Sons, 1991.
- [6] M. Linares, D. Beljonne, Jérôme Cornil, K. Lancaster, J. L. Brédas, S. Verlaak, A. Mityashin, P. Heremans A. Fuchs, C. Lennartz, and et. Al. On the interface dipole at the pentacenefullerene heterojunction: a theoretical study. *J. Phys. Chem. C*, 114:3215–3224, 2010.
- [7] M. Del Ben, R. W. A. Havenith, R Broer, and M. Stener. Density functional study on the morphology and photoabsorption of cdse nanoclusters. *J. Phys. Chem. C*, 115:16782–16796, 2011.
- [8] U. Schnupf and F. A. Momany. Dft energy optimization of a large carbohydrate: cyclomaltohexaicosaoase (ca-26). *J. Phys. Chem. B*, 116:6618–6627, 2012.
- [9] J. H. Yum, P. Walter, S. Huber, D. Rentsch, T. Geiger, F. Nüesch, F. De Angelis, M. Grätzel, and M. K. Nazeeruddin. Efficient far red sensitization of nanocrystalline tio2 films by an unsymmetrical squaraine dye. 129:10320–10321, 2007.

- [10] J.L. Bredás, D. Beljonne, V. Coropceanu, and J. Cornil. Charge-transfer and energy-transfer processes in pi-conjugated oligomers and polymers: a molecular picture. *Chem. Rev.*, 104:4971–5003, 2004.
- [11] Z. Guo, S. A. Jenekhe, and VO. V. Prezdhho. Overcoming exciton bottleneck in organic solar cells: electronic structure and spectra of novel semiconducting donor-acceptor block copolymers. *Phys. Chem. Chem. Phys.*, 13:7630–7636, 2011.
- [12] R. Colle, G. Grosso, A. Rozzani, and C. M. Zicovich-Wilson. Structure and x-ray spectrum of crystalline poly(3-hexylthiophene) from dft-vander waals calculations. *Phys. Status Solidi B*, 248:1360–1368, 2011.
- [13] R. G. Parr and W. Yang. *Density-Functional Theory of atoms and molecules*. Oxford University Press, New York, 1989, 1989.
- [14] M. A. L. Marques, C. A. Ullrich, F. Nogueira, A. Rubio, K. Burke, and E. K. U. Gross. *Time-Dependent Density Functional Theory*. Springer, 2012.
- [15] C. A. Ullrich. *Time-Dependent Density-Functional Theory: concepts and applications*. Oxford University Press, 2011.
- [16] C. Herrmann, K. Ruud, and M. Reiher. Can raman optical activity separate axial from local chirality? a theoretical study of helical decalanine. *Chem. Phys. Chem.*, 7:2189–2196, 2006.
- [17] R. Orlando and R. Bast, K. Ruud, U. Ekström, M. Ferrabone, B. Kirtman, and R. Dovesi. The first and second static electronic hyperpolarizabilities of zigzag boron nitride nanotubes. an ab initio approach through the coupled perturbed kohnsham scheme. *J. Phys. Chem. A*, 115:12631–12637, 2011.
- [18] C. Curuchet and B. Mennucci. Toward a molecular scale interpretation of excitation energy transfer in solvated bichromophoric systems. 127:11733–16744, 2005.
- [19] T. M. Figueira-Duarte and K. Mullen. Pyrene-based materials for organic electronics. *Chem. Rev.*, 111:7260–7314, 2011.
- [20] H. Sirringhaus. The reliability of organic field-effect transistors. *Adv. Mater.*, 21:38–39, 2010.
- [21] B. Kippelen and J.L. Bredás. Organic photovoltaics. *Energy Environ. Sci.*, 2:251–261, 2009.
- [22] A. W. Hains, Z. Liang, A. Woodhouse, and B. A. Gregg. Molecular semiconductors in organic photovoltaic cells. *Chem. Rev.*, 110:6689–6735, 2010.

- [23] J. Weickert, R. B. Dunbar, H. C. Hesse, W. Weidemann, and L. Schmidt-Mende. Nanostructured organic and hybrid solid cells. *Adv. Mater.*, 23:1810–1828, 2011.
- [24] C-Y. Chang, C-E. Wu, S-Y. Chen, C. Cui, Y-J. Cheng, C-S. Hsu, Y-L Wang, and Y Li. Enhanced performance and stability of a polymer solar cell by incorporation of vertically aligned, cross-linked fullerene nanorods. *Angew. Chem.*, 50:9386–9390, 2011.
- [25] S. H. Park, A. Roy, S. Beaupré, S. Cho, N. Coates, K Lee J . S. Moon D. Moss, M. Leclerc, and A. J. Heeger. Bulk heterojunction solar cells with internal quantum efficiency approach 100%. *Nature Photonics*, 3:297–303, 2009.
- [26] O. Ostroverkhova, D. G. Cooke, F. A. Hegmann, J. E. Anthony, V. Podzorov, M. E. Gershenson, o. D. Jurchescu, and T. T. M. Palstra. Ultrafast carrier dynamics in pentacene, functionalized pentacene, tetracene and rubrene single crystals. *Appl. Phys. Lett.*, 88:162101, 2006.
- [27] S. Yoo, B. Domercq, and B. Kippelen. Efficient thin-filmorganic solar cells based on pentacene/c60 heterojunction. *J. Appl. Phys.*, 85:5427–5429, 2004.
- [28] M. Pope and C. E. Swenberg. *Electronic processes in organic crystals*. Oxford University presst New York, 1982.
- [29] J. Jortner. Temperature dependent activation energy for electron transfer between biological molecules. *J. Chem. Phys.*, 64:4860–4867, 1976.
- [30] M. B. Smith and J. Michl. Singlet fission. *Chem. Rev.*, 110:6891–6936, 2010.
- [31] S. Singh, W. J. Jones, W. Siebrand, B. P. Stoicheff, and W. G. Schneider. Laser generation of excitons and fluorescence in anthracene crystals. *J. Chem. Phys.*, 42:333–342, 1965.
- [32] M. W. B. Wilson, A. Rao J. Clark, R. Sai Santosh Kumar, D. Brida, G. Cerullo, and R. H. Friend. Ultrafast dynamics of exciton fission in polycrystalline pentacene. 133:11830–11833, 2011.
- [33] A. Rao, M. W. B. Wilson, J. M. Hodgkiss, S. Albert-Seifried, H. Bassler, and R. H. Friend. Exciton fission and charge generation via triplet excitons in pentacene/c60 bilayers. 132:12698, 2010.
- [34] H. Liu, F. Yan, W. li, C-S. Lee, B. Chu, Y. Chen, X. Li, L. Han, Z. Su, J. Zhu, X. Kong, L. Zhang, and Y. Luo. Up-conversion luminescence

- of crystalline rubrene without any sensitizers. *Organic Electronics*, 11:946–950, 2010.
- [35] C. Wang, D. E. Schlamadinger, V. Desai, and M. J. Tauber. Triplet excitons in carotenoids formed by singlet fission in a membrane. *Chem. Phys. Chem.*, 12:2891–2894, 2011.
- [36] C. Wang and M. J. Tauber. High-yield singlet fission in a zeaxanthin aggregate observed by picosecond resonance Raman spectroscopy. 132:13988–13991, 2010.
- [37] M. R. Antognazza, L. Lüer, D. Polli, R. L. Christensen, R. R. Schrock, G. Lanzani, and G. Cerullo. Ultrafast excited state relaxation in long-chain polyenes. *Chem. Phys.*, 373:115–121, 2010.
- [38] S. T. Hoffmann, J.-M. Koenen, U. Scherf, I. Bauer, P. Strohriegel, H. Bassler, and A. Köler. Triplet-triplet annihilation in a series of poly(p-phenylene) derivatives. *J. Phys. Chem. B*, 115:8417–8423, 2011.
- [39] S. T. Roberts, R. E. McAnally, J. N. Mastron, D. H. Webber, W. T. Whited, R. L. Brutchey, M. E. Thompson, and S. E. Bradforth. Efficient singlet fission discovered in a disordered acene film. 134:6388–6400, 2012.
- [40] S. T. Roberts, C. W. Schlenker, V. Barlier, R. E. McAnally, Y. Zhang, J. N. Mastron, D. H. Webber, M. E. Thompson, and S. E. Bradforth. Observation of triplet exciton formation in a platinum-sensitized organic photovoltaic device. *J. Phys. Chem. Lett.*, 2:48–54, 2010.
- [41] A. Monguzzi, R. Tubino, and F. Meinardi. Multicomponent polymeric film for red to green low power sensitized up-conversion. *J. Phys. Chem. A*, 113:1171–1174, 2009.
- [42] A. Monguzzi, R. Tubino, and F. Meinardi. Diffusion enhanced up-conversion in organic systems. *Int. J. Photoenergy*, XXX:1–5, 2008.
- [43] A. Monguzzi, J. Mezyk, F. Scotognella, R. Tubino, and F. Meinardi. Upconversion-induced fluorescence in multicomponent systems: steady-state excitation power threshold. *Phys. Rev. B*, 78:195112/1–5, 2008.
- [44] S. Balushev, V. Yakutkin, T. Miteva, G. Wegner, T. Roberts, G. Nelles, A. Yasuda, S. Cherenov, S. Avlasevich, S. Aleshchenkov, and A. Cheprakov. A general approach for non-coherently excited annihilation up-conversion: transforming the solar-spectrum. *New J. Phys.*, 10:013007/1–12, 2008.

- [45] S. Balushev, V. Yakutkin, T. Miteva, G. Wegner, T. Roberts, G. Nelles, A. Yasuda, S. Cherenov, S. Avlasevich, S. Aleshchenkov, and A. Cheprakov. qualcos'altro. *New J. Phys.*, 999:999, 999.
- [46] H. Shpaisman, O. Niitsoo, I. Lubomirsky, and D. Cahen. Can up- and down- conversion and multi-exciton generation improve photovoltaics? *Sol. Energy Mater. Sol. Cells*, 92:1541–1546, 2008.
- [47] M. C. Hanna and A. J. Nozik. Solar conversion efficiency of photovoltaic and photoelectrolysis cells with carrier multiplication absorbers. *J. Appl. Phys.*, 100:074510/1–8, 2006.
- [48] J. Jortner, S. Choi, J. L. Katz, and S. A. Rice. Triplet energy transfer and triplet-triplet interaction in aromatic crystals. *J. Appl. Phys.*, 11:323–326, 1963.
- [49] J. Frenkel. On transformation of light into heat in solids. i. *Phys. Rev.*, 37:17–44, 1931.
- [50] A. S. Davydov. *Theory of molecular excitons*. McGraw-Hill, New York, 1962.
- [51] J. Jortner, S. A. Rice, J. L. Katz, and S. I. Choi. Triplet excitons in crystals of aromatic molecules. *J. Chem. Phys.*, 42:309–323, 1965.
- [52] R. Silbey, J. Jortner, and S. A. Rice. On the singlet-exciton states of crystalline anthracene. *J. Chem. Phys.*, 42:1515–1534, 1965.
- [53] G. D. Scholes and K. P. Ghiggino. Electronic interactions and interchromophore excitation transfer. *J. Phys. Chem.*, 98:4580–4590, 1994.
- [54] S. Yeganeh and T. Van Voorhis. Triplet excitation transfer with constrained density functional theory. *J. Phys. Chem. C*, 114:20756–20763, 2010.
- [55] Z. Q. You and C. P. Hsu. Ab initio study on triplet excitation energy transfer in photosynthetic light harvesting complexes. *J. Phys. Chem. A*, 115:4092–4100, 2011.
- [56] C. P. Hsu, P. T. Walls, M. Head-Gordon, and G. R. Fleming. The role of the s1 state of carotenoids in photosynthetic energy transfer: the light harvesting complex ii of purple bacteria. *J. Phys. Chem. B*, 105:11016–11025, 2001.
- [57] J. Neugebauer, C. Curuchet, A. Muñoz Losa, and B. Mennucci. A subsystem tddft approach for solvent screening effects on excitation energy transfer couplings. *J. Chem. Theory Comput.*, 6:1843–1851, 2010.

- [58] F. Lipparini and B. Mennucci. Embedding effects on charge-transport parameters in molecular organic materials. *J. Chem. Phys.*, 127:144706, 2007.
- [59] G. D. Scholes and Fleming. Calculation of couplings and energy-transfer pathways between the pigments of lh2 by the ab initio transition density cube method. *J. Phys. Chem. B*, 102:5378–5386, 1998.
- [60] D. Beljonne, J. Cornil, R. Silbey, P. Millié, and J. L. Brédas. Interchain interactions in conjugated materials: the exciton model versus the supermolecular approach. *J. Chem. Phys.*, 112:4749–4757, 2000.
- [61] J. Cornil, D. A. dos Santos, X. Crispin, R. Silbey, and J. L. Brédas. Influence of interchain interactions on the absorption and luminescence of conjugated oligomers and polymers: a quantum-chemical characterization. 120:1289–1299, 1998.
- [62] D. W. Schlosser and M. R. Philpott. Energy transfer in molecular crystals: nondipolar coulomb exciton transfer interactions in crystalline naphthalene and anthracene. 120:1289–1299, 1998.
- [63] C. P. Hsu. The electronic couplings in electron transfer and excitation energy transfer. *Acc. Chem. Res.*, 42:509–518, 2009.
- [64] T. Förster. Zwischenmolekulare energiewanderung und fluoreszenz. *Ann. Phys.*, 437:55–75, 1948.
- [65] S. Tretiak and S. Mukamel. Density matrix analysis and simulation of electronic excitations in conjugated aggregated molecules. *Chem. Rev.*, 102:3171–3212, 2002.
- [66] E. I. Rashba. Analysis of the exciton band spectrum using electron vibration spectra. *Soviet. Phys. Solid State*, 5:757–, 1963.
- [67] C. E. Swenberg and W. T. Stacy. Bimolecular radiationless transitions in crystalline tetracene. *Chem. Phys. Lett.*, 2:327–328, 1968.
- [68] T. S. Ahn, A. M. Müller, R. O. Al-Kaysi, F. C. Spano, J. E. Norton³, D. Beljonne, J.L. Brédas, and C. J. Bardeen. Experimental and theoretical study of temperature dependent exciton delocalization and relaxation in anthracene thin films. *J. Chem. Phys.*, 128:054505/1–11, 2008.
- [69] H. Najafov, B. Lee, Q. Zhou, L. C. Feldman, and V. Podzorov. Observation of long-range exciton diffusion in highly ordered organic semiconductors. *Nature Mater.*, 9:938–943, 2010.

- [70] L. S. Loo and K. K. Gleason. Fourier transform infrared investigation of the deformation behavior of montmorillonite in nylon-6/nanoclay nanocomposite. *Macromol.*, 36:2587–2590, 2003.
- [71] J. Shan and H. Tenhu. Recent advances in polymer protected gold nanoparticles: synthesis, properties and applications. *Chem. Commun.*, pages 4580–4598, 2007.
- [72] F. Granato, A. Bianco, C. Bertarelli, and G. Zerbi. Composite polyamide 6/polypyrrole conductive nanofibers. *Macromol. Rapid Commun.*, 30:453–458, 2009.
- [73] A. Bianco, G. Iardino, A. Manuelli, A. Bertarelli, and G. Zerbi. Strong orientation of polymer chains and small photochromic molecules in polyamide 6 electrospun fibers. *Chem. Commun.*, 8:510–514, 2007.
- [74] L. Eldada and L. W. Shacklette. Advances in polymer integrated optics. *IEEE J. Sel. Topics Quantum Electron.*, 6:54–68, 2000.
- [75] A. C. Grimsdale, K. L. Chan, R. E. Martin, P. G. Jokisz, and A. B. Holmes. Synthesis of light-emitting conjugated polymers for applications in electroluminescent devices. *Chem. Rev.*, 109:897–1091, 2009.
- [76] Y. J. Cheng, S. H. Yang, and C. S. Hsu. Synthesis of conjugated polymers for organic solar cell applications. *Chem. Rev.*, 109:5868–5923, 2009.
- [77] P. C. Painter, M. M. Coleman, and J. L. Koenig. *The theory of vibrational spectroscopy and its application to polymeric materials*. John Wiley and Sons, 1982.
- [78] G. Zerbi, H. W. Siesler, and I. Noda. *Modern polymer spectroscopy*. John Wiley and Sons Canada, 1999.
- [79] G. Zerbi, R. Magni, M. Gussoni, K. Holland Moritz, A. Bigotto, and S. Dirlikov. Molecular mechanics for phase transition and melting of *n*-alkanes: a spectroscopic study of molecular mobility of solid *n*-nonadecane. *Chem. Rev.*, 75:3175–3194, 1981.
- [80] G. Zerbi R. Piazza and K. Holland-Moritz. Transport of matter upon annealing in crystalline polymethylene systems: a calorimetric and spectroscopic study. *Polymer*, 23:1921–1928, 1982.
- [81] M. Tasumi and T. Shimanouchi. Crystal vibrations and intermolecular forces of polymethylene crystals. *J. Chem. Phys.*, 43:1245–1258, 1965.
- [82] S. Dasgupta, W. B. Hammond, and W. A. Goddard. Crystal structures and properties of nylon polymers from theory. 118:12291–12301, 1996.

- [83] S. Hirata and S. Iwata. Density functional crystal orbital study on the normal vibrations and phonon dispersion curves of all-trans polyethylene. *J. Chem. Phys.*, 108:7901–7908, 1998.
- [84] F. Javier Torres, B. Civalleri, C. Pisani, P. Musto, A. R. Albuñia, and G. Guerra. Normal vibrational analysis of a trans-planar syndiotactic polystyrene chain. *J. Phys. Chem. B*, 111:6327–6335, 2007.
- [85] A. R. Albuñia, P. Rizzo, G. Guerra, F. Javier Torres, B. Civalleri, and C. M. Zicovich-Wilson. Uniplanar orientations as a tool to assign vibrational modes of polymer chain. *Macromolecules*, 40:3895–3897, 2007.
- [86] J. Javier Torres, B. Civalleri, A. Meyer, P. Musto, A. R. Albuñia, P. Rizzo, and G. Guerra. Normal vibrational analysis of the syndiotactic polystyrene $s(2/1)_2$ helix. *J. Phys. Chem. B*, 113:5059–5071, 2003.
- [87] C. M. Zicovich-Wilson, B. Kirtman, B. Civalleri, and A. Ramírez-Solis. Periodic density functional theory calculations for 3-dimensional polyacetylene with empirical dispersion terms. *Phys. Chem. Chem. Phys.*, 12:3289–3293, 2010.
- [88] A. M. Ferrari, B. Civalleri, and R. Dovesi. Ab initio periodic study of the conformational behaviour of glycine helical homopeptides. *J. Comput. Chem.*, 31:1777–1784, 2011.
- [89] E. Dovesi, R. Orlando, B. Civalleri, C. Roetti, V. R. Saunders, and C. M. Zicovich-Wilson. Crystal: a computational tool for the ab initio study of the electronic properties of crystals. *Z. Kristallogr.*, 220:571–573, 2005.
- [90] M. J. Frisch, G. W. Trucks, H. B. Schlegel, G. E. Scuseria, M. A. Robb, J. R. Cheeseman, G. Scalmani, V. Barone, B. Mennucci, and G. A. Petersson et Al. Gaussian 09 Revision A.02. Gaussian Inc. Wallingford CT 2009.
- [91] G. Zerbi, F. Ciampelli, and V. Zamboni. Classification of crystallinity bands in the infrared spectra of polymers. *J. Polym. Sci. part. C*, 7:141–151, 1964.
- [92] P. Jurečka, Jiří Šponer, Jiří Černý, and Pavel Hobza. Benchmark database of accurate (mp2 and ccSD(T) complete basis set limit) interaction energies of small model complexes, dna base pairs and amino acid pairs. *Phys. Chem. Chem. Phys.*, 8:1985–1993, 2006.

- [93] J. G. Hill, J. A. Platts, and H. J. Werner. Calculation of intermolecular interactions in the benzene dimer using coupled-cluster and local electron correlation methods. *Phys. Chem. Chem. Phys.*, 8:4072–4778, 2006.
- [94] M. Schütz, G. Hetzer, and H. J. Werner. Low-order scaling local electron correlation methods. i. linear scaling local mp2. *J. Chem. Phys.*, 111:5691–5706, 1999.
- [95] S. Grimme. Improved second-order møllerplesset perturbation theory by separate scaling of parallel- and antiparallel-spin pair correlation energies. *J. Chem. Phys.*, 118:9095–9102, 2003.
- [96] S. Grimme. Density functional theory with london dispersion corrections. *WIRE Comput. Mol. Sci.*, 1:211–228, 2011.
- [97] M. Dion, H. Rydberg, E. Schröder, D. C. Langreth, and B. I. Lundqvist. Van der waals density functional for general geometries. *Phys. Rev. Lett.*, 92:246401/1–4, 2004.
- [98] D. C. Langreth, B. I. Lundqvist, S.D Chakarova-Käck, V. R. Cooper, M. Dion, P. Hyldgaard, A. Kelkkanen, J. Kleis, K. Lingzhu, L. Shen, P. G. Moses, E. Murray, A. Puzder, H. Rydberg, E. Schröder, and T. Thonhauser. A density functional for sparse matter. *J. Phys: Condens Matter*, 82:081101/1–15, 2009.
- [99] J. Kleis, B.I. Lundqvist D.C., Langreth, and E. Schrder. Towards a working density-functional theory for polymers: First-principles determination of the polyethylene crystal structure. *Phys. Rev. B*, 76:100201/1–4, 2007.
- [100] O. A. Vydrov and T. van Voorhis. Nonlocal van der waals density functional made simple. *Phys. Rev. Lett.*, 103:063004/1–4, 2009.
- [101] R. Ahlrichs, R. Penco, and G. Scoles. Intermolecular forces in simple systems. *Chem. Phys.*, 19:119–130, 1977.
- [102] W. T. M. Mooij, F. B. van Duijneveldt, J. G. C. M. van Duijneveldt-van de Rijdt, and B. P. van Eijck. Transferable ab initio intermolecular potentials. 1. derivation from methanol dimer and trimer calculations. *J. Phys. Chem. A*, 103:9872–9882, 1999.
- [103] M. Elstner, P. Hobza, T. Frauenheim, S. Suhai, and E. Kaxiras. Hydrogen bonding and stacking interactions of nucleic acid base pairs: A density-functional-theory based treatment. *J. Chem. Phys.*, 114:5149–5155, 2001.

- [104] Q. Wu and W. Yang. Empirical correction to density functional theory for van der waals interactions. *J. Chem. Phys.*, 116:515–524, 2002.
- [105] Urs Zimmerli, Michele Parrinello, and Petros Koumoutsakos. Dispersion corrections to density functionals for water aromatic interactions. *J. Chem. Phys.*, 120:2693–2699, 2004.
- [106] B. Civalleri, C. M. Zicovich-Wilson, L. Valenzano, and P. Ugliengo. B3lyp augmented with an empirical dispersion term (b3lyp-d*) as applied to molecular crystals. *Cryst. Eng. Comm.*, 10:405–410, 2008.
- [107] S. Grimme. Accurate description of van der waals complexes by density functional theory including empirical corrections. *J. Comput. Chem.*, 25:1463–1473, 2004.
- [108] S. Grimme. Semiempirical gga-type density functional constructed with a long-range dispersion correction. *J. Comput. Chem.*, 27:1788–1799, 2006.
- [109] M. P. Waller, H. Kruse, C. MÜch Lichtenfeld, and S. Grimme. Investigating inclusion complexes using quantum chemical methods. *Chem. Soc. Rev.*, 41:3119–3128, 2012.
- [110] A. Tkatchenko and M. Scheffler. Accurate molecular van der waals interactions from ground-state electron density and free-atom reference data. *Phys. Rev. Lett.*, 102:073005, 2009.
- [111] A. Bondi. van der waals volume radii. *J. Phys. Chem.*, 66:441–451, 1964.
- [112] C. R. Jacob and M. Reiher. Localizing normal modes in large molecules. *J. Chem. Phys.*, 130:084106/1–15, 2009.
- [113] M. Gussoni, C. Castiglioni, and G. Zerbi. *Handbook of vibrational spectroscopy*. Wiley and Sons: Chichester, U. K., 2001.
- [114] E. S. Clark. The molecular conformation of polytetrafluoroethylene: forms ii and iv. *Polymer*, 40:4659–4665, 1999.
- [115] E. S. Clark. The crystal structure of polyethylene, forms i and iv. *J. Macromol. Sci. B*, 45:201–213, 2006.
- [116] R. G. Brown. Vibrational spectra of polytetrafluoroethylene: Effects of temperature and pressure. *J. Chem. Phys.*, 40:2900–2908, 1964.
- [117] M. D’amore, G. Talarico, and V. Barone. Periodic and high-temperature disordered conformations of polytetrafluoroethylene chains: an ab initio modeling. 128:1099–1108, 2006.

- [118] M. Kimmig, G. Strobl, and B. Stühn. Chain reorientation in poly(tetrafluoroethylene) by mobile twin-helix reversal defects. *Macromolecules*, 27:2481–2495, 1994.
- [119] E. Espí, A. Salmerón, A. Fontecha, Y. Garcia, and I. Real. Plastic films for agricultural applications. *J. of Plastic films and sheeting*, 22:85–102, 2006.
- [120] W. G. van Sark, K. W. J. Barnham, L. H. Slooff, A. J. Chatten, A. Bchtemann, A. Meyer, S. J. McCormack, R. Koole, D. J. Farrell, R. Bose, E. E. Bende, A.R. Burgers, and T. Budel et Al. Luminescent solar concentrators - a review of recent results. *Optic Express*, 16:21773–, 2008.
- [121] M. Suzuki, Y. Husimi, H. Komatsu, K. Suzuki, and K. T. Douglas. Quantum dot fret biosensors that respond to ph, to proteolytic or nucleolytic cleavage, to dna synthesis, or to a multiplexing combination. 130:5720–5725, 2008.
- [122] A. Sukhanova, A. S. Sussha, A. Bek, S. Mayilo, A. L. Rogach, J. Feldmann, V. Oleinikov, B. Reveil, B. Donvito, J. H. M. Cohen, and I. Nabiev. Nanocrystal-encoded fluorescent microbeads for proteomics: antibody profiling and diagnostics of autoimmune diseases. *Nano Lett.*, 7:2322–2327, 2007.
- [123] Q. Zhang, T. Atay, J. R. Tischler, M. S. Bradley, V. Bulovi, and A. V. Nurmikko. Highly efficient resonant coupling of optical excitations in hybrid organic/inorganic semiconductor nanostructures. *Nat. Nanotechnol.*, 2:555–559, 2007.
- [124] D. M. Willard, L. L. Carillo, J. Jung, and A. Van Orden. Cdsezns quantum dots as resonance energy transfer donors in a model protein-protein binding assay. *Nano Lett.*, 1:469–474, 2001.
- [125] A. R. Clapp, I. L. Medintz, J. Matthew Mauro, B. R. Fisher, M. G. Bawendi, and H. Mattoussi. Fluorescence resonance energy transfer between quantum dot donors and dye-labeled protein acceptors. 126:301–310, 2004.
- [126] A. R. Clapp, I. L. Medintz, H. Tetsuo Uyeda, B. R. Fisher, E. R. Goldman, M. G. Bawendi, and H. Mattoussi. Quantum dot-based multiplexed fluorescence resonance energy transfer. 127:18212–18221, 2005.
- [127] T. Pons, I. L. Medintz, X. Wang, D. S. English, and H. Mattoussi. Solution-phase single quantum dot fluorescence resonance energy transfer. 128:15324–15331, 2006.

- [128] H. Lu, O. Schöps, U. Woggon, and C. M. Niemeyer. Self-assembled donor comprising quantum dots and fluorescent proteins for long-range fluorescence resonance energy transfer. *130*:4815–4827, 2008.
- [129] M. Artemyev, E. Ustinovich, and I. Nabiev. Efficiency of energy transfer from organic dye molecules to cdse/zns nanocrystals: nanorods versus nanodots. *131*:8061–8065, 2009.
- [130] M. Hardzei, M. Artemyev, M. Molinari, M. Troyon, A. Sukhanova, and I. Nabiev. Comparative efficiency of energy transfer from cdse-zns quantum dots or nanorods to organic dye molecules. *Chem. Phys. Chem.*, *13*:330–335, 2012.
- [131] D. Jacquemine, V. Wathelet, E. A. partète, and C. Adamo. Extensive td-dft benchmark: singlet-excited states of organic molecules. *J. Chem. Theory Comput.*, *5*:2420–2435, 2009.
- [132] J. Tomasi, B. Mennucci, and Roberto Cammi. Quantum mechanical continuum solvation models. *Chem. Rev.*, *105*:2999–3094, 2005.
- [133] A. Dreuw, J. L. Weissman, and M. Head-Gordon. Long-range charge-transfer excited states in time-dependent density functional theory require non-local exchange. *J. Chem. Phys.*, *119*:2943–2946, 2003.
- [134] G. J. Zhao and K. L. Han. Early time hydrogen-bonding dynamics of photoexcited coumarin 102 in hydrogen-donating solvents: theoretical study. *J. Phys. Chem. A*, *111*:2469–2474, 2007.
- [135] G. J. Zhao, J. Y. Liu, L. C. Zhou, and K. L. Han. Site-selective photoinduced electron transfer from alcoholic solvents to the chromophore facilitated by hydrogen bonding: a new fluorescence quenching mechanism. *J. Phys. Chem. B*, *111*:8940–8945, 2007.